QUANTUM COHERENCE AND SUPERRADIANT EMISSION: FROM LASING WITHOUT INVERSION TO SKY LASER AND THE QASER

A Dissertation

by

LUQI YUAN

Submitted to the Office of Graduate and Professional Studies of
Texas A&M University
in partial fulfillment of the requirements for the degree of

DOCTOR OF PHILOSOPHY

Chair of Committee,	Marlan O. Scully
Committee Members,	Alexei V. Sokolov
	M. Suhail Zubairy
	Goong Chen
Head of Department,	George R. Welch

December 2014

Major Subject: Physics

ABSTRACT

This work is focused on quantum coherence and superradiant emission in a dense pencil-like multi-level medium where many novel effects appear such as transient lasing without inversion, coherence-brightened sky laser, and quantum amplification by superradiant emission of radiation.

We start from an interesting cascade model where quantum coherence effects can lead to surprising phenomena, gain without population inversion and gain suppression, under different parameters. We further show superradiant emission inside helium plasma. The population evolution shows the decay is significantly faster than collisional decoherence and spontaneous decay rates. This indicates superradiant coherent behavior of the atomic system inside the plasma.

Based on these results, we demostrate lasing without inversion on a time scale shorter than the decoherence time. The possibility of transient lasing without inversion holds promise for lasing in the extreme-ultraviolet/x-ray regime. We propose experiments to demonstrate this in helium or helium-like ions plasma.

We also study coherent emission from ambient air and demonstrate efficient generation of laser-like beams directed both forward and backward with respect to a nanosecond ultraviolet pumping laser beam. The emission process exhibits nonadiabatic quantum coherence, which is similar in nature to Dicke superradiance. This coherence-brightened backward light source in air provides possibility for atmospheric remote sensing through a phase-matched coherent Raman scattering process.

Finally, we present a new kind of quantum amplifier, the QASER (quantum amplification by superradiant emission of radiation), based on collective superradiant emission which does not require initial population in the excited state. We show

that parametric resonance between the driving field and collective superradiant oscillations of the atomic polarization can yield light amplification at high frequencies. The resulting superradiant amplifier is many orders of magnitude more efficient than nonlinear multiphoton excitation and holds promise as a new way to generate high-frequency coherent radiation.

ACKNOWLEDGEMENTS

I hereby thank all my family, my advisor, my colleagues, and my friends for their support and help during my Ph.D. career.

I would like to first thank my advisor, Marlan O. Scully who gives me various opportunities to study and do research in the field of quantum optics. I also want to thank my colleagues: Alexei Sokolov, Aleksei Zheltikov, Anatoly Svidzinsky, Da-wei Wang, Andrew Traverso, Christopher O'Brien, Kai Wang, Miaochan Zhi, Xi Wang, Brett Hokr, Zhenhuan Yi, Hui Xia, Konstantin Dorfman, Olga Kocharovskaya, Torsten Siebert, Szymon Suckewer, Yuri Rostovtsev, Vladimir Sautenkov, George Welch, Suhail Zubairy, Goong Chen, Wolfgang Schleich, Dmitry Pestov, Sumanta Das, Pankaj Jha, Dmitri Voronine, Gombojav Ariunbold, Kimberly Chapin, Han Cai, Luojia Wang, Moochan Kim and many others. Their help made this dissertation possible. I also thank all my friends for giving me a wonderful time in College Station.

Last, but not least, I would like to thank my family (my wife, Ziyun Di, my daughter, Amelia D. Yuan, and my parents, Aimei Huang and Zhongping Yuan) for accompanying me no matter where they are.

TABLE OF CONTENTS

Page

LIST OF FIGURES

FIGURE Page

1. INTRODUCTION

1.1 Quamtum coherence and superradiant emission

The effects of quantum coherence [1, 2] in laser physics have been the subject of substantial theoretical and experimental study. For example, mitigation of spontaneous emission effects (in order to reduce the laser line width) in the correlated emission laser have been predicted [3, 4] and observed [5]. Large quantum coherence triggers superradiant emission in both the superradiance and the superfluorescence processes.

Superradiance (speed up of spontaneous emission) of atomic ensembles is a collective phenomenon which offers interesting directions of exploration [6]. It was first predicted by Dicke in 1954 [7]. Later on it was observed by Feld and co-workers in HF gas [8] who also gave a theoretical explanation of how an initially inverted two-level system evolves into a superradiant state [9, 10]. It features an enhanced spontaneous decay rate much greater than that of an isolated single atom. Influence of virtual transitions on collective emission as well as non-local (retardation) effects are both subjects of current theoretical [11, 12, 13, 14, 15] and experimental [16] investigation. Cooperative effects of spontaneous emission can be used for optical quantum-state storage, quantum cryptography [17] and quantum information [18].

Superfluorescence is another collective process in which the superradiant state is developed in a system of initially uncorrelated excited atoms [19]. This process starts with normal spontaneous emission but later develops correlations between the atoms [20]. The main distinction between superradiance and superfluorescence is the initial coherence. In superradiance, the system is initially coherent, whereas in superfluorescence, the coherence builds up in an initially incoherent inverted medium. In the

past half century, both types of phenomena, superradiance and superfluorescence, were extensively studied theoretically and experimentally.

The presence of quantum coherence yields many interesting effects. In particular, it can lead to superfluorescence without inversion [21, 22, 23, 24, 25]. In such systems coherence created by a driving field on one transition influences superfluorescence on another transition. Quantum coherence can also yield lasing without inversion [26, 27, 28] which has been extensively studied during the last two decades [29, 30, 31, 32]. In Section 2, quantum coherence effect in the superradiant emission in a three-level cascade scheme will be studyed [33]. Gain without population inversion and gain suppression in different propagation directions are discussed .

1.2 Lasing without inversion*

The concept of lasing without population inversion (LWI) holds promise for making lasers in the extreme ultraviolet (XUV) and x-ray spectral regions where population inversion is hard to achieve. Many schemes for LWI have been proposed for various media in the literature, such as in gas [34], circuit quantum electrodynamics [35], and terahertz intersubband-based devices [36].

Coherence between excited and lower level doublets is frequently associate with Λ and V atomic configurations as in Fig. 1.1. In the past, LWI experiments typically required $\gamma_{a\to c}$ in Λ and $\gamma_{c\to b}$ in V systems to be greater than $\gamma_{a\to b}$. Here $\gamma_{i\to j}$ is the spontaneous decay rate from level i to level j. The physical reason for this condition on the rates can be seen by considering the dark and bright states in the Λ system

*Reprinted with permission from "Transient lasing without inversion via forbidden and virtual transitions" by L. Yuan, D. Wang, A. A. Svidzinsky, H. Xia, O. Kocharovskaya, A. Sokolov, G. R. Welch, S. Suckewer, and M. O. Scully, 2014. Phys. Rev. A, vol. 89, pp. 013814, Copyright [2014] by the American Physical Society.

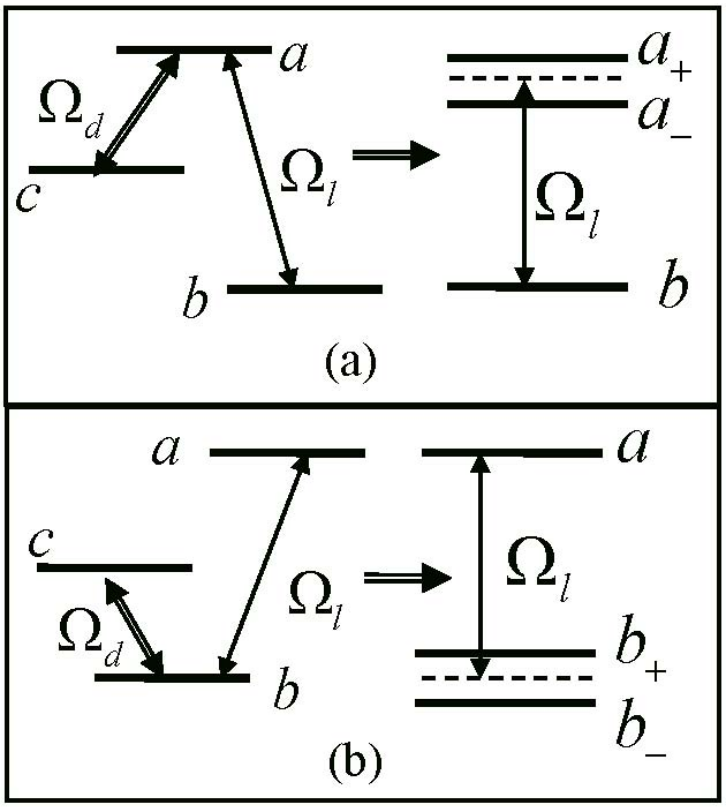

Figure 1.1: Upper (a) [lower (b)] level doublet in the dressed state basis as produced by drive laser between a and c (b and c). The drive Rabi frequency is Ω_d and the laser Rabi frequency is Ω_l. The double line means a much larger Rabi frequency in the drive transition than the Rabi frequency in the lasing transition as indicated by the single line.

as an example

$$|D\rangle = \frac{\Omega_l|c\rangle - \Omega_d|b\rangle}{\sqrt{\Omega_l^2 + \Omega_d^2}}, \tag{1.1}$$

$$|B\rangle = \frac{\Omega_d|c\rangle + \Omega_l|b\rangle}{\sqrt{\Omega_l^2 + \Omega_d^2}}. \tag{1.2}$$

The drive field Rabi frequency Ω_d is much larger than the lasing field Rabi frequency Ω_l. Thus, if the injection is in the state $|c\rangle$ then there is (small) probability $\Omega_l/\sqrt{\Omega_l^2 + \Omega_d^2}$ of finding the atom in the dark state where it stays never absorbing laser radiation. There is a larger probability $\Omega_d/\sqrt{\Omega_l^2 + \Omega_d^2}$ of injection in the bright state. The bright state can be excited to the $|a\rangle$ level where the atom can decay to $|c\rangle$ with a rate $\gamma_{a\to c}$ and the process is repeated. Every cycle has a chance of emitting a laser photon and going into the dark state. However, if the atom decays from state $|a\rangle$ to state $|b\rangle$ (with a rate $\gamma_{a\to b}$) then this atom is lost from the game (without contributions to the laser) since it is essentially the $|b\rangle$ state in the dark state $|D\rangle$ for $\Omega_d \gg \Omega_l$.

Therefore the decay rate on the drive transitions must be greater than the decay rate of the lasing transitions $\gamma_{a\to b}$. Then coherence ρ_{ac} reaches quasi steady state. Under such condition ρ_{ac} can yield LWI at the $a - b$ transition [37]. Several experiments have provided evidence of amplification and LWI in the optical domain [38, 39].

The present work has been stimulated by and is an extension of our recent experiment [40] of atomic coherence effects in the triplet manifold of Helium and Helium-like ions. The details of this study are given in Section 3. In that case, coherence effects can play a role in systems with fast collisions. In Section 4, we study the possibility of LWI occuring on a time scale much shorter than spontaneous decay and fast collision times [41]. This allows us to take advantage of coherence effects, but

requires investigation of the system's dynamics in a transient regime far from steady state. We further combine the concepts of transient LWI and of the sideband generation to realize frequency comb generation at high frequencies. This result provides a new route toward a multiple-frequency coherent light source and have implications for table-top short-wavelength coherent light sources in the XUV and x-ray regime [42, 43].

1.3 Coherence-brightened laser source

It has been proposed that a mirrorless laser can be used as a superradiant source where coherence is large, such as a coherence brightened laser [7, 44, 45, 46]. This type of superradiance was first demonstrated in optically pumped HF gas [8]. Sweeping the gain, where multiple gain regions are used to stimulate each other, can enhance the superradiant emission [47]. Gain-swept superradiance in air may be used to realize various nonlinear optical remote sensing schemes such as, two-photon absorption [48], stimulated Raman scattering [49, 50], polarization Kerr effect (RIKES) spectroscopy [51], and others. Nonadiabatic coherence is a fundamental characteristic of coherence brightened emission processes like superradiance and superfluorescence, and occurs when the macroscopic polarization of the medium changes more quickly than the decoherence rates.

Stimulated emission in atomic oxygen - the key physical effect behind laser-like beam generation from ultraviolet-pumped atmospheric air - was first observed by Aldén et al. [52]. They used 3 mJ, 5 ns, 226 nm laser pulses to simultaneously photodissociate molecular oxygen and excite the atomic oxygen product along the $2p^3P \rightarrow 3p^3P$ transition causing a population inversion and allowing for the stimulated emission via the $3p^3P \rightarrow 3s^3S$ transition at 845 nm. This discovery initiated an in-depth examination of the stimulated emission as a tool for flame and flow di-

agnostics in the early 1990s, including the analysis of laser-power and gas-pressure dependence of the stimulated emission signal [53], as well as the kinetics of the relevant populations [54].

Nearly two decades after the work on the stimulated emission performed in the context of flame and flow diagnostics, a renewed interest in laser-like emission from open air is motivated by the need for chemically selective stand-off detection of trace gases in the atmosphere [55]. Laser-like emission provides a promising tool for a broad class of all-optical stand-off detection methods, as it suggests a physical mechanism whereby a high-brightness, highly directional back-propagating light beam can be generated directly in ambient air. As proposed by earlier work on stimulated emission via femtosecond filamentation [56], the generation of backward-directed lasing in air, using air's dominant constituents such as nitrogen or oxygen, is very promising for remote atmospheric spectroscopy.

The possibility of remote lasing of atmospheric oxygen has been shown by using sub-mJ picosecond UV laser pulses at 226 nm that produce a bright near-infrared laser source at 845 nm wavelength using atomic oxygen as the gain medium [57]. In Section 5, we show the work on the creatation of a laserlike source in air by pumping with a nanosecond pulse [58]. The source generates radiation in the forward and backward directions. We find that the spiky emission in the experiment is due to quantum coherence via cooperation between atoms of an ensemble, which leads to strong-oscillatory superfluorescence [59]. Understanding these coherence-brightened processes in air should lead to improvements in environmental, atmospheric remote sensing and other applications.

1.4 Coherent backscattering for standoff spectroscopy

The universal requirement of momentum conservation in coherent light matter interactions imposes stringent limitations on the range of wave-vector directions allowed for coherent signals [2, 60, 61]. Specifically, generation of backward-propagating beams in nonlinear wave-mixing processes has been a long-standing problem in optical science, impeding the application of wave-mixing-based techniques to standoff detection [47, 62]. When applied to a generic third-order process generating a field with a frequency ω_4 through the coherent mixing $\omega_1 \pm \omega_2 \pm \omega_3$ of light fields with frequencies ω_1, ω_2, and ω_3, momentum conservation translates into the following requirement for the wave vectors $\mathbf{k_i} = n_i\omega_i/c$ of the optical fields $i = 1, 2, 3$ involved in the wave-mixing process (c is the speed of light in vacuum and $n_i = n(\omega_i)$ is the index of refraction at the frequency ω_i): $\Delta\mathbf{k} = \mathbf{k_4} \pm (\mathbf{k_1} \pm \mathbf{k_2} \pm \mathbf{k_3}) = 0$. With properly designed periodic structures, this phase-matching condition can be satisfied by picking up the momentum deficit from the reciprocal lattice of the structure. This approach has been successfully demonstrated with a variety of photonic structures [63, 64]. In the standoff detection mode, however, creation of subwavelength lattices, needed to phase-match the backward wave, is technically difficult requiring a complex arrangement of auxiliary high-power laser beams [62] or modulating the index of refraction [65]. In the microscopy mode, backward coherent anti-Stokes Raman scattering (CARS) becomes possible [66] due to the specific geometry of tightly focused light beams scattered by microinhomogeneities in a biotissue. None of such epi-CARS microscopy beam-interaction geometries, however, seems to suggest a realistic way of scaling to larger beam propagation paths that are needed for optical standoff detection.

Experimental demonstrations of backward stimulated emission from atomic oxy-

gen produced by UV laser pulses in the air, yielding a highly directional backward-propagating light beam with an excellent quality and an average power well above the microwatt level (see Section 5), offers a powerful tool for standoff spectroscopy. Still, in order to benefit from the chemical selectivity provided by the Raman effect, and to obtain efficient (coherent) signal generation, the $\Delta\mathbf{k} = 0$ momentum conservation (phasematching) needs to be satisfied. Coherent Raman scattering of laser fields can give rise to a highly directional (phase-matched) nearly backpropagating CARS signals, and to use phasematching to resolve individual signal components in space. This regime of the Raman effect, referred to hereinafter as coherent Raman Umklappscattering, by analogy with phonon-phonon and electron-phonon Umklapp-scattering in solids [67], is shown to be well suited for standoff detection applications, including remote sensing of trace gases in the atmosphere and on the surfaces of distant objects, paving the way for the development of a new class of security and ecological safety monitoring systems.

Coherent anti-Stokes Raman scattering by molecular vibrations [66, 68] and molecular rotations [69, 70] has a broad range of applications. For example, the real-time detection of a low concentration of bacterial endospores ($\approx 10^4$ spores) via CARS was demonstrated [71, 72]. The waveguide Raman effect in a variety of specialty fibers [73, 74, 75, 76] is promising for bio and chemical sensing applications. We note that the traditional CARS cannot be used in a standoff mode in scenarios involving perfectly parallel forward and backward propagating laser beams, because of the phasematching constraints. However, we show that under certain conditions, a small angle between laser beams satisfies phasematching. Moreover, the angled geometry provides a convenient spatial separation of the applied laser and generated signal beams [77, 78]. The corresponding spatial separation of various Raman transition lines allows improving detection capabilities which in conventional spec-

trally separated methods may be limited by detector resolution or by spectral line broadening.

In Section 6, we will present two different Raman spectroscopy methods, which are powered by quantum coherence, for remote sensing. In the first method, we identify the conditions for coherent Raman scattering to enable the geenration of phase-matched, highly directional, nearly-backward-propagating light beams with the use of the backward coherence-brightened laser source in air [79]. In the second method, we show the possibility to generate an intense coherent backwrad signal via a Raman-type four-wave-mixing process using forward propagating fields only [80]. Modulations of the quantum coherence to make phasematching, via either the geometry of the beams or the reflective index due to plasma, are the key to make both technologies possible.

1.5 Collective oscillation of superradiant emission[†]

Phase matching between intense classical laser fields is another essential feature of nonlinear optics. But with the advent of giant nonlinearities made possible by electromagnetically included transparency and ultra-slow light we were asked: Can we have phase matching at the single photon level? Our answer is yes and this interesting question stimulated much of the recent work on single photon superradiance which focuses on collective, virtual and nonlocal effects [6, 11, 16, 81, 82, 83, 84]. In particular, in the Dicke model of N two level ($|a\rangle$ and $|b\rangle$) atoms [7] in a small atomic sample of radius R much less than the radiation wavelength λ the symmetric

[†]Reprinted with permission from "Quantum Amplification by Superradiant Emission of Radiation" by A. A. Svidzinsky, L. Yuan, and M. O. Scully, 2013. Phys. Rev. X, vol. 3, pp. 041001, Copyright [2013] by the American Physical Society.

state with only one atom excited

$$|\Psi_s\rangle = \frac{1}{\sqrt{N}} \sum_{j=1}^{N} |b_1, b_2 \cdots a_j \cdots b_N\rangle, \tag{1.3}$$

decays to the ground state $|b_1, b_2 \cdots b_j \cdots b_N\rangle$ at the rate $\Gamma_s = N\gamma$ where γ is the single atom spontaneous decay rate. Dicke called this "the greatest radiation anomaly" of superradiance. However, if $R \gg \lambda$ the state (1.3) will trap light decreasing the emission rate.

Nevertheless it is possible to prepare a phased (timed) state excited by a photon of wave vector $\mathbf{k}_0$ and frequency ν_0 [81]

$$|\Psi_p\rangle = \frac{1}{\sqrt{N}} \sum_{j=1}^{N} e^{i\mathbf{k}_0 \cdot \mathbf{r}_j} |b_1, b_2, \cdots a_j \cdots b_N\rangle, \tag{1.4}$$

which, to a good approximation, decays with the enhanced rate $\Gamma_p \cong N\gamma\lambda^2/R^2$. Physically the phase factors in Eq. (1.4) $\exp(i\mathbf{k}_0 \cdot \mathbf{r}_j) = \exp(i\nu_0 \Delta t_j)$, where $\Delta t_j = \hat{k}_0 \cdot \mathbf{r}_j/c$, arise from the fact that atoms at the front of the sample are excited first and atoms further down stream at position $\mathbf{r}_j$ are excited later [81].

However, when the cloud radius is large compared to the superradiant pulse length c/Γ_p things become even more interesting [6, 11, 15]. In such a case the emitted photon is reabsorbed and reemitted many times as shown in Fig. 1.2. This limit is the essence of cavity QED where photons in a cavity resonantly interact with a single atom. If initially there are $N_{\rm ph}$ photons and the atom is in the ground state than the probability to find the atom excited oscillates as

$$P_{\rm cavity} = \sin^2\left(\frac{\wp}{\hbar}\sqrt{\frac{\hbar\nu N_{\rm ph}}{\epsilon_0 V_{\rm ph}}}t\right), \tag{1.5}$$

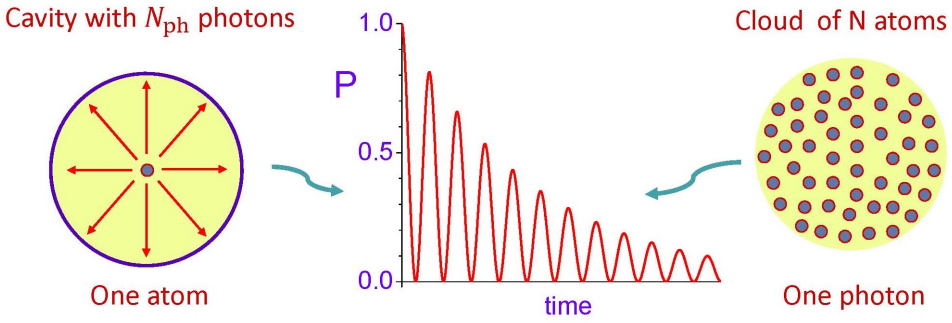

Figure 1.2: For a very large cloud, the photon is reabsorbed and reemitted many times and the atomic state oscillates with a frequency that goes as $\sqrt{N}$. This is to be compared to the cavity QED scenario in which an atom is cycled between the ground and excited states with a frequency which goes as $\sqrt{N_{ph}}$ where N_{ph} is the number of photons in the cavity. P is the probability that an atom is excited.

here $\wp$ is the atomic transition matrix element, $\hbar\nu$ is the photon energy and $V_{\rm ph}$ is the cavity volume. However in the present case, when a single photon interacts with a large cloud of N atoms in free space the probability to find an atom excited is [11, 15]

$$P_{\rm cloud} = \sin^2\left(\frac{\wp}{\hbar}\sqrt{\frac{\hbar\nu N}{\epsilon_0 \mathcal{V}}}t\right), \tag{1.6}$$

where the cavity volume $V_{\rm ph}$ and the photon number $N_{\rm ph}$ is replaced with the cloud volume $\mathcal{V}$ and the number of atoms N.

The question naturally arises: "The stimulated emission implied by Eq. (1.5) is the basis for the laser. Does Eq. (1.6) suggest a corresponding new but different (since collective spontaneous emission is different from stimulated emission) source of coherent radiation?" As we shall see the answer is yes, module certain somewhat subtle considerations. In particular we here show, for the first time, that utilizing collective superradiant emission we can generate coherent light at high frequency in the UV or X-ray bands by driving the atomic system with a low frequency (e.g. infrared) source. This involves a phase dependent quantum gain as in the case of

lasing without inversion (LWI) which is another example of quantum amplification. We call the present device which generates high frequency light through quantum amplification by superradiant emission of radiation the QASER.

We present our recent work on QASER in Section 7 [85]. As a new kind of quantum amplifier based on collective superradiant emission, QASER does not need any population in the excited state. We show that parametric resonance between the driving (e.g. infrared) field and collective superradiant oscillations of the atomic polarization can yield light amplification at high (e.g. XUV) frequencies. The resulting superradiant amplifier is many orders of magnitude more efficient than the usual nonlinear multiphoton excitation and holds promise for a new kind of generator of high frequency coherent radiation.

2. QUANTUM COHERENCE EFFECT IN YOKED SUPERFLUORESCENCE SCHEME*

2.1 Introduction

Yoked superfluorescence [86] is an example of manifestation of quantum coherence. It occurs in a three-level cascade system initially prepared with coherence between the upper and the ground states. Such coherence can be produced by a laser pump pulse propagating through the medium (the direction along the pump we call "forward", and against the pump "backward"). The laser pulse can excite the upper level from the ground state, e.g., by a two-photon process which creates some initial population in the upper level. Since the intermediate level is initially empty there is population inversion between the upper and the intermediate levels which triggers superfluorescence in this transition. Both experimental and theoretical studies show suppression of the gain in the forward direction [87, 88, 89] at early times, when there is no population in the intermediate level, *i.e.* there is population inversion between the upper two levels but no population inversion between the lower two. As soon as the intermediate level becomes populated it decays into the ground state emitting photons mainly in the forward direction [86, 90, 91].

In this section,we here consider a medium composed of three-level atoms (cascade scheme) which is prepared with arbitrary uniform population distribution [33]. There is initial coherence between the upper and the ground state levels (Yoked superfluorescence system), which is assumed to be generated by a strong multi-photon resonant driving field propagating in the positive (forward) $z-$direction. Such gener-

*Reprinted with permission from "Gain without population inversion in a yoked superfluorescence scheme" by L. Yuan and A. A. Svidzinsky, 2012. Phys. Rev. A, vol. 85, pp. 033836, Copyright [2012] by the American Physical Society.

ated coherence contains the phase factors e^{ikz}, where $k = \omega/c$ and ω is the transition frequency. We are interested in propagation of weak seed pulses through the system in forward and backward directions. The pulses have carrier frequency which corresponds to the energy of the upper and lower transitions. We treat the problem semiclassically and use the Maxwell-Bloch equations. In the linear approximation we obtain exact analytical solution for the evolution of an arbitrary initial pulse propagating through the medium. The seed pulse (vacuum fluctuations) undergoes grows or decay depending on the level populations and initial coherence. We find that if the initial coherence is large enough and intermediate level is populated the system can have gain without population inversion. Coherence can also yield gain suppression in the inverted medium. We obtain conditions for the gain in terms of level populations and coherence.

2.2 Evolution of weak pulses in Yoked superfluorescence scheme

The three-level cascade scheme is shown in Fig. 2.1. The system is uniformly excited by a pump pulse multi-photon resonant with the $a \leftrightarrow c$ forbidden transition propagating along the $z-$axis (forward direction). This process generates coherence ρ_{ac} between the upper and ground states, thus, there is correlation between atoms. Population can decay through the allowed transitions $a \rightarrow b$ and $b \rightarrow c$. We study how weak seed pulses Ω_{ab} and Ω_{bc}, having carrier frequency corresponding to the $a \leftrightarrow b$ and $b \leftrightarrow c$ transitions, propagate through the medium. In our analytical calculations we assume that during the seed pulse propagation the level populations ρ_{aa}, ρ_{bb} and ρ_{cc}, as well as coherence ρ_{ac}, remain constant. However initial seed pulse shapes $\Omega_{ab}(0, z)$ and $\Omega_{bc}(0, z)$ are arbitrary.

We treat the problem semiclassically in the framework of the Maxwell-Bloch equations assuming that electric field and atomic density matrix depend only on

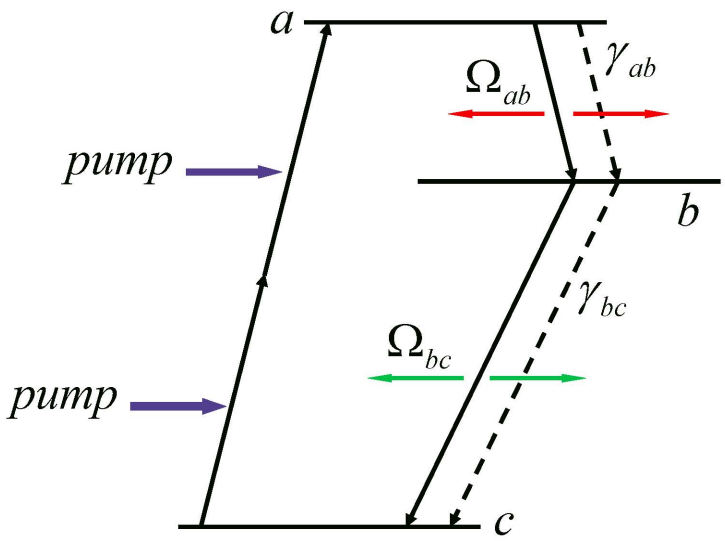

Figure 2.1: Cascade scheme of atomic energy levels.

coordinate z and time t. Equations of motion for the atomic density matrix read

$$\dot{\rho}_{ab}(t,z) = -\Gamma_{ab}\rho_{ab}(t,z) - i\Omega_{ab}(t,z)n_{ab} - i\Omega^*_{bc}(t,z)\rho_{ac}, \tag{2.1}$$

$$\dot{\rho}_{bc}(t,z) = -\Gamma_{bc}\rho_{bc}(t,z) - i\Omega_{bc}(t,z)n_{bc} + i\Omega^*_{ab}(t,z)\rho_{ac}, \tag{2.2}$$

where $n_{ab} = \rho_{aa} - \rho_{bb}$, $n_{bc} = \rho_{bb} - \rho_{cc}$ and ρ_{ac} are constants, $\Gamma_{ij} = \Gamma + \gamma_{ij}/2$, Γ is the dephasing rate due to collisional broadening and γ_{ij} is the spontaneous decay rate of the corresponding transition.

Propagation equations for the electric field are

$$\frac{\partial\Omega_{ab}(t,z)}{\partial z} + \frac{1}{c}\frac{\partial\Omega_{ab}(t,z)}{\partial t} = i\eta_{ab}\rho_{ab}(t,z), \tag{2.3}$$

$$\frac{\partial\Omega_{bc}(t,z)}{\partial z} + \frac{1}{c}\frac{\partial\Omega_{bc}(t,z)}{\partial t} = i\eta_{bc}\rho_{bc}(t,z), \tag{2.4}$$

where Ω_{ij} is the Rabi frequency corresponding to the electric field envelope, $\eta_{ij} =$

$3N\lambda_{ij}^2\gamma_{ij}/8\pi$ is the atom-field interaction constant, N is the atomic density and λ_{ij} is the transition wavelength. Eqs. (2.1) and (2.2) are written for the fields Ω_{ab} and Ω_{bc} propagating in the forward direction. For the backward propagating fields there is no ρ_{ac} term in Eqs. (2.1) and (2.2) because in this case the phases of ρ_{ab} and ρ_{bc} can not match the phase of the coherence ρ_{ac}. Indeed, for the backward propagation, ρ_{ab} and ρ_{bc} have the same phases as the backward fields Ω_{ab} and Ω_{bc}, that is $ik_{ab}z$ and $ik_{bc}z$. However, the phase of the initial coherence ρ_{ac} is produced by the forward pump field and has the value $-i(k_{ab}+k_{bc})z$. Therefore, for backward direction, the last term in Eq. (2.1) has the phase $-i(k_{ab}+k_{bc})z - ik_{bc}z$, which differs from the phase of ρ_{ab} by $-2i(k_{ab}+k_{bc})z$. The phase difference leads to a fast oscillating term as a function of z. In the rotating wave approximation such terms have to be omitted. As a result, solution for the backward propagation can be obtained from the forward one by taking $\rho_{ac}=0$.

We solve Eqs. (2.1)-(2.4) with the initial condition $\rho_{ab}(0,z)=\rho_{bc}(0,z)=0$ and initial pulse shapes $\Omega_{ab}(0,z)$ and $\Omega_{bc}(0,z)$. Eq. (2.1) gives

$$\rho_{ab}(t,z) = -in_{ab}\int_0^t \Omega_{ab}(t',z)e^{-\Gamma_{ab}(t-t')}dt' - i\rho_{ac}\int_0^t \Omega_{bc}^*(t',z)e^{-\Gamma_{ab}(t-t')}dt'. \qquad (2.5)$$

Then using Eq. (2.3) we obtain

$$\frac{\partial\Omega_{ab}(t,z)}{\partial z} + \frac{1}{c}\frac{\partial\Omega_{ab}(t,z)}{\partial t} = \eta_{ab}n_{ab}\int_0^t \Omega_{ab}(t',z)e^{-\Gamma_{ab}(t-t')}dt' + \eta_{ab}\rho_{ac}\int_0^t \Omega_{bc}^*(t',z)e^{-\Gamma_{ab}(t-t')}dt'. \qquad (2.6)$$

Introducing the Laplace transform in time

$$\hat{\Omega}(s,z) = \mathcal{L}\{\Omega(t,z)\} = \int_0^\infty e^{-st}\Omega(t,z)dt \qquad (2.7)$$

yields

$$\frac{\partial\hat{\Omega}_{ab}(s,z)}{\partial z}+\frac{s}{c}\hat{\Omega}_{ab}(s,z)-\frac{1}{c}\Omega_{ab}(0,z)=\eta_{ab}n_{ab}\frac{\hat{\Omega}_{ab}(s,z)}{s+\Gamma_{ab}}+\eta_{ab}\rho_{ac}\frac{\hat{\Omega}^{*}_{bc}(s,z)}{s+\Gamma_{ab}}. \tag{2.8}$$

Similarly for Ω_{bc} we obtain the equation

$$\frac{\partial\hat{\Omega}^{*}_{bc}(s,z)}{\partial z}+\frac{s}{c}\hat{\Omega}^{*}_{bc}(s,z)-\frac{1}{c}\Omega^{*}_{bc}(0,z)=\eta_{bc}n_{bc}\frac{\hat{\Omega}^{*}_{bc}(s,z)}{s+\Gamma_{bc}}-\eta_{bc}\rho^{*}_{ac}\frac{\hat{\Omega}_{ab}(s,z)}{s+\Gamma_{bc}}. \tag{2.9}$$

Solution of Eqs. (2.8) and (2.9) can be rewritten as

$$\hat{\Omega}_{ab}(s,z)=\frac{1}{c}\int_{-\infty}^{z}dz'\frac{F(z')}{\lambda_1-\lambda_2}\left[e^{\lambda_1(z-z')}-e^{\lambda_2(z-z')}\right], \tag{2.10}$$

where the source function is

$$F(z)=\frac{\eta_{ab}\rho_{ac}}{s+\Gamma_{ab}}\Omega^{*}_{bc}(0,z)+\left(\frac{s}{c}-\frac{\eta_{bc}n_{bc}}{s+\Gamma_{bc}}\right)\Omega_{ab}(0,z)+\frac{\partial\Omega_{ab}(0,z)}{\partial z} \tag{2.11}$$

and the constants $\lambda_{1,2}$ are

$$\begin{aligned}\lambda_{1,2}=\frac{1}{2}\Bigg[&\left(-\frac{2s}{c}+\frac{\eta_{ab}n_{ab}}{s+\Gamma_{ab}}+\frac{\eta_{bc}n_{bc}}{s+\Gamma_{bc}}\right)\\&\pm\sqrt{\left(\frac{\eta_{ab}n_{ab}}{s+\Gamma_{ab}}-\frac{\eta_{bc}n_{bc}}{s+\Gamma_{bc}}\right)^{2}-4\frac{\eta_{ab}\rho_{ac}}{s+\Gamma_{ab}}\frac{\eta_{bc}\rho^{*}_{ac}}{s+\Gamma_{bc}}}\Bigg].\end{aligned} \tag{2.12}$$

In the limit that collisional dephasing Γ is much larger than the spontaneous decay rates γ_{ij} we have $\Gamma_{ab}\approx\Gamma_{bc}\approx\Gamma$ and constants $\lambda_{1,2}$ reduce to

$$\lambda_{1,2}=-\frac{s}{c}-\frac{\xi_{1,2}}{s+\Gamma}, \tag{2.13}$$

where

$$\xi_{1,2} = -\frac{1}{2}\left[\eta_{ab}n_{ab} + \eta_{bc}n_{bc} \pm \zeta\right], \tag{2.14}$$

$$\zeta = \sqrt{\left(\eta_{ab}n_{ab} - \eta_{bc}n_{bc}\right)^2 - 4\eta_{ab}\eta_{bc}\left|\rho_{ac}\right|^2}. \tag{2.15}$$

In this limit the inverse Laplace transform of Eq. (2.10) yields the following final answer for pulse evolution in the forward direction

$$\begin{aligned}
\Omega_{ab}(t,z) = {} & \Omega_{ab}(0,z-ct) + \int_{z-ct}^{z} dz' \Omega_{ab}(0,z') e^{-\frac{\Gamma}{c}(z'+ct-z)} \\
& \times \left\{ \frac{\xi_1 + \eta_{bc}n_{bc}}{\zeta} \sqrt{\frac{\xi_1(z-z')/c}{z'+ct-z}} \mathrm{J}_1\left[2\sqrt{\frac{\xi_1}{c}(z-z')\left(z'+ct-z\right)}\right] \right. \\
& \left. - \frac{\xi_2 + \eta_{bc}n_{bc}}{\zeta} \sqrt{\frac{\xi_2(z-z')/c}{z'+ct-z}} \mathrm{J}_1\left[2\sqrt{\frac{\xi_2}{c}(z-z')\left(z'+ct-z\right)}\right] \right\} \\
& - \int_{z-ct}^{z} dz' \frac{\eta_{ab}\rho_{ac}}{\zeta} \Omega^*_{bc}(0,z') e^{-\frac{\Gamma}{c}(z'+ct-z)} \\
& \times \left\{ \sqrt{\frac{\xi_1(z-z')/c}{z'+ct-z}} \mathrm{J}_1\left[2\sqrt{\frac{\xi_1}{c}(z-z')\left(z'+ct-z\right)}\right] \right. \\
& \left. - \sqrt{\frac{\xi_2(z-z')/c}{z'+ct-z}} \mathrm{J}_1\left[2\sqrt{\frac{\xi_2}{c}(z-z')\left(z'+ct-z\right)}\right] \right\},
\end{aligned} \tag{2.16}$$

where $\xi_{1,2}$ and ζ are defined in Eqs. (2.14) and (2.15), $J_1(z)$ is the Bessel function. Similarly, the solution for the field Ω_{bc} reads

$$\begin{aligned}
\Omega^*_{bc}(t,z) = {} & \Omega^*_{bc}(0,z-ct) + \int_{z-ct}^{z} dz' \Omega^*_{bc}(0,z') e^{-\frac{\Gamma}{c}(z'+ct-z)} \\
& \times \left\{ \frac{\xi_1 + \eta_{ab}n_{ab}}{\zeta} \sqrt{\frac{\xi_1(z-z')/c}{z'+ct-z}} \mathrm{J}_1\left[2\sqrt{\frac{\xi_1}{c}(z-z')\left(z'+ct-z\right)}\right] \right. \\
& \left. - \frac{\xi_- + \eta_{ab}n_{ab}}{\zeta} \sqrt{\frac{\xi_2(z-z')/c}{z'+ct-z}} \mathrm{J}_1\left[2\sqrt{\frac{\xi_2}{c}(z-z')\left(z'+ct-z\right)}\right] \right\}
\end{aligned}$$

$$+\int_{z-ct}^{z} dz' \frac{\eta_{bc}\rho_{ac}^{*}}{\zeta}\Omega_{ab}(0,z')e^{-\frac{\Gamma}{c}(z'+ct-z)}$$
$$\times\left\{\sqrt{\frac{\xi_1(z-z')/c}{z'+ct-z}}\mathrm{J}_1\left[2\sqrt{\frac{\xi_1}{c}(z-z')\,(z'+ct-z)}\right]\right.$$
$$\left.-\sqrt{\frac{\xi_2(z-z')/c}{z'+ct-z}}\mathrm{J}_1\left[2\sqrt{\frac{\xi_2}{c}(z-z')\,(z'+ct-z)}\right]\right\}. \tag{2.17}$$

To obtain the evolution of the backward pulse we put $\rho_{ac}=0$ in the above equations and find

$$\Omega_{ab}(t,z) =\Omega_{ab}(0,z-ct)+\sqrt{\frac{\eta_{ab}n_{ab}}{c}}\int_{z-ct}^{z} dz'\Omega_{ab}(0,z')e^{-\frac{\Gamma}{c}(z'+ct-z)}$$
$$\times\sqrt{\frac{z-z'}{z'+ct-z}}\mathrm{I}_1\left[2\sqrt{\frac{\eta_{ab}n_{ab}}{c}}\sqrt{(z-z')\,(z'+ct-z)}\right], \tag{2.18}$$

$$\Omega_{bc}(t,z) =\Omega_{bc}(0,z-ct)+\sqrt{\frac{\eta_{bc}n_{bc}}{c}}\int_{z-ct}^{z} dz'\Omega_{bc}(0,z')e^{-\frac{\Gamma}{c}(z'+ct-z)}$$
$$\times\sqrt{\frac{z-z'}{z'+ct-z}}\mathrm{I}_1\left[2\sqrt{\frac{\eta_{bc}n_{bc}}{c}}\sqrt{(z-z')\,(z'+ct-z)}\right], \tag{2.19}$$

where $I_1(z)$ is the modified Bessel function.

Eqs. (2.16)-(2.19) give the exact analytical answer on how initial weak pulses $\Omega_{ab}(0,z)$ and $\Omega_{bc}(0,z)$ propagate through the medium. As an illustration, we consider a simple example of δ-function initial pulse $\Omega_{ab}(0,z)=\Omega_{ab}^{(0)}\delta(z)$ and no initial pulse at the $b\leftrightarrow c$ transition $\Omega_{bc}(0,z)=0$. Then Eqs. (2.16) and (2.17) yield for forward direction

$$\Omega_{ab}(t,z)=\Omega_{ab}^{(0)}\delta(z-ct)+\Omega_{ab}^{(0)}e^{-\Gamma(t-z/c)}\left\{\frac{\xi_1+\eta_{bc}n_{bc}}{\zeta}\sqrt{\frac{\xi_1 z/c}{ct-z}}\mathrm{J}_1\left[2\sqrt{\frac{\xi_1}{c}z\,(ct-z)}\right]\right.$$
$$\left.-\frac{\xi_2+\eta_{bc}n_{bc}}{\zeta}\sqrt{\frac{\xi_- z/c}{ct-z}}\mathrm{J}_1\left[2\sqrt{\frac{\xi_2}{c}z\,(ct-z)}\right]\right\}\theta(ct-z), \tag{2.20}$$

$$\Omega^*_{bc}(t,z) = \frac{\eta_{bc}\rho^*_{ac}}{\zeta}\Omega^{(0)}_{ab}e^{-\Gamma(t-z/c)} \times \left\{ \sqrt{\frac{\xi_1 z/c}{ct-z}}\mathrm{J}_1\left[2\sqrt{\frac{\xi_1}{c}z\,(ct-z)}\right] - \sqrt{\frac{\xi_2 z/c}{ct-z}}\mathrm{J}_1\left[2\sqrt{\frac{\xi_2}{c}z\,(ct-z)}\right]\right\}\theta(ct-z). \tag{2.21}$$

For the backward direction we obtain

$$\Omega_{ab}(t,z) = \Omega^{(0)}_{ab}\delta(z-ct) + \sqrt{\frac{\eta_{ab}n_{ab}}{c}}\Omega^{(0)}_{ab}e^{-\frac{\Gamma}{c}(ct-z)}\sqrt{\frac{z}{ct-z}} \times \mathrm{I}_1\left[2\sqrt{\frac{\eta_{ab}n_{ab}}{c}}\sqrt{z\,(ct-z)}\right]\theta(ct-z), \tag{2.22}$$

$$\Omega_{bc}(t,z) = 0. \tag{2.23}$$

The first term in Eqs. (2.20) and (2.22) corresponds to the initial seed pulse propagating in free space. The other terms are coming from the interaction between atoms and electric field.

2.3 Forward gain suppression and forward gain without population inversion

We assume that atomic sample is $L = 1$ cm long, so it takes 0.033 ns for the photon to travel through the system. Density of atoms is large enough so that the coupling constants are $\eta = \eta_{ab} = \eta_{bc} = 1000$ cm^{-1}ns^{-1}. We take the dephasing rate $\Gamma = 1$ ns^{-1}. Pulse evolution is mainly governed by collective (superradiant) effects and occurs on a time scale much faster than the dephasing time. Thus assumption about constant ρ_{ac} is valid.

In Fig. 2.2 we plot the output fields $\Omega_{ab}(t,z)$ and $\Omega_{bc}(t,z)$ given by Eqs. (2.20)-(2.22) at the edge of the sample $z = L$ as a function of time. We assume the following population distribution $\rho_{aa} = 0.2$, $\rho_{bb} = 0.05$, $\rho_{cc} = 0.75$ and coherence $\rho_{ac} = \sqrt{0.15}i$. Both forward and backward fields at the $a \to b$ transition are shown. Please note

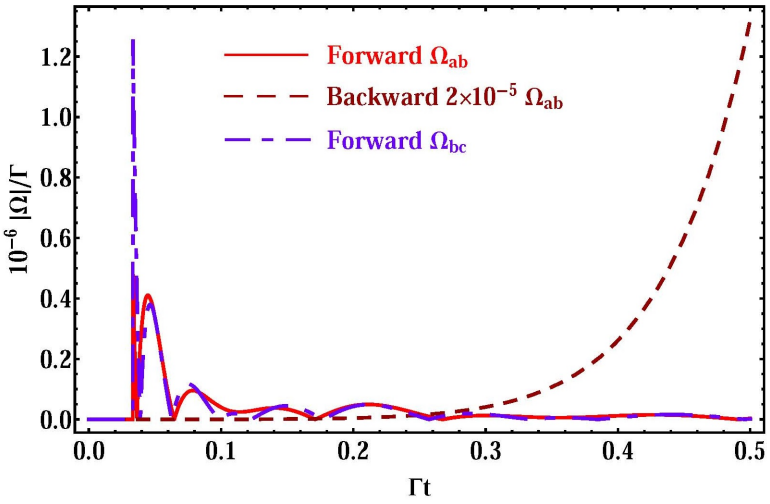

Figure 2.2: Output fields at the edge of the sample as a function of time given by Eqs. (2.20)-(2.22) with population distribution $\rho_{aa} = 0.2$, $\rho_{bb} = 0.05$, $\rho_{cc} = 0.75$ and coherence $\rho_{ac} = \sqrt{0.15}i$. Solid line shows output forward field at the $a \to b$ transition, dashed line is the output backward field at the $a \to b$ transition divided by 5×10^4, while dash-dot line is the forward field at the $b \to c$ transition.

that in the plot we do not show the $\delta-$function term in Eqs. (2.20) and (2.22).

Emission in the backward direction grows exponentially with time as expected for the inverted medium (in the present example there is population inversion between levels a and b). According to Eq. (2.22) it follows asymptotic of the modified Bessel function. However, forward emission is affected by the coherence ρ_{ac}. The presence of such coherence makes the forward field oscillate and decay at large time. This behavior indicates a forward gain suppression which was previously reported in the literature [86, 87]. The forward field on the $b \to c$ transition shows similar features. In the present example we do not include the backward field on the $b \to c$ transition.

Next we take the population distribution $\rho_{aa} = 0.1$, $\rho_{bb} = 0.3$, $\rho_{cc} = 0.6$ and coherence $\rho_{ac} = \sqrt{0.06}i$. Now there is no population inversion in both transitions. The output fields $\Omega_{ab}(t, z)$ and $\Omega_{bc}(t, z)$ at the edge of the sample are shown in Fig.

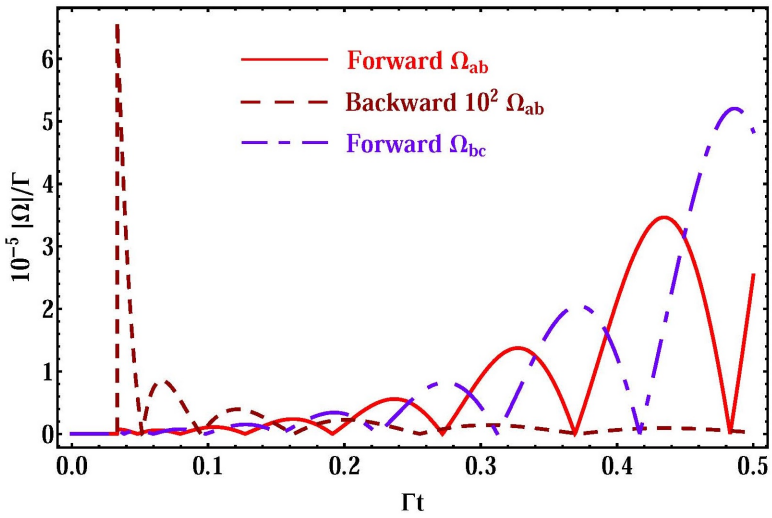

Figure 2.3: Output fields at the edge of the sample as a function of time given by Eqs. (2.20)-(2.22) with population distribution $\rho_{aa} = 0.1$, $\rho_{bb} = 0.3$, $\rho_{cc} = 0.6$ and coherence $\rho_{ac} = \sqrt{0.06}i$. Solid line shows output forward field at the $a \to b$ transition, dashed line is the output backward field at the $a \to b$ transition multiplied by 100, while dash-dot line is the forward field at the $b \to c$ transition.

2.3. In the present example the backward field in the $a \to b$ transition decays because there is no population inversion. Namely, for $n_{ab} < 0$ Eq. (2.22) yields

$$\Omega_{ab}(t,z) = \Omega_{ab}^{(0)}\delta(z-ct) - \sqrt{\frac{\eta_{ab}|n_{ab}|}{c}}\Omega_{ab}^{(0)}e^{-\frac{\Gamma}{c}(ct-z)}\sqrt{\frac{z}{ct-z}} \times \mathrm{J}_1\left[2\sqrt{\frac{\eta_{ab}|n_{ab}|}{c}}\sqrt{z\,(ct-z)}\right]\theta(ct-z), \tag{2.24}$$

that is pulse decays according to the asymptotic of the Bessel function J_1. However, coherence ρ_{ac} yields enhancement of both forward fields $\Omega_{ab}(t,z)$ and $\Omega_{bc}(t,z)$. Thus, there is forward gain without population inversion in our system.

2.4 Numerical solutions

In addition to our analytical results we solve the full Maxwell-Bloch equations numerically including population dynamics and pulse propagation both in forward and

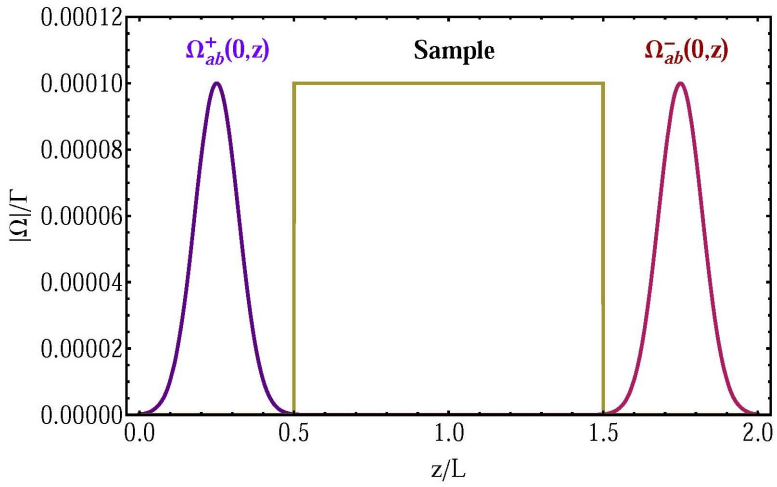

Figure 2.4: Gaussian-shape initial seed pulses for the forward and backward fields used in numerical simulations

backward directions. In numerical simulations, instead of delta function, Gaussian-shape pulses are used for the initial seed for forward and backward fields at the $a \to b$ transition (see Fig. 2.4). The FWHM of the seed pulse is taken as $\Delta z = 0.167L$. The results of simulations are shown in Fig. 2.5. Numerical solution exhibits similar features as the analytical result with delta function seed. When there is population inversion between levels a and b, the numerical simulations show the forward gain suppression in the $a \to b$ transition (see Fig. 2.5a), while with no population inversion there is forward gain (see Fig. 2.5b).

To show that lasing would also occur starting from atomic fluctuations we calculated numerically forward and backward emission using quantum noise as a seed instead of sending seed pulses. We found that if there is gain in the medium then simulations with the seed pulses and noise give very similar results. Thus, our analysis based on the seed pulse propagation adequately describes system's evolution.

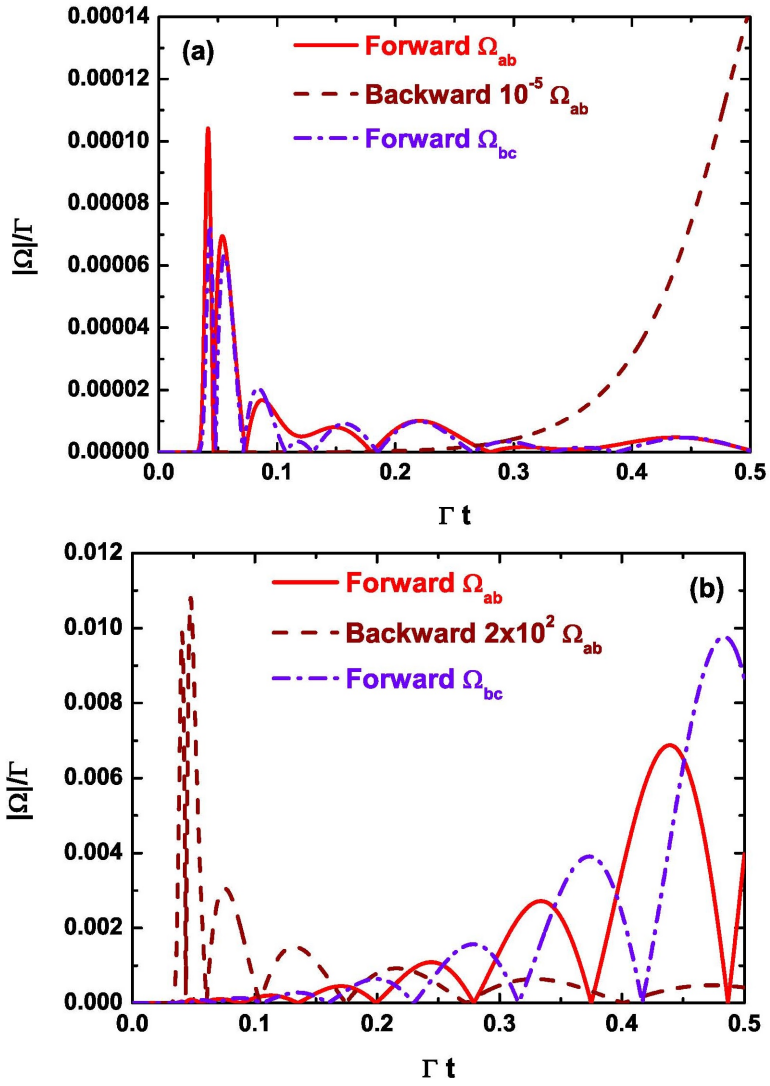

Figure 2.5: Output fields at the edge of the sample as a function of time obtained by numerical solution of the Maxwell-Bloch equations with Gaussian seed pulses and initial conditions $\rho_{aa} = 0.2$, $\rho_{bb} = 0.05$, $\rho_{cc} = 0.75$, $\rho_{ac} = \sqrt{0.15}i$ (a) and $\rho_{aa} = 0.1$, $\rho_{bb} = 0.3$, $\rho_{cc} = 0.6$, $\rho_{ac} = \sqrt{0.06}i$ (b).

2.5 Conditions for gain in forward direction

Analytical results we obtained allow us to find condition for positive gain in the forward direction. If we disregard dephasing Γ the gain is positive if ζ in Eq. (2.15) is imaginary which yields condition

$$4\eta_{ab}\eta_{bc}\left|\rho_{ac}\right|^2 > \left(\eta_{ab}n_{ab} - \eta_{bc}n_{bc}\right)^2. \tag{2.25}$$

Also gain is positive if ξ_1 or ξ_2 have negative real part, that is

$$\eta_{ab}n_{ab} + \eta_{bc}n_{bc} + \sqrt{\left(\eta_{ab}n_{ab} - \eta_{bc}n_{bc}\right)^2 - 4\eta_{ab}\eta_{bc}\left|\rho_{ac}\right|^2} > 0. \tag{2.26}$$

If $\eta_{ab} = \eta_{bc}$ then conditions (2.25) and (2.26) reduce to

$$2\left|\rho_{ac}\right| > \left|n_{ab} - n_{bc}\right| = \left|1 - 3\rho_{bb}\right|, \tag{2.27}$$

$$\rho_{aa} - \rho_{cc} + \sqrt{\left(1 - 3\rho_{bb}\right)^2 - 4\left|\rho_{ac}\right|^2} > 0. \tag{2.28}$$

If one of the inequalities (2.27) and (2.28) is satisfied then there is positive gain in the forward direction. If $\rho_{ac} = 0$ then Eq. (2.28) yields the requirement that $\rho_{aa} > \rho_{bb}$. If we increase $|\rho_{ac}|$ then condition (2.28) may no longer be satisfied even if there is population inversion between levels a and b. This yields forward gain suppression due to coherence. However, if $|\rho_{ac}|$ is large enough and level b is populated ($\rho_{bb} \neq 0$) then one can fulfil inequality (2.27) even if there is no population inversion on the $a \to b$ and $b \to c$ transitions. In this range of parameters the system has forward gain without inversion. Please note that the requirement $\rho_{bb} \neq 0$ is crucial and, thus, to observe such a regime one should wait until level b becomes populated.

Physics behind our results can be understood by noting an analogy between Eqs.

(2.1)-(2.4) and equations of motion of the coupled damped harmonic oscillators. Let us consider spatially uniform case assuming that medium, as well as pulses, is infinitely long. Then, introducing notations $\Omega_{ab} = x$ and $\Omega_{bc} = y$ Eqs. (2.1)-(2.4) can be written as

$$\ddot{x} + \Gamma_{ab}\dot{x} - c\eta_{ab}n_{ab}x - c\eta_{ab}\rho_{ac}y = 0, \tag{2.29}$$

$$\ddot{y} + \Gamma_{bc}\dot{y} - c\eta_{bc}n_{bc}y + c\eta_{bc}\rho_{ac}x = 0. \tag{2.30}$$

These equations show that coherence ρ_{ac} provides coupling between the two oscillators. Equilibrium point $x = y = 0$ is unstable (positive gain) if the oscillator matrix

$$\begin{pmatrix} c\eta_{ab}n_{ab} & c\eta_{ab}\rho_{ac} \\ -c\eta_{bc}\rho_{ac} & c\eta_{bc}n_{bc} \end{pmatrix} \tag{2.31}$$

has eigenvalues which are complex or have positive real part. Taking into account that matrix eigenvalues are

$$\lambda_{1,2} = \frac{c}{2}\left(\eta_{ab}n_{ab} + \eta_{bc}n_{bc} \pm \sqrt{(\eta_{ab}n_{ab} - \eta_{bc}n_{bc})^2 - 4\eta_{ab}\eta_{bc}|\rho_{ac}|^2}\right) \tag{2.32}$$

we obtain conditions for the gain which coincide with Eqs. (2.25) and (2.26). So, physics behind forward gain without inversion and forward gain suppression with inversion is the same as physics of stability of the coupled harmonic oscillators.

2.6 Conclusion

In this section, we consider pulse propagation through a medium composed of three-level (cascade scheme) atoms with initial coherence between the upper and ground states. We obtain analytical solutions for pulse evolution for arbitrary initial populations and pulse shapes. Emission in the forward direction is similar to Yoked superfluorescence, that is there is simultaneous emission on the upper and lower

transitions. We find that initial coherence can result in gain in the forward direction without inversion if the intermediate level is populated. On the other hand, coherence can suppress forward gain even in inverted medium.

The phenomenon in this model combines lasing and superradiance together. In the case of a laser (with or without inversion) a weak seed pulse exponentially grows in the linear regime. In the case of superradiance in extended medium the emitted pulse decays undergoing oscillations with the collective frequency. The present problem combines these two effects which yields a possibility of exponential grow and oscillations of the pulse at the same time.

3. SUPERRADIANT DECAY IN A SHORT TIME SCALE*

3.1 Introduction

In a plasma of modest to high electron density, electron-ion or electron-atom collisions are usually the dominating decoherence mechanisms limiting the effect of atomic coherence, unless coherence manifests in a time scale shorter than the collisional time. One such scenario is the cooperative spontaneous emission for an ensemble of coherently excited atoms. Over the years both superradiance and superfluorescence have been extensively studied in a wide range of systems. Recently, superfluorescence from helium atoms following excitation by free-electron-laser has been observed with the aim of generation of VUV and X-ray superfluorescence pulses [92]. For table-top systems, plasma based collisional or recombination schemes are perspective approaches for producing VUV and X-ray lasers [93], and it is of significant interest to explore whether coherence effects can be incorporated there in a suitable way.

In this section, we obtain analytical solution for the superradiant decay in the two-level atom system [40]. To verify this phenomenom, we report femto-second absorption spectroscopy measurement of helium atoms from 2^3P to 2^3S state in a plasma created through optical field ionization. Coherence between levels 2^3P and 2^3S is created by a short laser pump pulse resonant with $2^3S - 2^3P$ transition. Evolution of the population on the 2^3P level is probed with sub-ps temporal resolution by measuring absorption of a short probe pulse resonant with $2^3P - 3^3D$ transition which is sent with a delay. Population decay pattern shows the signature of the superradiant enhancement with a rapid decay component more than three orders of

*Reprinted with permission from "Observing Superradiant Decay of Excited-State Helium Atoms Inside Helium Plasma" by H. Xia, A. A. Svidzinsky, L. Yuan, C. Lu, S. Suckewer, and M. O. Scully, 2012. Phys. Rev. Lett., vol. 109, pp. 093604, Copyright [2012] by the American Physical Society.

magnitude faster than the single atom decay time at density of atoms in the 2^3S state on the order of 10^{13}cm^{-3}. We also observed the effects of so called "perturbed free induction decay" when the probe precedes the strong pump pulse. In such case, the phase and amplitude of the atomic polarization excited by the probe which is responsible for the coherent radiation of the $3^3D - 2^3P$ transition is controlled by a delayed strong pump pulse that resonantly couples 2^3P and 2^3S levels. As a result, oscillations as well as significant changes appear in the collected transmission spectra of the probe pulse.

3.2 Analytical solution for the superradiant decay

With a theoretical model of superradiant decay upon coherent excitation, we consider a medium composed of two level atoms (the upper level a and the lower level b). Particle density n is assumed to be uniform inside the sample. A laser pulse of Rabi frequency $\Omega(t, z)$ enters the medium and propagates along the $z-$ axis. We use semiclassical approach in which evolution of $\Omega(t, z)$ is described by Maxwell's equation that in slowly varying envelope approximation reads

$$\frac{\partial \Omega}{\partial z} + \frac{1}{c}\frac{\partial \Omega}{\partial t} = i\eta\rho_{ab}, \tag{3.1}$$

where $\eta = 3n\lambda^2\gamma/8\pi$, λ is the wavelength of the atomic transition and γ is the single atom spontaneous decay rate. Eq.(3.1) is supplemented by quantum mechanical equations for the atomic density matrix

$$\dot{\rho}_{aa} = -\gamma\rho_{aa} - i(\Omega^*\rho_{ab} - c.c.), \tag{3.2}$$

$$\dot{\rho}_{ab} = -\frac{\gamma}{2}\rho_{ab} + i\Omega(\rho_{bb} - \rho_{aa}), \tag{3.3}$$

$$\rho_{aa} + \rho_{bb} = 1. \tag{3.4}$$

For weak excitation, one can approximate $\rho_{bb} - \rho_{aa} \approx 1$ in Eq.(3.3). As a result, equations for $\Omega(t,z)$ and $\rho_{ab}(t,z)$ decouple and system of Eqs.(3.1), (3.3) can be solved analytically for arbitrary initial conditions. For a very short pulse (shorter than any other characteristic time scales in the problem) it can be treated as a $\delta-$function, $\Omega(0,z) \propto \delta(z)$. For this initial condition Eqs. (3.1)-(3.4) yield

$$\rho_{aa}(t,z) \propto J_0^2\left(2\sqrt{\eta z(t-z/c)}\right) e^{-\gamma(t-z/c)}\theta(ct-z), \tag{3.5}$$

where $J_0(x)$ is the Bessel function.

A propagation of a delayed (Δt) probe pulse sees the following population of atoms in the excited state

$$\rho(z) = \rho_{aa}(t = \Delta t + z/c, z) \propto J_0^2\left(2\sqrt{\eta z \Delta t}\right) e^{-\gamma \Delta t}. \tag{3.6}$$

Using

$$\frac{1}{L}\int_0^L J_0^2\left(2\sqrt{\eta z \Delta t}\right) dz = J_0^2\left(2\sqrt{\Gamma_N \Delta t}\right) + J_1^2\left(2\sqrt{\Gamma_N \Delta t}\right), \tag{3.7}$$

we obtain that the integrated population seen by the second pulse after propagation through the whole sample of length L is

$$\frac{\rho(\Delta t)}{\rho(0)} = \left[J_0^2\left(2\sqrt{\Gamma_N \Delta t}\right) + J_1^2\left(2\sqrt{\Gamma_N \Delta t}\right)\right] e^{-\gamma \Delta t}, \tag{3.8}$$

where

$$\Gamma_N = \eta L = \frac{3}{8\pi} n \lambda^2 L \gamma, \tag{3.9}$$

is the characteristic collective decay rate proportional to the atomic density n. For

$\Delta t \leq 1/\Gamma_N$ Eq. (3.8) yields $\rho(\Delta t) \propto e^{-(\Gamma_N+\gamma)\Delta t}$, while for $\Delta t \gg 1/\Gamma_N$ we obtain $\rho(\Delta t) \propto e^{-\gamma\Delta t}/\sqrt{\Delta t}$.

3.3 Transient absorption spectroscopy on excited-state helium atoms in a plasma created through optical field ionization

In the experiments, excited helium is prepared via optical field ionization followed by non-radiative three-body (two electrons and one ion) recombination and collisional de-excitation whose cross-section is approximately proportional to the fourth power of the principal quantum number of atomic states. Under intense laser field, atoms are stripped off electrons through Keldysh tunneling [94]. In order for three-body recombination to dominate over radiative decay as well as collisional ionization, a plasma of low electron temperature with high initial electron density is required. With the ionization laser pulses shorter than the electron collision time, plasma heating can be minimized.

The typical experimental setup has a glass cell of 5 cm in diameter and 30 cm long, flowed with helium at various pressures. A Ti: Sapphire femto-second regenerative amplifier system (KML) produces 50 fs pulses of central wavelength 790 nm and pulse energy of 3 mJ at a repetition rate of 1 kHz. Part of the beam is used to pump two optical parametric amplifiers (OPA, from Light Conversion, Inc), and the remaining portion is focused into the helium cell as the ionizing beam, with peak intensity of 2×10^{15} W/cm^2. At such intensity, nearly 100% of helium atoms will be ionized at the central part of the beam. The output from the OPA is tunable in the wavelength range from 550 nm to 2200 nm. One of the OPA output is used as the probe beam, and is focused into the helium cell at diameter of around 50 μm. All the beams are linearly polarized and the relative delay between the beams is controlled by varying the beam optical paths.

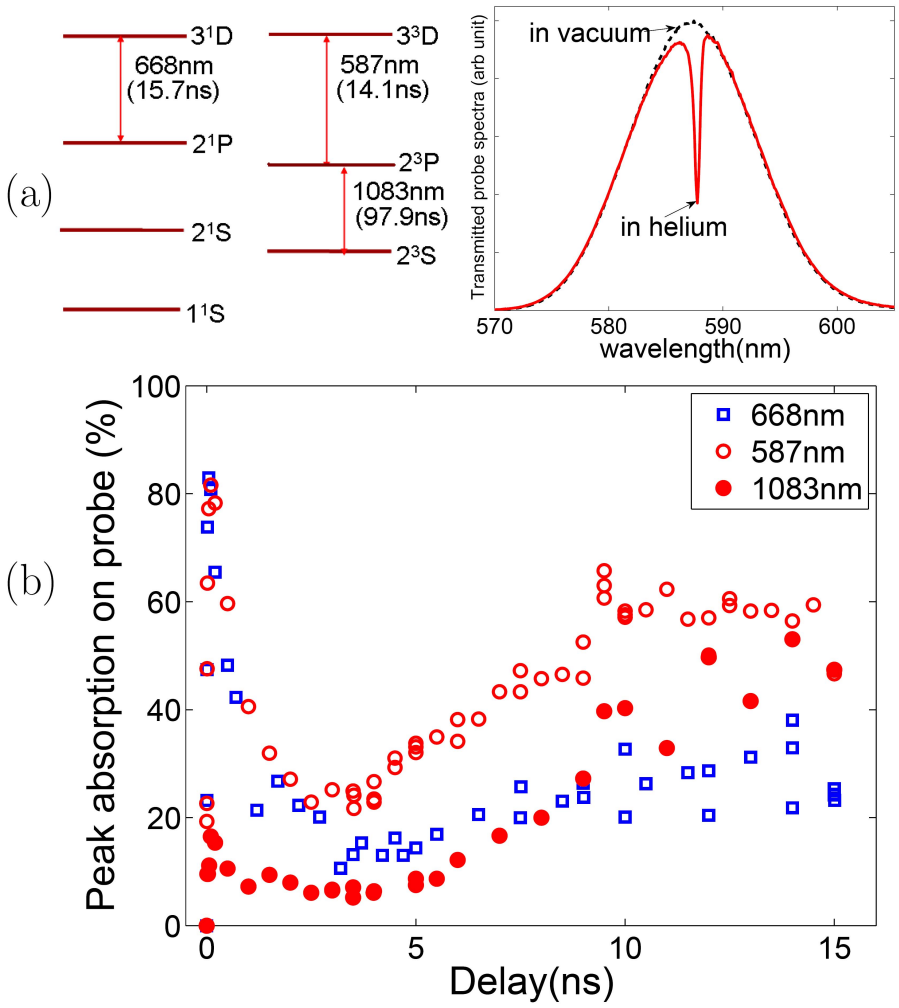

Figure 3.1: (a) Energy levels of helium atom (not to scale) and the typical transmitted spectra of the probe pulse at $2^3P - 3^3D$ (587nm) transition sent 10 ns after helium ionization. (b) Peak absorption on the probe for $2^1P - 3^1D$ (668 nm), $2^3P - 3^3D$ (587 nm) and $2^3S - 2^3P$ (1083 nm) transitions as function of probe delay. The pressure of helium is 100 mbar which corresponds to the density of 2.5×10^{18} cm^{-3} of the initial neutral helium before ionization.

Population of the excited levels is monitored by measuring transmission spectra of probe pulses. Fig. 3.1(a) shows typical spectra of probe pulse transmitted through the ionized helium when its central wavelength is tuned to the resonance with $2^3P - 3^3D$ (587 nm) transition. The probe pulse has a pulse duration of 250 fs, with an energy on the order of 1 nJ per pulse. The broad probe beam spectrum is much wider than the linewidth of the transition. Therefore, the resonant feature is shown as a dip in the transmitted spectra. Taking into appropriate account of the spectrometer resolution(in our case about 0.2 nm at wavelength of 600 nm), the absorption profile can be used to calculate the population difference between 2^3P and 3^3D levels.

Fig. 3.1(b) shows the peak absorption on the probe beam as a function of delay, for the three transitions probed (shown in Fig. 3.1(a)).The population excited from the ionization process and from the recombination process can be distinctly seen as the early and slower components. This feature is qualitatively similar to the structures described in the emission spectroscopic measurement in [95]. The early component, on time scale less than a nano-second, is related to the excitation of helium atoms during the ionization process, as well as the impact excitation/de-excitation/ionization by the hot electrons right after the ionization pulse. The slower component is primarily attributed to the three-body-recombination process, which starts to fill the levels at time scale of several nanoseconds, and is pressure (density) and level dependent. It can also be seen that in the recombination process more absorption is observed for the triplet transition (587 nm triplet transition vs 668 nm singlet transition), which primarily is related to the higher degeneracy of states for triplet levels.

We conducted a pump-probe type of measurement of the population of the helium excited states by sending a pump beam from the output of a second OPA. The pump pulse has duration of 100 fs, a central wavelength of 1083 nm (in resonance with the

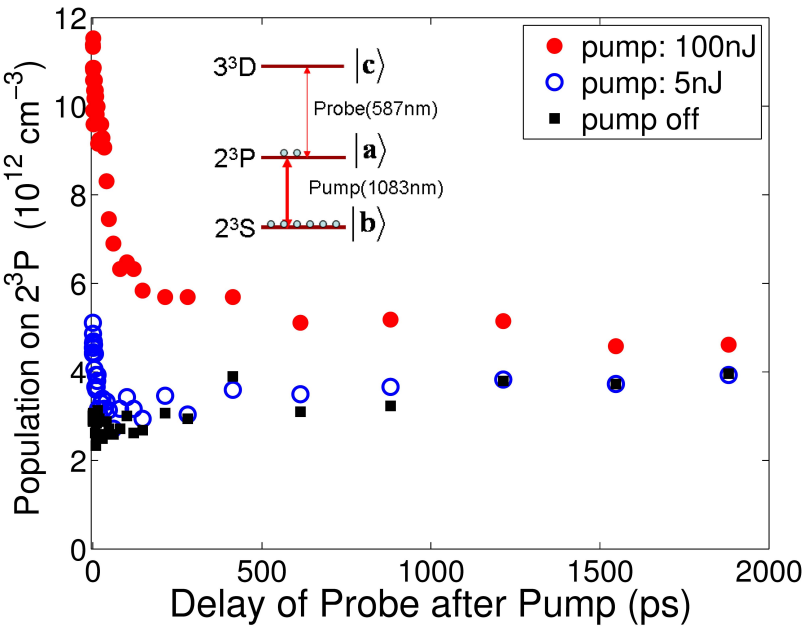

Figure 3.2: Population density of 2^3P level as a function of time after pump pulse. Initial helium pressure before ionization is 25 mbar.

2^3S-2^3P transition), and a typical energy of 100 nJ/pulse. The probe beam is tuned to 587 nm to probe the 2^3P-3^3D transition. The time delay of the pump pulse after helium ionization is fixed at 26 ns, while arrival of the probe relative to the pump pulse is varied by adjusting its optical path. Estimated from the absorption spectra, atomic densities prior to the pump pulse are 3×10^{12} cm^{-3} for 2^3P and 1.2×10^{13} cm^{-3} for 2^3S states respectively.

Fig. 3.2 shows population density of 2^3P level obtained from the measured transmission spectra of the probe as a function of time after the pump pulse. For these data, the absorption of the probe is attributed to the population of the 2^3P state (population of 3^3D level is negligibly small as compared to those of 2^3P). For the sake of simplicity we neglected the level splittings and degeneracies, and treated each triplet level as single state. The actual population of each sub level may be excited

differently by the pump pulse. However, the average population evolution should be well described by the simplified picture. Excitation by the pump beam adds population to the 2^3P level. Probe pulse allows us to measure how 2^3P population decays back to its balanced value. The data obtained show that decay curve has a fast and slow components. At pump energy of 100 nJ, corresponding to the pulse area of 1.1π (calibrated separately), the fast and slow components have time constants of about 50 ps and 1 ns respectively. With a weak pump of 5 nJ and pulse area of 0.25π, the fast component has shorter time constant ($\sim$ 10 ps) as compared to the case of strong pump, while the slow part of the decay curve is mostly below the experimental precision level for obtaining accurate time constant.

Next we estimate the electron-atom collision rate in the plasma environment. The initial plasma density is around 6×10^{17} cm^{-3}. Plasma's volume expands after the passage of the ionization pulse. Plasma expansion can be described using shock model [95, 96] in which the rate of radius expansion decreases with time as $1/\sqrt{t}$. At 26 ns after ionization, the plasma density is in range of 10^{16} to 10^{17} cm^{-3} and the electron temperature is of the order of 0.5 to 1 eV. Under such conditions the electron-atom collision time is estimated to be at least several hundred picoseconds or longer. Therefore, the observed rapidly decaying level population evolves at least one order of magnitude faster than the electron-atom collision time.

3.4 Superradiant coherent behavior in the experimental measurements

Here we compare our data with theoratical model of superradiant decay upon coherent excitation. In the experiment, the incident short pump pulse drives the 2^3S $\leftrightarrow 2^3$P transition which has wavelength $\lambda = 1083.3$ nm and spontaneous decay time $1/\gamma = 97.9$ ns. This pulse excites atomic medium so that population of atoms in the 2^3P state is given by Eq. (3.5). A second weak short probe pulse resonant with the

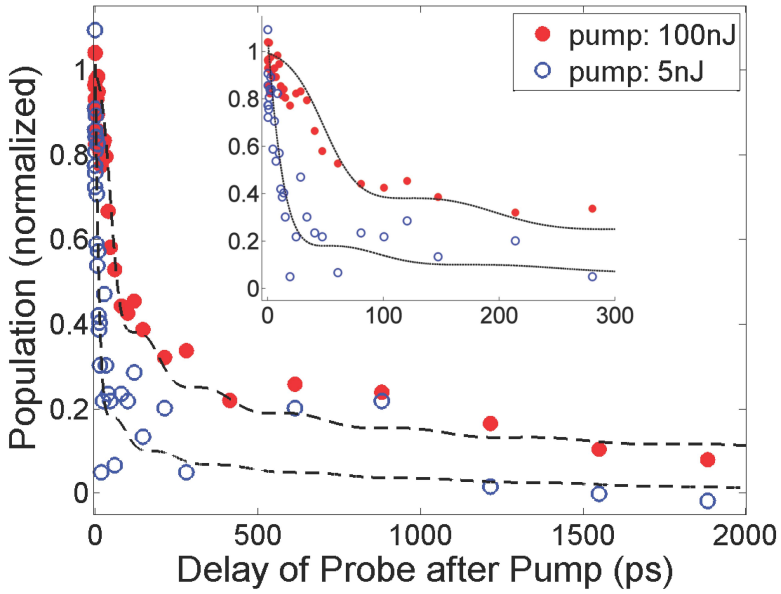

Figure 3.3: Normalized population of 2^3P level as a function of time Δt after pump pulse. Dots show experimental data. Dashed curves are obtained from the analytical formula (3.8) with $1/\Gamma_N = 12$ ps (for weak 5 nJ pump) and by numerically solving Eqs. (3.1)-(3.4) with pump pulse area of 1.1π (for strong 100 nJ pump).

$2^3\mathrm{P} \leftrightarrow 3^3\mathrm{D}$ transition is sent with a delay Δt. If atom concentration in the 2^3S state is $n = 1.2 \times 10^{13}$ cm^{-3} and $L = 0.5$ cm then Eq. (3.9) gives $1/\Gamma_N = 12$ ps. This superradiant time scale is much shorter than spontaneous decay time $1/\gamma = 97.9$ ns as well as the time between collisions in our experiment. Absorption of the second pulse is proportional to the integrated population (3.8) of the 2^3P level, which thus can be measured as a function of time Δt lapse since the level 2^3P is excited by the first pulse. For strong excitation the assumption of $\rho_{bb} - \rho_{aa} \approx 1$ is no longer valid and we use numerical simulations to obtain $\rho(\Delta t)$.

In Fig. 3.3 we plot $\rho(\Delta t)/\rho(0)$ obtained from Eq. (3.8) for $1/\Gamma_N = 12$ ps for weak excitation and from numerical calculations for strong excitation (pump pulse energy of 100 nJ which corresponds to the pulse area of 1.1π) and compare them with the experimental data (dots). The measured evolution of the 2^3P level population

agrees with numerical and analytical calculations to the extent of the experimental precision. Such agreement indicates on superradiant coherent behavior of the atomic system inside the plasma.

3.5 Perturbed free induction decay

Coherent nature of the superradiant emission also emerged when the probe precedes the pump, as shown in Fig. 3.4. Some population of the 2^3P level exists prior to the arrival of the probe pulse. The probe beam creates atomic coherence between the 2^3P and 3^3D states, which lives longer than the probe pulse duration. After passage of the probe pulse the coherent emission from the atomic polarization continues and contributes to the measured spectrum. Coherent emission occurs during the time of the order of the dephasing time for the atomic coherence and is called the "free-induction decay" (FID) field. When the pump pulse arrives at a delay Δt it perturbs state of the 2^3P level and, thus, modifies atomic polarization of the $2^3P - 3^3D$ transition. This perturbation leads to the ripples in the measured spectra of transmitted probe with the period $\Delta\omega \approx 2\pi/\Delta t$. Such effect has the same origin as the "perturbed free induction decay" observed in femtosecond spectroscopy applications studying dynamics of molecules and semiconductors [97, 98, 99].

When the probe and pump pulses have temporal overlap, the transmitted probe spectrum has a clear peak at the line center of the $2^3P - 3^3D$ transition, that is the spectral power density at the line center is greater than that of the probe input field. This indicates that the phase of the atomic coherence between $2^3P - 3^3D$ levels is altered by the pump in a way which leads to a FID radiation in-phase with the probe at the resonance frequency of the $2^3P - 3^3D$ transition. This is essentially the effect of cross phase modulation.

To describe the effect analytically we consider three-level system (upper level c,

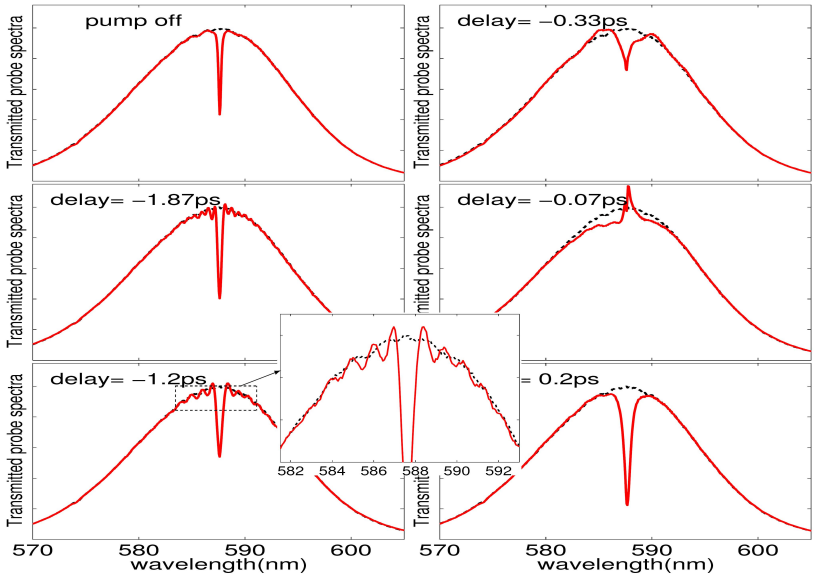

Figure 3.4: Trasmitted probe spectra for different delay between probe and pump (negative delay means probe precedes the pump). The intial helium pressure before ionization is 100 mbar. Dotted lines are spectra for probe transmitted through vacuum.

intermediate level a and lower level b) and assume that at $z = 0$, the weak input probe Ω_{ca} is a Gaussian pulse with the width 2τ, while the strong pump pulse Ω_{ab} has $\delta-$function shape:

$$\Omega_{ca}(t) = \Omega_{ca}^{(0)} e^{-\left(\frac{t-t_{pr}}{\sqrt{2}\tau}\right)^2}, \tag{3.10}$$

$$\Omega_{ab}(t) = \theta_{ab}^{(0)} \delta(t - t_p). \tag{3.11}$$

Here, t_{pr} (t_p) is the time that the probe (pump) pulse reaches the edge of the sample. We found that in the spectral domain the transmitted probe field has the form

$$\begin{aligned}\Omega_{ca}(\omega, L) =& \Omega_{ca}^{(0)} \sqrt{2\pi}\tau e^{-i\omega(L/c+t_{pr})} \\ &\times \left\{ e^{-\frac{1}{2}(\tau\omega)^2} - \frac{\eta L \rho_{aa}^{(0)} e^{\frac{1}{2}(\Gamma_{ca}\tau)^2}}{\Gamma_{ca} + i\omega} \left[1 - |\theta_{ab}^{(0)}|^2 e^{-(\Gamma_{ca}+i\omega)(t_p - t_{pr})} \right] \right\},\end{aligned} \tag{3.12}$$

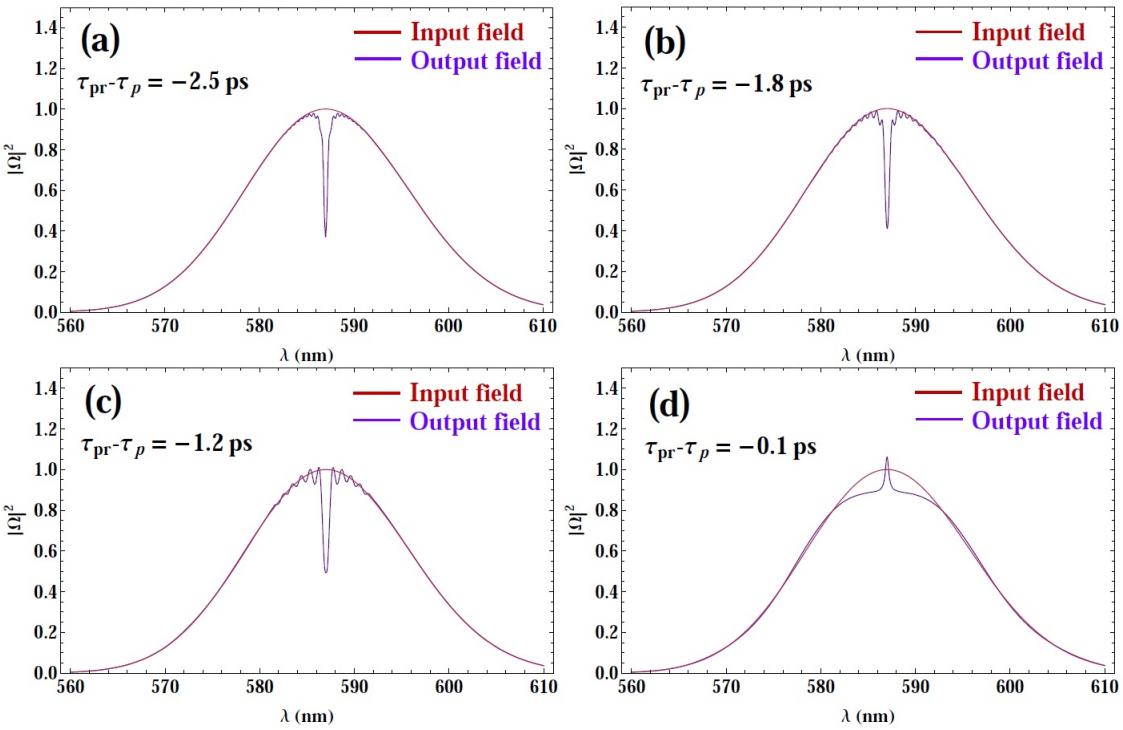

Figure 3.5: Spectrum from the analytical solution in Eq. (3.12) with different time delay between the probe pulse and pump pulse: (a) $\tau_{pr} - \tau_p = -2.5$ ps; (b) $\tau_{pr} - \tau_p = -1.8$ ps; (c) $\tau_{pr} - \tau_p = -1.2$ ps; and (d) $\tau_{pr} - \tau_p = -0.1$ ps.

where Γ_{ij} is the decoherence rate, $\omega = 2\pi\left(\frac{c}{\lambda} - \frac{c}{\lambda_{pr}}\right)$, $\lambda_{pr} = 587$ nm is the central wavelength of the probe pulse. The square of Eq.(3.12) gives the spectrum. The second term in the curly bracket is essentially the absorption of the probe pulse by the medium. The term $e^{-(\Gamma_{ca}+i\omega)(t_p-t_{pr})}$ shows the effect of the pump pulse which leads to the ripples with a frequency proportional to $1/(t_p - t_{pr})$, and the amplitude of the ripples decays as $e^{-\Gamma_{ca}(t_p-t_{pr})}$. When the pump pulse area is large enough, i.e. $|\theta_{ab}^{(0)}| > 1$, the spectrum will have a peak instead of a dip at the line center if the two pulses are temporally overlapping.

Fig. 3.5 shows the spectrum from the analytical solution from Eq. (3.12) with different time delay between the probe pulse and pump pulse. We let probe pulse

comes before the pump pulse. We set the parameters as $\Gamma_{ca} = 1.2 \times 10^{12}$ s^{-1}, $\theta_{ab}^{(0)} = 1.1$, $\Delta_{pr} = 15$ fs, $\eta L \rho_{aa}^{(0)} = 0.5 \times 10^{12}$ s^{-1}. We see similar features as the experiment measurement. Namely, there are ripples in both Fig. 3.5(b) and Fig. 3.5(c), while the ripple is almost washed out in Fig. 3.5(a) when the time delay is large. The frequencies of these ripples become larger with the time delay increasing. When the time delay is small enough ($\tau_{pr} - \tau_p = -0.1$ ps in Fig. 3.5(d)), there is a peak at the center wavelength instead of the dip. Although there is more energy at the center wavelength for the output probe field, the total energy of it is about 97.5% of the input probe field in Fig. 3.5(d).

3.6 Conclusion

In summary, speed up of the population decay of coherently excited helium atoms inside helium plasma is observed. This indicates on the presence of superradiant coherent emission in such system. The measured decay curve of atomic population agrees well with the analytical and numerical calculations. This result represents the first direct probing with femto-second transient absorption spectroscopy on the dynamics and evolution of level populations during post-ionization and recombination processes as well as direct observation on the cooperative (superradiant) decay of excited-state helium atoms with sub-picosecond temporal resolution. The demonstration of laser induced coherence effects among excited states of helium prepared with optical field ionization and in medium containing helium plasma shows that coherence can play an important role in such systems which, in principle, can advance performance of plasma based VUV/X-ray sources.

4. TRANSIENT LASING WITHOUT INVERSION

4.1 Introduction

It is possible to create atomic coherence to suppress absorption resulting in LWI by preparing an atomic system in a coherent superposition of states. The well-studied steady-state LWI takes advantage of the aids from the incoherent pump or the spontaneous decay rate. For example, it is usually requires that the spontaneous decay rate of the pumping transition is larger than the one of the lasing transition [37], which is difficult to achieve when the frequency of the lasing transition is higher than the drive field frequency. In Section 3, we show that the large collective atomic coherence can be built up on a superradiant time scale much shorter than the collisional decoherence time [40]. Thanks to this observation, these obstacles can be overcome in LWI in the transient regime, where the lasing happens at a much shorter time than the decoherence time. Having in mind short time scale, in Section 4.2 we study transient LWI completely disregarding assisting factors such as spontaneous decay or incoherent pumping [41]. In particular, we obtain an analytical expression for the gain which provides insight on LWI conditions, e.g., at what frequency the seed laser pulse is being amplified. This paves the way for more complicated manipulation of the quantum coherence to achieve sideband lasing at multiple frequencies without initial population inversion, which is discussed in Section 4.3 [42, 43].

4.2 LWI in a V-scheme in transient regime*

In this section, we demonstrate LWI on a time scale shorter than the decoherence time. We show that in such a regime LWI is possible in a V-scheme with a strong

*Reprinted with permission from "Transient lasing without inversion" by A. A. Svidzinsky, L. Yuan, and M. O. Scully, 2013. New J. Phys., vol. 15, pp. 053044, Copyright [2013] by IOP Publishing.

coherent drive on the low-frequency transition and obtain an analytical expression for the gain of the laser pulse at high frequency, which is confirmed by the numerical simulations.

4.2.1 Analytical treatment

We consider a model in which transient amplification of high frequency laser field by driving a low frequency transition is pronounced. Our model consists of off-resonant V-scheme in which ground state b is dipole coupled with states a and c (see Fig. 4.1). For simplicity of the analysis we assume that strong field with Rabi frequency

$$\Omega^{\text{drive}}(t,z) = \Omega_d \cos(\nu_d t - k_d z) \tag{4.1}$$

drives only $c-b$ transition, while the weak laser filed $\Omega^{\text{laser}}(t,z)$ couples only with the $a-b$ transition. We study how a weak seed laser field evolves in time and space. Our analysis shows that in such scheme one can achieve gain at frequencies $\nu_{\text{laser}} = \omega_{ac} + m\nu_d$, where $m = \pm 1, \pm 3, \ldots$ is an odd number, even if there is no population inversion between a and the lower levels b and c . This process can be interpreted as atomic transition from the level a to c that is dipole forbidden with emission/absorption of an even number of photons (one laser photon is emitted and an odd number of the driving field photons is absorbed or emitted). (This will be discussed in details in Section 4.3.) In the present problem evolution occurs on a time scale much faster then collision times and, hence, we can overcome atomic decoherence. Our results also remain applicable if level c lies below level b.

Under the influence of the off-resonance driving field atomic evolution is described by the following equations for the density matrix

$$\dot{\rho}_{cb} = -i\omega_{cb}\rho_{cb} + i\Omega^{\text{drive}}\left(\rho_{bb} - \rho_{cc}\right), \tag{4.2}$$

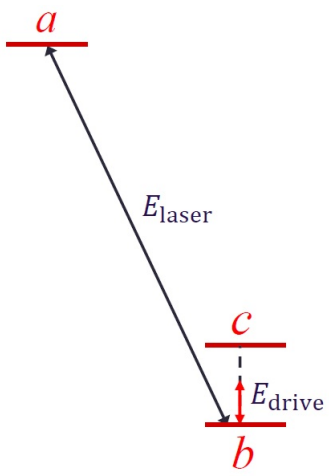

Figure 4.1: Energy level diagram in V-schemes.

$$\dot{\rho}_{cc} = i\Omega^{\text{drive}}\rho_{bc} - i\Omega^{\text{drive}*}\rho_{cb}, \tag{4.3}$$

$$\rho_{bb} + \rho_{cc} = \text{const}, \tag{4.4}$$

where $\omega_{cb} = \omega_c - \omega_b$ is the $c-b$ transition frequency.

Applying the slowly varying envelope approximation for the laser field Ω^{laser} we obtain the following evolution equations for the slowly varying functions Ω_l, ρ^l_{ab} and ρ^l_{ac}

$$\dot{\rho}^l_{ab} = i\Omega_l(\rho_{bb} - \rho_{aa}) - i\Omega^{\text{drive}}\, e^{i\omega_{cb}t}\rho^l_{ac}, \tag{4.5}$$

$$\dot{\rho}^l_{ac} = i\left(\Omega_l\rho_{bc} - \Omega^{\text{drive}*}\rho^l_{ab}\right) e^{i\omega_{bc}t}, \tag{4.6}$$

which have to be supplemented by Maxwell's equation

$$\left(c\frac{\partial}{\partial z} + \frac{\partial}{\partial t}\right)\Omega_l = i\Omega_a^2\rho^l_{ab}, \tag{4.7}$$

where

$$\Omega_a = \sqrt{\frac{3N\lambda^2_{ab}\gamma c}{8\pi}} \tag{4.8}$$

is the collective atomic frequency, N is the atomic density and γ is spontaneous decay rate of the $a-b$ transition. Since the laser field is assumed to be weak, in Eqs. (4.5) and (4.6) ρ_{bb}, ρ_{aa} and ρ_{bc} are determined only by the driving field and initial conditions.

Taking the time derivative of both sides of Eq. (4.7), taking $\dot{\rho}^l_{ab}$ from Eq. (4.5) and introducing

$$\tilde{\Omega}^{\rm drive} = \Omega^{\rm drive} e^{i\omega_{cb}t}, \qquad \tilde{\rho}_{bc} = \rho_{bc} e^{-i\omega_{cb}t},$$

we find

$$\left(c\frac{\partial}{\partial z} + \frac{\partial}{\partial t}\right)\frac{\partial \Omega_l}{\partial t} + \Omega_a^2(\rho_{bb} - \rho_{aa})\Omega_l - \Omega_a^2 \tilde{\Omega}^{\rm drive}\rho^l_{ac} = 0, \tag{4.9}$$

where ρ^l_{ac} obeys equation

$$\dot{\rho}^l_{ac} = i\Omega_l \tilde{\rho}_{bc} - \frac{\tilde{\Omega}^{\rm drive*}}{\Omega_a^2}\left(c\frac{\partial}{\partial z} + \frac{\partial}{\partial t}\right)\Omega_l. \tag{4.10}$$

Next we solve Eqs. (4.2)-(4.4), (4.9), (4.10) and find laser modes which grow exponentially with time. We assume that at $t = 0$ there is some population at the levels a and b, but no population at the level c and no initial coherence. The driving field is turned on adiabatically. We assume that under the influence of the driving field populations of the levels b and c undergo small changes. Then Eqs. (4.2)-(4.4) yield

$$\tilde{\rho}_{bc} = -\frac{\Omega_d}{2}\left(\frac{e^{i\nu_d t - ik_d z}}{\nu_d - \omega_{cb}} - \frac{e^{-i\nu_d t + ik_d z}}{\nu_d + \omega_{cb}}\right) e^{-i\omega_{cb}t}\rho_{bb}(0), \tag{4.11}$$

$$\rho_{bb} = \rho_{bb}(0) - \delta\left[1 - \cos(2\nu_d t - 2k_d z)\right], \tag{4.12}$$

where

$$\delta = \frac{\Omega_d^2 \rho_{bb}(0)}{2\left(\nu_d^2 - \omega_{cb}^2\right)} \ll 1. \tag{4.13}$$

Next we write ρ_{ac}^{l} as

$$\rho_{ac}^{l} = e^{i(\nu_d - \omega_{cb})t - ik_d z}\rho_1 + e^{-i(\nu_d + \omega_{cb})t + ik_d z}\rho_2 \tag{4.14}$$

which gives the following equations for Ω_l, ρ_1 and ρ_2

$$\left(c\frac{\partial}{\partial z} + \frac{\partial}{\partial t}\right)\frac{\partial \Omega_l}{\partial t} + \Omega_a^2\left[\rho_{bb}(0) - \rho_{aa} + \delta\cos(2\nu_d t - 2k_d z)\right]\Omega_l$$

$$-\frac{\Omega_d \Omega_a^2}{2}\left(\rho_1 + \rho_2 + e^{2i\nu_d t - 2ik_d z}\rho_1 + e^{-2i\nu_d t + 2ik_d z}\rho_2\right) = 0, \tag{4.15}$$

$$\dot{\rho}_1 + i(\nu_d - \omega_{cb})\rho_1 = -\frac{\Omega_d}{2}\left[\frac{1}{\Omega_a^2}\left(c\frac{\partial}{\partial z} + \frac{\partial}{\partial t}\right) + \frac{i\rho_{bb}(0)}{\nu_d - \omega_{cb}}\right]\Omega_l, \tag{4.16}$$

$$\dot{\rho}_2 - i(\nu_d + \omega_{cb})\rho_2 = -\frac{\Omega_d}{2}\left[\frac{1}{\Omega_a^2}\left(c\frac{\partial}{\partial z} + \frac{\partial}{\partial t}\right) - \frac{i\rho_{bb}(0)}{\nu_d + \omega_{cb}}\right]\Omega_l. \tag{4.17}$$

We look for solution for Ω_l in the form

$$\Omega_l = e^{ikz - i\nu t}, \tag{4.18}$$

where ν is detuning of Ω_l from the transition frequency ω_{ab}. We assume that k is real. Then the imaginary part of ν gives gain G (absorption) per unit time of the mode with wavenumber k. During propagation of the seed laser pulse Ω_l through the medium it grows as $\exp(Gt)$, where $G = \mathrm{Im}(\nu)$.

Substituting Eq. (4.18) into Eqs. (4.16) and (4.17) gives

$$\rho_1 = -\frac{\Omega_d}{2(\nu_d - \omega_{cb} - \nu)}\left[\frac{1}{\Omega_a^2}(ck - \nu) + \frac{\rho_{bb}(0)}{\nu_d - \omega_{cb}}\right]e^{ikz - i\nu t}, \tag{4.19}$$

$$\rho_2 = \frac{\Omega_d}{2(\nu_d + \omega_{cb} + \nu)}\left[\frac{1}{\Omega_a^2}(ck - \nu) - \frac{\rho_{bb}(0)}{\nu_d + \omega_{cb}}\right]e^{ikz - i\nu t}. \tag{4.20}$$

Plugging Eqs. (4.18), (4.19) and (4.20) into Eq. (4.15) and disregarding terms oscillating with frequency $2\nu_d$ yields the following equation for ν

$$\nu\left(ck-\nu\right)+\Omega_a^2\left(\rho_{bb}(0)-\rho_{aa}\right)-\frac{\Omega_d^2\Omega_a^2}{4}\left(\frac{1}{\left(\nu+\nu_d+\omega_{cb}\right)}\left[\frac{ck-\nu}{\Omega_a^2}-\frac{\rho_{bb}(0)}{\nu_d+\omega_{cb}}\right]\right.$$
$$\left.+\frac{1}{\left(\nu-\nu_d+\omega_{cb}\right)}\left[\frac{ck-\nu}{\Omega_a^2}+\frac{\rho_{bb}(0)}{\nu_d-\omega_{cb}}\right]\right)=0. \quad (4.21)$$

This equation has resonant character, namely, when $\nu=\pm\nu_d-\omega_{cb}$ the last terms become large. This is the region of maximum gain. The optimum value of k is obtained from the condition that one of the roots of the quadratic equation $\nu\left(ck-\nu\right)+\Omega_a^2\left(\rho_{bb}(0)-\rho_{aa}\right)=0$ is equal to $\nu=\pm\nu_d-\omega_{cb}$ which gives

$$ck=\pm\nu_d-\omega_{cb}+\frac{\Omega_a^2\left(\rho_{bb}(0)-\rho_{aa}\right)}{\omega_{cb}\mp\nu_d}. \quad (4.22)$$

Plugging this in Eq. (4.21) yields the final expression for the maximum gain per unit time

$$G=\frac{\Omega_d\Omega_a\sqrt{\rho_{aa}}}{2\sqrt{\left(\nu_d\mp\omega_{cb}\right)^2+\Omega_a^2\left(\rho_{bb}(0)-\rho_{aa}\right)}}. \quad (4.23)$$

Eq. (4.23) is valid provided that G is much larger then decoherence rate $\gamma_{\rm tot}$. Laser light is emitted at frequencies $\nu_{\rm laser}=\nu+\omega_{ab}=\omega_{ac}\pm\nu_d$.

Gain per unit length $G_{\rm L}$ can be obtained in a similar way. Now one should treat ν as real and introduce decoherence $\gamma_{\rm tot}$ in Eq. (4.21). Then imaginary part of k gives gain (absorption) per unit length $G_{\rm L}$ of the mode with frequency ν: $G_{\rm L}=-{\rm Im}(k)$. The gain is maximum near resonance when $\nu\approx\pm\nu_d-\omega_{cb}$ which gives

$$G_{\rm L}=-{\rm Im}(k)=\frac{3N\lambda_{ab}^2\gamma}{32\pi\gamma_{\rm tot}}\frac{\left[\rho_{aa}\Omega_{\rm d}^2-4\gamma_{\rm tot}^2\ \left(\rho_{bb}(0)-\rho_{aa}\right)\right]}{\left(\nu_d\mp\omega_{cb}\right)^2+\gamma_{\rm tot}^2+\Omega_{\rm d}^2/2}. \quad (4.24)$$

Eq. (4.24) shows that there is gain if

$$\Omega_{\rm d}^2 > 4\gamma_{\rm tot}^2 \left(\frac{\rho_{bb}(0)}{\rho_{aa}} - 1 \right), \tag{4.25}$$

that is, to achieve LWI, strength of the driving field $\Omega_{\rm d}$ must exceed decoherence rate.

4.2.2 Numerical simulations

If levels b and c are degenerate then Eqs. (4.2)-(4.4) have exact solution for any strength of the driving field

$$\rho_{bb}(t) = \rho_{bb}(0) \cos^2 \left[\frac{\Omega_d}{\nu_d} \sin(\nu_d t - k_d z) \right], \tag{4.26}$$

$$\rho_{bc}(t) = -\frac{i}{2} \rho_{bb}(0) \sin \left[\frac{2\Omega_d}{\nu_d} \sin(\nu_d t - k_d z) \right], \tag{4.27}$$

where $\rho_{bb}(0)$ is the initial population of the level b and $\rho_{cc}(0) = 0$.

We solve Eqs. (4.9) and (4.10) with $\Omega^{\rm drive}$, $\rho_{bb}(t)$ and $\rho_{bc}(t)$ given by Eqs. (4.1), (4.26), (4.27) and $k_d = 0$ numerically and compare the results with our analytical findings. We look for solution in the form $\Omega_l(t,z) = e^{ikz}\Omega_l(t)$, $\rho_{ac}^l(t,z) = e^{ikz}\rho_{ac}^l(t)$, where k is a real number. We found that if $\rho_{aa} \neq 0$ then for certain k laser field Ω_l exponentially grows even if there is no population inversion between levels a and b.

Fig. 4.2 shows gain per unit time G on the lasing transition as a function of the driving field frequency ν_d for optimum value of k which maximizes G. Initial populations are $\rho_{bb} = 0.9$, $\rho_{aa} = 0.1$ and $\rho_{ab} = 0$. Driving field strength is $\Omega_d/\nu_d = 0.4$ and 0.1. For such parameters there is no population inversion between levels a and b at any moment of time. Fig. 4.2 demonstrates that there is large gain in a broad range of the driving field frequencies. We plot the analytical result (4.23) as

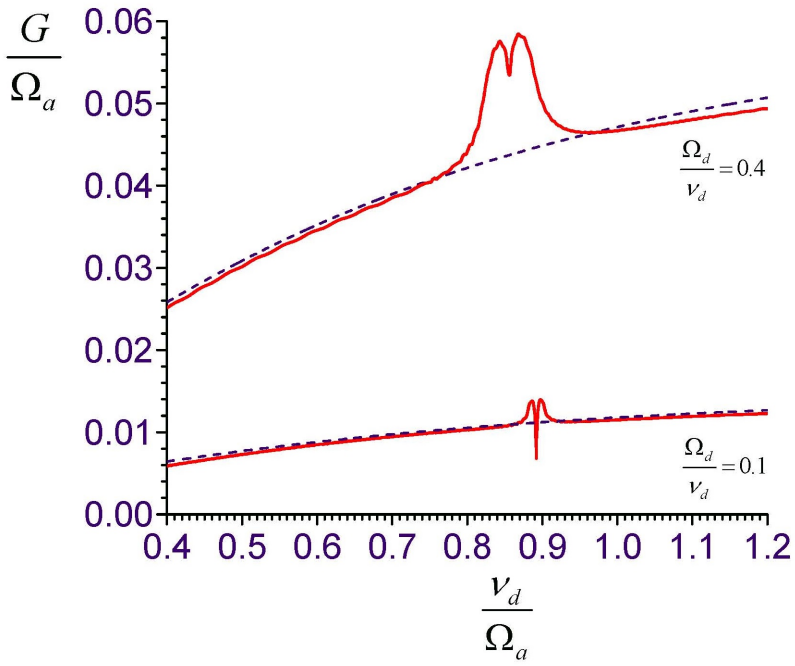

Figure 4.2: Maximum gain as a function of the driving field frequency ν_d in V-scheme. Initial population of the ground state is $\rho_{bb}(0) = 0.9$ and $\rho_{aa} = 0.1$. Driving field strength is $\Omega_d/\nu_d = 0.4$ and 0.1. Plot is obtained by numerical solution of Eqs. (4.9) and (4.10). Analytical result (4.23) is shown by dash line.

dash lines in Fig. 4.2. Features in the vicinity of $\nu_d = \Omega_a\sqrt{\rho_{bb}(0) - \rho_{aa}} = 0.89\Omega_a$ are manifestation of collective parametric resonance which is beyond our analytical treatment and will be further developed in Section 7.

To demonstrate that the seed laser pulse gains its energy from atomic population of the level a (and not from the driving field) we solve the full system of Maxwell-Schrödinger equations numerically. We take initially $\rho_{bb} = 0.9$, $\rho_{aa} = 0.1$ and $\rho_{ab} = 0$. In simulations we assume that levels b and c are degenerate and the driving field is given by Eq. (4.1) with $\Omega_d = 0.3\nu_d$ and $k_d = \nu_d/c$. We send a weak laser pulse of Gaussian shape and duration 1.6 ps into atomic sample of length $L = 0.3$ cm and calculate how pulse energy W^{laser} evolves with time. Strength of the $a - b$ transition

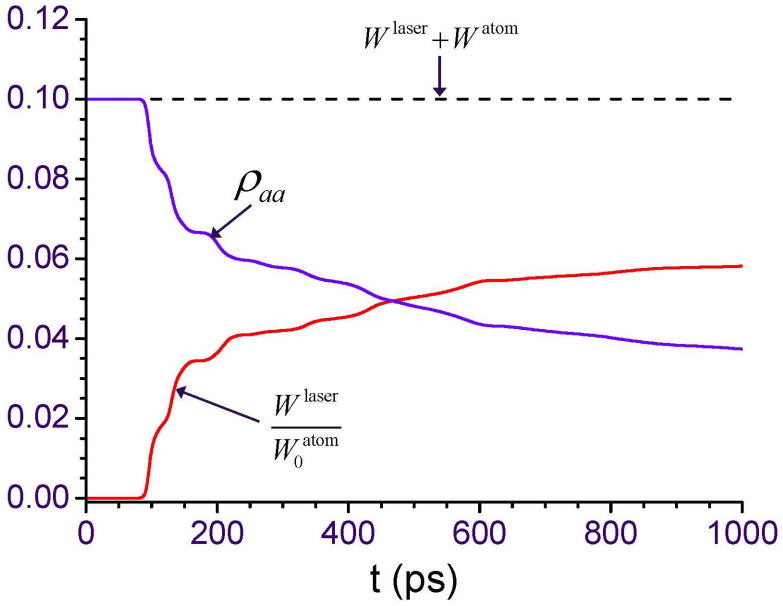

Figure 4.3: Energy of the seed laser pulse W^{laser} (lower curve) and average population ρ_{aa} of the level a (upper curve) as a function of time obtained by numerical solution of the Maxwell-Schrö dinger equations with initial conditions $\rho_{bb} = 0.9$, $\rho_{aa} = 0.1$ and $\rho_{ab} = 0$. Degenerate levels b and c are driven by coherent field (4.1) with $\Omega_d = 0.3\nu_d$ and $k_d = \nu_d/c$. Dash line is the sum of two curves.

and atomic density are chosen such that collective atomic frequency is $\Omega_a = 10^{13}$ s^{-1} (which corresponds to atomic density $N \sim 10^{18}$ cm^{-3}). Fig. 4.3 shows $W^{\text{laser}}/W_0^{\text{atom}}$ as a function of time (lower curve). Here W_0^{atom} is the initial energy stored in atomic excitation. The upper curve shows average (over atomic sample) population of the excited state $\rho_{aa}(t)$. For short evolution time the laser pulse grows exponentially but remains weak to affect ρ_{aa}. This is linear gain regime. Later on pulse energy starts to saturate and population ρ_{aa} gets depleted. Sum of two curves (the net energy of atoms and field) remains constant which is shown as dash line in Fig. 4.3. This implies that laser pulse energy grows in the expense of ρ_{aa}.

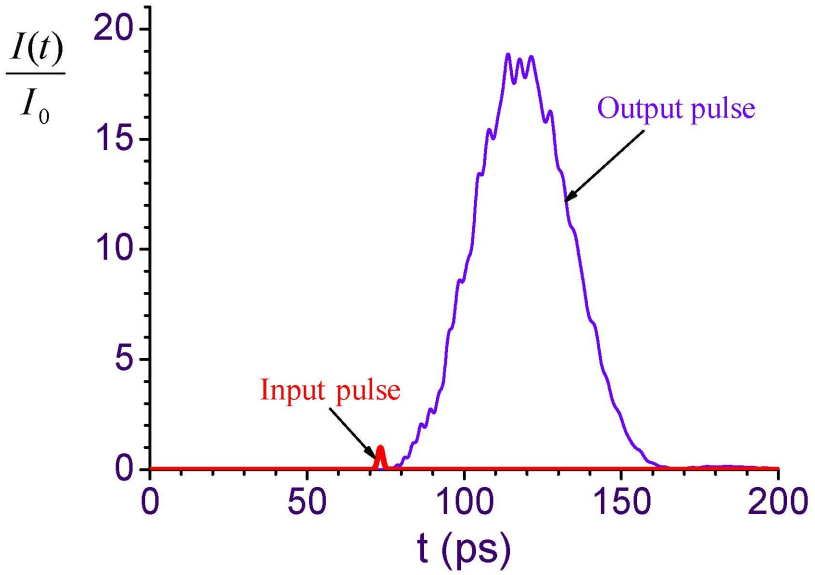

Figure 4.4: Intensity $I(t)$ of the input and output UV laser pulse after it propagates through 1 cm of He gas driven by IR coherent field.

4.2.3 Proposal of experimental realization

We discuss a possible experiment to demonstrate transient LWI at high frequency transition produced by driving a lower frequency transition. Active medium could be, e.g., gas of He atoms partially excited in the metastable triplet 2 ^{3}S$_1$ state (level b in the present notations) inside helium plasma. One can drive an infrared 2 ^{3}P$_1$ $\rightarrow$ 2 ^{3}S$_1$ (1083 nm) transition and generate lasing at the UV 3 ^{3}P$_1$ $\rightarrow$ 2 ^{3}S$_1$ (388.9 nm, $\gamma = 10^7$ s^{-1}) frequency without population inversion. For density of atoms in the metastable state $N = 10^{16}$ cm^{-3} collective atomic frequency for the lasing transition is $\Omega_a = 7.54 \times 10^{11}$ s^{-1}.

We assume that initially $\rho_{bb} = 0.85$, $\rho_{aa} = 0.15$ and $\rho_{cc} = 0$. If the IR transition is driven by a laser with Rabi frequency $\Omega_d = 6 \times 10^{11}$ s^{-1} detuned by $\Delta = \Omega_d$ from the resonance and decoherence rate is $\gamma_{\rm tot} = 10^{10}$ s^{-1} then Eq. (4.23) yields that gain of the UV laser pulse per unit time is $G = 10^{11}$ s^{-1} $\gg \gamma_{\rm tot}$, while Eq. (4.24)

predicts that gain per unit length is $G_{\mathrm{L}} = 47\ \mathrm{cm}^{-1}$. As a demonstration, we solve the Maxwell-Schrödinger equations for the evolution of a weak Gaussian laser pulse with duration 1.6 ps numerically for the present parameters. Fig. 4.4 shows intensity $I(t)$ of the input and output UV laser pulse after it propagates through the medium of length $L = 1$ cm. Intensity is normalized by the peak intensity of the input pulse I_0. The plot indicates that pulse energy increases by several orders of magnitude.

4.3 Sideband LWI in transient regime[†]

We combine the concepts of transient LWI and of the sideband generation to realize a frequency comb generation at high frequencies in this section. We use a pencil-like medium driven by a low-frequency field to create a single-pass superradiant gain where the ringing effect takes place (energy oscillation between the medium and the field) [45]. The superradiant atomic coherence builds up in a time scale much shorter than all decoherence times. The sidebands are generated by the large collective atomic coherence induced by a monochromatic driving field, where counter-rotating terms play an equally important role as the rotating terms. Our results provides a new route toward multiple-frequency coherent light source and have implications for the short-wavelength coherent light sources in the XUV and X-ray regime, tunable THz laser generation, and ultrashort pulse creation.

4.3.1 Theoretical model

The mechanism of is shown in Fig. 4.5 (Left) based on a three-level V-type system. The system is initially prepared such that most of the population remains in the ground state but a little population is in the excited state $|a\rangle$. A strong driving field Ω^{drive} propagates into the pencil-like active medium and couples the transition

[†]Reprinted with permission from "Sideband generation of transient lasing without population inversion" by L. Yuan, D. -W. Wang, C. O'Brien, A. A. Svidzinsky, and M. O. Scully, 2014. Phys. Rev. A, vol. 90, pp. 023836, Copyright [2014] by the American Physical Society.

$c \leftrightarrow b$ and generates a Floquet ladder [100] in the dressed state picture (see Fig. 4.5 (Right)). The transitions from a to the Floquet ladder produce various lasing fields with frequency $\nu_l \sim \omega_{ab} \pm 2n\nu_d$ ($n = 1, 2, 3, \dots$) in a time scale much shorter than any decay time. Here ν_l is the lasing frequency, ω_{ab} is the atomic transition, ν_d is the driving field frequency. These fields are coupled by Ω^{drive} via the atomic coherence. The frequency difference between sidebands is always an even multiple of ν_d since an atom in state $|i\rangle$ needs an even number of photons to return to its original state $|i\rangle$, through successive real and virtual processes (where the counter-rotating terms play a role) [101]. Although there is no population inversion in the bare basis, there may be inversion between the dressed state levels. For these inverted dressed states the corresponding lasing mode is amplified, and through the coupled atomic coherence, other larger sideband modes are consequently amplified if their gain is larger than their loss. The lasing threshold can be reached by tuning the driving field intensity and the medium length.

We list the full-set of the density matrix equations

$$\dot{\rho}_{ab} = -(i\omega_{ab} + \gamma_t)\rho_{ab} + i\Omega^{\text{laser}}(\rho_{bb} - \rho_{aa}) - i\Omega^{\text{drive}}\rho_{ac}, \tag{4.28}$$

$$\dot{\rho}_{ac} = -(i\omega_{ac} + \gamma_t)\rho_{ac} + i\Omega^{\text{laser}}\rho_{bc} - i\Omega^{\text{drive}*}\rho_{ab}, \tag{4.29}$$

$$\dot{\rho}_{cb} = -(i\omega_{cb} + \gamma_t)\rho_{cb} + i\Omega^{\text{drive}}(\rho_{bb} - \rho_{cc}) - i\Omega^{\text{laser}}\rho_{ca}, \tag{4.30}$$

$$\dot{\rho}_{bb} = -i\Omega^{\text{drive}}\rho_{bc} + i\Omega^{\text{drive}*}\rho_{cb} - i\Omega^{\text{laser}}\rho_{ba} + i\Omega^{\text{laser}*}\rho_{ab}, \tag{4.31}$$

$$\dot{\rho}_{cc} = i\Omega^{\text{drive}}\rho_{bc} - i\Omega^{\text{drive}*}\rho_{cb}, \tag{4.32}$$

$$\rho_{aa} + \rho_{bb} + \rho_{cc} = 1, \tag{4.33}$$

where γ_t is the total decoherence rate. These equations are supplemented by Maxwell's

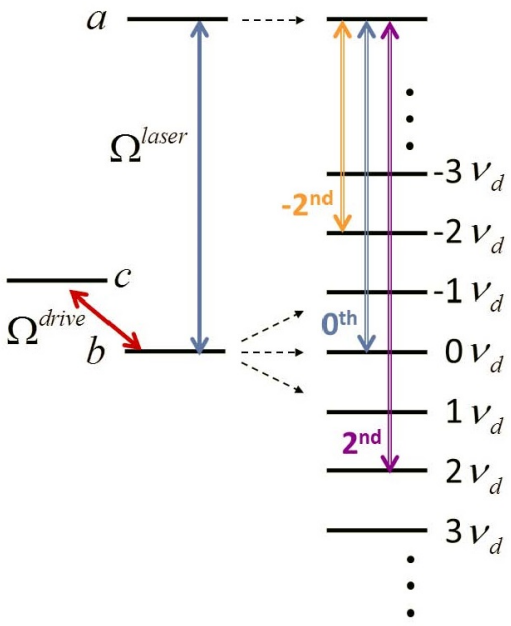

Figure 4.5: Left: Energy diagram for V-scheme; Right: Floquet ladder of states produced by the $c \to b$ transition driven by a laser field with frequency ν_d. Possible lasing transitions are the 0^{th}-order transition ($\sim \omega_{ab}$), and at the even sidebands $\pm 2^{\text{nd}}$-order ($\sim \omega_{ab} \pm 2\nu_d$), etc.

equation

$$\left(\frac{\partial^2}{\partial z^2} - \frac{1}{c^2}\frac{\partial^2}{\partial t^2}\right) E^{\text{laser}} = \mu_0 \frac{\partial^2 P^{\text{laser}}}{\partial t^2}, \tag{4.34}$$

where $P^{laser} = N(\wp_{ba}\rho_{ab} + c.c.)$.

Here we consider two-level system ($c \to b$) with a detuned drive field $\Omega^{\text{drive}} = \Omega_d \cos[\nu_d(t - z/c)]$ as shown in Fig. 4.5. We look for the solutions in the forms $\rho_{bc}(t,z) = \sum_m \rho_{bc}^m e^{-im\nu_d(t-z/c)}$ and $\rho_{bb}(t,z) = \sum_m \rho_{bb}^m e^{-im\nu_d(t-z/c)}$ for the equations,

$$\dot{\rho}_{bc} = (i\omega_{cb} - \gamma/2)\rho_{bc} - i\Omega^{\text{drive}}\left(\rho_{bb} - \rho_{cc}\right), \tag{4.35}$$

$$\dot{\rho}_{bb} = \gamma\rho_{cc} - i\Omega^{\text{drive}}\rho_{bc} + i\Omega^{\text{drive}*}\rho_{cb}, \tag{4.36}$$

$$\rho_{bb} + \rho_{cc} = \rho_{bb}(0) + \rho_{cc}(0), \tag{4.37}$$

where the depopulation decay rate γ is a very small number and is present in order to avoid zero in the denominator. Therefore, the set of coupled algebraic equations are found to be

$$\begin{aligned}
&(m\nu_d + \omega_{cb} + i\gamma/2)\,\rho_{bc}^m - \Omega_d\left(\rho_{bb}^{m-1} + \rho_{bb}^{m+1}\right) \\
&= -\frac{\Omega_d}{2}(\delta_{m,1} + \delta_{m,-1})[\rho_{bb}(0) + \rho_{cc}(0)], \qquad (4.38)
\end{aligned}$$

$$\begin{aligned}
&(m\nu_d + i\gamma)\rho_{bb}^m - \frac{\Omega_d}{2}\left(\rho_{bc}^{m+1} + \rho_{bc}^{m-1} - \rho_{bc}^{-m+1*} - \rho_{bc}^{-m-1*}\right) \\
&= i\gamma[\rho_{bb}(0) + \rho_{cc}(0)]\delta_{m0}. \qquad (4.39)
\end{aligned}$$

General results for ρ_{bc}^m and ρ_{bb}^m can be found by solving infinite coupled Eqs. (4.38) and (4.39) numerically. Note from Eq. (4.39) that $\rho_{bb}^m = \rho_{bb}^{-m*}$, which lead to the real solution for ρ_{bb}.

The propagation of the laser pulse in Eq. (4.34) can be re-written as

$$\left(c^2\frac{\partial^2}{\partial z^2} - \frac{\partial^2}{\partial t^2}\right)\Omega^{\text{laser}} = \frac{2\Omega_a^2}{\omega_{ab}}\frac{\partial^2}{\partial t^2}(\rho_{ab} + c.c.), \qquad (4.40)$$

where $\Omega_a \equiv \sqrt{\frac{3N\lambda_{ab}^2\gamma c}{8\pi}}$, where N is the density, λ_{ab} is the $a \to b$ transition wavelength, γ is the $a \to b$ radiative decay rate, and c is the speed of light. We are looking for a solution in the form of a superposition of spectral components without the rotating-wave-approximation (RWA) [102],

$$\Omega^{\text{laser}}(t,z) = \sum_m \Omega_l^m(z)e^{-i(\omega_{ab}+m\nu_d+\Delta\nu)(t-z/c)} + c.c., \qquad (4.41)$$

$$\rho_{ab}(t,z) = \sum_m \rho_{ab}^m(z)e^{-i(\omega_{ab}+m\nu_d+\Delta\nu)(t-z/c)}, \qquad (4.42)$$

$$\rho_{ac}(t,z) = \sum_m \rho_{ac}^m(z)e^{-i(\omega_{ab}+m\nu_d+\Delta\nu)(t-z/c)}, \qquad (4.43)$$

where $m = 0, \pm 1, \pm 2, \ldots$, and $\Delta\nu$ is the small detuning of the lasing frequency from the frequency $\omega_{ab} + m\nu_d$. By using the expressions in Eqs. (4.41)-(4.43) and taking the components for the same frequency mode m with slowly-varying-envelope approximation (SVEA), the equations of the evolution of the laser field becomes

$$\frac{\partial}{\partial z}\Omega_l^m = i\frac{\omega_m}{\omega_{ab}}\frac{\Omega_a^2}{c}\rho_{ab}^m, \tag{4.44}$$

where $\omega_m \equiv \omega_{ab} + m\nu_d + \Delta\nu$. Here introduce next set of coupled algebraic equations which combines the equations that describe the evolution of the coherence ρ_{ab} and ρ_{ac}

$$\Phi_m^- \rho_{ab}^{m-2} + \Phi_m^0 \rho_{ab}^m + \Phi_m^+ \rho_{ab}^{m+2} = -\sum_q \Theta_m^{2q} \Omega_l^{m-2q}, \tag{4.45}$$

where we define $\eta_m^\pm \equiv 1/\left(\omega_{cb} \pm \nu_d + m\nu_d + \Delta\nu + i\gamma_t\right)$, and

$$\Phi_m^\pm \equiv -\frac{\Omega_d^2}{4}\eta_m^\pm, \tag{4.46}$$

$$\Phi_m^0 \equiv (m\nu_d + \Delta\nu + i\gamma_t) - \frac{\Omega_d^2}{4}\left(\eta_m^- + \eta_m^+\right), \tag{4.47}$$

$$\Theta_m^{2q} \equiv \rho_{bb}^{2q} - \rho_{aa}(0)\delta_{q0} + \frac{\Omega_d}{2}\left(\eta_m^- \rho_{bc}^{2q-1} + \eta_m^+ \rho_{bc}^{2q+1}\right). \tag{4.48}$$

Eq. (4.45) indicates that the component of the field at the mode m is coupled with those at modes $m \pm 2n$, where n is the positive integer.

We search for a solution of Eq. (4.45) is searched in the form,

$$\Omega_l^m(z) = \sum_n u_n \varepsilon_n^m e^{ik_n z}. \tag{4.49}$$

Using this form in Eq. (4.44), we obtain

$$\rho_{ab}^{m}(z) = \frac{\omega_{ab}}{\omega_{ab} + m\nu_d + \Delta\nu} \frac{c}{\Omega_a^2} \sum_n u_n \varepsilon_n^m k_n e^{ik_n z}. \tag{4.50}$$

With the trial solutions of Ω_l^m and ρ_{ab}^m, Eq. (4.45) results in a set of infinite linear equations with eigenvalues k_n and their corresponding eigenvectors $\hat{\varepsilon}_n = (\dots, \varepsilon_n^{m-2}, \varepsilon_n^m, \varepsilon_n^{m+2}, \dots)^T$. The coefficient u_n is determined by the boundary conditions for $\Omega_l^m(z = 0)$ and it reads $u_n = \sum_m \varepsilon_n^m \Omega_l^m(z = 0)$. There are infinite frequency modes coupled in the system. However, the spectra must have a central spectral region where all the frequency modes have relatively strong intensities while the other frequencies far away from this region fade out gradually. Therefore, we can solve Eq. (4.45) numerically in a central spectral region where it has central mode $m = 0$ and boundary modes $m = m_0$. The set of infinite equations is truncated to dimension $(m_0 + 1) \times (m_0 + 1)$ [103].

4.3.2 Frequency comb generation in transient LWI

We first show the basic result in Fig. 4.6. The gain is characterized by the imaginary parts of eigenvalues k_n (n =1, 2,... with descending magnitudes of their imaginary parts) of Eq. (4.45), since the fields generally follow $\sim e^{-\mathrm{Im}k_1 z}$. Especially, we focus on the leading eigenvalue k_1 whose imaginary part has a magnitude several orders larger than the rest. A peak of $-\mathrm{Im}(k_1)$ appears at $\Delta\nu \sim 1.05\Delta$ with width $\sim 0.01\Delta$ where $\Delta \equiv \nu_d - \omega_{cb}$. We therefore can observe sideband LWI in this region.

The amplitude of the output field at different frequency mode m (Ω_l^m) is determined by Eq. (4.49). The gain of each frequency component is not only dependent on the imaginary part of the eigenvalues, but also dependent on the coefficients such as ε_n^m, the elements in the eigenstates and u_n due to the boundary condition. It results

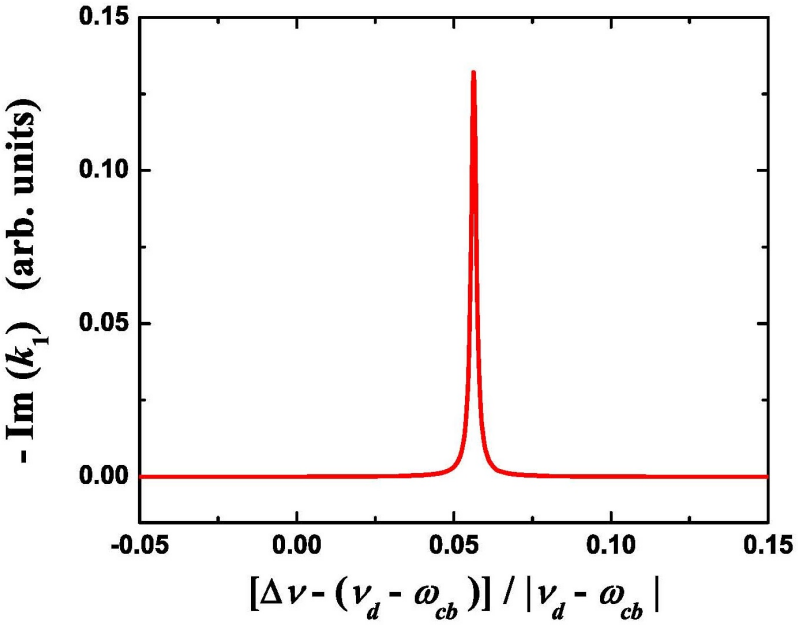

Figure 4.6: The imaginary part of k_1 as a function of the lasing frequency detuning $\Delta\nu$. The populations are $\rho_{aa}(0) = 0.1$, $\rho_{bb}(0) = 0.9$ and $\rho_{cc}(0) = 0$, i.e., without inversion. $\omega_{ab} = 5.0\omega_{cb}$, $\Omega_a = 0.05\omega_{cb}$, $\gamma_t = 10^{-4}\omega_{cb}$. We drive the $c \to b$ transition with a weak detuned field with $\nu_d = 1.1\omega_{cb}$ and $\Omega_d = 0.05\omega_{cb}$. We cut off our calculation at $m = \pm 10$.

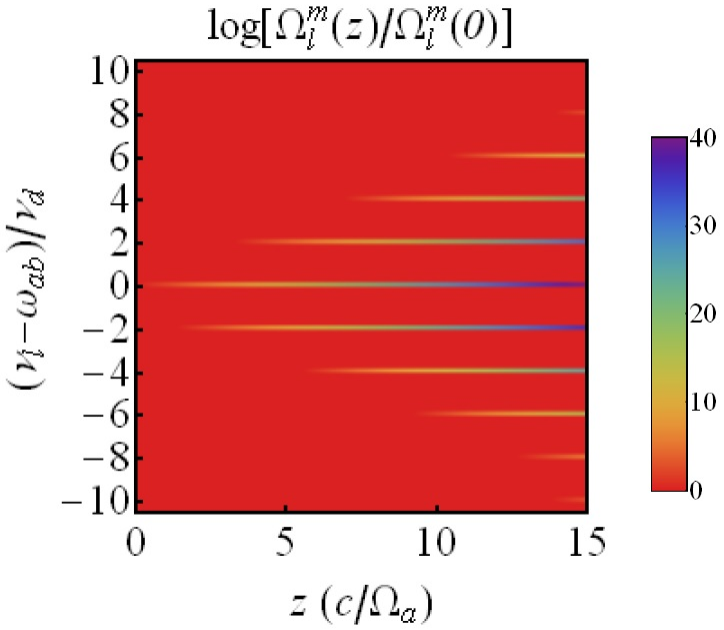

Figure 4.7: The amplification of the output field in the whole spectral region with different propagation distance z.

in different lasing amplifications for different frequency modes. If the field component has smaller coefficients, it requires a longer propagation length to be amplified. The result is plotted in Fig. 4.7. We find that we generate the frequency comb at a long propagation distance ($z = 15\ (c/\Omega_a)$). With longer propagation length, sideband lasing at the higher-order modes gets amplified. For the field at mode $m \neq 0$ ($\Omega_l^m(z)$) with frequency $\sim \omega_{ab} + m\nu_d$, the component of k_1 in Eq. (4.49) does not dominate over the components of the other eigenvalues for small z, so the field component $\Omega_l^m(z)$ is not get amplified compared to its initial value ($\Omega_l^m(0)$). This means that laser field has threshold behavior and the one at a larger frequency mode has a higher threshold value (see Fig. 4.7). The amplification quantity $\log[\Omega_l^m(L)/\Omega_l^m(0)]$ is linearly dependent on the propagation length L only if the propagation length L exceeds the threshold value. In this regime, the linear coefficients for each curve at different frequency modes are the same because the leading terms in Eq. (4.49) for all modes m are the components of k_1 for large z and all those terms grow according to $\exp(-\mathrm{Im}k_1 z)$.

To confirm our results, we show a detailed numerical simulation with the full-set of Maxwell and Schrödinger equations including population evolutions without any approximation except SVEA in Fig. 4.8. We use the polarization source term in the equations to describe production rate of the dipole due to the spontaneous emission [9]. We see multiple single-pass gain peaks above the noise level and they are located at the lasing frequencies $\nu_l^{\pm 2n} \sim \omega_{ab} \pm 2n\nu_d$. There is no population inversion in the system. Coherent emission is generated directly from vacuum fluctuations without an initial seed pulse. The results of the amplification are generally linearly dependent on $\Omega_a L$. This feature gives us flexibility for choosing parameters in future experiments. For example, if the system has a smaller Ω_a than what we propose, it can still produce the same amount of gain as what we expect by increasing L.

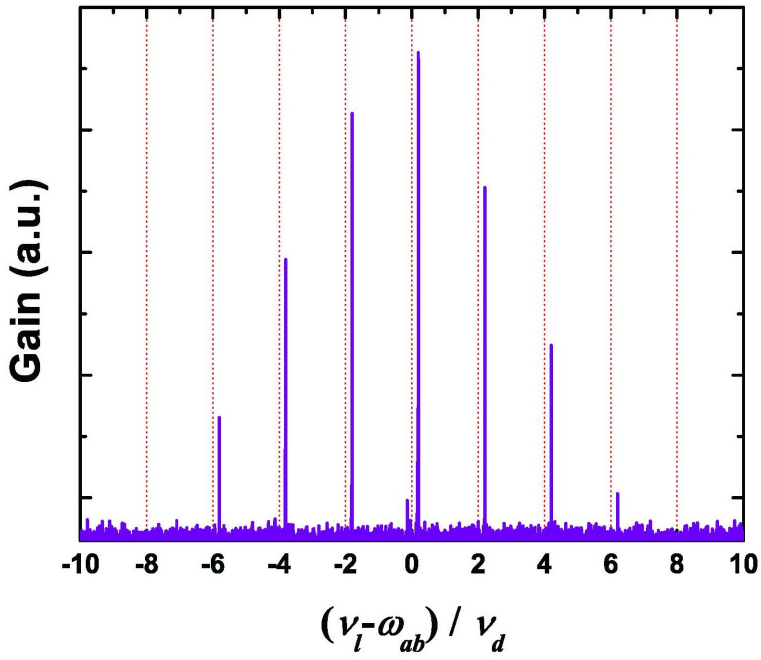

Figure 4.8: Detailed numerical experiments with parameters: $\nu_d = 1.06\omega_{cb}$, $\Omega_d = 0.18\omega_{cb}$, $\Omega_a = 0.0754\omega_{cb}$, $L = 7.54c/\Omega_a$, $\rho_{aa}(0) = 0.15$, $\rho_{bb}(0) = 0.85$, $\rho_{cc}(0) = 0$, and $\gamma_t = 10^{-4}\omega_{cb}$.

4.3.3 LWI in the dressed state picture

The amplification of the laser pulse in the whole spectral region has a common source $-\mathrm{Im}(k_1)$. We study the relation between k_1 and the drive field Rabi frequency Ω_d with all the other parameters fixed. We solve Eq. (4.45) numerically for various Ω_d and search the maximum value of $-\mathrm{Im}(k_1)_{\max}$, by scanning the lasing frequency detuning $\Delta\nu$ for each set of parameters. The dependence of the quantity $-\mathrm{Im}(k_1)_{\max}$ with its corresponding lasing frequency detuning $\Delta\nu$ on different Ω_d are plotted in Fig. 4.9. All of the other parameters are the same as in Fig. 4.6. We find that the quantity $-\mathrm{Im}(k_1)_{\max}$ is increasing with the drive field Rabi frequency Ω_d when Ω_d is small. Nevertheless $-\mathrm{Im}(k_1)_{\max}$ has a maximum after which it drops counter-intuitively with increasing Ω_d.

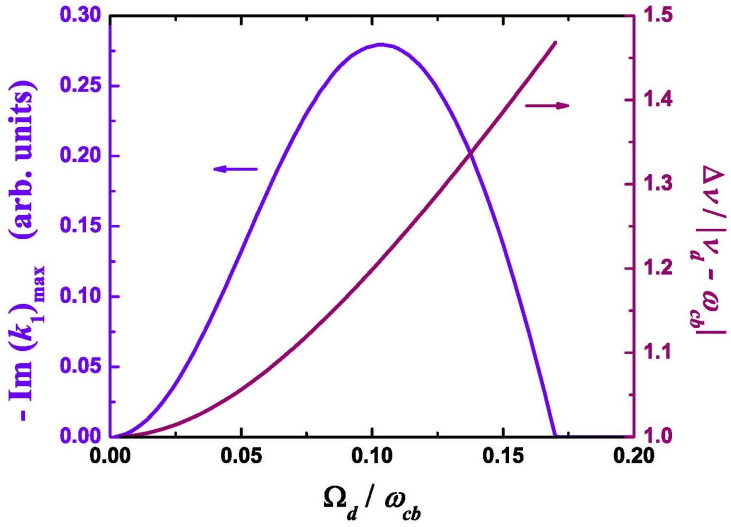

Figure 4.9: The maximum value of the negative imaginary part of the eigenvalue k_1, $-\mathrm{Im}(k_1)_{\max}$, (left blue) with its corresponding lasing frequency detuning $\Delta\nu$ (right purple) for various drive field Rabi frequency Ω_d. The corresponding $\Delta\nu$ is only plotted for positive $-\mathrm{Im}(k_1)$.

The simple but important physics behind the gain profile shown in Fig. 4.9 can be understood by considering the dressed state picture with only the 0^{th}-order lasing transition. By driving the $c \to b$ transition, the excited state a is coupled with two dressed states and both of the transition frequencies are on the order of ω_{ab}. The energy difference of two dressed states depends on the drive field Rabi frequency Ω_d and the drive field detuning Δ. The initial population in the ground state b is redistributed to the two dressed states. While there is no population inversion in the bare-state system, it is still possible to achieve transient lasing because of the population inversion in dressed-state picture. If $\Omega_d \to 0$, one of the two dressed states has ~ 0 population, but the corresponding coupling strength between this dressed state and the excited state is also $\to 0$. Larger Ω_d leads to the enhancement of this coupling strength and results in the increase of the gain or the quantity $-\mathrm{Im}(k_1)_{\max}$. However, the increase of Ω_d also leads to more population in this dressed

state, resulting in less population inversion. The competition between these two mechanisms is the reason that the quantity $-\mathrm{Im}(k_1)_{\max}$ has the maximum positive value when Ω_d is near the resonance $\sim 0.1\omega_{cb}$ (see Fig. 4.9). Only one of the two dressed states can have less population than the excited state, so there is only one peak of the imaginary part of the eigenvalue k_1 as shown in Fig. 4.6. Changing the drive field Rabi frequency also modifies the energies of the two dressed states, so the corresponding lasing frequency detuning $\Delta\nu$ is increasing versus Ω_d (right purple curve in Fig. 4.9). The detailed derivation in the dressed state picture is shown in the following to support our argument.

The drive field couples the $c \to b$ transition and has the form $\Omega^{\mathrm{drive}} = \Omega_d \cos(\nu_d \tau)$, where $\tau = t - z/c$. With the rotating-wave-approximation, the interaction Hamiltonian is

$$V = -\hbar\Delta|c\rangle\langle c| - \frac{\hbar\Omega_d}{2}|c\rangle\langle b| - \frac{\hbar\Omega_d}{2}|b\rangle\langle c|, \tag{4.51}$$

where $\Delta = \nu_d - \omega_{cb}$. It has two eigenstates as

$$|+\rangle = \sqrt{\frac{\Omega_{\mathrm{eff}} - \Delta}{\Omega_{\mathrm{eff}}}}|c\rangle - \sqrt{\frac{\Omega_d^2}{2\Omega_{\mathrm{eff}}(\Omega_{\mathrm{eff}} - \Delta)}}|b\rangle, \tag{4.52}$$

$$|-\rangle = \sqrt{\frac{\Omega_{\mathrm{eff}} + \Delta}{\Omega_{\mathrm{eff}}}}|c\rangle + \sqrt{\frac{\Omega_d^2}{2\Omega_{\mathrm{eff}}(\Omega_{\mathrm{eff}} + \Delta)}}|b\rangle, \tag{4.53}$$

where $\Omega_{\mathrm{eff}} \equiv \sqrt{\Omega_d^2 + \Delta^2}$ and their corresponding eigenvalues are

$$\omega_{\pm} = \frac{1}{2}(-\Delta \pm \Omega_{\mathrm{eff}}). \tag{4.54}$$

For a system which is initially at state $|b\rangle$ at $\tau = 0$, the system evolves as

$$|\psi(\tau)\rangle = -\sqrt{\frac{\Omega_{\mathrm{eff}} + \Delta}{2\Omega_{\mathrm{eff}}}}\sqrt{\rho_{bb}(0)}e^{-i\omega_+\tau}|+\rangle + \sqrt{\frac{\Omega_{\mathrm{eff}} - \Delta}{2\Omega_{\mathrm{eff}}}}\sqrt{\rho_{bb}(0)}e^{-i\omega_-\tau}|-\rangle \tag{4.55}$$

at $\tau = t - z/c \geq 0$. Therefore, the density matrix elements are

$$\rho_{++}(t,z) = \frac{\Omega_{\text{eff}} + \Delta}{2\Omega_{\text{eff}}}\rho_{bb}(0), \tag{4.56}$$

$$\rho_{--}(t,z) = \frac{\Omega_{\text{eff}} - \Delta}{2\Omega_{\text{eff}}}\rho_{bb}(0), \tag{4.57}$$

$$\rho_{+-}(t,z) = -\frac{\sqrt{\Omega_{\text{eff}}^2 - \Delta^2}}{2\Omega_{\text{eff}}}\rho_{bb}(0)e^{-i(\omega_+ - \omega_-)(t-z/c)}, \tag{4.58}$$

$$\rho_{-+}(t,z) = -\frac{\sqrt{\Omega_{\text{eff}}^2 - \Delta^2}}{2\Omega_{\text{eff}}}\rho_{bb}(0)e^{i(\omega_+ - \omega_-)(t-z/c)}, \tag{4.59}$$

Now, we introduce weak lasing field E_l with frequency $\nu_l \sim \omega_{ab}$ coupling with the $a \to b$ transition. The Hamiltonian reads

$$H = \omega_a|a\rangle\langle a| + \omega_+|+\rangle\langle +| + \omega_-|-\rangle\langle -| - \wp_{ab}E_l e^{-i\nu_l t}|a\rangle\langle b| - \wp_{ba}E_l^* e^{i\nu_l t}|b\rangle\langle a|$$

$$= \omega_a|a\rangle\langle a| + \omega_+|+\rangle\langle +| + \omega_-|-\rangle\langle -| + \left(-\wp_{a+}E_l e^{-i\nu_l t}|a\rangle\langle +| - \wp_{a-}E_l e^{-i\nu_l t}|b\rangle\langle -| + H.c.\right), \tag{4.60}$$

where

$$\wp_{a+} \equiv -\sqrt{\frac{\Omega_{\text{eff}} + \Delta}{2\Omega_{\text{eff}}}}\wp_{ab}, \tag{4.61}$$

$$\wp_{a-} \equiv \sqrt{\frac{\Omega_{\text{eff}} - \Delta}{2\Omega_{\text{eff}}}}\wp_{ab}. \tag{4.62}$$

We assume that E_l is so weak that it doesn't change the populations and the coherence between states $|+\rangle$ and $|-\rangle$. Therefore we find

$$\frac{d}{dt}\tilde{\rho}_{a+} = -i(\omega_{a+} - \nu_l)\tilde{\rho}_{a+} - i\wp_{a+}E_l\left[\rho_{aa}(0) - \rho_{++}\right] + i\wp_{a-}E_l\rho_{-+}, \tag{4.63}$$

$$\frac{d}{dt}\tilde{\rho}_{a-} = -i(\omega_{a-} - \nu_l)\tilde{\rho}_{a-} - i\wp_{a-}E_l\left[\rho_{aa}(0) - \rho_{--}\right] + i\wp_{a+}E_l\rho_{+-}, \tag{4.64}$$

where $\omega_{a\pm} \equiv \omega_a - \omega_\pm$, and $\tilde{\rho}_{a\pm} \equiv \rho_{a\pm} e^{i\nu_l t}$. The Maxwell's equation has the expression

$$\left(\frac{\partial}{\partial t} + c\frac{\partial}{\partial z}\right) E_l = \frac{i\nu_l}{2\epsilon_0} \wp_{ab} \tilde{\rho}_{ab} = \frac{i\nu_l}{2\epsilon_0} \left(\wp_{a+}\tilde{\rho}_{a+} + \wp_{a-}\tilde{\rho}_{a-}\right). \tag{4.65}$$

If we take RWA and neglect all the fast-oscillating terms, then E_l is only possible to get amplified at the resonant frequency $\nu_l^{\pm} = \omega_{a\pm}$ with the corresponding coherence as

$$\frac{d}{dt}\tilde{\rho}_{a\pm} = -i\wp_{a\pm} E_l \left[\rho_{aa}(0) - \frac{\Omega_{\text{eff}} \pm \Delta}{2\Omega_{\text{eff}}} \rho_{bb}(0)\right]. \tag{4.66}$$

Hence the electrical field E_l evolves as

$$\left(\frac{\partial}{\partial t} + c\frac{\partial}{\partial z}\right) \dot{E}_l = \frac{\nu_l \wp_{ab}^2}{2\epsilon_0} \left\{\frac{\Omega_{\text{eff}} \pm \Delta}{2\Omega_{\text{eff}}} \left[\rho_{aa}(0) - \frac{\Omega_{\text{eff}} \pm \Delta}{2\Omega_{\text{eff}}} \rho_{bb}(0)\right]\right\} E_l. \tag{4.67}$$

From this result, we find that the electrical field E_l can get amplified if there is population inversion between state $|a\rangle$ and state $|\pm\rangle$ in the dressed state picture. We consider the case that $\rho_{aa}(0) \ll \rho_{bb}(0)$ and assume $\Delta > 0$. Lasing happens at the transition between the state $|a\rangle$ and the state $|-\rangle$ and gain is dependent on the quantity $\frac{\Omega_{\text{eff}}-\Delta}{2\Omega_{\text{eff}}} \left[\rho_{aa}(0) - \frac{\Omega_{\text{eff}}-\Delta}{2\Omega_{\text{eff}}} \rho_{bb}(0)\right]$. When $\Omega_d \to 0$, gain $\to 0$ since $\frac{\Omega_{\text{eff}}-\Delta}{2\Omega_{\text{eff}}} \to 0$ though there is population inversion $\rho_{aa}(0) > \frac{\Omega_{\text{eff}}-\Delta}{2\Omega_{\text{eff}}} \rho_{bb}(0)$. Gain is increasing with the increase of Ω_d initially. When it reaches the maximum value, it will decrease until it becomes zero when there is no population inversion $\rho_{aa}(0) \leq \frac{\Omega_{\text{eff}}-\Delta}{2\Omega_{\text{eff}}} \rho_{bb}(0)$ for a very large Ω_d. The corresponding lasing frequency is $\nu_l = \omega_{a-} = \omega_{ab} + \frac{1}{2}(\Delta + \Omega_{\text{eff}})$, which is increasing with Ω_d. It has the similar result for the case $\Delta < 0$ and the lasing happens at the transition between the state $|a\rangle$ and the state $|+\rangle$.

4.4 Potential applications in short-wavelength laser[‡]

Transient lasing without inverion and its sideband generation (in particular the pulses at the blue-shifted sidebands, $m > 0$), provides a promising choice for generating the high-frequency laser. We choose the triplet levels of Helium atoms or Helium-like ions for proposed experimental realization of the above concept. Our approach utilizes advantages of the recombination XUV lasers [93, 104] and the effects of quantum coherence. The population in the excited state atoms are prepared through optical field ionization followed by non-radiative three-body (two electrons and one ion) recombination. In order for three-body recombination rates to dominate collisional ionization rates, the recombining plasma should have a low electron temperature. Low temperature plasma can be realized with ultra-short laser pulses (at intensity in the order of 10^{15} W/cm^2 for Helium) through tunneling ionization [94, 105, 106]. Use of ultra-short laser pulses is crucial to minimize plasma heating. Ti:Sapphire laser at wavelength 800 nm with pulses of 30-100 fs duration can be used to generate the plasma. It has been demonstrated that 4 mm long plasma channel can be achieved with the aid of Axicon lenses [107].

We first give three experimental proposals in a S-P-P scheme with Helium (Fig. 4.10a). This is a V-like scheme. The drive laser is provided by Nd: YAG laser or its 2nd or 4th harmonic, and is used to drive the 2^3S-2^3P transition of the helium atoms. The lasing transition which we are interested in is from the 3^3P to the virtual level at wavelength of UV regime. We choose the typical experimental parameters and conditions as the following. The atomic system has density 10^{18} cm^{-3} and we prepare 15% population at the exited state 3 ^{3}P. The system has the decoherence rate

[‡]Reprinted with permission from "Transient lasing without inversion via forbidden and virtual transitions" by L. Yuan, D. Wang, A. A. Svidzinsky, H. Xia, O. Kocharovskaya, A. Sokolov, G. R. Welch, S. Suckewer, and M. O. Scully, 2014. Phys. Rev. A, vol. 89, pp. 013814, Copyright [2014] by the American Physical Society.

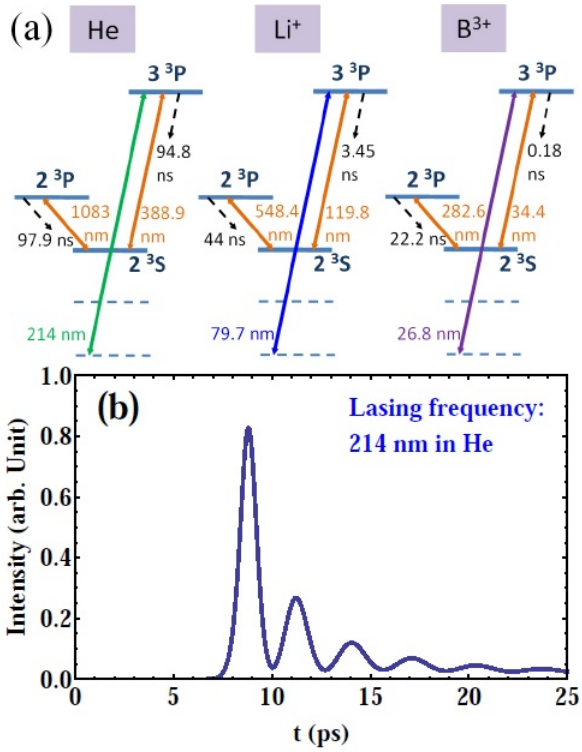

Figure 4.10: (a) Energy diagrams (S-P-P scheme) of He, Li^+, and B^{3+}; (b) Simulated output intensity of the lasing fields versus time.

as 0.3×10^{11} s^{-1} and has the length as 1 mm. We pump the lower transition with a strong laser pulse at 1064 nm wavelength, with 1 mJ energy/pulse and $\sim$ 30 ps pulse duration. We send the seed which is near resonant with the 3 ^{3}P$\rightarrow$2 ^{3}S transition and has the energy $\sim$ 10 pJ. Lasing without inversion at the resonant frequency is emitted in the transient regime. Furthermore, we also detect the emission at the higher frequency ($\sim$ 214 nm) and find the emission energy at this frequency is $\sim$ 1 nJ. Time evolution of the intensity of the lasing emission at 214 nm wavelength versus time is presented in Fig. 4.10b.

We also show the gain in the S-P-D scheme with Helium. In this time, we choose the same drive field as we used in the previous calculation, but we only need the

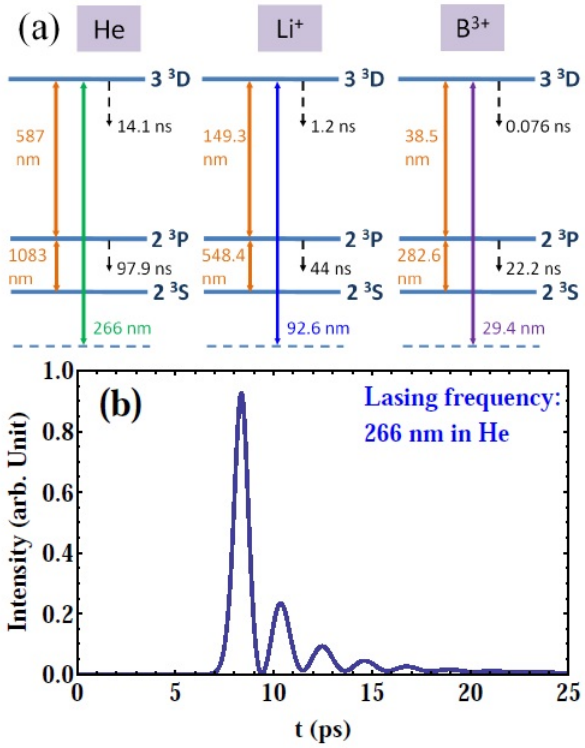

Figure 4.11: (a) Energy diagrams (S-P-D scheme) of He, Li^+, and B^{3+}; (b) Simulated output intensity of the lasing fields versus time.

atom medium with 10^{17} cm^{-3} and 10% population prepared at the exited state 3 ^{3}D. The seed pulse has the same energy $\sim$ 10 pJ but wavelength $\sim$ 587 nm. The output lasing without inversion also has the frequency component at $\sim$ 266 nm and corresponding energy $\sim$ 1 nJ. (We show the similar temporal behavior of the output field at the wavelength $\sim$ 266 nm in Fig. 4.11b.) These calculations can be extended to other Helium-like ions such as Li^+ and B^{3+} with energy schemes in Figs. 4.10a and 4.11a.

Although the experimental conditions for both proposals are different, there is no fundamental difference between the mechanism of generation of higher-frequency lasing without population inversion in the S-P-P and the S-P-D schemes. In a sample

as short as 1 mm, we achieve a nano-Joule emission via the 1^{st}-order sideband. Possible higher-frequency generation is possible due to higher-order sideband generation. Experiments may be complicated by requirements of high atomic density, etc.. Nevertheless, the high frequency field amplification without population inversion driven by a low frequency intensive field holds real promise.

4.5 Conclusion

We show that LWI can be achieved in systems with fast collisional decoherence on short time scale which utilizes coherence effects. This is relevant to experiments on XUV and $X-$ray lasers in which transient atomic population is created by ionization-recombination processes. In particular, we find that transient LWI is possible in the V-scheme in which the low frequency transition is coherently driven by a field with Rabi frequency exceeding the decoherence rate. Frequency comb generation via sideband transient LWI is further studied. We use the Floquet method to solve the system in the weak lasing field limit (the population is unchanged due to the lasing field) and find amplified emission at different frequency modes. Threshold behavior is seen for high-order sidebands. We sketch the V scheme LWI analysis in a dressed state picture where a weak ultrashort laser seed pulse is amplified by using a strong driving field. Experimental proposals of the concept in three levels Helium atoms or Helium-like ions are investigated numerically. We find that the higher frequency sideband lasing without inversion can be generated in both S-P-P and S-P-D schemes. In principle, this method can make table-top laser pulses in XUV and X-ray regime with a visible driving field.

5. COHERENCE-BRIGHTENED LASER IN AIR*

5.1 Introduction

The coherence brightened laser, a superradiant source, can be realized from a pencil-shaped gain medium without mirrors as proposed by Dicke [7, 44]. A backward lasing source in air has been achieved recently by two-photon excitation of oxygen atoms using a picosecond forward-propagating pump pulse [57]. In this section, we show an experiment in which a laserlike source is created in air by pumping with a nanosecond pulse [58]. Difference from the picosecond-pump experiment, we see cooperative nonadiabatic coherence present. A detailed theoretical study is followed to understand the coherence effects in the system [59].

5.2 Experimental procedure

We investigate the forward and backward directed emission of oxygen when pumped by nanosecond UV laser pulses. The experimental scheme is sketched in Fig. 5.1. The laser system consists of 532 nm output from an injection-seeded Spectra Physics PRO-290-10 Nd:YAG laser which pumps a Sirah Cobra Stretch pulsed dye laser producing 622 nm output when a mixture of Rhodamine 610 and Rhodamine 640 in methanol is used. This 622 nm output is mixed with the residual 355 nm from the Nd:YAG laser in a Sirah SFM-355 frequency mixing unit to produce $\sim$ 10 ns pulses of 226 nm light with $\sim$10 mJ/pulse at 10 Hz [108]. The resulting

*Reprinted with permission from "Coherence brightened laser source for atmospheric remote sensing" by A. J. Traverso, R. Sanchez-Gonzalez, L. Yuan, K. Wang, D. V. Voronine, A. M. Zheltikov, Y. Rostovtsev, V. A. Sautenkov, A. V. Sokolov, S. W. North, and M. O. Scully, 2012. Proc. Natl. Acad. Sci. USA, vol. 109, pp. 15185, Copyright [2012] by the National Academy of Sciences of the United States of America; "Theoretical analysis of the coherence-brightened laser in air" by L. Yuan, B. H. Hokr, A. J. Traverso, D. V. Voronine, Y. Rostovtsev, A. V. Sokolov, and M. O. Scully, 2013. Phys. Rev. A, vol. 87, pp. 023826, Copyright [2013] by the American Physical Society.

beam is focused using a convex lens (1 m focal length). Emission in both the forward and backward direction is detected and characterized. Particularly, a 300 nJ signal is detected in the backward direction, which is an order of magnitude higher than in the previous experiment using picosecond pump pulses [57].

To determine the dimensions of the gain region, we first calculate the radius at the beam waist and the focal depth of the 226 nm beam assuming a beam radius of 0.25 cm incident on the 1 m focusing lens and a Gaussian beam profile. This is accomplished by solving

$$r(z) = r_0\sqrt{1 + \left(\frac{z\lambda}{\pi r_0^2}\right)^2}, \tag{5.1}$$

for r_0, the radius at the beam waist, where $r(z)$ is the beam radius a distance z away from the focal point. This gives a radius of $r_0 = 28.8$ μm. Likewise, the focal depth, b, can be calculated via

$$b = \frac{2\pi r_0^2}{\lambda}. \tag{5.2}$$

This gives a length of $b = 2.3$ cm. If this was a single photon process it would scale with the intensity, I, but we must account for the fact that this is a four photon process (two photons to dissociate an oxygen molecule and two more to excite atomic oxygen to the $3p\ ^3P$ state). Therefore, the rate of excitation is proportional to I^4, and using the definition for the intensity

$$I(x,z) = I_0\left(\frac{r_0}{r(z)}\right)^2 e^{-\frac{2x^2}{r(z)}}, \tag{5.3}$$

where x is the radial distance, we can solve for the dimensions at FWHM of the gain region. This gives the gain region of the length $b \sim 1$ cm and the waist $r_0 \sim 17$ μm.

The power of both signals is measured versus the pump power using a pyroelectric power meter from Ophir (Fig. 5.2). A characteristic threshold behavior is observed

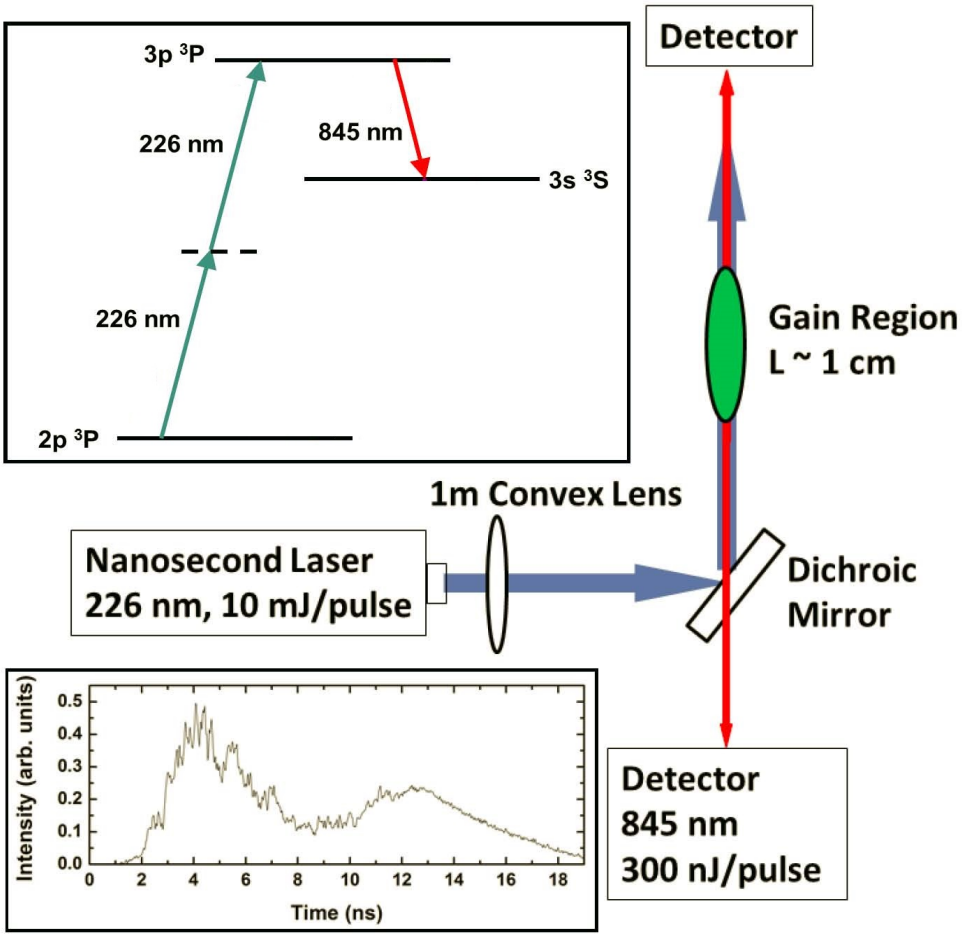

Figure 5.1: Simplified experimental scheme. Nanosecond 226 nm laser pulses are focused with a 1 m lens dissociating the oxygen molecules at the focal point in ambient air. The 226 nm pulse further excites the newly dissociated oxygen atoms via two-photon absorption causing a population inversion. The backward detection is performed through a dichroic mirror. [Bottom Inset] An example of the pump pulse's intensity profile. [Top Inset] The energy level scheme is depicted for oxygen atoms undergoing two-photon excitation and stimulated emission at 845 nm.

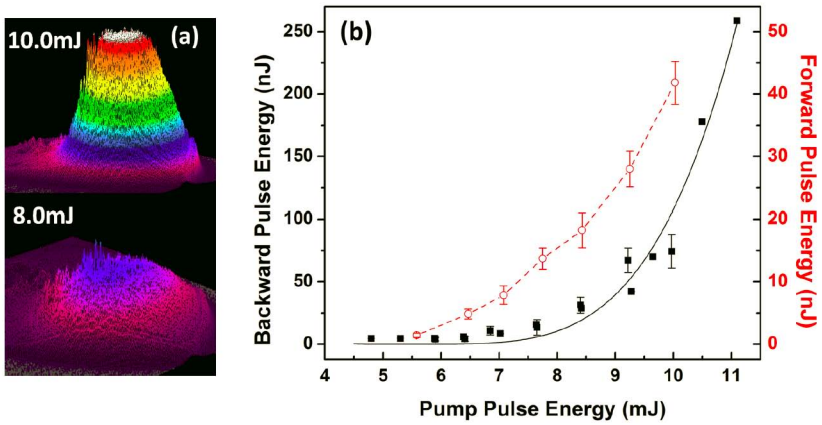

Figure 5.2: (a) Spatial beam profiles of the 845 nm emitted backward pulse at pump energies above (10.0 mJ), and at (8.0 mJ) threshold; (b) The energy per pulse of both the forward (red circles), and backward (black squares) signals versus the pump power.

for both forward and backward 845 nm beams indicating a laser-like process instead of simple fluorescence. Also, there is a distinct energy difference between the forward and backward emission, which is discussed below. The spatial beam profiles of the backward pulse are made using a Spiricon beam profiler (SP620U). A distinct threshold is observed at $\sim$ 8 mJ with a Gaussian profile. The width of the beam profile right at the threshold (8 mJ) is significantly wider than the profiles for any of the pump powers above threshold. Above threshold, all of the beam profiles have approximately the same width. These features are indicative of a laser-like source for the measured signals.

The temporal pulses shapes are measured using a Tektronix MSO72004C fast oscilloscope (20 GHz bandwidth, 50 GigaSamples/sec, and $\sim$ 20 ps resolution) and a New Focus high speed photodiode (model: 1437; 25 GHz bandwidth and 14 ps risetime). As can be seen in Fig. 5.3, the temporal profiles varied from shot to shot mainly due to the rapid intensity fluctuations in the individual 226 nm pump pulses

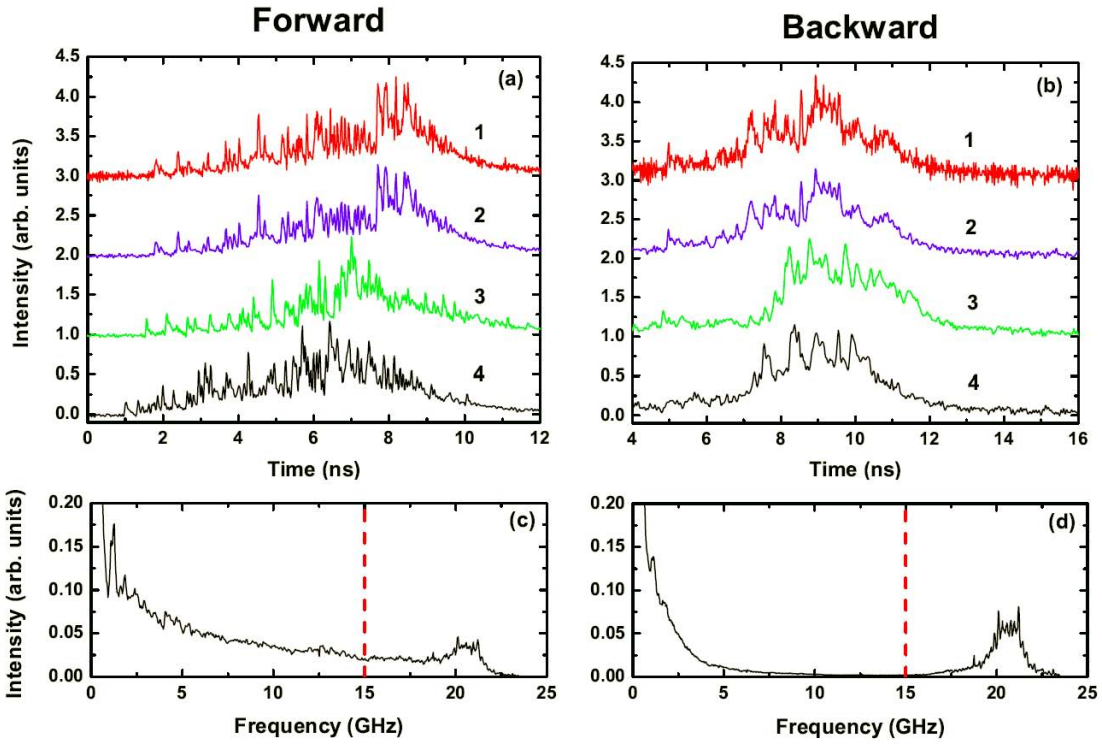

Figure 5.3: Single shot temporal profiles of both forward (a) and backward (b) pulses at full pump energy (10 mJ). The top pulses, **1**, in both are shown without any frequency filtering while the pulses immediately below, **2**, are the same pulses after Fourier filtering. Pulses **3** and **4** are other examples of filtered pulses, vertically shifted for convenience. Averaged Fourier transforms of the forward (c) and backward (d) pulses. The Fourier transforms depict and help quantify spectral intensity modulations for both pulses. Filtering is applied by subtracting the Fourier spectrum of the background as well as removing all frequency components beyond the red dashed line as they are artifacts of the electronics.

(an example is shown in the bottom inset of Fig. 5.1). Due to instrumental artifacts centered around 20 GHz, near the oscilloscope's bandwidth limit, all frequency components above 15 GHz are removed.

Single-shot temporal profiles of forward and backward pulses are measured simultaneously using the same photodiode (New Focus, described above) and are presented in Figs. 5.3(a) and 5.3(b), respectively. The main feature of the temporal profiles

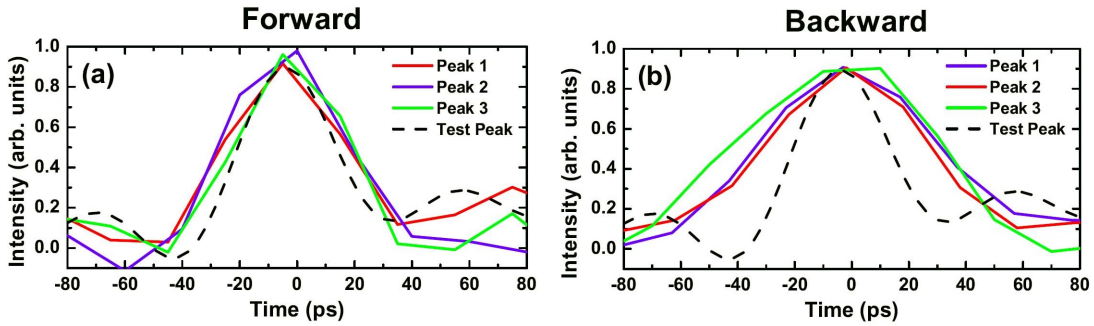

Figure 5.4: Typical individual spikes for both the forward (a) and backward (b) pulses. In both figures, the dashed trace, Test Peak, is the response function of a 35 fs pulse at 800 nm used to test the resolution limit of the detection system. All traces are normalized for ease of comparison.

is the high frequency oscillation, which is similar to spiking that was previously observed and believed to be caused by intensity fluctuations in the pump pulse [109]. In contrast to this previous experiment, our observed spiky structure is higher in both frequency and amplitude. Besides the rapid oscillations, several other features can be discerned from the data. Namely, the forward signal exhibits a higher rate of oscillation with more high frequency components (broadband, $5 - 15$ GHz), as can be seen in the Fourier transforms in Figs. 5.3(c) and 5.3(d). Furthermore, from shot to shot, there are significant variations in the amplitude and number of oscillations.

In Fig. 5.4, we compare the typical narrowest spikes in the emitted pulses with a measured response of a femtosecond test pulse (Ti:Sapphire, 35 fs, 800 nm) which is well below the resolution limit. As can be seen in Fig. 5.4(a), the forward spiking is most likely narrower than can be resolved by our detection system. In contrast, the narrowest peaks observed in the backward direction are ~ 60 ps (FWHM) in duration (Fig. 5.4(b)). These measurements along with the Fourier transforms depicted in Figs. 5.3(c) & 5.3(d), emphasize the distinction between the forward and backward emission, as well as differentiate these results from previous experiments where no

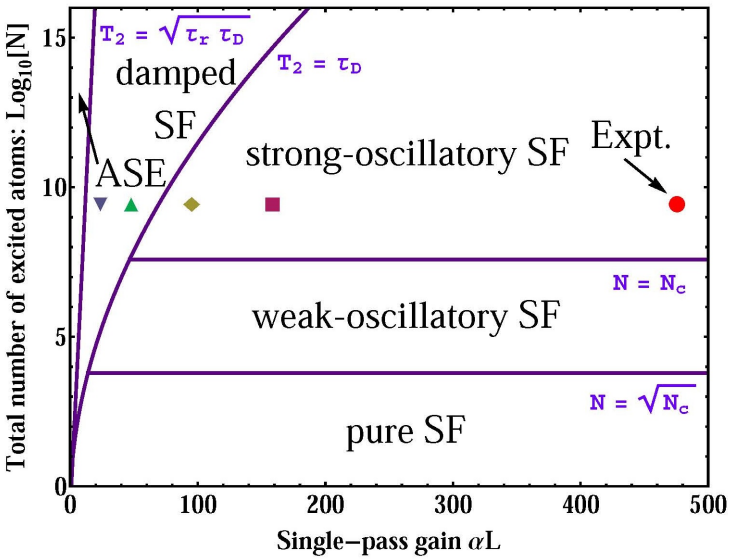

Figure 5.5: Regimes of N-atom cooperative spontaneous emission (adapted from Ref. [114]). The experimental parameters correspond to the strong-oscillatory SF regime (red circle). The four other points (purple square, yellow diamond, green triangle, and blue inverted triangle) correspond to four distinct sets of parameters used in simulations in the following sections.

difference between forward and backward spike duration was observed [109]. Also, given how narrow these spikes are, it is clear that the peak Rabi frequency is higher than the average measured Rabi frequency, which extends this experiment further into the regime of strong nonadiabatic atomic coherence [110]. The spiky emission is interesting and attracts detailed study in the following.

5.3 Regimes of N-atom cooperative spontaneous emission

There has been interest in coherence effects in lasing processes for decades [111, 112, 113]. To start our discussion, we will first introduce several characteristic parameters and hence various regimes of N-atom cooperative spontaneous emission. We will show that our experiment happens in a so-called strong-oscillatory superfluorescence (SF) regime, which indicates that the coherence effects take place.

The regimes of N-atom cooperative spontaneous emission are defined by the values of different characteristic parameters [114], such as the single-pass gain [115]

$$\alpha L = \frac{2T_2}{\tau_r}, \tag{5.4}$$

where T_2 is the collisional dephasing time; the collective damping time [116]

$$\tau_r = \frac{8\pi}{3}\frac{T_1}{n\lambda^2 L}, \tag{5.5}$$

where T_1 is the spontaneous lifetime, λ is the wavelength, L is the gain length and n is the excited atom density; the delay time [117]

$$\tau_D = \tau_r \left[\frac{1}{4}\ln(2\pi N)\right]^2, \tag{5.6}$$

where $N = nAL$ is the total number of excited atoms in the gain volume (with the cross-sectional area A of the gain medium); and the cooperation number [118]

$$N_c = \frac{8\pi c T_1 A}{3\lambda^2 L} = N\frac{\tau_r c}{L}. \tag{5.7}$$

The physical meaning of each regime is discussed in detail in Ref. [114]. We summarize it briefly here. In the limit that $T_2 \to \infty$, there is no collisional dephasing, so SF is radiated for the duration τ_r with a delay time of τ_D. In the regime that $T_2 > \tau_D$, the coherence can be built up during the time τ_D before it decays by collisions and the cooperative emission process may occur. However, in the opposite regime where $T_2 < \sqrt{\tau_r \tau_D}$, the large collisonal dephasing rate prevents coherence from building up. Thus the system generates ASE (amplified spontaneous emission). In the intermediate regime (damped SF), both coherence and collisions play a role. The cooperation

number N_c gives the maximum number of atoms that can emit cooperatively. When the total number of excited atoms, N, is larger than N_c, the propagation effect is present, and atoms undergo reabsorption and reemission processes. The SF emission has temporal ringing behavior. But when $N < \sqrt{N_c}$, the propagation effect is negligable and pure SF is emitted. Fig. 5.5 shows these various regimes determined by these parameters labelled ASE, damped SF, and SF (including strong-oscillatory SF, weak-oscillatory SF and pure SF) [114].

With the parameters in the experiment as $T_2 \sim 0.1$ ns, $T_1 = 0.108$ μs, $\lambda = 845$ nm, $L \sim 1$ cm, $A \sim 10^{-5}$ cm^2, and $n \sim 3 \times 10^{14}$ cm^{-3}, we obtain $\tau_r \approx 0.4$ ps, $\tau_D \approx 15$ ps, $\alpha L \approx 476$ and $N_c \approx 4 \times 10^7$. These parameters place the experiment in the strong-oscillatory SF regime. Detailed theoretical analysis of the strong-oscillatory temporal behavior of atmospheric oxygen emission will be presented in the following sections.

5.4 Theoretical model

We consider a 226 nm pulse (propagating in the forward direction) dissociates oxygen molecules and is used as a pump in a three-level atomic oxygen system (see Fig. 5.6). Emission fields are generated from the $a \leftrightarrow b$ transition in both the forward and backward directions. As noted above, the field from the $b \leftrightarrow c$ transition can only be coherently generated in the forward direction. The backward field from the $b \leftrightarrow c$ transition is zero because of the phase-mismatching with the forward pump field and the absence of the population inversion. The fields from the $a \leftrightarrow b$ transition have a wavelength of 845 nm and have been detected in both directions in the experiment. The forward UV field at 130 nm from the $b \leftrightarrow c$ transition is also involved in the dynamics and affects the 845-nm fields, but has not been detected due to its strong absorption in air.

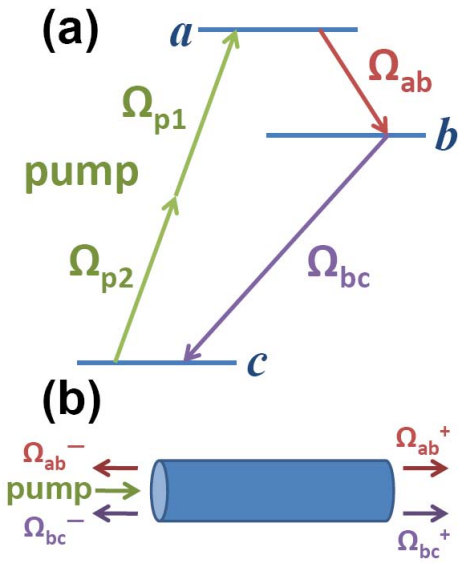

Figure 5.6: (a) Three-level energy diagram of an oxygen atom. Levels a, b, and c represent the states 3p ^{3}P, 3s ^{3}S, and 2p ^{3}P, respectively. (b) The pump pulse propagates in the forward direction. We consider fields from the $a \leftrightarrow b$ and $b \leftrightarrow c$ transitions both in the forward and backward directions in the theoretical model.

For our model, we use a pencil-like active medium, with a length of 1 cm and a cross-sectional area of 10^{-5} cm^2, as in the experiment. We assume the atomic density in this active medium is constant at 10^{15} cm^{-3} (with population initially in the ground state). The two-photon excitation of the $a \leftrightarrow c$ transition by the pump pulse is treated as two excitation processes via two allowed transitions with the smallest detuning between the pump field and the transition from the ground level to an intermediate level. This intermediate level corresponds to the 3s ^{3}S state (level b) in the atomic oxygen energy scheme. The detuning Δ is 6.1×10^{15} rad/s. The Rabi frequencies for the pump pulse coupled to the $a \leftrightarrow b$ and $b \leftrightarrow c$ transitions are $\Omega_{p1} = \wp_{ab}\mathcal{E}_p/\hbar$ and $\Omega_{p2} = \wp_{bc}\mathcal{E}_p/\hbar$, respectively, where $\wp_{ab}$, $\wp_{bc}$ are the matrix elements of the electric dipole moment and $\mathcal{E}_p$ is the slowly varying envelope amplitude with $E_p = \mathcal{E}_p e^{-i(\nu_p t - k_p z)} + c.c.$ Here E_p is the electric field, ν_p is the

frequency and k_p is the wave-vector of the pump, and z is taken to be positive for the forward propagation direction. The detailed derivation of the two-photon excitation is shown in Appendix A. The generated fields from the $a \leftrightarrow b$ and $b \leftrightarrow c$ transitions have both forward and backward contributions, which lead to the Rabi frequencies of $\Omega_{ab}^{+}e^{-i(\nu_{ab}t-k_{ab}z)} + \Omega_{ab}^{-}e^{-i(\nu_{ab}t+k_{ab}z)}$ and $\Omega_{bc}^{+}e^{-i(\nu_{bc}t-k_{bc}z)} + \Omega_{bc}^{-}e^{-i(\nu_{bc}t+k_{bc}z)}$, respectively. Here "+" and "−" represent forward and backward propagation, respectively. Ω_{ab}^{+}, Ω_{ab}^{-}, Ω_{bc}^{+}, and Ω_{bc}^{-} are assumed to be slowly varying functions. These fields are coupled with the active atomic medium. The semiclassical Maxwell-Bloch (MB) equations are used to describe the physics of this 3-level system. The phase-matching conditions are considered. The rotating wave approximation (RWA) is used, so the terms coupling the fields and the polarization in the medium which are not phase-matched are neglected. The detailed equations are derived in the following.

5.4.1 Maxwell-Bloch equations

Using the slowly varying approximation and RWA and the assumption that the pump Rabi frequencies $\Omega_{p1}(t,z)$ and $\Omega_{p2}(t,z)$ are positive real functions, the Hamiltonian in the interaction picture reads

$$\begin{aligned} H_I = &- \hbar\Omega_{p1}e^{-i\Delta t+ik_pz}|a\rangle\langle b| - \hbar\Omega_{p2}e^{i\Delta t+ik_pz}|b\rangle\langle c| \\ &- \hbar(\Omega_{ab}^{+}e^{ik_{ab}z} + \Omega_{ab}^{-}e^{-ik_{ab}z})|a\rangle\langle b| - \hbar(\Omega_{bc}^{+}e^{ik_{bc}z} + \Omega_{bc}^{-}e^{-ik_{bc}z})|b\rangle\langle c| + H.c., \end{aligned} \tag{5.8}$$

The density matrix equations for the coherence are

$$\begin{aligned} \dot{\rho}_{ab} = &- \Gamma_{ab}\rho_{ab} - i(\Omega_{ab}^{+}e^{ik_{ab}z} + \Omega_{ab}^{-}e^{-ik_{ab}z})(\rho_{aa} - \rho_{bb}) - i\Omega_{p1}e^{-i\Delta t+ik_pz}(\rho_{aa} - \rho_{bb}) \\ &- i(\Omega_{bc}^{+*}e^{-ik_{bc}z} + \Omega_{bc}^{-*}e^{ik_{bc}z})\rho_{ac} - i\Omega_{p2}^{*}e^{-i\Delta t-ik_pz}\rho_{ac}, \end{aligned} \tag{5.9}$$

$$\dot{\rho}_{bc} = -\Gamma_{bc}\rho_{bc} - i(\Omega_{bc}^{+}e^{ik_{bc}z} + \Omega_{bc}^{-}e^{-ik_{bc}z})(\rho_{bb} - \rho_{cc}) - i\Omega_{p2}e^{i\Delta t + ik_p z}(\rho_{bb} - \rho_{cc})$$
$$+ i(\Omega_{ab}^{+*}e^{-ik_{ab}z} + \Omega_{ab}^{-*}e^{ik_{ab}z})\rho_{ac} + i\Omega_{p1}^{*}e^{i\Delta t - ik_p z}\rho_{ac}, \tag{5.10}$$

$$\dot{\rho}_{ac} = -\Gamma_{ac}\rho_{ac} + i(\Omega_{ab}^{+}e^{ik_{ab}z} + \Omega_{ab}^{-}e^{-ik_{ab}z})\rho_{bc} + i\Omega_{p1}e^{-i\Delta t + ik_p z}\rho_{bc}$$
$$- i(\Omega_{bc}^{+}e^{ik_{bc}z} + \Omega_{bc}^{-}e^{-ik_{bc}z})\rho_{ab} - i\Omega_{p2}e^{i\Delta t + ik_p z}\rho_{ab}, \tag{5.11}$$

where the dephasing rates are $\Gamma_{ab} = \frac{1}{2}(\gamma_{ab} + \gamma_{bc}) + \gamma_{col}$, $\Gamma_{bc} = \frac{1}{2}\gamma_{bc} + \gamma_{col}$, and $\Gamma_{ac} = \frac{1}{2}\gamma_{ab} + \gamma_{col}$, with γ_{col} being the collisional dephasing rate, and γ_{ab} and γ_{bc} are spontaneous decay rates at the $a \leftrightarrow b$ and $b \leftrightarrow c$ transitions, respectively. Expressing the coherence as a sum of the slow and fast varying terms (the latter oscillating at a frequency as the detuning Δ)

$$\rho_{ab} = \sigma_{ab} + u_{ab}e^{-i\Delta t}, \tag{5.12}$$

$$\rho_{bc} = \sigma_{bc} + u_{bc}e^{i\Delta t}, \tag{5.13}$$

plugging those two definitions into Eqs. (5.9)-(5.11) and using RWA to neglect the fast oscillating terms we obtain

$$\dot{\sigma}_{ab} = -\Gamma_{ab}\sigma_{ab} - i(\Omega_{ab}^{+}e^{ik_{ab}z} + \Omega_{ab}^{-}e^{-ik_{ab}z})(\rho_{aa} - \rho_{bb}) - i(\Omega_{bc}^{+*}e^{-ik_{bc}z} + \Omega_{bc}^{-*}e^{ik_{bc}z})\rho_{ac}, \tag{5.14}$$

$$\dot{u}_{ab} = -(\Gamma_{ab} - i\Delta)u_{ab} - i\Omega_{p1}e^{ik_p z}(\rho_{aa} - \rho_{bb}) - i\Omega_{p2}^{*}e^{-ik_p z}\rho_{ac}, \tag{5.15}$$

$$\dot{\sigma}_{bc} = -\Gamma_{bc}\sigma_{bc} - i(\Omega_{bc}^{+}e^{ik_{bc}z} + \Omega_{bc}^{-}e^{-ik_{bc}z})(\rho_{bb} - \rho_{cc}) + i(\Omega_{ab}^{+*}e^{-ik_{ab}z} + \Omega_{ab}^{-*}e^{ik_{ab}z})\rho_{ac}, \tag{5.16}$$

$$\dot{u}_{bc} = -(\Gamma_{bc} + i\Delta)u_{bc} - i\Omega_{p2}e^{ik_p z}(\rho_{bb} - \rho_{cc}) + i\Omega_{p1}^{*}e^{-ik_p z}\rho_{ac}, \tag{5.17}$$

$$\dot{\rho}_{ac} = -\Gamma_{ac}\rho_{ac} + i(\Omega_{ab}^{+}e^{ik_{ab}z} + \Omega_{ab}^{-}e^{-ik_{ab}z})\sigma_{bc} + i\Omega_{p1}e^{ik_{p}z}u_{bc}$$
$$- i(\Omega_{bc}^{+}e^{ik_{bc}z} + \Omega_{bc}^{-}e^{-ik_{bc}z})\sigma_{ab} - i\Omega_{p2}e^{ik_{p}z}u_{ab}. \tag{5.18}$$

Because the detuning Δ in Eqs. (5.15) & (5.17) is much larger than any relaxation process, we assume that the terms u_{ab} and u_{bc} reach steady state quickly. Therefore, we write them as

$$u_{bc} = \frac{-\Omega_{p2}e^{ik_{p}z}(\rho_{bb} - \rho_{cc}) + \Omega_{p1}^{*}e^{-ik_{p}z}\rho_{ac}}{\Delta - i\Gamma_{bc}}, \tag{5.19}$$

$$u_{ab} = \frac{\Omega_{p1}e^{ik_{p}z}(\rho_{aa} - \rho_{bb}) + \Omega_{p2}^{*}e^{-ik_{p}z}\rho_{ac}}{\Delta + i\Gamma_{ab}}. \tag{5.20}$$

Plugging these two solutions into Eq. (5.18) with the assumption that $\Delta \gg \Gamma_{ij}$, we find

$$\dot{\rho}_{ac} = -\Gamma_{ac}\rho_{ac} + i\frac{|\Omega_{p1}|^2 - |\Omega_{p2}|^2}{\Delta}\rho_{ac} - i\frac{\Omega_{p1}\Omega_{p2}}{\Delta}e^{i2k_{p}z}(\rho_{aa} - \rho_{cc})$$
$$+ (\Omega_{ab}^{+}e^{ik_{ab}z} + \Omega_{ab}^{-}e^{-ik_{ab}z})\sigma_{bc} - (\Omega_{bc}^{+}e^{ik_{bc}z} + \Omega_{bc}^{-}e^{-ik_{bc}z})\sigma_{ab}. \tag{5.21}$$

Next, we express the coherence as slowly varying terms with position z

$$\sigma_{ab} = \rho_{ab}^{+}e^{ik_{ab}z} + \rho_{ab}^{-}e^{-ik_{ab}z}, \tag{5.22}$$

$$\sigma_{bc} = \rho_{bc}^{+}e^{ik_{bc}z} + \rho_{bc}^{-}e^{-ik_{bc}z}, \tag{5.23}$$

and

$$\rho_{ac} \rightarrow \rho_{ac}e^{i2k_{p}z}. \tag{5.24}$$

Keeping in mind that the phase-matching condition gives $2k_p - k_{ab} - k_{bc} = 0$, we plug Eqs. (5.22)-(5.24) back into Eq. (5.14), Eq. (5.16), and Eq. (5.21) and use RWA to

remove the terms with fast oscillation with z. (The treatment of the density matrix equations for the population is the same as for ρ_{ac}). Then we derive the full set of the density matrix equations, which is summarized in the following

$$\dot{\rho}^{+}_{ab} = -\Gamma_{ab}\rho^{+}_{ab} - i\Omega^{+}_{ab}(\rho_{aa} - \rho_{bb}) - i\Omega^{+*}_{bc}\rho_{ac}, \tag{5.25}$$

$$\dot{\rho}^{-}_{ab} = -\Gamma_{ab}\rho^{-}_{ab} - i\Omega^{-}_{ab}(\rho_{aa} - \rho_{bb}), \tag{5.26}$$

$$\dot{\rho}^{+}_{bc} = -\Gamma_{bc}\rho^{+}_{bc} - i\Omega^{+}_{bc}(\rho_{bb} - \rho_{cc}) + i\Omega^{+*}_{ab}\rho_{ac}, \tag{5.27}$$

$$\dot{\rho}^{-}_{bc} = -\Gamma_{bc}\rho^{-}_{bc} - i\Omega^{-}_{bc}(\rho_{bb} - \rho_{cc}), \tag{5.28}$$

$$\dot{\rho}_{ac} = -\left[\Gamma_{ac} - i\frac{|\Omega_{p1}|^2 - |\Omega_{p2}|^2}{\Delta}\right]\rho_{ac} - i\frac{\Omega_{p1}\Omega_{p2}}{\Delta}(\rho_{aa} - \rho_{cc}) + i\Omega^{+}_{ab}\rho^{+}_{bc} - i\Omega^{+}_{bc}\rho^{+}_{ab}, \tag{5.29}$$

$$\dot{\rho}_{aa} = -\gamma_{ab}\rho_{aa} + \left(i\Omega^{+}_{ab}\rho^{+}_{ba} + i\Omega^{-}_{ab}\rho^{-}_{ba} + i\frac{\Omega_{p1}\Omega_{p2}}{\Delta}\rho_{ca} + c.c.\right), \tag{5.30}$$

$$\dot{\rho}_{bb} = \gamma_{ab}\rho_{aa} - \gamma_{bc}\rho_{bb} + \left(-i\Omega^{+}_{ab}\rho^{+}_{ba} - i\Omega^{-}_{ab}\rho^{-}_{ba} + i\Omega^{+}_{bc}\rho^{+}_{cb} + i\Omega^{-}_{bc}\rho^{-}_{cb} + c.c.\right), \tag{5.31}$$

$$\rho_{aa} + \rho_{bb} + \rho_{cc} = 1, \tag{5.32}$$

We neglect Doppler broadening in the simulation because the collisional dephasing rate is the dominating relaxation process in the current experiment. The Maxwell-Bloch equations read

$$\pm\frac{\partial\Omega^{\pm}_{ab}}{\partial z} + \frac{1}{c}\frac{\partial\Omega^{\pm}_{ab}}{\partial t} + \kappa\Omega^{\pm}_{ab} = i\eta_{ab}\rho^{\pm}_{ab}, \tag{5.33}$$

$$\pm\frac{\partial\Omega^{\pm}_{bc}}{\partial z} + \frac{1}{c}\frac{\partial\Omega^{\pm}_{bc}}{\partial t} = i\eta_{bc}\rho^{\pm}_{bc}, \tag{5.34}$$

where $\eta_{ij} = \frac{3}{8\pi}n_a\lambda^2_{ij}\gamma_{ij}$ is the field-atom coupling constant, where n_a is the atomic density and κ is the decay rate of the 845-nm field due to the Rayleigh diffraction

limit.

5.4.2 Rate equations

We will further present the calculations of rate equations on the experiment and hence discuss the validity of such method on explanation of the coherence effects. To serve that purpose, we derive and list the full set of rate equations here.

The rate equations are derived from the density matrix equations Eqs. (5.25)-(5.34) by the "adiabatic approximation". This approximation eliminates the equations of the rapidly decaying dipole moment. Namely, Eqs. (5.25)-(5.29) become

$$0 \simeq -\Gamma_{ab}\rho_{ab}^{\pm} - i\Omega_{ab}^{\pm}(\rho_{aa} - \rho_{bb}), \tag{5.35}$$

$$0 \simeq -\Gamma_{bc}\rho_{bc}^{\pm} - i\Omega_{bc}^{\pm}(\rho_{bb} - \rho_{cc}), \tag{5.36}$$

$$0 \simeq -\left[\Gamma_{ac} - i\frac{|\Omega_{p1}|^2 - |\Omega_{p2}|^2}{\Delta}\right]\rho_{ac} - i\frac{\Omega_{p1}\Omega_{p2}}{\Delta}(\rho_{aa} - \rho_{cc}), \tag{5.37}$$

where the transient parts of coherence $\rho_{ab}^{\pm}$, $\rho_{bc}^{\pm}$ can be neglected, and they follow adiabatically from the population difference [119]. The full set of rate equations may be derived by plugging the results of Eqs. (5.35)-(5.37) into all the rest of the density matrix equations [Eqs. (5.30)-(5.34)]:

$$\dot{\rho}_{aa} = -\gamma_{ab}\rho_{aa} - \frac{2|\Omega_{ab}^{+}|^2 + 2|\Omega_{ab}^{-}|^2}{\Gamma_{ab}}(\rho_{aa} - \rho_{bb}) - \frac{2\Gamma_{ac}|\Omega_{p1}\Omega_{p2}|^2}{\Gamma_{ac}^2\Delta^2 + \left(|\Omega_{p1}|^2 - |\Omega_{p2}|^2\right)^2}(\rho_{aa} - \rho_{cc}), \tag{5.38}$$

$$\dot{\rho}_{bb} = \gamma_{ab}\rho_{aa} - \gamma_{bc}\rho_{bb} + \frac{2|\Omega_{ab}^{+}|^2 + 2|\Omega_{ab}^{-}|^2}{\Gamma_{ab}}(\rho_{aa} - \rho_{bb}) - \frac{2|\Omega_{bc}^{+}|^2 + 2|\Omega_{bc}^{-}|^2}{\Gamma_{bc}}(\rho_{bb} - \rho_{cc}), \tag{5.39}$$

$$\rho_{aa} + \rho_{bb} + \rho_{cc} = 1, \tag{5.40}$$

$$\pm\frac{\partial\Omega_{ab}^{\pm}}{\partial z} + \frac{1}{c}\frac{\partial\Omega_{ab}^{\pm}}{\partial t} + \kappa\Omega_{ab}^{\pm} = \frac{\eta_{ab}\Omega_{ab}^{\pm}}{\Gamma_{ab}}(\rho_{aa} - \rho_{bb}), \tag{5.41}$$

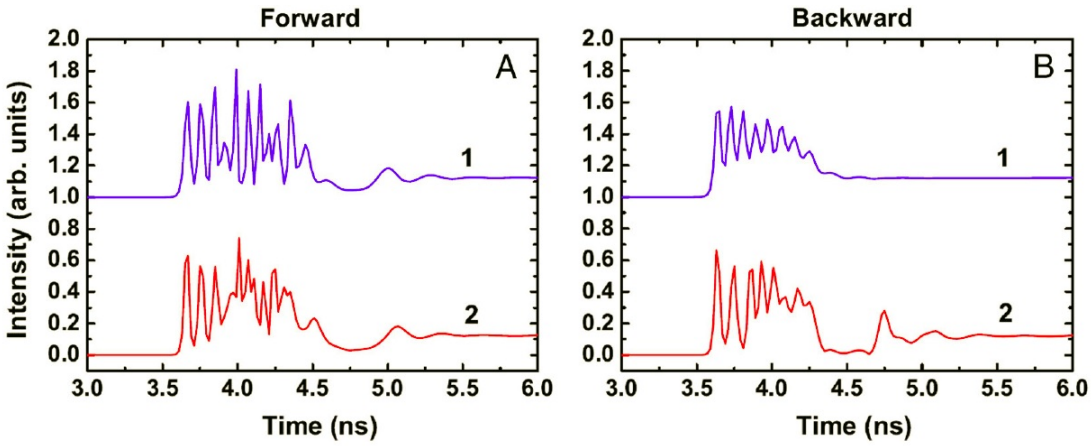

Figure 5.7: Simulated forward (a) and backward (b) signals with a dephasing rate of $\gamma_{col} = 10$ ns^{-1}. Curves **1** (blue) are obtained using a smooth pump pulse as the initial input, while **2** (red) used a pump pulse with random intensity fluctuations to mimic the experiment. The curves are vertically shifted for convenience.

$$\pm\frac{\partial\Omega_{bc}^{\pm}}{\partial z} + \frac{1}{c}\frac{\partial\Omega_{bc}^{\pm}}{\partial t} = \frac{\eta_{bc}\Omega_{bc}^{\pm}}{\Gamma_{bc}}(\rho_{bb} - \rho_{cc}). \tag{5.42}$$

5.5 Simulations

In the experiment, a nanosecond laser pulse (FWHM $\sim$ 10 ns) is used to pump oxygen atoms. The density of the atomic oxygen in a pencil-like cylinder with the length $L = 1$ cm and cross-sectional area $A \sim 10^{-5}$ cm^2 is $n_a = 10^{15}$ cm^{-3}. The spontaneous emission rates are $\gamma_{ab} = 9.3 \times 10^6$ s^{-1} and $\gamma_{bc} = 1.97 \times 10^8$ s^{-1}. Hence the transition dipole moments are $\wp_{ab} \sim 1.38 \times 10^{-29}$ C·m and $\wp_{bc} \sim 0.38 \times 10^{-29}$ C·m. According to the peak power in the experiment (~ 0.5 MW), we can take the peak Rabi frequencies $\Omega_{p1} \sim 3.2 \times 10^{13}$ rad/s and $\Omega_{p2} \sim 8.4 \times 10^{12}$ rad/s and an effective Rabi frequency $\Omega_{eff} \equiv \Omega_{p1}\Omega_{p2}/\Delta \sim 4.4 \times 10^{10}$ rad/s. Doppler broadening is not included in this simulation because we assume that the collisional dephasing is the dominant relaxation process ($\gamma_{col} = 10$ ns^{-1}).

A one-dimensional simulation is performed assuming a fixed population of atoms

that is uniformly distributed throughout the gain region. A smooth pump pulse resembling those found in the experiment (Fig. 5.1) is used as the initial input for the simulations; i.e. it is fit to the averaged pump pulse to mimic the overall pulse shape, but lacked any rapid intensity oscillations. The results of the theoretical simulations are shown as curves **1** in Figs. 5.7(a) & 5.7(b). Despite the absence of rapid intensity oscillations in the pump, the simulations reveal rapid intensity oscillations with spike widths on the same order as those found experimentally. Essentially, the generated field becomes so strong that the corresponding time scale for the evolution of the atomic system becomes faster than dephasing. Rapid intensity fluctuations are added to the pump pulse to resemble the experimental pump pulse shape. This is done to test whether pump fluctuations could cause the observed rapid spiking seen in our emitted pulses as had been seen previously [109]. Rapid intensity spiking is still observed (curves **2** in Figs. 5.7(a) & 5.7(b)), but it is quite apparent that the pump fluctuations do effect the rapid oscillations found in the emitted pulses. However it does not rule out atomic coherence.

The temporal behavior of the emitted pulses are complicated in the case of long nanosecond pump field. The atomic oxygen system is the same as the Yoked superfluroescence scheme that we treated in Section 2. In the experiment, the system experiences both gain without inversion regime and gain suppression regime. The pump pulse first excites partially the upper level a which produces population inversion between the upper two levels. This yields backward lasing at early time, which transfers the population from the upper level to the middle level b. During this process, the forward gain is suppressed. After some time, the upper state population is depleted. This promotes the system into the state with $\rho_{aa} < \rho_{bb} < \rho_{cc}$ while the long pump pulse continues to generate coherence ρ_{ac}. For these conditions the forward gain can be achieved. These processes are repeated as long as the pump field is on.

To clearly see the coherence effect in the strong-oscillatory SF regime as our experiment is, we will perform simulations and reveal the coherence-brightened nature of the emission using picosecond pump excitation. We will further study the validity of using rate equations to describe the emitted fields.

5.5.1 Picosecond pump excitation

We first consider a shorter picosecond pump pulse to better understand the physics of the system. We choose a 20 ps pump pulse with the same order of the peak power in the experiment. The pump pulse enters the medium at time 0.5 ns. The emission fields at 845 nm are generated in both forward and backward directions. We fixed the boundary conditions for the 845-nm fields to be a small constant to play the role of a spontaneous emission source, but assume that there is no spontaneous emission source for the 130-nm field (the UV field is strongly absorbed in air). The decay rate for the 845-nm fields is $\kappa \sim 1.5$ cm^{-1} due to the Rayleigh diffraction length. The simulation results of the temporal behavior of the 845-nm fields ($|\Omega_{ab}^{\pm}|$) for different collisional dephasing rates (γ_{col}) are shown in Fig. 5.8.

Strong-oscillatory SF with large peak Rabi frequencies is seen in both the forward and backward directions when $\gamma_{col} = 10$ ns^{-1} (Fig. 5.8a). The SF oscillations are damped and the intensity decreases for larger γ_{col}. The simulation results are consistent with the various regimes described in Fig. 5.5. The physics is clear with this short picosecond pump pulse excitation. The upper transition of the oxygen atom is inverted after this pump pulse. In the small dephasing rate limit, the inverted system radiates SF and generates a large quantum coherence via cooperation between ensemble atoms. After the population is transferred from the upper level to the middle level, the coherence plays an important role by producing a weaker radiation, which in turn transfers a portion of population back to the upper level. The small

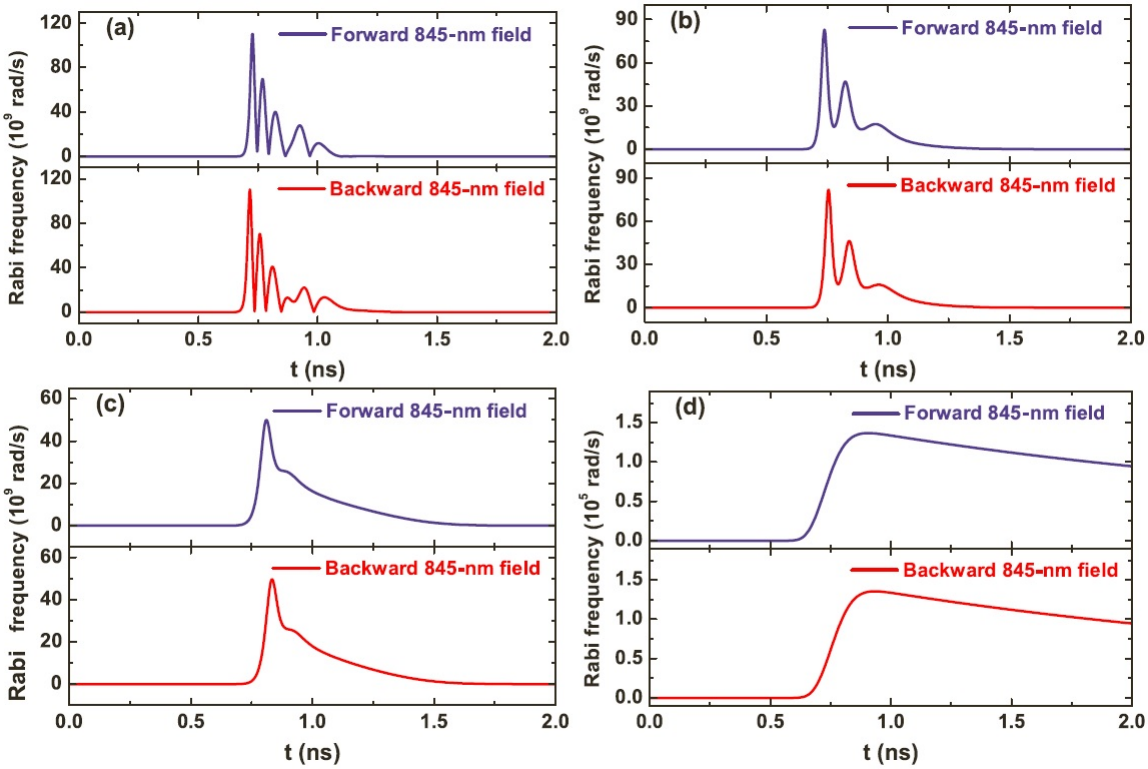

Figure 5.8: Temporal behavior of the 845-nm forward and backward fields generated by a 20-ps 226-nm pump pulse with different collisional dephasing rates: (a) $\gamma_{col} = 10$ ns^{-1} (leading to the regime labelled by the red circle in Fig. 5.5), (b) 30 ns^{-1} (labelled by purple square), (c) 50 ns^{-1} (labelled by yellow diamond), and (d) 100 ns^{-1} (labelled by green triangle).

portion of the population in the upper level then continues to radiate cooperatively. This process repeats and results in the ringing (*i.e.* Burnham-Chiao ringing [120]) in Fig. 5.8a. In the large dephasing rate limit (see Fig. 5.8c), the radiation generated by the inverted system produces a small amount of coherence because of the larger decoherece terms (Γ_{ab} and Γ_{bc}). The amount of coherence is not large enough to re-emit the field after the population moves to the middle level. However, there is a burst in the emission field because the process is still in the SF regime and the atoms radiate collectively. Nevertheless, with a significantly large dephasing rate (e.g. $\gamma_{col} = 100$ ns^{-1}) (Fig. 5.8d), the inverted system cannot produce enough coherence so the radiation is closer to ASE than to SF. The difference between the forward and backward fields is not prominent in this regime. Phase-matching condition and the asymmetric scheme (*i.e.* forward and backward fields at the $a \leftrightarrow b$ and $b \leftrightarrow c$ transitions but only forward propagating pump pulse) are the main reasons for the difference, which is discussed in detail in the next section. We find in this simulation with a simple short pump pulse that the atomic coherence is responsible for the spiky features.

5.5.2 Comparison of Maxwell-Bloch and rate equations

In this section, we match simulations more closely to the experiment by using a nanosecond pump pulse. The long pump pulse makes the dynamics more complicated than in the previous section. Namely, it keeps pumping the populations from the lower to the upper level, generating coherence between these two levels and coupling with the forward propagating generated fields. We consider a 2-ns square-shaped pump pulse entering the medium at 0.5 ns and exiting at 2.5 ns, with the same peak Rabi frequency as in the previous section.

The simulations are done using both the Maxwell-Bloch (MB) and the rate equa-

tions. It is well-known that the rate equations can be derived from more general Maxwell-Bloch equations in the density matrix treatment by the "adiabatic approximation", which assumes that the transient part of the evolution of the atomic coherence can be neglected and the amplitude of such coherence follows adiabatically the changes of the population distribution [119]. This approximation eliminates the equations of the rapidly decaying dipole moment, such as Eqs. (5.25) & (5.26) and describes the coherence terms as

$$\rho_{ab}^{\pm} = -\frac{i\Omega_{ab}^{\pm}(\rho_{aa} - \rho_{bb})}{\Gamma_{ab}}. \tag{5.43}$$

This approximation is only valid when the dephasing time is much shorter than the population relaxation time. Therefore, the atomic coherence is no longer included explicitly.

The simulation results using both the Maxwell-Bloch and the rate equations are shown in Fig. 5.9. In the small dephasing limit ($\gamma_{col} = 10$ ns^{-1}), the resulting fields $|\Omega_{ab}^{\pm}|$ and the coherence $\rho_{ab}^{\pm}$ at the upper transition from the Maxwell-Bloch equations are shown in Figs. 5.9a & 5.9b, respectively. Highly oscillatory SF radiation is generated similar to that in Fig. 5.8a, but with a more complicated temporal profile. The long pump pulse continues to excite the population to the upper level while the SF radiation depletes the excited atoms. The peak amplitude of the Rabi frequency is $\sim 10^{11}$ rad/s, which is consistent with the measurement in the experiment. The forward field has a different shape from the backward field, as does the coherence $\rho_{ab}^{\pm}$. The real part of the coherence ρ_{ab}^{-}, which contributes to the backward field generation, is zero, but the real part of the coherence ρ_{ab}^{+}, which helps the forward field generation, is non-zero. This is the major cause of the difference between the forward and backward fields. The backward coherence (or field) is only generated

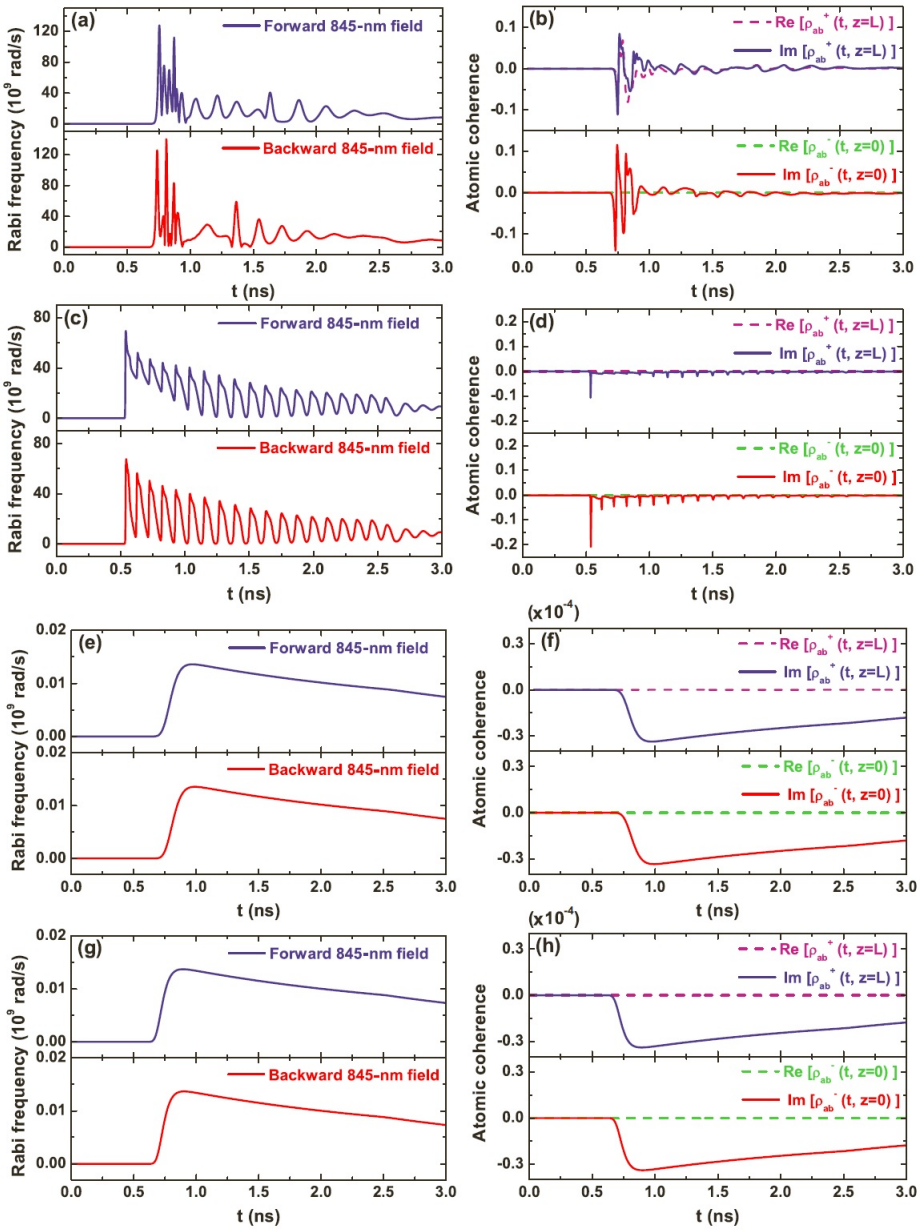

Figure 5.9: Temporal behavior of the fields $\Omega_{ab}^{\pm}$ and the atomic coherence $\rho_{ab}^{\pm}$ pumped by a nanosecond pulse simulated using the Maxwell-Bloch (MB) and rate equations for different dephasing rates $\gamma_{col} = 10$ ns^{-1} (leading to the regime labelled by the red circle in Fig. 5.5) and $\gamma_{col} = 200$ ns^{-1} (labelled by blue inverted triangle): (a)&(b) MB equations with $\gamma_{col} = 10$ ns^{-1}; (c)&(d) rate equations with $\gamma_{col} = 10$ ns^{-1}; (e)&(f) MB equations with $\gamma_{col} = 200$ ns^{-1}; (g)&(h) rate equations with $\gamma_{col} = 200$ ns^{-1}. The coherence in the simulations with the rate equations was calculated using Eq. (5.43).

by the population difference; however, the forward coherence can also result from the four-wave mixing. Namely, the two-photon excited coherence ρ_{ac} interacts with the radiation at the lower transition and contributes to the ρ_{ab}^{+} and to the forward 845-nm field (and vice versa). In this simulation, a large amount of coherence (~ 0.1) at the $a \leftrightarrow b$ transition is produced. The fast change of the coherence makes it a nonadiabatic process. To prove this point, a simulation with the same decay rate but using the rate equations is shown in Figs. 5.9c & 5.9d. Comparing the results with Figs. 5.9a & 5.9b from the Maxwell-Bloch equations, we see a different temporal behavior of the fields and the coherence. Therefore, the adiabatic approximation in the small dephasing limit ($\gamma_{col} = 10$ ns^{-1}) is not valid and the rate equations give an incorrect result. The coherence effects play an important role when the Rabi frequency is larger than any relaxation rate. In this regime they can only be described by Maxwell-Bloch equations without the adiabatic approximation.

On the other hand, in the large dephasing limit ($\gamma_{col} = 200$ ns^{-1}), both the Maxwell-Bloch and rate equations give similar results for the fields and the coherence (see Figs. 5.9e - 5.9h). The amplitude of the Rabi frequency at the 845-nm emission is $\sim 10^7$ rad/s, which is much smaller than the dephasing rate. In this regime, since the coherence effects are not important, the adiabatic approximation works well and the simplified rate equations are adequate to describe the physical process.

In Fig. 5.10, we show two-dimensional plots of the generated 845-nm forward and backward fields inside the active medium with the parameters the same as in Fig. 5.9a. The fields are plotted for the position z from 0 to 1 cm and the time t from 0.7 to 1 ns. We show the evolution of the spiky features of the fields in space and time. We notice that the forward and backward fields dominate in different regions; namely, the forward field is much larger in the region $z > 0.5$ cm and the backward field in $z < 0.5$ cm. The fields evolve from a broad peak to spiky oscillations

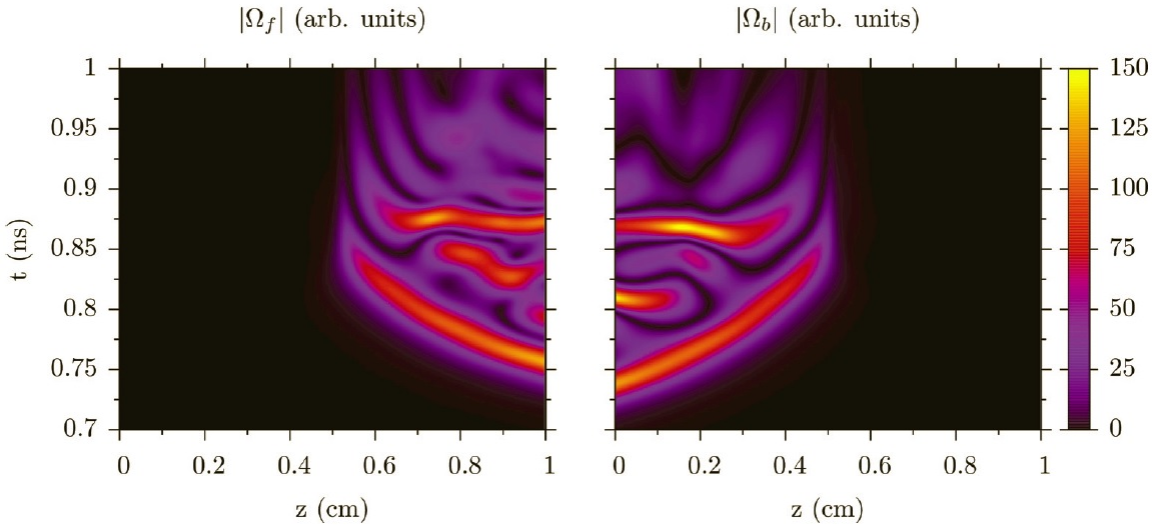

Figure 5.10: Generated 845-nm forward (left) and backward (right) fields dependent on time and position. The parameters are the same as those in Fig. 5.9a.

with changing position because the single-pass gain [Eq. (5.4)] increases with the propagation distance. The non-adiabatic coherence makes the fields evolve fast both in the temporal and spatial domains.

5.6 Conclusion

We presented a detailed study of the coherence-brightened oxygen lasing experiment. The observed average Rabi frequency, $\Omega \sim 10^{12}\ rad/s$, is more than an order of magnitude larger than the estimated dephasing rate $\gamma_{col} = 1 \times 10^{10} s^{-1}$. Furthermore, the peak Rabi frequency is higher than the average as evidenced by the very short timescale of the intensity spiking (Fig. 5.4). These two results are strong evidence that places the emission process into the regime of nonadiabatic atomic coherence [110, 114]. We further confirm the strong-oscillatory superfluorescence in the simulations. We concude that the spiky features of the emission fields are mainly due to coherence effects. The rate equations are not adequate to describe

this behavior. The theoretical study supports the experimental demonstration of a coherence-brightened laser source in air in the Dicke sense [44].

These results provide another step towards the implementation of stand-off spectroscopy of gases in the atmosphere. The high beam quality, stability and power will allow detection of impurities in air with high sensitivity. In fact, this coherent emitted beam with a nanosecond pulse duration will be advantageous in nonlinear optical processes. It should provide higher peak intensity which is crucial for techniques such as counter-propagating two-photon absorption, stimulated Raman scattering or Raman-induced Kerr effect spectroscopies. The 845 nm wavelength is in a suitable range of most common realizations of these techniques for detecting vibrational fingerprints of relevant molecules.

6. COHERENT BACKWARD SCATTERING

6.1 Introduction

Standoff detection of trace gases in the atmosphere is one of the greatest challenges in modern science and technolog. Recent discoveries and impressive technical process in ultrafast optics suggest new powerful tools for remote sensing. Current techniques such as lidar have a 4π scattering cross section and the detected signal is incoherent. The search for the strategies capable of enhancing the return of the standoff coherent signal is ongoing. The fundamental difficulty of coherent signal generation in the backward direction through a nonlinear wave-mixing process is due to phase matching, which expresses a universal physical principle of momentum conservation.

Given the coherence-brightened backward laser source, it is possible to shot up lasers from the ground to interact with the atmospheric laser in the targeted region. Our analysis will indicate a unique possiblity for standoff detection of trace gases using their rotational and vibrational spectroscopic signals in Section 6.2 [79]. We will demonstrate spatial selectivity of Raman transitions and variability of possible Umklappscattering implementation schemes and laser sources. On the other hand, as an alternative method, we also show that an intense coherent backward signal can be generated through a Raman-type four-wave mixing process using forward propagating fields only in Section 6.3 [80]. Phase matching for this process is achieved through a plasma modulation of the refractive index.

6.2 Coherent Raman Umklappscattering*

6.2.1 Implementation schemes

We consider a coherent Raman scattering process where optical fields with frequencies ω_1 and ω_2, referred to as the pump and Stokes fields, are used for a coherent selective excitation of a Raman-active mode with the frequency Ω in a medium. The third field, with frequency ω_3, is used to probe this coherence, giving rise to Stokes and anti-Stokes signal fields with frequencies $\omega_4 = \omega_3 - (\omega_1 - \omega_2) = \omega_3 - \Omega$ and $\omega_4 = \omega_3 + (\omega_1 - \omega_2) = \omega_3 + \Omega$, respectively. Detection of these signals would allow a chemically selective detection of trace gases in the beam interaction region. Throughout the rest of the paper, we focus on anti-Stokes generation, as shown in Fig. 6.1; Stokes generation can be easily calculated in an analogous way.

To set the framework for our analysis, we consider the application where our pump field ω_1 in Fig. 6.1(a) (or probe field ω_3 in Fig. 6.1(b)) is generated in the air at a point beyond the Raman-active region we want to detect or analyze, and that this field is directed back towards the ground where our Stokes and probe (or pump) fields originate. This could be accomplished by creating a backward-propagating oxygen laser as described in the previous section. Our analysis shows that the small-angle CARS phasematching requires that two of the three applied laser frequencies are nearly equal. Two possibilities exist, as shown in Fig. 6.1. In both cases, two laser beams are sent from the ground: one counter-propagating with respect to the air-laser beam, and the other one slightly angled. In the lower part of Fig. 6.1 [both (a) and (b)] we denote beams by their k-vectors and show how these k-vectors align

*Reprinted with permission from "Coherent Raman Umklappscattering" by L. Yuan, A. A. Lanin, P. K. Jha, A. J. Traverso, D. V. Voronine, K. E. Dorfman, A. B. Fedotov, G. R. Welch, A. V. Sokolov, A. M. Zheltikov, and M. O. Scully, 2011. Laser Phys. Lett., vol. 8, pp. 736, Copyright [2011] by Astro Ltd. Reproduced by permission of IOP Publishing. All rights reserved. http://iopscience.iop.org/1612-202X/8/10/007/

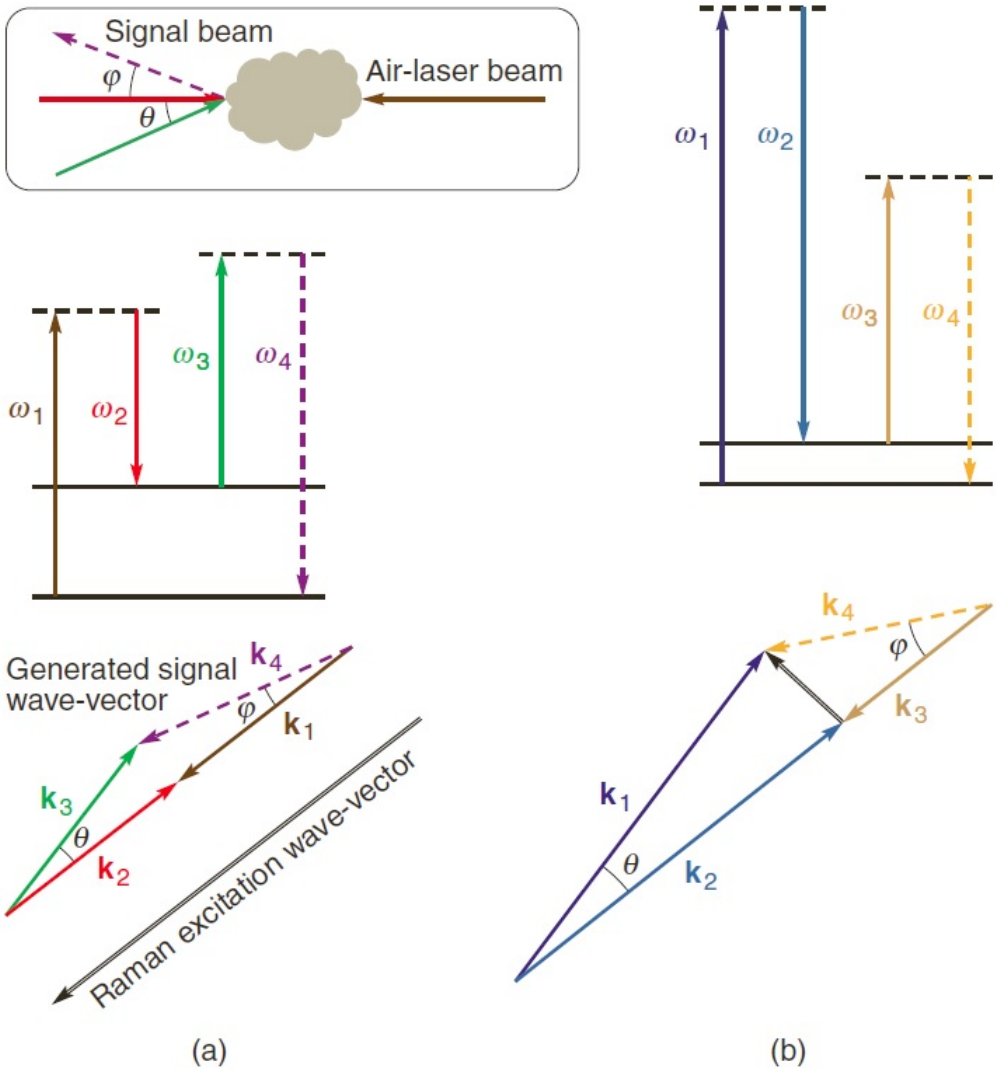

Figure 6.1: Energy level and k-vector diagrams for coherent Raman Umklappscattering using angled counter-propagating ground- and air-laser beams. Signal wave is generated in the direction $\mathbf{k_4}$. Coherent Raman scattering is realized by molecular vibrations (a) and molecular rotations (b). On the energy-level diagrams (top), solid horizontal lines denote real molecular energy levels of the species to-be-detected, and dashed lines correspond to virtual states. (Inset: General configuration of the beams in a cloud.)

to satisfy phasematching. We consider two cases [(a) and (b)] that differ in the way how molecular excitation is prepared. In case (a), molecular coherence (in the species to be detected) is excited by the air-laser beam ($\mathbf{k_1}$, pump, frequency ω_1) together with the counter-propagating beam sent from the ground ($\mathbf{k_2}$, Stokes, frequency ω_2), while in case (b) molecular oscillations (whose k-vector is shown in Fig. 4.5 by a double-line arrow) are driven by two beams sent from the ground, at a small angle with respect to each other ($\mathbf{k_1}$ and $\mathbf{k_2}$, pump and Stokes). The beam at $\mathbf{k_3}$ then scatters off the molecular coherence wave. In both cases, the anti-Stokes signal beam $\mathbf{k_4}$ is then generated in the direction toward the observer. The molecular frequency (equal to $\omega_1 - \omega_2$) is small in case (b). Below, we present detailed calculations for the situation described in Fig. 6.1(b).

6.2.2 Phasematching options for backward CARS

We examine phasematching options for backward CARS due to molecular rotations induced in a gas medium by forward pump and Stokes fields and probed by a backward field with an arbitrary frequency ω_3. Neglecting the frequency dependence of the refractive index $n_i = 1$, and analyzing the wave-vector arrangement shown in Fig. 6.1(b), we find in the case of small θ

$$\theta \approx 2\left(\frac{\omega_3\Omega}{\omega_1^2+\omega_1\omega_3}\right)^{\frac{1}{2}}, \tag{6.1}$$

$$\varphi \approx 2\frac{\omega_1}{\omega_3}\left(\frac{\omega_3\Omega}{\omega_1^2+\omega_1\omega_3}\right)^{\frac{1}{2}}. \tag{6.2}$$

In Fig. 6.2, we compare predictions of Eqs. (6.1) and (6.2) with the results of exact calculations performed using the relevant frequency dependence of $n(\omega)$ for

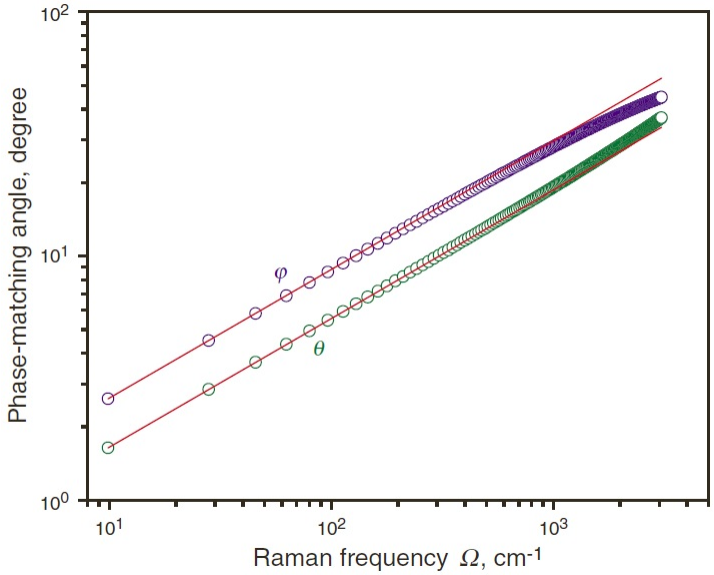

Figure 6.2: The angles between the pump and Stokes beams θ and probe and anti-Stokes beams φ providing phasematching for the anti-Stokes field generation in the noncollinear beam geometry shown in Fig. 4.5 versus the Raman frequency calculations using the exact formula for $|\Delta k|$ with dispersion included (circles) and the approximation of Eqs. (6.1) and (6.2) (solid lines). The pump wavelength is 532 nm.

the atmospheric air. As can be seen from these calculations, the simplified formulas of Eqs. (6.1) and (6.2) give reasonably accurate predictions within a broad range of Ω, providing useful insights into the limitations of the angled beam-interaction geometry imposed by the momentum conservation.

In the case of molecular vibrations, typically used for the standoff detection of trace gases in the atmosphere, the Raman frequencies $(2\pi c)^{-1}\Omega_v$ are on the order of 1000 cm^{-1}. Specifically, for the central frequency of rovibrational Q-branch transitions in molecular oxygen, $(2\pi c)^{-1}\Omega_v \approx 1556$ cm^{-1} and $\lambda = 2\pi c\omega^{-1} = 845$ nm (the central wavelength of stimulated emission by atomic oxygen in the atmosphere), we find $\theta_0 \approx 21^o$. With such big angles between the pump and Stokes beam, practical implementation of standoff detection based on coherent Raman scattering would en-

counter serious difficulties, as probing the atmosphere would require on-ground laser sources and detectors for the coherent backward signal separated by a prohibitively large distance.

Rotational Raman frequencies Ω_r of molecular systems are much lower than Ω_v, with the Ω_r/Ω_v ratio scaling roughly as $(m/M)^{1/2}$ with the ratio of the electron mass m to the relevant atomic mass M. Purely rotational spontaneous Raman scattering is widely used for a lidar remote sensing of the atmosphere [121, 122, 123]. The coherent regime of Raman scattering would radically enhance the Raman signal return due to a higher directionality and a higher magnitude of the coherent Raman response.

In the rigid-rotor approximation, the frequencies of molecular rotational transitions are given by $\Omega_J = 4\pi Bc(2J+3)$, where J is the rotational quantum number, B is the rotational constant, and c is the speed of light. The amplitudes of rotational Raman lines centered at ω_J are given by

$$F_J = \frac{(J+2)(J+1)}{(2J+3)} Z_J(\rho_{J+1} - \rho_J), \tag{6.3}$$

where

$$\rho_J = \frac{\exp\left[-\frac{chBJ(J+1)}{kT}\right]}{\sum\limits_J Z_J(2J+1)\exp\left[-chBJ(J+1)/kT\right]}, \tag{6.4}$$

h is the Planck constant, k is the Boltzmann constant, T is the gas temperature, and Z_J is a factor describing the quantum nuclear statistics.

In Fig. 6.3, we plot the amplitudes F_J of rotational Raman lines versus the phasematching angle $\theta_J \approx (2\Omega_J/\omega)^{1/2}$ for molecular nitrogen ($B \approx 1.99\text{cm}^{-1}$, $Z_J = 1$ and 2 for odd and even J, respectively [124]) and oxygen ($B \approx 1.44\ \text{cm}^{-1}$, $Z_J = 1$ and 0 for odd and even J, respectively [124]) with $\omega_3 \approx \omega_1 = \omega$, $\omega_2 = \omega - \Omega_J$, $\omega_4 = \omega + \Omega_J$

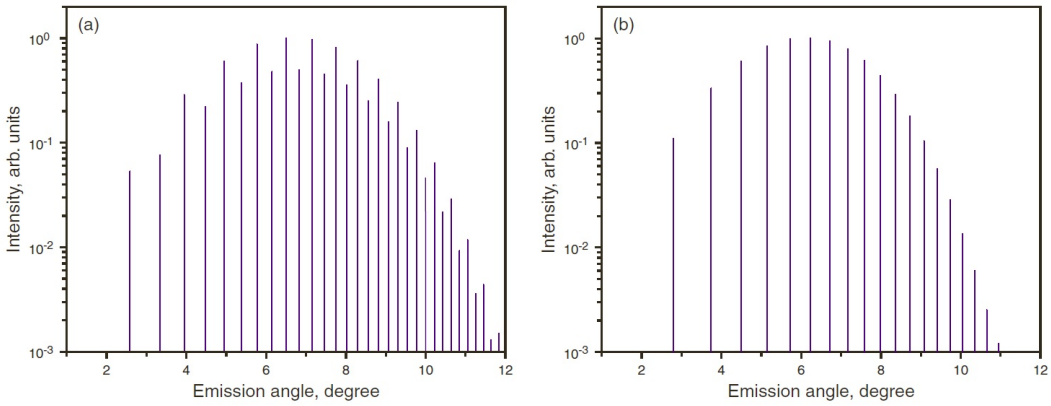

Figure 6.3: The amplitudes F_J of rotational Raman lines versus the phasematching angle $\theta_J \approx (2\Omega_J/\omega)^{1/2}$ for molecular nitrogen (a) and oxygen (b) with $\omega_3 \approx \omega_1 = \omega$, $\omega_2 = \omega - \Omega_J$, $\omega_4 = \omega + \Omega_J$, and $\lambda = 2\pi c\omega^{-1}$ =845 nm.

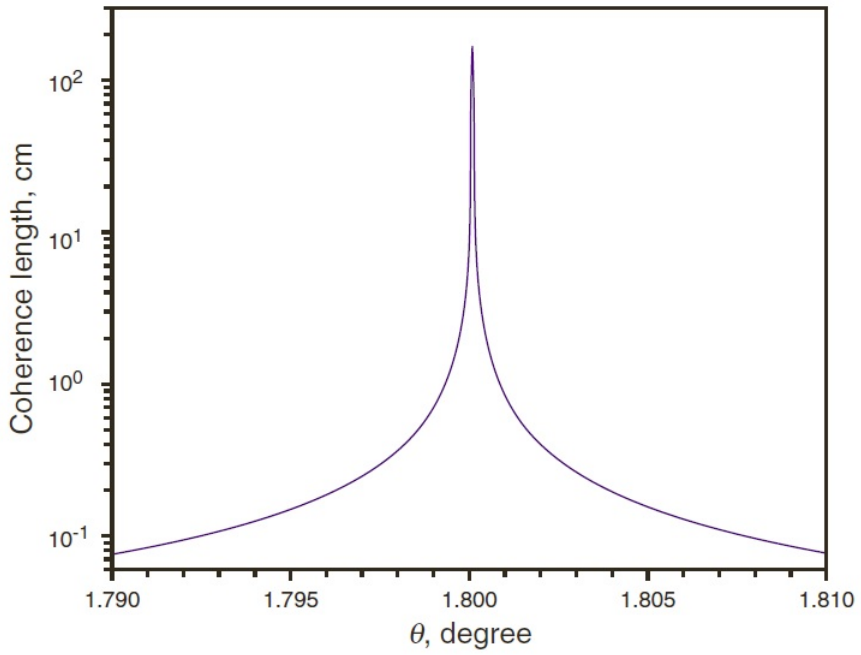

Figure 6.4: Coherence length $l = \pi(2|\Delta k|)^{-1}$ calculated as a function of the angle θ between the pump and Stokes beams for the Ω_0 ≈12 cm^{-1} rotational Raman component of molecular nitrogen in the atmospheric air for a pump wavelength of 532 nm and a probe wavelength of 845 nm.

and $\lambda = 2\pi c\omega^{-1} = 845$nm. These plots model rotational coherent Raman spectra in the beam geometry as shown in Fig. 6.1(b). The magnitudes of the Raman lines differ within a range covering two orders of magnitude which provides a suitable dynamic range for the experimental detection of molecular-specific spectroscopic fingerprints.

Fig. 6.4 displays the coherence length $l = \pi(2|\Delta k|)^{-1}$ calculated as a function of the angle θ between the pump and Stokes beams for the $(2\pi c)^{-1}\Omega_0 \approx 12$ cm^{-1} rotational Raman component of molecular nitrogen in the atmospheric air for a pump wavelength of 532 nm and a probe wavelength of 845 nm. Phasematching is achieved for backward CARS at $\theta_0 \approx 1.8^o$. This small value of θ and a narrow width provide a high directionality and an almost backward propagation of the desired signals.

The scheme in Fig. 6.1(a) is also phase-matched with a small angle θ between the Stokes and the probe on-ground beams, and with a small angle (φ) between the backwards propagating sky and signal beams. The energy level detuning, Δ, between the Stokes and probe beams is now small compared to all the optical frequencies and does not need to be resonant with the vibrational spacing. These angles are given by equations analogous to Eqs. (6.1) and (6.2)

$$\theta \approx 2\left(\frac{\omega_1\Delta}{\omega_1^2+\omega_1\omega_2}\right)^{\frac{1}{2}}, \tag{6.5}$$

$$\varphi \approx 2\frac{\omega_2}{\omega_1}\left(\frac{\omega_1\Delta}{\omega_1^2+\omega_1\omega_2}\right)^{\frac{1}{2}}. \tag{6.6}$$

By suitably selecting the Stokes and probe beam frequencies from the ground it may be possible to detect the vibrational coherent Raman spectrum of the target molecules in the sky and realize the standoff spectroscopy.

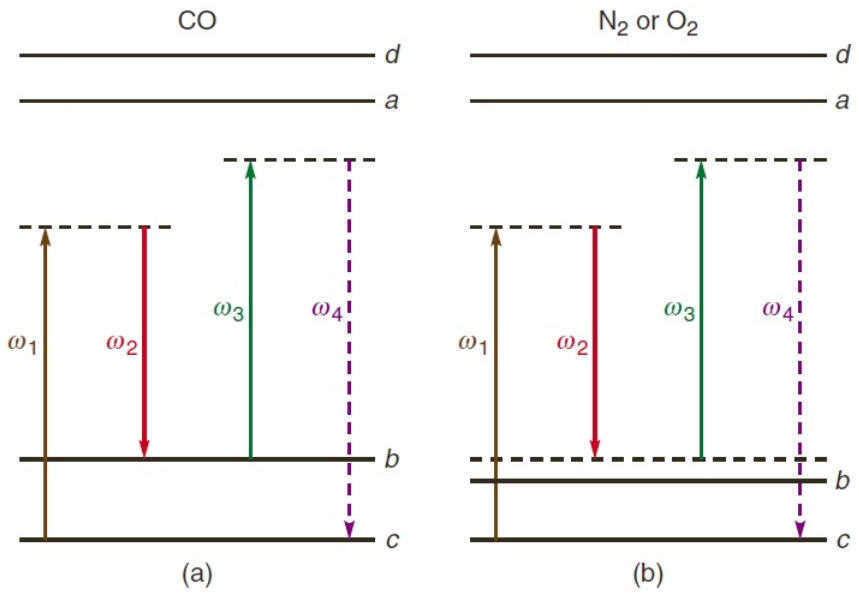

Figure 6.5: Diagrams of (a) CARS by CO molecules and (b) coherent nonresonant background generation by nitrogen and oxygen molecules.

6.2.3 Specific example

We now consider a specific example of CO trace molecules to be detected using the backward CARS schemes considered above against the background signal, related to molecular nitrogen and oxygen in the atmospheric air. The pump and Stokes frequencies are tuned to the Raman resonance with transition between rotational or vibrational b and c levels of CO molecules in the electronic ground state (Fig. 6.5). The pump and Stokes wavelengths are taken to be close to 500 nm and off resonance with an excited electronic state of the molecules (levels a and d in Fig. 6.5) in order to avoid absorption of these fields over long propagation paths in the atmosphere.

Coherent Raman scattering by rotations and vibrations of molecular oxygen and nitrogen in the atmosphere give rise to a coherent background, which masks the CARS signal from CO molecules. The intensities of both the CARS signal from CO

molecules and the nonresonant background are given by $I_{CARS,NR} \sim |\chi^{(3)}_{CARS,NR}|^2 I_1 I_2 I_3$, where I_1, I_2, and I_3 are the intensities of the pump, Stokes, and probe fields, and $\chi^{(3)}_{CARS,NR}$ is the third-order susceptibility of the form [61, 125]

$$\begin{aligned}\chi^{(3)}_{CARS,NR} = \frac{N}{4\pi\varepsilon_0\hbar^3}\Bigg\{&\left(\frac{1}{\omega_{bc}-(\omega_1-\omega_2)-i\gamma_{bc}}\right)\\ &\times\sum_d\left(\frac{\wp_{cd}\wp_{db}}{\omega_{dc}-\omega_4-i\gamma_{dc}}+\frac{\wp_{db}\wp_{cd}}{\omega_{db}+\omega_4+i\gamma_{db}}\right)\\ &\times\sum_a\Bigg[\rho^{(0)}_{cc}\left(\frac{\wp_{ac}\wp_{ba}}{\omega_{ac}-\omega_1-i\gamma_{ac}}+\frac{\wp_{ba}\wp_{ac}}{\omega_{ac}+\omega_2-i\gamma_{ac}}\right)\\ &-\rho^{(0)}_{bb}\left(\frac{\wp_{ac}\wp_{ba}}{\omega_{ab}-\omega_2+i\gamma_{ab}}+\frac{\wp_{ba}\wp_{ac}}{\omega_{ab}+\omega_1+i\gamma_{ab}}\right)\Bigg]\Bigg\}.\end{aligned} \tag{6.7}$$

Here N is the density of molecules, ω_{ij} is the frequency of transitions between levels i and j, ω_k are the optical frequencies ($k = 1, 2, 3, 4$; see Fig. 6.5), γ_{ij} are the relaxation rates, $\wp_{ij}$ are the dipole moments, and $\rho^{(0)}_{ii}$ is the initial population of the level i. The dipole moments are estimated as $\wp_{ij} \approx ea_0$ for all transitions of different molecules. The sum over a in Eq. (6.7) yields a spontaneous Raman crosssection on the order $10^{-31}\text{cm}^2/\text{sr}$ [125]. The nonresonant frequency denominators in Eq. (6.7) are of the order of 10^{16}rad/s for both CO and nitrogen and of the order of 10^{15}rad/s for oxygen. As the frequencies ω_1 and ω_2 are chosen such that $\omega_{bc} - (\omega_1 - \omega_2) = 0$ for the bc transition of CO molecules, the frequency denominator $|\omega_{bc} - (\omega_1 - \omega_2) - i\gamma_{bc}|$ in Eq. (6.7) is estimated as 10^8s^{-1} in the case of CO molecules. For the coherent background, this denominator is 10^{12}rad/s and 10^{11}rad/s in the case of molecular rotations of O_2 and N_2, and 10^{14}rad/s and 10^{13}rad/s for molecular vibrations of O_2 and N_2 respectively. For these parameters, the ratio of the intensities of the CARS signal from CO molecules to the coherent background intensity is estimated as $1 : 10^{-10}$ for molecular vibrations. The intensity of the CARS signal provided by 1 ppm of CO molecules in the atmospheric air will be thus at the level of 1%

of the coherent background intensity, which still allows a reliable detection using appropriate nonresonant background suppression methods [126].

6.3 Plasma-assisted coherent backscattering for standoff spectroscopy[†]

6.3.1 Coherent backscattering model in a double Λ scheme

Here we will demonstrate the possibility of producing a strong backward coherent signal through a four-wave mixing (FWM) process via Raman-excited molecular vibrational coherence. In this process, two strong near-UV laser pulses (pump and Stokes) generate the coherence between two vibrational molecular levels. A weak infrared pulse then probes this coherence and generates an infrared signal in the backward direction (Fig. 6.6(a)). A local ionization of a gas by a nanosecond pulse enables a remote control of the refraction [62], facilitating phase matching of the considered FWM process.

Let us consider an FWM process $\omega_4 = -\omega_1 + \omega_2 + \omega_3$ involving a pump, Stokes, probe, and FWM fields with frequencies ω_1, ω_2, ω_3, and ω_4 and wave vectors $\mathbf{k}_1$, $\mathbf{k}_2$, $\mathbf{k}_3$, and $\mathbf{k}_4$, respectively, in a double Λ level scheme (as shown in Fig. 6.6b). The vibrational coherence ρ_{cb} generated by the pump and Stokes fields in a steady state reads $\rho_{cb} = \Xi/D$, where $\Xi = \Omega_1\Omega_2^*\left[\Gamma_{ac}^*(\rho_{aa} - \rho_{bb}) + \Gamma_{ab}(\rho_{aa} - \rho_{cc})\right]$ and $D = \Gamma_{ab}\Gamma_{cb}\Gamma_{ac}^* + \Gamma_{ab}|\Omega_1|^2 + \Gamma_{ac}^*|\Omega_2|^2$. Here $\Omega_{1,2}$ are the Rabi frequencies for the pump and Stokes fields, and $\Gamma_{ij} = \gamma_{ij} + i\Delta_{ij}$, where γ_{ij} are the relaxation rates and Δ_{ij} are the relevant frequency detunings. The evolution of the probe and scattered fields Ω_3 and Ω_4 in the retarded frame is governed by the equations

$$-\frac{\partial\Omega_4}{\partial z} - ik_4\Omega_4 = i\eta_4\rho_{dc}, \frac{\partial\Omega_3}{\partial z} - ik_3\Omega_3 = i\eta_3\rho_{db}, \tag{6.8}$$

[†]Reprinted with permission from "Plasma-assisted coherent backscattering for standoff spectroscopy" by L. Yuan, K. E. Dorfman, A. M. Zheltikov, and M. O. Scully, 2012. Opt. Lett., vol. 37, pp. 987, Copyright [2012] by the Optical Society.

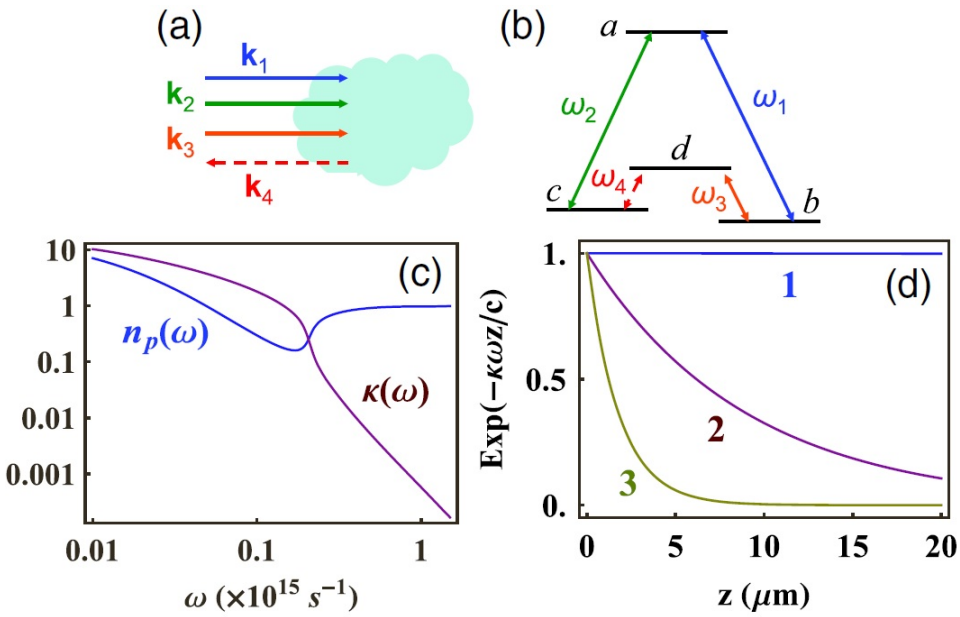

Figure 6.6: Wave-vector (a) and energy (b) diagrams of coherent backscattering in a double Λ scheme in the standoff mode. (c) The real ($n_p(\omega)$) and imaginary part ($\kappa(\omega)$) of the refractive index of plasma as a function of the field frequency ω. Here $n_e = 1.357 \times 10^{19}$ cm^{-3}, $\omega_p = 2.076 \times 10^{14}$ Hz and $\nu = 2.596 \times 10^{13}$ Hz. (d) Attenuation $e^{-\kappa\omega z/c}$ for pump/Stokes (1), probe (2), and signal fields (3) in plasma.

where $\eta_4 = N\lambda_{dc}^2\gamma_r$ and $\eta_3 = N\lambda_{db}^2\gamma_r$ are the coupling constants, N is the density of the molecules, k_j is the wavenumber, and κ_j is the imaginary part of the refractive index modified by free electrons generated in the ionization process. The total refractive index of the ionized gas is given by [127] $n = n_p + i\kappa$ with $2n_p^2 = \varepsilon + \left[\varepsilon^2 + (4\pi\sigma/\omega)^2\right]^{1/2}$, $2\kappa^2 = -\varepsilon + \left[\varepsilon^2 + (4\pi\sigma/\omega)^2\right]^{1/2}$, where $\varepsilon = 1 - \omega_p^2/(\omega^2 + \nu^2)$ is the dielectric function, $\sigma = e^2 n_e \nu/[m(\nu^2 + \omega^2)]$ is the conductivity, $\omega_p = (4\pi e^2 n_e/m)^{1/2}$ is the plasma frequency, ω is the radiation frequency, ν is the effective collision frequency, and n_e is the electron density.

The signal field at the frequency ω_4 can then be calculated as

$$\Omega_4 \sim \int dz \Omega_1^* \Omega_2 \Omega_3 e^{-i(k_1 - k_2 - k_3 + k_4)z}. \tag{6.9}$$

The phase-matching condition for the process shown in Fig. 6.6a is $\mathbf{k}_1 - \mathbf{k}_2 - \mathbf{k}_3 + \mathbf{k}_4 = 0$ for the real parts of vectors $\mathbf{k}_j$. With the pump, Stokes and probe fields propagating along the z-direction toward the target and the coherent Raman signal propagating in the backward direction, the phase-matching condition yields an equation

$$n_{p1}(n_e)\omega_1 - n_{p4}(n_e)\omega_4 = n_{p2}(n_e)\omega_2 + n_{p3}(n_e)\omega_3, \tag{6.10}$$

where $n_{pj}(n_e)$ is the real part of the refractive index at the frequency ω_j, $j = 1, 2, 3, 4$, altered by the presence of the plasma with given electron density n_e.

6.3.2 Phase-matching through a plasma modulation of the refractive index

We assume that a plasma spark is produced in the air by a nanosecond laser pulse via multiphoton ionization. For a typical Nd:YAG laser with a few-nanosecond pulse duration, the breakdown threshold at atmospheric pressure is of the order of $10^{10} - 10^{11}$ W/cm^2 [128]. Laser-induced breakdown by nanosecond pulses is described in the vast literature (see, e.g., Refs. [128, 129] for a review). Its physics is different from the physics behind femtosecond filamentation. In contrast to femtosecond filamentation [130, 131, 132, 133, 134], the Kerr effect does not play a significant role in laser-spark generation by nanosecond pulses. Indeed, with a typical nanosecond-regime laser-breakdown-threshold intensity of $10^{10} - 10^{11}$ W/cm^2 and a nonlinear refractive index of atmospheric air $n_2 \sim 5 \times 10^{-19}$ cm^2/W, we find a refractive-index change of $10^{-8} - 10^{-7}$, which is much smaller than the ionization-induced change in the refractive index. Another important difference from the regime of femtosecond

filamentation is that the laser spark induced by nanosecond pulses does not produce any background due to supercontinuum radiation, which is usually emitted by femtosecond filaments and which may stretch over an ultrabroad spectral range from the UV to the terahertz region [130]. High-contrast forward coherent Raman scattering free of the terahertz background has been observed from laser plasmas produced by nanosecond pulses in the extensive earlier experiments (see Ref. [135] for review). Nanosecond pulses with intensities well above the GW/cm^2 level, on the other hand, may give rise to backward stimulated Brillouin scattering (SBS), which may have important implications for standoff detection. However, backward coherent Raman scattering would have important advantages over SBS due to its chemical specificity, allowing the type of chemical species to be identified in the standoff mode.

The typical electron temperature in the laser-produced plasma in air is $T_e \sim 2-3$ eV. The electron density, as verified by extensive experimental studies (see, e.g., Refs. [128, 129] for a review), can be up to $n_e \sim 2\times10^{19}$ cm^{-3}. For such a density, plasma can be treated as ideal with plasma parameter $\Lambda = \pi n_e \lambda_D^3 \sim 10$, where λ_D is the Debye radius. The corresponding plasma frequency is $\omega_p \sim 10^{14}$ s^{-1}. For efficient plasma–field interaction, the laser pulse should be much longer than the plasma oscillation cycle. Therefore, nano- and picosecond pulses can be used for probe and signal fields. The temperature and density of electrons determine the effective collision frequency between electrons and ions $\nu_{ei} = 4\pi n_e Z_i^2 e^2 \mu^{-1/2} (kT_e)^{-3/2} \log\Lambda_{ei} \sim 10^{13}$ s^{-1}, where Λ_{ei} is a Coulomb logarithm, $\mu = (m_e m_i)/(m_e + m_i) \approx m_e$ is reduced mass and $Z_i = 1$ for single ionization. The collision between electrons and neutral molecules can be estimated as $\nu_{en} \sim v_{th}\sigma_{en} n_e$, where v_{th} is the electron thermal velocity, σ_{en} is the cross section and n_e is the electron density. For $T_e \sim 1$ eV, $\sigma_{en} \sim 10^{-15}$ cm^2, and $n_e \sim 10^{19}$ cm^{-3}, we have $\nu_{en} \sim 10^{11}$ s^{-1}. Thus, the dominant collision process contributing to the refractive index change is electron–ion scattering.

In the case of an SO_2 molecule, the double Λ scheme shown in Fig. 6.6 involves lower vibrational energy levels b (ground vibrational state), c ($\nu_2(a_1)$) and d ($\nu_1(a_1)$) in the ground electronic state $\tilde{X}^1A_1$, and first vibrational level a, in the excited electronic state $\tilde{a}(^3B_1)$ [136]. Thus, the wavelengths $\lambda_{ab} = 388.1$ nm, $\lambda_{ac} = 396.5$ nm, $\lambda_{db} = 8.69$ μm, and $\lambda_{dc} = 16.50$ μm correspond to pump, Stokes, probe and signal fields, respectively. For a given collisional rate ν_{ei} phase matching in Eq. (6.10) can be satisfied with an appropriate choice of electron density n_e. For instance, if $\nu_{ei} = 2.596\times10^{13}$ Hz, Eq.(6.10) is satisfied with $n_e = 1.357\times10^{19}$ cm^{-3}, corresponding to a plasma frequency $\omega_p = 2.076 \times 10^{14}$ Hz. As is seen from the above expressions, the refractive index of an ionized gas is controlled by the electron density, which, in its turn, may depend on the laser intensity. However, in the regime of laser breakdown of a gas induced by nanosecond laser pulses, this dependence becomes very weak, since, above the laser breakdown threshold, plasma absorption on the moving front of the laser-produced spark leads to effective screening, preventing further energy deposition inside the spark [129]. In this regime, variations in laser intensity are not expected to result in dramatic changes in the phase matching. Another universal tendency in the temporal evolution of laser plasmas induced by nanosecond pulses is the flattening of the transverse electron density profile [128]. This effect is favorable for improving the lateral uniformity of ionization-assisted phase matching across the ionized gas region.

Fig. 6.6(c) shows that the refractive index has a dip in the infrared part of the spectrum ($\lambda > 1\mu m$), while it is almost a constant in the shorter wavelength region. In particular, the refractive index for the probe and backward signals is reduced down to 0.348 and 0.241, respectively, in order to satisfy the phase-matching condition Eq. (6.10). For such parameters of the plasma, absorption of the UV pump/Stokes pulses is weak, but the probe and signal fields may experience strong attenuation, as shown

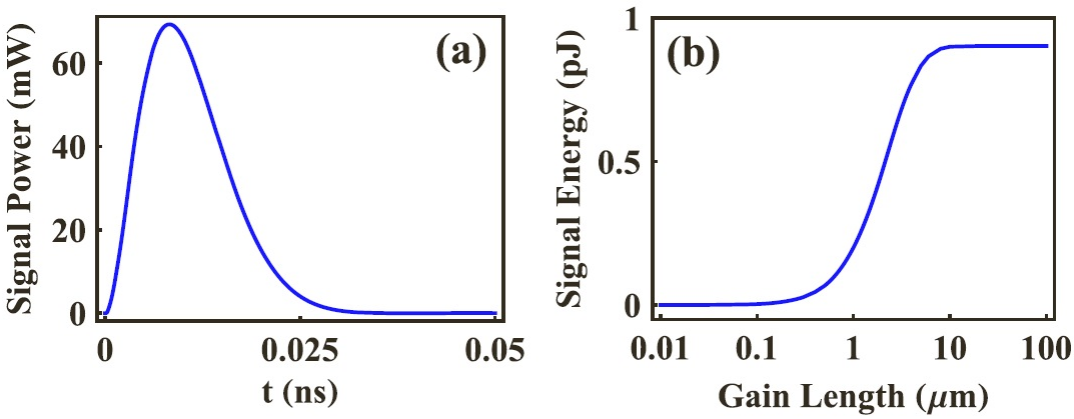

Figure 6.7: (a) The power of the coherent backward signal versus the time after the probe field is turned on; (b) the energy of the coherent backward signal as a function of the gain length.

in Fig. 6.6(d). However, with a proper optimization of plasma parameters, as shown below, a sufficient efficiency of backward signal generation can be provided to yield a detectable backward signal. Beyond the region of ionized gas, the attenuation of the backward signal in the atmospheric air is low (below 10 dB/km at 16.5 μm).

6.3.3 Intuitive theoretical example

As an intuitive theoretical example, we consider detection of sulfur dioxide with a concentration of 5 ppm. After the plasma has been prepared, we first send strong pump/Stokes pulses (with a typical energy of 10 mJ and a pulse width of 10 ns) to prepare the system with maximum coherence ρ_{cb}. Then a $\sim$ 1-mJ probe field with a 100-ps pulse duration is sent to generate the backward signal. With the pump, Stokes and probe beams all focused into a beam-waist area of 5×10^{-4} cm^2, the intensities of the pump, Stokes, and probe pulses are 2×10^9, 2×10^9, and 2×10^{10} W/cm^2, respectively.

In Figs. 6.7a and 6.7b, we present the results of joint numerical solution of the relevant density matrix equations and field propagation equations (6.8) for the power

of the backward signal versus the time after the probe field is turned on (Fig. 6.7a) and the energy of the backward signal as a function of the gain length (Fig. 6.7b). These simulations show that the signal pulse duration is around 0.01 ns and is limited by the large collisional broadening. The maximum peak power can reach 70 mW. The dependence of the backward signal energy on the gain length (plasma spark size) is shown in Fig. 6.7(b). At small gain length (< 0.1 μm), the backward signal is negligible. When increasing the gain length (from 0.1 to 10 μm), a rapid growth of backward signal can be detected. However, when the gain length is larger than 10 μm, it reaches saturation because of the strong plasma absorption of the probe field. As a result, the generation of the coherent backward signal is confined to a short beam-interaction length where the probe field is still high enough. For a plasma region of 100 μm, 1-pJ coherent signal can be generated in the backward direction from a single laser shot (see Fig. 6.7b). The number of trace-gas molecules probed within the beam-interaction volume in the considered geometry with a trace-gas concentration of 5 ppm is $\sim 5 \times 10^7$. The coherent backward signal produced by nonlinear-optical interaction is highly directional, with its intensity decaying with distance r much slower than $1/r^2$. This advantage of proposed approach can overcome one of the key limitations of the lidar methods based on incoherent signals.

6.4 Conclusion

We have shown several realistic schemes for generating backward CARS in a stand-off (remote sensing) configuration. Coherent Raman Umklappscattering of laser fields by molecular rotations and vibrations is shown to enable the generation of phase-matched highly directional, high brightness, nearly backpropagating light beams. The two proposed angled-beam schemes in Fig. 6.1 have complimentary capabilities. Scheme (a) allows a flexible selection of the frequency difference $\omega_3 - \omega_2$

such that the angle can be set to any convenient (small) value. Scheme (b) does not give this flexibility (since the difference $\omega_1 - \omega_2$, and therefore the angle θ, are fixed by the Raman frequency), but instead it allows a free choice of the pump wavelength which now does not have to be close to the air-laser wavelength. For example, if the air-laser wavelength turns out to lie in the near IR range (845 nm, from the oxygen laser in air), the wavelength of the forward-going pump and Stokes beams can still be chosen in the UV range, such as to take advantage of electronic-resonance enhancement. This coherent Raman Umklapp process is well suited for standoff detection of trace gases in the atmosphere with a sensitivity at the level of 1 ppm.

Furthermore, we also demonstrated an alternative method to create backward coherent Raman signal generation using only forward propagating pump, Stokes, and probe fields with ionization-assisted phase matching. As an application to standoff detection, this process has been shown to generate a backward signal of pJ energy through the scattering off the vibrational coherence in sulfur dioxide molecules at the ppm level of trace-gas concentrations.

By phase-matching, the intensity of the backward signal in both methods has a quadratic dependence on the density due to the quantum coherence effects. It provides efficient tools for remote optical sensing and can facilitate applications ranging from enviromental diagnostics and probing to chemical surveillance and biohazard detection.

7. QUANTUM AMPLIFICATION BY SUPERRADIANT EMISSION OF RADIATION*

7.1 Introduction

During the last two decades lasing without inversion (LWI) has been discussed in the literature for various schemes [26, 27, 28]. Typically LWI is achieved due to quantum interference in emission or absorption channels. Such interference appears in systems with coherence created by an external source. However, LWI models require nonzero population of atoms in the excited state. In this section, we go further and show that light amplification (gain) can be obtained even if initially there is no population in the excited state [85].

To set the stage let us first recall the equations that describe conventional lasing and superradiance. We consider a medium composed of two-level ($|a\rangle$ and $|b\rangle$) atoms with population of the excited and ground states being ρ_{aa} and ρ_{bb} respectively. We are interested in the evolution of a weak laser (superradiant) pulse at the atomic transition frequency ω_{ab} that propagates along the $z-$axis. Since the pulse is weak the populations ρ_{aa} and ρ_{bb} can be treated as constant. In the semiclassical approach evolution of the envelope Ω_s of the superradiant pulse is described by the Maxwell-Schrödinger equations

$$\left(\frac{\partial}{\partial t}+c\frac{\partial}{\partial z}\right)\Omega_s = i\Omega_a^2\rho_{ab}^s, \tag{7.1}$$

$$\dot{\rho}_{ab}^s = -\gamma_{\rm tot}\rho_{ab}^s + i\Omega_s(\rho_{bb}-\rho_{aa}), \tag{7.2}$$

*Reprinted with permission from "Quantum Amplification by Superradiant Emission of Radiation" by A. A. Svidzinsky, L. Yuan, and M. O. Scully, 2013. Phys. Rev. X, vol. 3, pp. 041001, Copyright [2013] by the American Physical Society.

where

$$\Omega_a = \sqrt{\frac{3n\lambda_{ab}^2\gamma c}{8\pi}} \tag{7.3}$$

is a collective atomic frequency, $n = N/\mathcal{V}$ is the atomic density, λ_{ab} is the wavelength of the $a-b$ transition, γ is spontaneous decay rate of a single atom, ρ_{ab}^s is slowly varying envelope of atomic coherence, $\Omega = \wp_{ab} \cdot \mathbf{E}/\hbar$ is the Rabi frequency corresponding to electric field $\mathbf{E}$, $\wp_{ab} = \langle a| e\mathbf{r} |b\rangle$ is the matrix element of the electric dipole moment and γ_{tot} is the decoherence rate. Ω_a is the collective frequency with which the resonant pulse is absorbed and reemitted [11, 15, 120].

Taking the time derivative of both sides of Eq. (7.1) and using Eq. (7.2) we obtain for the pulse envelope Ω_s the following linear equation with constant coefficients

$$\left(\frac{\partial}{\partial t} + \gamma_{\text{tot}}\right)\left(\frac{\partial}{\partial t} + c\frac{\partial}{\partial z}\right)\Omega_s + \Omega_a^2(\rho_{bb} - \rho_{aa})\Omega_s = 0. \tag{7.4}$$

One can look for the solution of Eq. (7.4) in the form

$$\Omega_s = A\exp\left(ikz - i\nu t\right), \tag{7.5}$$

where A is a constant, ν is the detuning of superradiant field from the atomic transition frequency and k is the envelope wave number. If we treat k as real then the imaginary part of ν gives gain (absorption) per unit time $G = \text{Im}(\nu)$ for a mode with wave number k and $\Omega_s \propto e^{Gt}$. Plugging (7.5) into Eq. (7.4) yields

$$\nu = \frac{1}{2}\left[-i\gamma_{\text{tot}} + ck \pm \sqrt{(i\gamma_{\text{ tot}} + ck)^2 + 4\Omega_a^2(\rho_{bb} - \rho_{aa})}\right], \tag{7.6}$$

which for the mode with $k \ll \Omega_a/c$ gives the gain

$$G = \Omega_a \sqrt{\rho_{aa} - \rho_{bb}}, \qquad G \gg \gamma_{\rm tot}, \tag{7.7}$$

$$G = \frac{\Omega_a^2}{\gamma_{\rm tot}} \left(\rho_{aa} - \rho_{bb}\right), \qquad G \ll \gamma_{\rm tot}. \tag{7.8}$$

If there is population inversion, $\rho_{aa} > \rho_{bb}$, then gain is positive and the weak seed field grows exponentially with time. The limit $G \gg \gamma_{\rm tot}$ corresponds to superradiance in which the pulse evolves on a time scale much faster then the single atom decay time. In such a limit $G \sim \sqrt{n}$. On the other hand, if $\rho_{aa} = 0$ (all population is in the ground state) and $\gamma_{\rm tot} = 0$ then Eq. (7.7) yields imaginary G which means Ω_s oscillates with collective frequency Ω_a. Such oscillations describe collective absorption and superradiant reemission of light by the atomic system.

Quantum amplification by superradiant emission of radiation (QASER) can be obtained even if initially $\rho_{aa} = 0$. This can occur in the superradiant regime due to a resonance between the driving field frequency ν_d and collective polarization oscillation at Ω_a. Before going into details and lengthy calculations we next motivate the present gain mechanism in a simple way. Let us assume that in Eq. (7.4) population is periodically modulated with frequency ν_d such that

$$\rho_{bb} - \rho_{aa} = 1 - \delta \cos(2\nu_d t), \tag{7.9}$$

where $\delta \ll 1$ is a small modulation amplitude. Writing the slowly varying envelope $\Omega_s(t, z)$ in the form

$$\Omega_s(t, z) = \Omega_s(t) \exp\left[ik\left(z - \frac{ct}{2}\right)\right], \tag{7.10}$$

where k is the envelope wave number and neglecting decoherence we obtain the

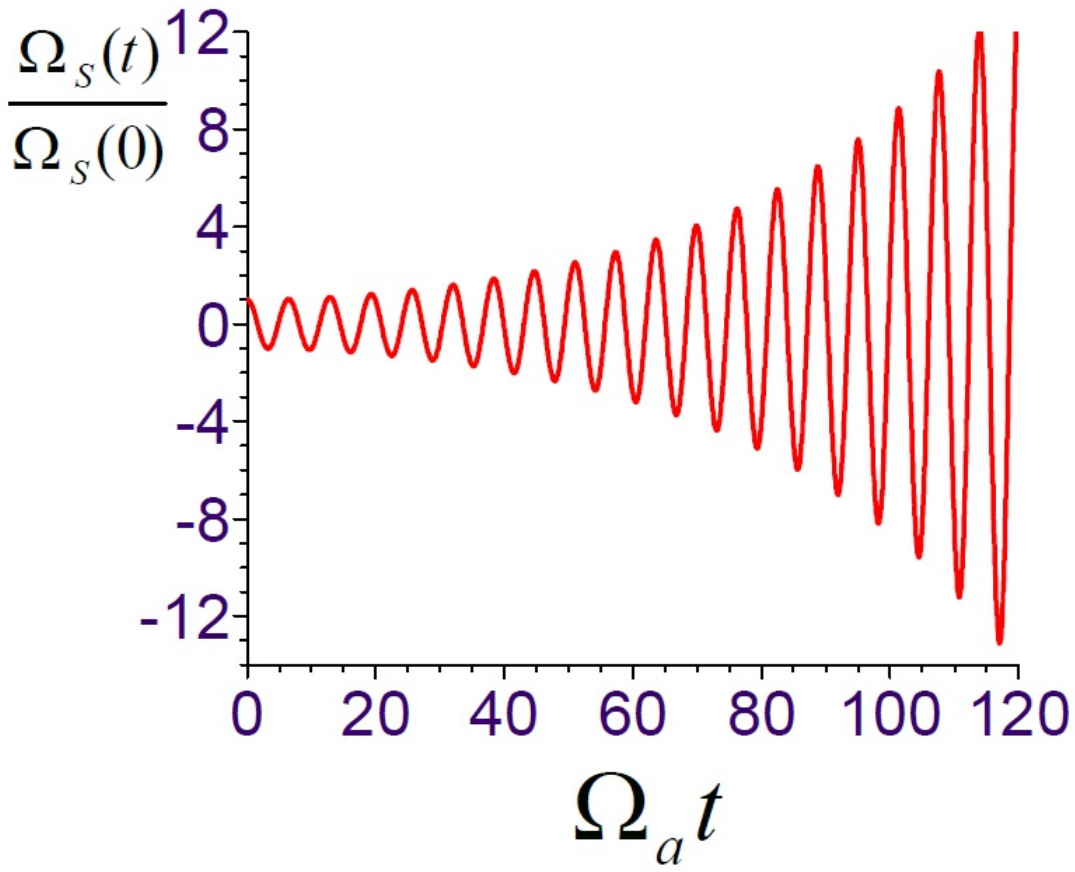

Figure 7.1: Superradiant field as a function of time obtained by numerical solution of Eq. (7.11) with $\tilde{\delta} = 0.1$, $\nu_d = \tilde{\Omega}_a$ and initial condition $\dot{\Omega}_s(0) = 0$. The signal amplitude $\Omega_s(t)$ is normalized to its initial value $\Omega_s(0)$. The time is scaled to a dimensionless quantity $\Omega_a t$.

simple equation for $\Omega_s(t)$

$$\ddot{\Omega}_s + \tilde{\Omega}_a^2 \left[1 - \tilde{\delta}\cos(2\nu_d t)\right] \Omega_s = 0, \tag{7.11}$$

where

$$\tilde{\Omega}_a^2 = \Omega_a^2 + \frac{c^2 k^2}{4} \tag{7.12}$$

and $\tilde{\delta} = \Omega_a^2 \delta / \tilde{\Omega}_a^2$. Eq. (7.11) is known as the Mathieu equation [137] which yields exponentially growing oscillations in the vicinities of parametric resonances when $\nu_d \approx \tilde{\Omega}_a/m$, $m = 1, 2, 3, \ldots$ (see Fig. 7.1). In particular, for the (strongest) first order resonance ($\nu_d = \tilde{\Omega}_a$) gain per unit time is given by [138]

$$G = \frac{\tilde{\delta} \cdot \tilde{\Omega}_a}{4} = \frac{\delta \cdot \Omega_a^2}{4\nu_d}. \tag{7.13}$$

Eq. (7.12) implies that the wave number of the exponentially growing mode is

$$k = \pm \frac{2}{c} \sqrt{\nu_d^2 - \Omega_a^2}. \tag{7.14}$$

Hence, if the driving field frequency obeys condition

$$\nu_d > \Omega_a \tag{7.15}$$

there is a mode which is in parametric resonance with ν_d. Such a mode grows exponentially with gain given by Eq. (7.13). That is the system yields gain at the high atomic frequency with no population in the excited state. For example, for the $4^1\mathrm{P} \rightarrow 1^1\mathrm{S}$ transition of the He atom $\lambda_{ab} = 52.2$ nm and spontaneous decay rate is $\gamma = 2.4 \times 10^8$ s^{-1}. Then for atomic density $n = 10^{20}$ cm^{-3} Eq. (7.3) shows that the collective atomic frequency lies in the infrared band $\Omega_a = 0.48 \times 10^{14}$ s^{-1} while the

atomic frequency is in the XUV range $\omega_{ab} = 0.36 \times 10^{17}$ s^{-1}.

A key point of this article is that we have discovered a new mechanism of atomic excitation by means of collective resonance. This mechanism is different from the well-known multiphoton resonant excitation of an atom which occurs when the driving field frequency $\nu_d = \omega_{ab}/m$, $m = 1, 2, \ldots$. Ordinary multiphoton resonant excitation is a single atom phenomenon rather than a collective effect. In the present case there is a resonance between ν_d and collective oscillations which occurs for $\nu_d \geq \Omega_a$.

Excited state population ρ_{aa} grows with time differently in the two cases. For multiphoton resonance and a weak driving field we have for $\rho_{aa} \ll 1$ [2]

$$\rho_{aa} \approx \left(\frac{\Omega_d}{\omega_{ab}}\right)^{2m-2} (\Omega_d t)^2, \tag{7.16}$$

where Ω_d is the Rabi frequency of the driving field. However the present work is based on the collective parametric resonance and, as we show below, the growth is exponential

$$\rho_{aa} \approx |\rho_{ab}(0)|^2 \exp\left(\frac{\sqrt{2}}{3}\frac{\Omega_d^2}{\omega_{ab}^2}\Omega_a t\right), \tag{7.17}$$

here $\rho_{ab}(0)$ is the initial seed atomic coherence (produced by the seed XUV pulse).

Finally, excitation by multiphoton resonance yields emission of light at high atomic frequency ω_{ab} in the direction of the driving field. In contrast, in the present case the emission occurs in the opposite direction. We will see the detailed theoretical analysis as in the following.

7.2 Theoretical model — Evolution equation for superradiant pulse

Now we will start to present a rigorous analysis which demonstrates the possibility of having quantum gain by collective superradiance. We consider the same medium composed of two level (a and b) atoms with frequency ω_{ab} which are modulated by

a coherent driving field propagating along the $z-$axis and having Rabi frequency $\Omega^{\text{drive}}(t,z)$. We suppose that driving field frequency $\nu_d \ll \omega_{ab}$ and $|\Omega^{\text{drive}}| \ll \omega_{ab}$, so that modulation is weak.

Under the influence of electromagnetic field Ω atomic population and coherence ρ_{ab} evolve according to equations

$$\dot{\rho}_{aa} = -\gamma\rho_{aa} - i(\Omega^*\rho_{ab} - c.c.), \tag{7.18}$$

$$\rho_{aa} + \rho_{bb} = 1, \tag{7.19}$$

$$\dot{\rho}_{ab} = -\left(i\omega_{ab} + \gamma_{\text{tot}}\right)\rho_{ab} + i\Omega(\rho_{bb} - \rho_{aa}). \tag{7.20}$$

We consider regime of superradiance. Thus, one can omit spontaneous decay γ and decoherence γ_{tot} provided their rates are small compared to gain per unit time G.

Here we are interested in generation of coherent radiation at atomic frequency ω_{ab} and study evolution of a weak superradiant pulse Ω_s with carrier frequency ω_{ab} propagating along the $z-$ axis through the medium. In Eqs. (7.18)-(7.20) one can write the total field, the total coherence and population of the excited state as

$$\Omega = \Omega^{\text{drive}} + \Omega^{\text{super}}, \tag{7.21}$$

$$\rho_{ab} = \rho_{ab}^{\text{drive}} + \rho_{ab}^{\text{super}}, \tag{7.22}$$

$$\rho_{aa} = \rho_{aa}^{\text{drive}} + \rho_{aa}^{\text{super}}, \tag{7.23}$$

where Ω^{super}, ρ_{ab}^{super} and ρ_{aa}^{super} are small fast oscillating corrections which in the slowly varying envelope approximation have the form

$$\Omega^{\text{super}} = \Omega_s(t,z)e^{-i\omega_{ab}t + i\omega_{ab}z/c} + c.c., \tag{7.24}$$

$$\rho_{ab}^{\text{super}} = \rho_{ab}^{s}(t,z)e^{-i\omega_{ab}t+i\omega_{ab}z/c}, \tag{7.25}$$

$$\rho_{aa}^{\text{super}} = \rho_{aa}^{s}(t,z)e^{-i\omega_{ab}t+i\omega_{ab}z/c} + c.c., \tag{7.26}$$

here $\Omega_s(t,z)$, $\rho_{ab}^s(t,z)$ and $\rho_{aa}^s(t,z)$ are slowly varying functions as compared to the fast oscillating exponentials. Please note that Ω^{drive} can be complex, while modes of the field Ω^{super} we chose to be real functions.

Plug Eqs. (7.21)-(7.26) into Eqs. (7.18)-(7.20) and neglecting higher harmonics we obtain the following equations for $\Omega_s(t,z)$, $\rho_{ab}^s(t,z)$ and $\rho_{aa}^s(t,z)$

$$\dot{\rho}_{ab}^{s} = i\Omega_s(1-2\rho_{aa}^{\text{drive}}) - 2i\Omega^{\text{drive}}\rho_{aa}^{s}, \tag{7.27}$$

$$i\dot{\rho}_{aa}^{s} + \omega_{ab}\rho_{aa}^{s} = \Omega_s(\rho_{ab}^{\text{drive}} - c.c.) + \Omega^{\text{drive}*}\rho_{ab}^{s}. \tag{7.28}$$

Since the emission field is weak (regime of linear gain) it does not affect evolution of ρ_{ab}^{drive} and ρ_{aa}^{drive} which are governed by separate equations

$$\dot{\rho}_{ab}^{\text{drive}} = -i\omega_{ab}\rho_{ab}^{\text{drive}} + i\Omega^{\text{drive}}\left(1-2\rho_{aa}^{\text{drive}}\right), \tag{7.29}$$

$$\dot{\rho}_{aa}^{\text{drive}} = i\Omega^{\text{drive}}\rho_{ba}^{\text{drive}} - i\Omega^{\text{drive}*}\rho_{ab}^{\text{drive}}. \tag{7.30}$$

Eqs. (7.27)-(7.30) should be supplemented by the Maxwell's equation for the superradiant pulse which in the slowly varying envelope approximation reads

$$\left(\frac{\partial}{\partial t} + c\frac{\partial}{\partial z}\right)\Omega_s = i\Omega_a^2\rho_{ab}^{s}. \tag{7.31}$$

In Eq. (7.28) the term $i\dot{\rho}_{aa}^s$ can be treated as a small perturbation. Then Eq.

(7.28) gives

$$\rho_{aa}^{s} \approx 2i\mathrm{Im}[\rho_{ab}^{\mathrm{drive}}]\frac{\Omega_s}{\omega_{ab}} + \frac{\Omega^{\mathrm{drive}*}}{\omega_{ab}}\rho_{ab}^{s} - \frac{i}{\omega_{ab}^{2}}\frac{d}{dt}\left(2i\mathrm{Im}[\rho_{ab}^{\mathrm{drive}}]\Omega_s + \Omega^{\mathrm{drive}*}\rho_{ab}^{s}\right). \quad (7.32)$$

In this equation we keep terms upto the order $1/\omega_{ab}^{2}$. Since $\mathrm{Im}[\rho_{ab}^{\mathrm{drive}}] \propto 1/\omega_{ab}$ Eq. (7.32) reduces to

$$\rho_{aa}^{s} \approx 2i\mathrm{Im}[\rho_{ab}^{\mathrm{drive}}]\frac{\Omega_s}{\omega_{ab}} + \frac{\Omega^{\mathrm{drive}*}}{\omega_{ab}}\rho_{ab}^{s} - \frac{i}{\omega_{ab}^{2}}\frac{d}{dt}\left(\Omega^{\mathrm{drive}*}\rho_{ab}^{s}\right). \quad (7.33)$$

Plugging Eq. (7.33) into Eq. (7.27) yields

$$\left(1 + \frac{2}{\omega_{ab}^{2}}\left|\Omega^{\mathrm{drive}}\right|^{2}\right)\dot{\rho}_{ab}^{s} = -2\left(\frac{i}{\omega_{ab}}\left|\Omega^{\mathrm{drive}}\right|^{2} + \frac{\Omega^{\mathrm{drive}}\dot{\Omega}^{\mathrm{drive}*}}{\omega_{ab}^{2}}\right)\rho_{ab}^{s}$$

$$+i\left(1 - 2\rho_{aa}^{\mathrm{drive}} - i\frac{4\Omega^{\mathrm{drive}}}{\omega_{ab}}\mathrm{Im}[\rho_{ab}^{\mathrm{drive}}]\right)\Omega_s. \quad (7.34)$$

Taking time derivative from both sides of Eq. (7.31), using Eq. (7.34) and keeping the leading order terms we find the following evolution equation for the superradiant pulse

$$\left(\frac{\partial}{\partial t} + i\Delta\omega_{ab}(t) + \frac{2\Omega^{\mathrm{drive}}\dot{\Omega}^{\mathrm{drive}*}}{\omega_{ab}^{2}}\right)\left(c\frac{\partial}{\partial z} + \frac{\partial}{\partial t}\right)\Omega_s +$$

$$\Omega_a^{2}\left(1 - 2\rho_{aa}^{\mathrm{drive}} - \frac{2\left|\Omega^{\mathrm{drive}}\right|^{2}}{\omega_{ab}^{2}} - i\frac{4\Omega^{\mathrm{drive}}}{\omega_{ab}}\mathrm{Im}[\rho_{ab}^{\mathrm{drive}}]\right)\Omega_s = 0, \quad (7.35)$$

where

$$\Delta\omega_{ab}(t) = \frac{2\left|\Omega^{\mathrm{drive}}(t,z)\right|^{2}}{\omega_{ab}}$$

is the time-dependent Stark shift of the atomic transition frequency proportional to the instantaneous intensity of the driving field.

Eq. (7.35) shows that the driving field produces several effects which contribute

to evolution of the superradiant pulse Ω_s. The time-dependent Stark shift $\Delta\omega_{ab}(t)$ caused by the drive is the leading contribution since it is proportional to $1/\omega_{ab}$. Such a term suppresses collective resonance which is governed by the next order corrections. As a result, in order to obtain gain at the high atomic frequency one should compensate the unwanted Stark shift.

7.3 Gain produced by collective parametric resonance

In order to achieve gain with no population in the excited state one should suppress time-dependent Stark shift $\Delta\omega_{ab}(t)$ which washes out parametric resonance. In the following, we will show several ways to accomplish this suppression and then show the analytical solutions of gain.

7.3.1 Compensation of Stark shift by nearly circularly polarized driving field

Time-dependent Stark shift can be compensated if the driving field Rabi frequency has the form

$$\Omega^{\text{drive}}(t,z) = \Omega_1 e^{i\nu_d t - ik_d z} + \Omega_2 e^{-i\nu_d t + ik_d z}, \tag{7.36}$$

where Ω_1 and Ω_2 are real constants and k_d is the wave number of the driving field. As we show below, for certain ratio of Ω_2/Ω_1 the Stark shift vanishes. Such situation can be realized for elliptically polarized driving field $\mathbf{E}^{\text{drive}}$ if the dipole matrix element of two-level atom is

$$\mathbf{d}_{ab} = d_x\hat{x} + id_y\hat{y}, \tag{7.37}$$

where d_x and d_y are real. This is, e.g., the case if the excited state a corresponds to $p_x + ip_y$ atomic orbital and b is an $s-$ state.

We assume that $|\Omega^{\text{drive}}|, \nu_d \ll \omega_{ab}$, that is driving field produces small modulations. Then Eqs. (7.29) and (7.30) yield that under the influence of the driving field

(which is turned on adiabatically) atomic coherence and population evolve as

$$\rho_{ab}^{\text{drive}} = \frac{\Omega_1}{\omega_{ab}+\nu_d} e^{i(\nu_d t - k_d z)} + \frac{\Omega_2}{\omega_{ab}-\nu_d} e^{-i(\nu_d t - k_d z)}, \tag{7.38}$$

$$\rho_{aa}^{\text{drive}} \approx \frac{\Omega_1^2}{\left(\omega_{ab}+\nu_d\right)^2} + \frac{\Omega_2^2}{\left(\omega_{ab}-\nu_d\right)^2} + 2\frac{\Omega_1\Omega_2}{\omega_{ab}^2-\nu_d^2}\cos\left(2\nu_d t - 2k_d z\right). \tag{7.39}$$

Coherence given by Eq. (7.38) oscillates with the frequency of the driving field $\nu_d \ll \omega_{ab}$ and, hence, it does not generate light at the atomic frequency ω_{ab}.

Taking into account Eqs. (7.36) and (7.38) we obtain

$$\left|\Omega^{\text{drive}}\right|^2 = \Omega_1^2 + \Omega_2^2 + 2\Omega_1\Omega_2\cos\left(2\nu_d t - 2k_d z\right), \tag{7.40}$$

$$\Omega^{\text{drive}}\dot{\Omega}^{\text{drive}*} = i\nu_d\left(\Omega_2^2 - \Omega_1^2\right) - 2\nu_d\Omega_1\Omega_2\sin\left(2\nu_d t - 2k_d z\right), \tag{7.41}$$

$$\text{Im}[\rho_{ab}^{\text{drive}}] = \left(\frac{\Omega_1}{\omega_{ab}+\nu_d} - \frac{\Omega_2}{\omega_{ab}-\nu_d}\right)\sin\left(\nu_d t - k_d z\right). \tag{7.42}$$

Assuming that $\Omega_2 \ll \Omega_1$ (nearly circularly polarized field) Eq. (7.35) can be written as

$$\left(\frac{\partial}{\partial t} + \frac{2i\Omega_1^2}{\omega_{ab}} + \frac{4i\Omega_1\Omega_2}{\omega_{ab}}\cos\left(2\nu_d t - 2k_d z\right)\right)\left(c\frac{\partial}{\partial z} + \frac{\partial}{\partial t}\right)\Omega_s$$

$$+\Omega_a^2\left(1 - \frac{2\Omega_1^2}{\omega_{ab}^2} - \frac{2\Omega_1^2}{\omega_{ab}^2}e^{2i\nu_d t - 2ik_d z}\right)\Omega_s = 0. \tag{7.43}$$

To obtain quick insight on the gain conditions we consider spatially uniform driving field ($k_d = 0$) and look for solution of Eq. (7.43) in the form

$$\Omega_s(t,z) = \Omega_s(t) \tag{7.44}$$

which yields the following equation for $\Omega_s(t)$

$$\left(\frac{\partial}{\partial t}+\frac{2i\Omega_1^2}{\omega_{ab}}+\frac{4i\Omega_1\Omega_2}{\omega_{ab}}\cos\left(2\nu_d t\right)\right)\frac{\partial\Omega_s}{\partial t}+\Omega_a^2\left(1-\frac{2\Omega_1^2}{\omega_{ab}^2}-\frac{2\Omega_1^2}{\omega_{ab}^2}e^{2i\nu_d t}\right)\Omega_s=0. \quad (7.45)$$

Eq. (7.45) has the structure

$$\left(\frac{\partial}{\partial t}+\beta(t)\right)\frac{\partial\Omega_s}{\partial t}+\Omega_a^2 f(t)\Omega_s=0. \quad (7.46)$$

Making change of function

$$\Omega_s=\tilde{\Omega}_s\exp\left(-\frac{1}{2}\int_0^t\beta(t')dt'\right) \quad (7.47)$$

we obtain

$$\frac{\partial^2\tilde{\Omega}_s}{\partial t^2}+\left(\Omega_a^2 f(t)-\frac{1}{2}\frac{\partial\beta(t)}{\partial t}-\frac{\beta^2(t)}{4}\right)\tilde{\Omega}_s=0. \quad (7.48)$$

Since $\beta(t)$ is a small perturbation, one can omit term with $\beta^2(t)$. Using this formula Eq. (7.45) reduces to

$$\frac{\partial^2\tilde{\Omega}_s}{\partial t^2}+\Omega_a^2\left[1-\delta-\delta\cos\left(2\nu_d t\right)+\ i\delta\left(\frac{2\nu_d\omega_{ab}}{\Omega_a^2}\frac{\Omega_2}{\Omega_1}-1\right)\sin\left(2\nu_d t\right)\right]\tilde{\Omega}_s=0, \quad (7.49)$$

where

$$\delta=\frac{2\Omega_1^2}{\omega_{ab}^2}\ll 1 \quad (7.50)$$

is the dimensionless amplitude of modulation of collective oscillations. To suppress unwanted Stark shift one should chose

$$\frac{\Omega_2}{\Omega_1}=\frac{\Omega_a^2}{2\nu_d\omega_{ab}}. \quad (7.51)$$

Then Eq. (7.49) becomes equation of parametric harmonic oscillator

$$\frac{\partial^2 \tilde{\Omega}_s}{\partial t^2} + \Omega_a^2 \left[1 - \delta - \delta \cos\left(2\nu_d t\right)\right] \tilde{\Omega}_s = 0. \tag{7.52}$$

Near the parametric resonance $\nu_d \approx \Omega_a$ the seed pulse exponentially grows with time $\Omega_s(t) \propto e^{Gt}$ and gain per unit time is

$$G = \frac{\delta \cdot \Omega_a}{4} = \frac{\Omega_a}{2} \frac{\Omega_1^2}{\omega_{ab}^2}. \tag{7.53}$$

This example demonstrates the possibility of having gain in a simple model in which the Stark shift is compensated by driving two-level atoms with a field of certain polarization.

7.3.2 Compensation of Stark shift by magnetic field

In the general case the driving field and the growing XUV modes depend on coordinates. Here, we explore such a situation for a different model in which atoms are driven by linearly polarized light propagating along the $z-$axis and the time-dependent Stark shift is compensated by applying an additional magnetic field $H(t)$.

We assume that two-level atoms are described by the following model Hamiltonian

$$\hat{H} = \left[\hbar\omega_a - \mu H_z(t)\right] |a\rangle \langle a| + \hbar\omega_b |b\rangle \langle b| - \left(\mathbf{d}_{ab} |a\rangle \langle b| + \mathbf{d}_{ba} |b\rangle \langle a|\right) \mathbf{E}(t) \tag{7.54}$$

which implies that state a has magnetic moment μ along the $z-$axis which interacts with $z-$component of the magnetic field. In addition, levels a and b are dipole coupled by electric field and, e.g., $\mathbf{d}_{ab} = d(\hat{x} + i\hat{y})$. Magnetic field produces time-dependent Zeeman shift of the level a. As a result, atomic frequency in Eq. (7.20) is replaced with $\omega_{ab} \to \omega_{ab} - \Omega_H(t)$, where $\Omega_H(t) = \mu H_z(t)/\hbar$. Magnetic field

produces similar effect as Stark shift and, hence, those two can compensate each other. Analysis of the previous section can be applied here and yields the same evolution equation (7.35) for Ω_s but with

$$\Delta\omega_{ab}(t) = \frac{2\left|\Omega^{\rm drive}\right|^2}{\omega_{ab}} - \Omega_H. \tag{7.55}$$

Here we assume that atomic medium is driven by a strong linearly polarized laser pulse propagating along the $z-$axis

$$\Omega^{\rm drive}(t,z) = \Omega_d \cos\left(\nu_d t - k_d z\right), \tag{7.56}$$

where $\nu_d \ll \omega_{ab}$ and $\Omega_d \ll \omega_{ab}$. Eqs. (7.29) and (7.30) yield that under the influence of the driving field (which is turned on adiabatically) atomic population and coherence evolve as

$$\rho_{aa}^{\rm drive} = \frac{\Omega_d^2}{\omega_{ab}^2 - \omega_d^2}\cos^2\left(\nu_d t - k_d z\right), \tag{7.57}$$

$$\rho_{ab}^{\rm drive} = \frac{\Omega_d}{2}\left(\frac{e^{i(\nu_d t - k_d z)}}{\omega_{ab}+\nu_d} + \frac{e^{-i(\nu_d t - k_d z)}}{\omega_{ab}-\nu_d}\right). \tag{7.58}$$

In order to compensate for Stark shift the applied magnetic field should have form

$$\Omega_H(t,z) = \Omega_m \cos\left(2\nu_d t - 2k_d z\right). \tag{7.59}$$

Taking into account Eqs. (7.35), (7.55)-(7.59) we obtain the following evolution equation for the superradiant pulse Ω_s

$$\left[\frac{\partial}{\partial t} + i\omega_{ab}\delta + i\left(\omega_{ab}\delta - \Omega_m\right)\cos\left(2\nu_d t - 2k_d z\right) - \nu_d\delta\sin\left(2\nu_d t - 2k_d z\right)\right]\left(c\frac{\partial}{\partial z} + \frac{\partial}{\partial t}\right)\Omega_s$$

$$+\Omega_a^2\left[1 - 4\delta\cos^2\left(\nu_d t - k_d z\right)\right]\Omega_s = 0, \tag{7.60}$$

where

$$\delta = \frac{\Omega_d^2}{\omega_{ab}^2} \ll 1 \tag{7.61}$$

is the dimensionless modulation amplitude of collective atomic oscillations.

7.3.3 Gain per unit time: reduction to Mathieu's equation

To find exact analytical solution of Eq. (7.60) we first reduce it to Mathieu's equation. Eq. (7.60) has the structure

$$\left(\frac{\partial}{\partial t} + i\omega_{ab}\delta + \beta(t - z/v_d)\right)\left(c\frac{\partial}{\partial z} + \frac{\partial}{\partial t}\right)\Omega_s + \Omega_a^2 f(t - z/v_d)\Omega_s = 0, \tag{7.62}$$

where

$$v_d = \frac{\nu_d}{k_d} \tag{7.63}$$

is the phase velocity of the driving field along the $z-$axis. We look for solution of Eq. (7.62) in the form

$$\Omega_s(t, z) = e^{i(\nu - \omega_{ab}\delta)(t - z/c)}\Omega_s(\xi), \tag{7.64}$$

where $\xi = t - z/v_d$ and ν is complex. The imaginary part of ν gives gain per unit time G provided $\Omega_s(t, z)$ satisfies proper initial condition. Namely, at $t = 0$ function $\Omega_s(0, z)$ should be finite at all z.

Plugging (7.64) into Eq. (7.62) yields

$$\frac{\partial^2\Omega_s(\xi)}{\partial\xi^2} + [i\nu + \beta(\xi)]\frac{\partial\Omega_s(\xi)}{\partial\xi} + \frac{\Omega_a^2 f(\xi)}{1 - c/v_d}\Omega_s(\xi) = 0. \tag{7.65}$$

Making change of function

$$\Omega_s(\xi) = \tilde{\Omega}_s(\xi) \exp\left(-\frac{1}{2} i\nu\xi - \frac{1}{2}\int_0^{\xi} \beta(\xi')d\xi'\right) \tag{7.66}$$

we obtain

$$\frac{\partial^2 \tilde{\Omega}_s}{\partial \xi^2} + \left(\frac{\Omega_a^2 f(\xi)}{1 - c/v_d} - \frac{1}{2}\frac{\partial \beta(\xi)}{\partial \xi} - \frac{1}{4}\left[i\nu + \beta(\xi)\right]^2\right)\tilde{\Omega}_s = 0. \tag{7.67}$$

If expression in (...) is a periodic function of ξ than Eq. (7.67) is known as Hill's equation.

Suppose we find solution of Eq. (7.67) which grows exponentially, namely

$$\tilde{\Omega}_s(\xi) \propto e^{G_1 \xi}. \tag{7.68}$$

Then, according to Eqs. (7.64) and (7.66), function $\Omega_s(t, z)$ grows as

$$\Omega_s(t, z) \propto \exp\left(\left[\frac{i\nu}{2} + G_1\right] t\right) \exp\left(\left[i\nu\left(\frac{1}{2} - \frac{v_d}{c}\right) - G_1\right]\frac{z}{v_d}\right). \tag{7.69}$$

$\Omega_s(t, z)$ satisfies proper initial condition if $\Omega_s(0, z)$ remains finite at all z. This yields

$$\mathrm{Im}(\nu) = \frac{2cG_1}{2v_d - c}. \tag{7.70}$$

Gain of the pulse per unit time is then given by

$$G = G_1 - \frac{\mathrm{Im}(\nu)}{2} = 2G_1\left(\frac{c - v_d}{c - 2v_d}\right). \tag{7.71}$$

Eq. (7.71) shows that there is no gain in the forward direction ($v_d = c$).

Since $\beta(\xi)$ is a small perturbation, one can omit term with $\beta^2(\xi)$ and write Eq.

(7.67) as

$$\frac{\partial^2\tilde{\Omega}_s}{\partial\xi^2}+\left(\frac{\Omega_a^2 f(\xi)}{1-c/v_d}+\frac{\nu^2}{4}-\frac{1}{2}\frac{\partial\beta(\xi)}{\partial\xi}-\frac{i\nu}{2}\beta(\xi)\right)\tilde{\Omega}_s=0. \tag{7.72}$$

Using this formula and taking into account that

$$\beta(\xi)=i\left(\omega_{ab}\delta-\Omega_m\right)\cos\left(2\nu_d\xi\right)-\nu_d\delta\sin\left(2\nu_d\xi\right), \tag{7.73}$$

$$f(\xi)=1-4\delta\cos^2\left(\nu_d\xi\right), \tag{7.74}$$

one can reduce Eq. (7.60) to

$$\frac{\partial^2\tilde{\Omega}_s}{\partial\xi^2}+\left[\frac{\Omega_a^2}{1-c/v_d}\left(1-2\delta\right)+\frac{\nu^2}{4}+\left(\nu_d^2\delta-\frac{2\Omega_a^2\delta}{1-c/v_d}+\frac{1}{2}\nu\left(\omega_{ab}\delta-\Omega_m\right)\right)\cos\left(2\nu_d\xi\right)\right.$$

$$\left.+i\nu_d\left(\omega_{ab}\delta-\Omega_m+\frac{\nu\delta}{2}\right)\sin\left(2\nu_d\xi\right)\right]\tilde{\Omega}_s=0, \tag{7.75}$$

which can be written in the form of Mathieu's equation

$$\frac{\partial^2\tilde{\Omega}_s}{\partial\xi^2}+\tilde{\Omega}_a^2\left[1+\delta_0\cos\left(2\nu_d\xi+\phi\right)\right]\tilde{\Omega}_s=0, \tag{7.76}$$

where

$$\tilde{\Omega}_a^2=\frac{\Omega_a^2}{1-c/v_d}\left(1-2\delta\right)+\frac{\omega^2}{4}, \tag{7.77}$$

$$\delta_0=\left[\left(\nu_d^2\delta-\frac{2\Omega_a^2\delta}{1-c/v_d}+\frac{1}{2}\nu\left(\omega_{ab}\delta-\Omega_m\right)\right)^2\right.$$

$$\left.-\nu_d^2\left(\omega_{ab}\delta-\Omega_m+\frac{\nu\delta}{2}\right)^2\right]^{1/2}\frac{1}{\tilde{\Omega}_a^2}, \tag{7.78}$$

and ϕ is irrelevant constant. Since imaginary part of ν (gain) is small one can treat ν in Eqs. (7.77) and (7.78) as real. With the same accuracy one can disregard term 2δ in Eq. (7.77).

The condition of the first order resonance $\nu_d = \tilde{\Omega}_a$ yields the following expression for the frequency of the most unstable mode

$$\nu = \pm 2\sqrt{\nu_d^2 - \frac{\Omega_a^2}{1 - c/v_d}}. \tag{7.79}$$

For such frequency gain per unit time is

$$G = 2G_1 \left(\frac{c - v_d}{c - 2v_d}\right) = 2\left(\frac{c - v_d}{c - 2v_d}\right)\frac{\delta_0 \nu_d}{4} = \frac{c - v_d}{c - 2v_d}\frac{\Omega_a}{2\nu_d\sqrt{1 - c/v_d}} \times$$

$$\left[\delta^2\nu_d^2 - \left(\omega_{ab}\delta - \Omega_m \pm 2\delta\sqrt{\omega_d^2 - \frac{\Omega_a^2}{1 - c/v_d}}\right)^2\right]^{1/2}. \tag{7.80}$$

Eq. (7.79) gives the following necessary condition of existence of the first order parametric resonance

$$\nu_d^2 \geq \frac{v_d\Omega_a^2}{v_d - c}. \tag{7.81}$$

Eq. (7.80) predicts the following. If $c/v_d < 1$ (which includes gain in the backward direction $v_d = -c$ or the case of uniform drive $k_d = 0$, that is $v_d = \infty$) then the optimum value of Ω_m which maximizes gain is given by

$$\Omega_m = \omega_{ab}\delta \pm 2\delta\sqrt{\nu_d^2 - \frac{\Omega_a^2}{1 - c/v_d}}. \tag{7.82}$$

For such Ω_m gain is

$$G = \frac{c - v_d}{c - 2v_d}\frac{\delta \cdot \Omega_a}{2\sqrt{1 - c/v_d}}. \tag{7.83}$$

7.3.4 Gain per unit length: treatment in t, z coordinates

Here we solve original evolution equation (7.60) for the field and find how unstable modes grow in space. Making in Eq. (7.60) change of function

$$\Omega_s \to \Omega_s \exp\left[-i\left(t - \frac{z}{c}\right)\omega_{ab}\delta\right]$$

we obtain

$$\left(\frac{\partial}{\partial t} + \delta_1\nu_d \sin\left(2\nu_d t - 2k_d z\right) + i\delta_3\nu_d \cos\left(2\nu_d t - 2k_d z\right)\right) \times$$

$$\left(c\frac{\partial}{\partial z} + \frac{\partial}{\partial t}\right)\Omega_s + \Omega^2\left[1 + \delta_2 \cos\left(2\nu_d t - 2k_d z\right)\right]\Omega_s = 0, \tag{7.84}$$

where

$$\Omega = \Omega_a\sqrt{1 - 2\delta} \tag{7.85}$$

and

$$\delta_1 = -\delta, \tag{7.86}$$

$$\delta_2 = -\frac{2\delta}{1 - 2\delta}, \tag{7.87}$$

$$\delta_3 = \frac{1}{\nu_d}\left(\omega_{ab}\delta - \Omega_m\right) \tag{7.88}$$

are small numbers.

We look for solution for Ω_s in the form

$$\Omega_s = \left(1 + Ae^{2i(\nu_d t - k_d z)}\right)e^{ikz - i\nu t}, \tag{7.89}$$

where A is a constant and ν is detuning of Ω_s from the transition frequency ω_{ab}. We assume that ν is real. Then imaginary part of k gives gain G_{L} (absorption) per

unit length of the mode with frequency ν. During propagation of the seed pulse Ω_s through the medium it grows as $\exp(G_{\rm L} z)$, where $G_{\rm L} = -{\rm Im}(k)$.

Substituting Eq. (7.89) into Eq. (7.84) and making the rotating wave approximation, that is replacing

$$\cos(2\nu_d t - 2k_d z) e^{\pm 2i(\nu_d t - k_d z)} \to \frac{1}{2} \tag{7.90}$$

$$\sin(2\nu_d t - 2k_d z) e^{\pm 2i(\nu_d t - k_d z)} \to \pm \frac{i}{2} \tag{7.91}$$

and then eliminating A yields the following equation for k

$$\left[(\nu - 2\nu_d)\left(ck - \nu - 2ck_d + 2\omega_d\right) + \Omega^2\right]\left[\nu\left(ck - \nu\right) + \Omega^2\right]$$

$$= \frac{1}{4}\left[\delta_2\Omega^2 + (\delta_1 - \delta_3)\nu_d\left(ck - \nu\right)\right]\left[\delta_2\Omega^2 - (\delta_1 + \delta_3)\nu_d\left(ck - \nu - 2ck_d + 2\nu_d\right)\right]. \tag{7.92}$$

Eq. (7.92) has the structure

$$\left(k - k_1\right)\left(k - k_2\right) = H(k, \nu), \tag{7.93}$$

where k_1 and k_2 are real numbers given by the roots of Eq. (7.92) without the right hand side and

$$H(k,\nu) = \frac{\left[\delta_2\Omega^2 + (\delta_1 - \delta_3)\nu_d\left(ck - \nu\right)\right]}{c^2\left[4\left(\nu - 2\nu_d\right)\nu + (\delta_1^2 - \delta_3^2)\nu_d^2\right]} \times$$

$$\left[\delta_2\Omega^2 - (\delta_1 + \delta_3)\nu_d\left(ck - \nu - 2ck_d + 2\nu_d\right)\right] \tag{7.94}$$

is a small correction of the order of δ^2. The formal solution of Eq. (7.93) is

$$k = \frac{1}{2}\left(k_1 + k_2\right) \pm \sqrt{\frac{1}{4}\left(k_1 - k_2\right)^2 + H(k,\nu)}. \tag{7.95}$$

Gain is maximum when $k_1 = k_2$. This condition gives two equations for k and ν

$$(\nu - 2\nu_d)\,(ck - \nu - 2ck_d + 2\nu_d) + \Omega^2 = 0, \tag{7.96}$$

$$\nu\,(ck - \nu) + \Omega^2 = 0, \tag{7.97}$$

which yield

$$\nu = \nu_d \pm \sqrt{\nu_d^2 - \frac{\Omega^2}{1 - ck_d/\nu_d}}. \tag{7.98}$$

Plugging k and ν into Eq. (7.95) we obtain that gain per unit length is given by

$$G_{\mathrm{L}} = \sqrt{-H(k,\nu)} = \frac{\Omega\,|\nu_d - ck_d|}{c\sqrt{4\Omega^2 + (\delta_3^2 - \delta_1^2)\nu_d^2\,(1 - ck_d/\nu_d)}} \times$$

$$\sqrt{(\delta_2 - \delta_1)^2 - \left(\delta_2\sqrt{1 + \frac{\Omega^2}{\nu_d\,(ck_d - \nu_d)}} \pm \delta_3\right)^2}. \tag{7.99}$$

Plugging δ_1, δ_2 and δ_3 into the above equations, we finally obtain

$$G_{\mathrm{L}} \approx \frac{|\nu_d - ck_d|}{2c}\left[\delta^2 - \frac{1}{\nu_d^2}\left(\omega_{ab}\delta - \Omega_m \mp 2\delta\sqrt{\nu_d^2 + \frac{\Omega^2\nu_d}{(ck_d - \nu_d)}}\right)^2\right]^{1/2}, \tag{7.100}$$

under the condition $(\delta_3^2 - \delta_1^2)\nu_d^2\,(1 - ck_d/\nu_d) \ll \Omega^2$. The gain is maximum if the second term under the square root is equal to zero which yields the following expression for the optimum magnetic field strength

$$\Omega_m = \frac{\Omega_d^2}{\omega_{ab}^2}\left(\omega_{ab} \mp 2\sqrt{\nu_d^2 + \frac{\Omega^2\nu_d}{(ck_d - \nu_d)}}\right). \tag{7.101}$$

The maximum gain is

$$G_{\mathrm{L}} \approx \frac{|\nu_d - ck_d|}{2c}\frac{\Omega_d^2}{\omega_{ab}^2}. \tag{7.102}$$

Gain exists if Eq. (7.98) yields real ν. This imposes constraint on the driving field frequency

$$\nu_d^2 > \frac{\nu_d \Omega_a^2}{\nu_d - ck_d} \tag{7.103}$$

which coincides with Eq. (7.81).

As a short summary, Eqs. (7.83) and (7.102) show that there is no gain in the direction of the driving field (when $ck_d = \nu_d$). However, there is gain in the backward direction (when $ck_d = -\nu_d$) provided $\nu_d > \Omega_a/\sqrt{2}$, namely,

$$G = \frac{\Omega_a}{3\sqrt{2}} \frac{\Omega_d^2}{\omega_{ab}^2} \tag{7.104}$$

and

$$G_{\mathrm{L}} \approx \frac{\nu_d}{c} \frac{\Omega_d^2}{\omega_{ab}^2}. \tag{7.105}$$

7.4 Numerical simulations

We investigate numerically how the weak pulse evolves in time and space. We assume that atoms are driven by linearly polarized light and Stark shift is compensated by applying an additional magnetic field. The total field, the total coherence and population of the excited state are given by Eqs. (7.21)-(7.26) in which Ω^{drive} is a fixed function. In the presence of additional magnetic field shifting level a evolution of $\rho_{ab}^{\mathrm{drive}}$ and $\rho_{aa}^{\mathrm{drive}}$ are governed by

$$\dot{\rho}_{ab}^{\mathrm{drive}} = -i\left(\omega_{ab} - \Omega_H\right)\rho_{ab}^{\mathrm{drive}} + i\Omega^{\mathrm{drive}}\left(1 - 2\rho_{aa}^{\mathrm{drive}}\right), \tag{7.106}$$

$$\dot{\rho}_{aa}^{\mathrm{drive}} = i\Omega^{\mathrm{drive}}\rho_{ba}^{\mathrm{drive}} - i\Omega^{\mathrm{drive}*}\rho_{ab}^{\mathrm{drive}}. \tag{7.107}$$

Equations for slowly varying envelopes of quantities associated with the superra-

diant field $\Omega_s(t,z)$, $\rho^s_{ab}(t,z)$ and $\rho^s_{aa}(t,z)$ read

$$\dot{\rho}^s_{ab} = i\Omega_H \rho^s_{ab} + i\Omega_s(1 - 2\rho^{\rm drive}_{aa}) - 2i\Omega^{\rm drive}\rho^s_{aa}, \tag{7.108}$$

$$i\dot{\rho}^s_{aa} + \omega_{ab}\rho^s_{aa} = \Omega_s(\rho^{\rm drive}_{ab} - c.c.) + \Omega^{\rm drive*}\rho^s_{ab}, \tag{7.109}$$

$$\left(c\frac{\partial}{\partial z} + \frac{\partial}{\partial t}\right)\Omega_s = i\Omega_a^2\rho^s_{ab}. \tag{7.110}$$

Here we solve Eqs. (7.106)-(7.110) numerically. First we assume that $\Omega^{\rm drive}$ and Ω_s depends only on time and $\Omega^{\rm drive}$ is turned on adiabatically as

$$\Omega^{\rm drive}(t) = \frac{\Omega_d}{2}\left[1 + \tanh\left(-3 + 0.2\Omega_a t\right)\right]\sin\left(\nu_d t\right), \tag{7.111}$$

while Ω_H is chosen to compensate the Stark shift

$$\Omega_H(t) = \frac{2}{\omega_{ab}}\left[\Omega^{\rm drive}(t)\right]^2. \tag{7.112}$$

We solve equations with initial conditions $\rho_{aa}(0) = 0$, $\rho_{bb}(0) = 1$, $\rho_{ab}(0) = 0$ and $\dot{\Omega}_s(0) = 0$. In simulations we take $\omega_{ab} = 10.4\Omega_a$, $\Omega_d = \Omega_a$ and ν_d is chosen to maximize gain. We found that gain is maximum for $\nu_d = 0.990\Omega_a$, that is $\omega_{ab}/\nu_d = 10.5$ is far from multiphoton resonance. We plot the results of numerical simulations in Fig. 7.2 which shows $|\Omega_s|$ as a function of time. Superradiant field undergoes exponentially growing oscillations and gain per unit time is $G = 0.0018\Omega_a$. We performed numerical simulations of the Maxwell–Schrödinger equations without making the slowly varying amplitude approximation and obtained similar results.

Fig. 7.3 shows gain per unit time G for the optimal driving field frequency ν_d (corresponding to the parametric resonance) as a function of the strength of the driving field Ω_d. Parameters are the same as for Fig. 7.2. The plot demonstrates

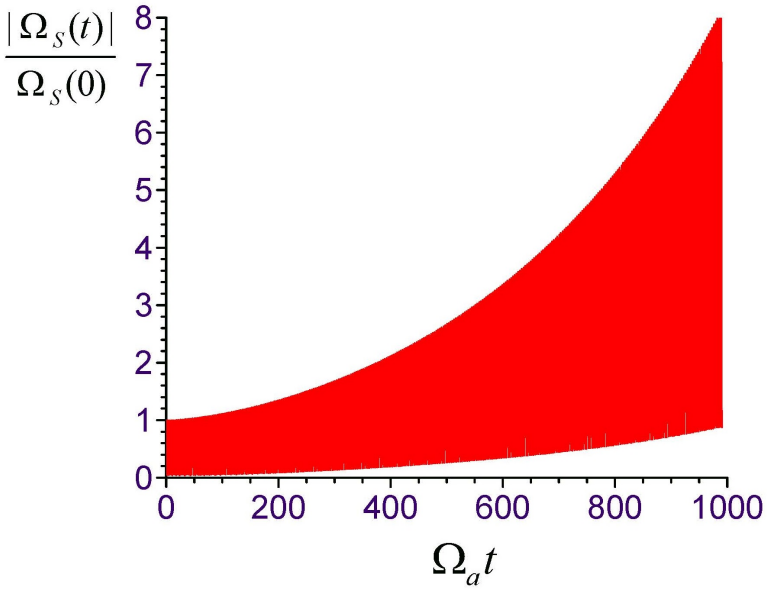

Figure 7.2: Evolution of the superradiant pulse as a function of time obtained by numerical solution of Eqs. (7.106)-(7.112) with $\rho_{aa}(0) = 0$, $\rho_{bb}(0) = 1$, $\rho_{ab}(0) = 0$, $\omega_{ab} = 10.4\Omega_a$, $\Omega_d = \Omega_a$ and $\nu_d = 0.990\Omega_a$.

that for small Ω_d gain is proportional to $|\Omega_d|^2$. The $|\Omega_d|^2$ dependence indicates that gain is not governed by the multiphoton resonance.

To demonstrate importance of Stark shift compensation we calculate maximum gain as a function of Ω_H. Full compensation of the Stark shift occurs at $\Omega_H^{\text{optimum}}$ given by Eq. (7.112). In Fig. 7.4 we plot maximum gain per unit time as a function of $\Omega_H/\Omega_H^{\text{optimum}}$. In numerical calculations we take $\omega_{ab} = 10.4\Omega_a$, $\Omega_d = 0.5\Omega_a$ and ν_d is chosen to maximize gain in the vicinity of parametric resonance $\nu_d \approx \Omega_a$. Figure shows that gain is positive if Ω_H lies in a narrow interval near the optimum value. Outside this interval the time-dependent Stark shift suppresses gain.

We further consider the propagation distance z dependence. Taking $\omega_{ab} = 5.2\nu_d$, $\nu_d = 0.64\Omega_a$ and $\Omega_d = \Omega_a$, we send a weak XUV pulse of Gaussian shape into a sample of length $L = 100c/\Omega_a$ and calculate how it evolves. The numerical results

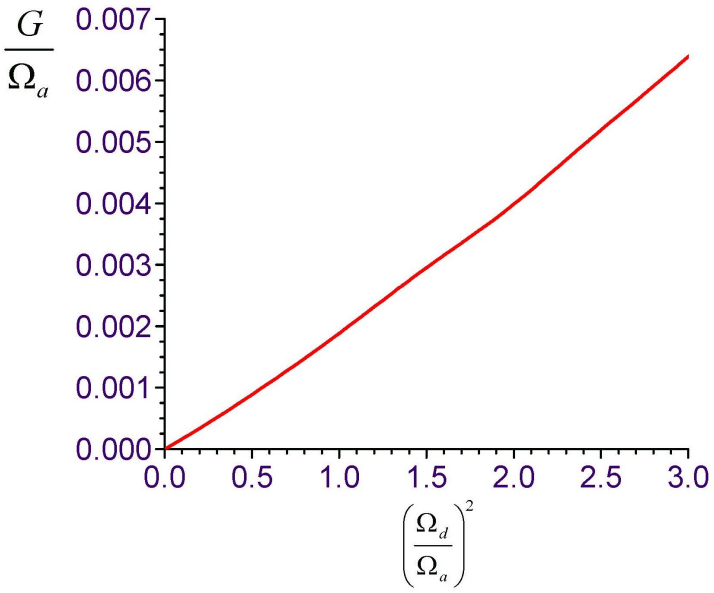

Figure 7.3: Maximum gain per unit time as a function of Ω_d obtained by numerical solution of Eqs. (7.106)-(7.112) (solid line). Initially all population is in the ground state b. In simulations we take $\omega_{ab} = 10.4\Omega_a$ and ν_d is chosen to maximize the gain.

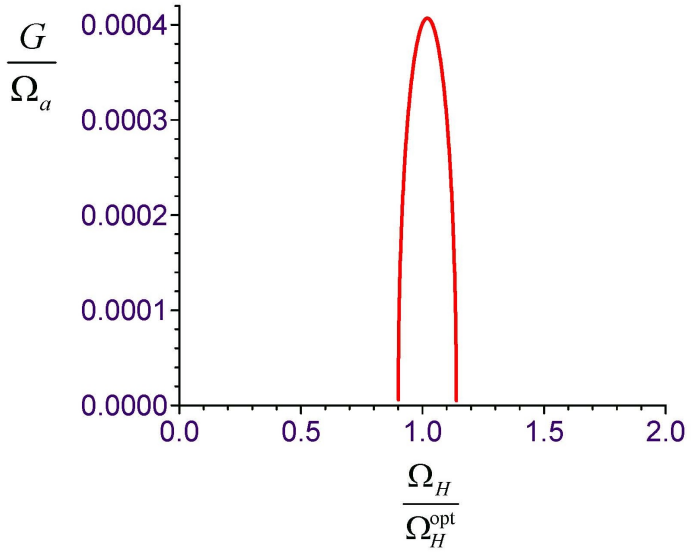

Figure 7.4: Maximum gain per unit time as a function of magnetic field amplitude which shifts energy of the excited state a and compensates for time-dependent Stark shift of the $a - b$ transition. Results are obtained by numerical solution of Eqs. (7.106)-(7.110) with $\omega_{ab} = 10.4\Omega_a$, $\Omega_d = 0.5\Omega_a$ and optimum value of ν_d that maximizes gain.

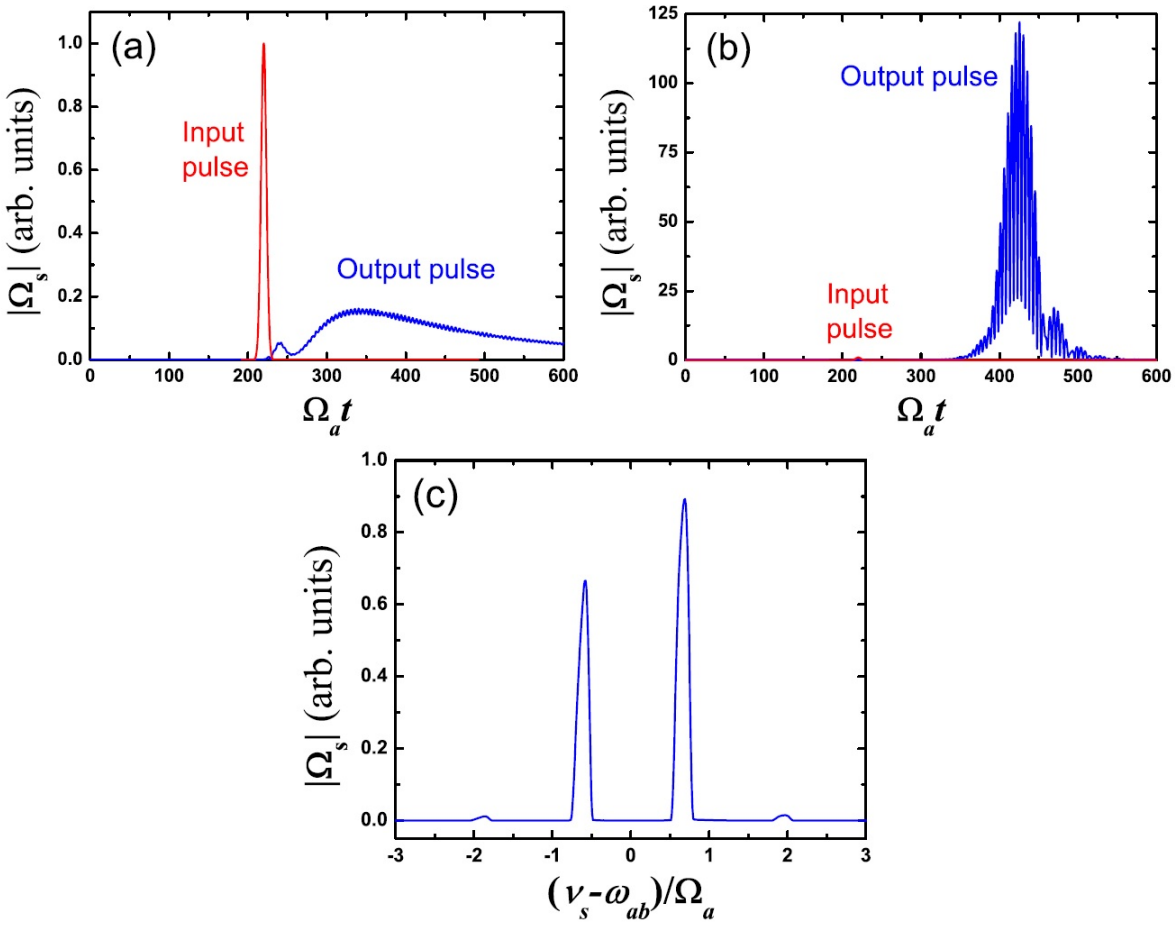

Figure 7.5: (a) Input and output superradiant pulse Ω_s as a function of time after it propagates through the sample of length $L = 100c/\Omega_a$. Atoms are driven by the electric field with the atomic Stark shift compensated by the magnetic field. Superradiant pulse is sent in the same direction as the driving field. Plots are obtained by numerical solution of Eqs. (7.106)-(7.110) with $\omega_{ab} = 5.2\nu_d$, $\nu_d = 0.64\Omega_a$ and $\Omega_d = \Omega_a$. Units of Ω_s are arbitrary. (b) The same parameters as in (a) but for the backward propagating superradiant pulse. (c) Spectrum of the backward propagating superradiant pulse in (b).

are shown in Fig. 7.5(a) (for an XUV pulse propagating in the same direction as the driving field) and Fig. 7.5(b) for backward propagation. Fig. 7.5(a) demonstrates that there is no gain in the forward direction. However, the XUV pulse grows in the backward direction and its intensity increases by several orders of magnitude after propagation through the sample, in agreement with our analytical findings. Fig. 7.5(c) shows the spectrum of the backward propagating superradiant pulse. We see two major peaks located on the symmetric positions regarding to the resonance and the difference is exactly $2\nu_d$. This will be explained later. We notice two weak peaks which are the higher-order generations compared to the two major peaks. This higher-order generation is not considered in the previous analytical analysis because they are weak in our case, as proven in the numerical simulations.

7.5 Growth of atomic population in the QASER

Here we derive Eq. (7.17) describing growth of the excited state population ρ_{aa}. Omitting spatial dependence, Eq. (7.1) yields

$$\rho_{ab}(t) = -i\frac{\dot{\Omega}_s(t)}{\Omega_a^2}. \tag{7.113}$$

Plugging in $\Omega_s(t) = \Omega_s(0)\exp(Gt)$ we find that the atomic coherence grows as

$$\rho_{ab}(t) = \rho_{ab}(0)e^{Gt}, \tag{7.114}$$

where $\rho_{ab}(0)$ is the initial coherence generated by the seed superradiant pulse. In the weak excitation limit $\rho_{aa}(t) \approx |\rho_{ab}(t)|^2$ and using Eqs. (7.114) and (7.104) we finally obtain

$$\rho_{aa}(t) \approx |\rho_{ab}(0)|^2 \exp\left(\frac{\sqrt{2}}{3}\frac{\Omega_d^2}{\omega_{ab}^2}\Omega_a t\right). \tag{7.115}$$

Atomic excitation can start to grow out of the vacuum fluctuations or the growth can be triggered by the seed pulse $\Omega_s(0)$. This can be understood considering excitation of a pendulum with periodically modulated frequency. Equation of motion for such parametric pendulum reads

$$\ddot{\phi} + \omega_0^2[1 + \delta \sin(\nu_d t)]\phi = 0, \tag{7.116}$$

where ϕ is a small angle describing deviation from equilibrium and $\delta \ll 1$ is the modulation amplitude. Frequency modulation can be produced by periodically changing the length of the pendulum.

If initially the pendulum is not excited, that is $\phi(0) = \dot{\phi}(0) = 0$, then Eq. (7.116) yields the null solution

$$\phi(t) = 0. \tag{7.117}$$

Hence, in order to amplify pendulum oscillations we should first deposit a small amount of energy, e.g. shift the pendulum from its equilibrium position by some angle ϕ_0. This is analogous to $\rho_{ab}(0)$ in Eq. (7.114). In the zero order approximation in parameter δ we then find

$$\phi(t) = \phi_0 \cos(\omega_0 t). \tag{7.118}$$

Plugging (7.118) back in Eq. (7.116) we obtain in first order the equation of forced harmonic oscillator

$$\ddot{\phi} + \omega_0^2 \phi = \frac{1}{2}\omega_0^2 \phi_0 \delta \left(\sin\left[(\nu_d - \omega_0)t\right] - \sin\left[(\omega_0 + \nu_d)t\right]\right). \tag{7.119}$$

For $\nu_d = 2\omega_0$ the first term in the right hand side of Eq. (7.119) acts as a driving force having resonant frequency ω_0 which yields growth of the pendulum oscillations.

However, the amplitude of the driving force is proportional to ϕ_0 and, thus, it would vanish unless the pendulum is initially excited.

7.6 Coupled parametric oscillators

Here we consider two coupled harmonic oscillators described by equations

$$\ddot{x}_1 + \omega_0^2 x_1 - \Omega^2 x_2 = 0, \tag{7.120}$$

$$\ddot{x}_2 + \omega_0^2 x_2 - \Omega^2 g(t) x_2 - \Omega^2 f(t)(x_1 - x_2) = 0, \tag{7.121}$$

where ω_0 is the frequency of free oscillator, $\Omega \ll \omega_0$ is a coupling constant,

$$f(t) = 1 + \delta \cos(\nu_d t), \tag{7.122}$$

$\nu_d \ll \omega_0$ is the driving frequency and $\delta \ll 1$ is a modulation amplitude. Function $f(t)$ describes modulation of the coupling strength between oscillators. Such modulation produces unwanted time-dependent frequency shift of the second oscillator. To compensate such shift we additionally modulate oscillator frequency by introducing function $g(t)$.

Making slowly varying amplitude approximation, that is writing

$$x_1 = A_1(t) e^{i\omega_0 t}, \qquad x_2 = A_2(t) e^{i\omega_0 t}, \tag{7.123}$$

where $A_{1,2}(t)$ are slowly varying functions on the time scale $1/\omega_0$, we obtain the following equations for $A_1(t)$ and $A_2(t)$

$$2i\omega_0 \dot{A}_1 - \Omega^2 A_2 = 0, \tag{7.124}$$

$$2i\omega_0\dot{A}_2 - \Omega^2 g(t)A_2 - \Omega^2 f(t)(A_1 - A_2) = 0. \tag{7.125}$$

Taking time derivative of both sides of Eq. (7.124) and using Eq. (7.125) we find

$$\ddot{A}_1 - i\frac{\Omega^2}{2\omega_0}\left[f(t) - g(t)\right]\dot{A}_1 + \frac{\Omega^4}{4\omega_0^2}f(t)A_1 = 0. \tag{7.126}$$

Eq. (7.126) shows that frequency shift is the dominant effect since it is proportional to $1/\omega_0$, while the term producing parametric resonance is of the order of $1/\omega_0^2$. If we compensate the unwanted frequency shift, that is chose $g(t) = f(t)$ then Eq. (7.126) reduces to parametric harmonic oscillator (Mathieu) equation

$$\ddot{A}_1 + \frac{\Omega^4}{4\omega_0^2}\left[1 + \delta\cos(\nu_d t)\right]A_1 = 0 \tag{7.127}$$

which yields exponentially growing oscillations in the vicinities of parametric resonances. In particular, the first order parametric resonance occurs at the driving frequency

$$\nu_d = \frac{\Omega^2}{\omega_0}. \tag{7.128}$$

This frequency is much smaller than the oscillator frequency ω_0. Nevertheless, Eq. (7.127) yields large gain

$$G = \frac{\delta \cdot \nu_d}{8} \tag{7.129}$$

because ν_d corresponds to the first-order parametric resonance. In the following, we will present two analogies of these two coupled harmonic oscillators in Eqs. (7.120) and (7.121).

7.6.1 Electromechanical analogy of the QASER

Gain with no excited state population produced by superradiant emission of radiation can be illustrated in a system of two pendulums weakly coupled by a spring

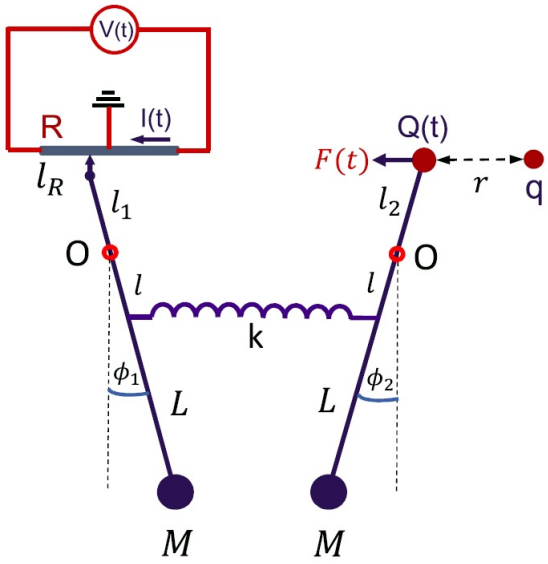

Figure 7.6: Electromechanical analog of the QASER. Masses M are attached to conducting rods which are pivoted at points O. The pendulums are weakly coupled with each other by a conducting spring. Pendulum 1 corresponds to the field and 2 to the atoms. A metallic sphere is attached to the top of the second pendulum, while the upper end of the first pendulum slides without friction along the resistor R connected to AC voltage supply $V(t)$. The middle point of the resistor is grounded. A charge q, placed at a fixed position, interacts with the charge on the metallic sphere $Q(t)$ which is proportional to $V(t)$ and to the displacement ϕ_1 of the first pendulum from equilibrium. This interaction modulates coupling strength between the pendulums.

as shown in Fig. 7.6. Due to the weak coupling, mechanical energy flows back and forth between pendulums on a time scale much longer than the oscillation period of each pendulum. This is analogous to photon absorption and reemission by atoms occurring with collective frequency Ω_a. Thus, in the present analogy, the first pendulum corresponds to the XUV field, while the second one represents the atomic system.

In this arrangement pendulums and the spring are made out of conducting materials. A metallic sphere of capacitance C is attached to the top of the second pendulum, while the upper end of the first pendulum slides without friction along the resistor R of length l_R connected to AC voltage supply $V(t) = V_0 \cos(\nu_d t)$. The middle point of the resistor is grounded (has zero electric potential). Electric potential of the pendulums Φ, and thus the charge of the metallic sphere $Q = C\Phi$, is determined by the displacement ϕ_1 of the first pendulum from equilibrium $\Phi = V(t) l_1 \phi_1 / l_R$ (for notation see Fig. 7.6). A charge q, placed at a fixed position, produces Coulomb force $F = qQ/4\pi\varepsilon_0 r^2$ on the second pendulum. One can write this force as $F = F_0 \cos(\nu_d t)\phi_1$, where $F_0 = qCV_0 l_1 / 4\pi\varepsilon_0 l_R r^2$ is approximately constant. Force F is proportional to ϕ_1 and modulates the coupling strength between oscillators via time dependence of $V(t)$ without producing undesirable frequency shift.

Equation of pendulum motion around the axis of rotation reads

$$\frac{d(I\dot{\phi})}{dt} = \tau, \tag{7.130}$$

where I is the moment of inertia, $\dot{\phi}$ is the angular velocity and τ is torque on the pendulum. Applying this equation for pendulum 1 and 2 we obtain for small

deviation from equilibrium

$$ML^2\ddot{\phi}_1 = -MgL\phi_1 + kl^2(\phi_2 - \phi_1), \tag{7.131}$$

$$ML^2\ddot{\phi}_2 = -MgL\phi_2 - kl^2(\phi_2 - \phi_1) + F_0 l_2 \cos(\nu_d t)\phi_1, \tag{7.132}$$

where k is the spring constant. Combining terms one can rewrite the equations of motion for the coupled pendulums equations as

$$\ddot{\phi}_1 + \omega_0^2\phi_1 - \Omega^2\phi_2 = 0, \tag{7.133}$$

$$\ddot{\phi}_2 + \omega_0^2\phi_2 - \Omega^2\left[1 + \delta\cos(\nu_d t)\right]\phi_1 = 0, \tag{7.134}$$

where

$$\omega_0^2 = \frac{g}{L} + \frac{kl^2}{ML^2} \tag{7.135}$$

is the frequency of the free pendulums,

$$\Omega^2 = \frac{kl^2}{ML^2} \tag{7.136}$$

is the coupling constant and

$$\delta = \frac{F_0 l_2}{kl^2} \tag{7.137}$$

is the modulation amplitude of the coupling strength.

Next we compare gain for the single and coupled oscillators assuming the same driving force for both systems. Namely, we assume that the two coupled pendulums are described by Eqs. (7.133) and (7.134) while evolution of the single oscillator

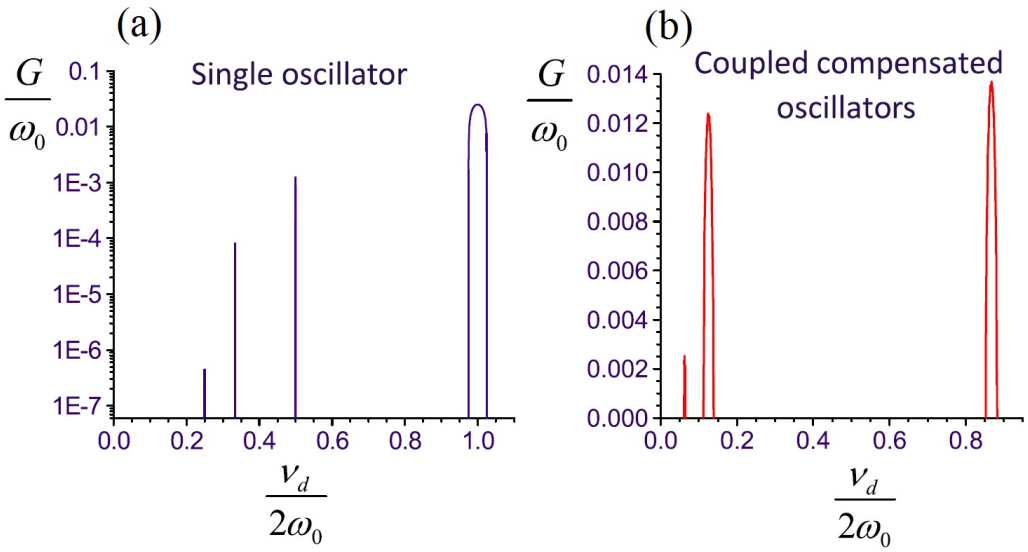

Figure 7.7: (a) Gain for a single oscillator as a function of modulation frequency ν_d obtained by numerical solution of Eq. (7.138) with $\Omega^2/\omega_0^2 = 0.25$ and $\delta = 0.4$. Vertical axis has logarithmic scale. (b) Gain for compensated coupled oscillators as a function of modulation frequency ν_d obtained by numerical solution of Eqs. (7.133), (7.134) with $\Omega^2/\omega_0^2 = 0.25$, $\delta = 0.4$ and initial condition $x_2(0) = 0$, $\dot{x}_1(0) = 0$ and $\dot{x}_2(0) = 0$..

obeys the Mathieu equation

$$\ddot{\phi} + \left[\omega_0^2 - \Omega^2 \delta \cos(\nu_d t)\right] \phi = 0. \tag{7.138}$$

In Fig. 7.7 we plot gain per unit time as a function of modulation frequency ν_d obtained by numerical solution of Eq. (7.138) (Fig. 7.7(a)) and Eqs. (7.133), (7.134) (Fig. 7.7(b)). In simulations we take $\Omega^2/\omega_0^2 = 0.25$ and $\delta = 0.4$. For a single oscillator the modulation yields exponential grow of the oscillation amplitude in the vicinity of parametric resonances $\nu_d = 2\omega_0/m$, where $m = 1, 2, 3, \ldots$. However, gain for higher order resonances (when $m > 1$) becomes very small (see Fig. 7.7(a)). That is if driving frequency ν_d is much smaller than ω_0 then excitation of a single

oscillator is very inefficient. On the other hand, as is seen from Fig. 7.7(b), for coupled oscillators there is strong resonance at driving frequency

$$\nu_d = \frac{\Omega^2}{\omega_0} = 0.25\omega_0. \tag{7.139}$$

At such a frequency we see that gain $G = 0.012\omega_0$ is comparable to those for $\nu_d \approx 2\omega_0$.

This simple mechanical example shows that a coupled system can be excited with high efficiency even if the driving frequency ν_d is much smaller than frequency of the system's oscillations. Similarly, in the case of superradiant gain the coupled field-atom system is efficiently excited by a low frequency coherent drive provided we compensate for the deleterious time-dependent Stark shift.

7.6.2 Electronic circuit analogy of the QASER

In the next section, we present an electronic circuit experiment to demonstrate the QASER amplification mechanism. The experiment can be easily described theoretically in a somewhat ideal electronic circuit model, shown in Fig. 7.8. The model consists of two ideal LC circuits which are weakly coupled by an inductor L_0 and a multiplier M. Output voltage V_{out} of the multiplier is proportional to the product of the two input voltages $V(t)$ and $V_1 : V_{\text{out}} = \kappa V(t)V_1$, where κ is the gain of the multiplier and $V(t) = V_0 \cos(\nu_d t)$ is the voltage produced by a function generator. The multiplier makes coupling between the two LC circuits nonreciprocal. The multiplier has high input resistance, so one can disregard its input current.

Let electric charges of the capacitors be Q_1 and Q_2. Applying Kirchhoff's laws to the system we obtain (for notation see Fig. 7.8)

$$L_1(\ddot{Q}_1 + \dot{I}_0) + \frac{Q_1}{C_1} = 0, \tag{7.140}$$

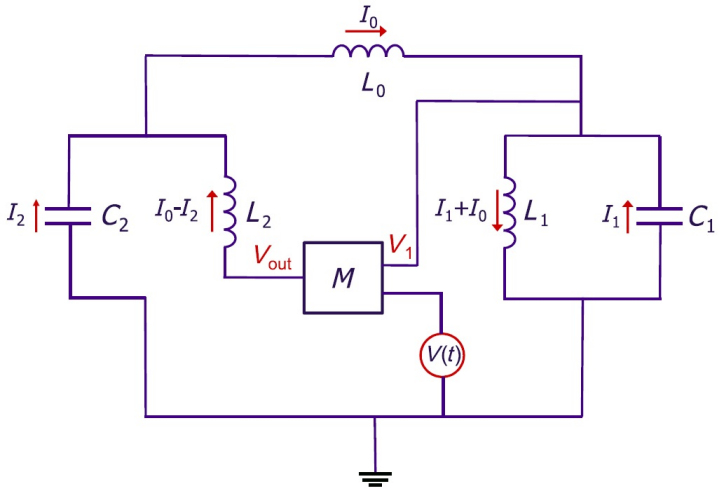

Figure 7.8: Electronic curcuit analog of the QASER. Two LC circuits weakly coupled by an inductor L_0 correspond to the atoms and to the field. Modulation of the coupling strength is provided by a feedback mechanism in which voltage V_1 from the capacitor C_1 is applied to the input terminal of the multiplier M; its output voltage $V_{\rm out}$ is proportional to the product of the two input voltages $V(t)$ and V_1, where $V(t) = V_0 \cos(\nu_d t)$ is the voltage produced by a function generator.

$$L_2(\ddot{Q}_2 - \dot{I}_0) + \frac{Q_2}{C_2} - \kappa \frac{Q_1}{C_1} V(t) = 0, \tag{7.141}$$

$$L_0 \dot{I}_0 = \frac{Q_1}{C_1} - \frac{Q_2}{C_2}. \tag{7.142}$$

Elimination of $\dot{I}_0$ from Eqs. (7.140)-(7.142) yields two coupled equations

$$\ddot{Q}_1 + \frac{Q_1}{L_1 C_1}\left(1 + \frac{L_1}{L_0}\right) - \frac{Q_2}{L_0 C_2} = 0, \tag{7.143}$$

$$\ddot{Q}_2 + \frac{Q_2}{L_2 C_2}\left(1 + \frac{L_2}{L_0}\right) - \frac{Q_1}{L_0 C_1}\left[1 + \kappa \frac{L_0}{L_2} V(t)\right] = 0. \tag{7.144}$$

Assuming that $L_1 = L_2 = L$, $C_1 = C_2 = C$ and introducing notations

$$\omega_0^2 = \frac{1}{LC}\left(1 + \frac{L}{L_0}\right), \tag{7.145}$$

$$\Omega^2 = \frac{1}{L_0 C}, \qquad \delta = \kappa V_0 \frac{L_0}{L}, \tag{7.146}$$

one can write Eqs. (7.143) and (7.144) as

$$\ddot{Q}_1 + \omega_0^2 Q_1 - \Omega^2 Q_2 = 0, \tag{7.147}$$

$$\ddot{Q}_2 + \omega_0^2 Q_2 - \Omega^2 \left[1 + \delta \cos(\nu_d t)\right] Q_1 = 0, \tag{7.148}$$

which are identical to Eqs. (7.133) and (7.134) of the previous section and, thus, the present electronic circuit model displays similar parametric excitation.

The two LC circuits are weakly coupled provided $L_0 \gg L$. Driving the system with small frequency $\nu_d \approx \Omega^2/\omega_0 = \omega_0 L/L_0 \ll \omega_0$ yields the difference resonance which results in the efficient excitation of oscillations in the LC circuits at the high natural frequencies $\omega_0 \left(1 \pm L/2L_0\right)$.

7.6.3 Experimental demonstration of the QASER amplification mechanism in electronic circuit

In this section we present an experiment which illustrates the QASER amplification mechanism in an electronic system shown in Fig. 7.9. The system consists of two RLC circuits weakly coupled by a capacitor and a multiplier M which makes coupling nonreciprocal. In our experiment M is an AD633JN analog multiplier connected as a linear amplitude modulator. Its output voltage V_{out} is given by

$$V_{\text{out}} = \frac{V_1 \cdot V(t)}{10\text{V}} + V(t), \tag{7.149}$$

where $V(t)$ is the voltage produced by the DS345 synthesized function generator which is fed to the carrier input of AD633JN and V_1 is the voltage applied to the modulation input (see Fig. 7.9). The circuit is set up on a breadboard using appa-

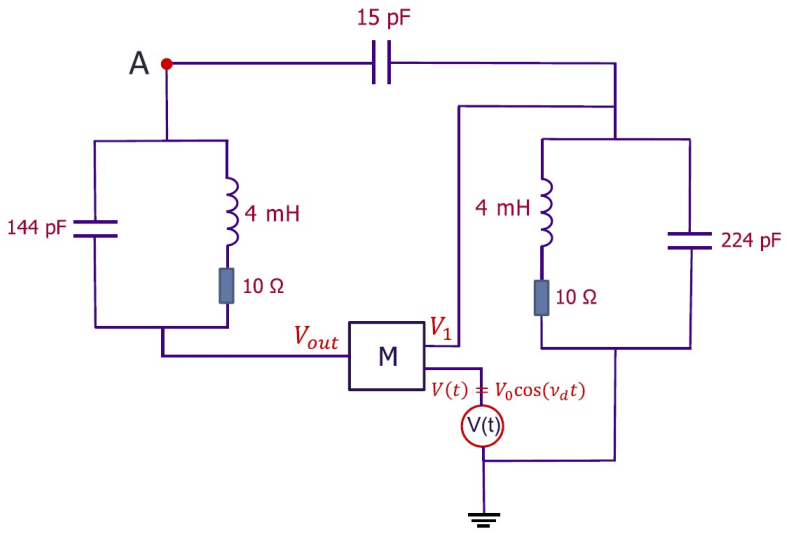

Figure 7.9: Experimental setup: two RLC circuits are connected by a capacitor and a multiplier M which yields nonreciprocal coupling between the two circuits. The transfer function of the multiplier is given by Eq. (7.149). Sinusoidal voltage from a function generator is applied to one of the multiplier's inputs which produces modulation of the coupling strength. Voltage $V_A(t)$ at the point A is measured by an oscilloscope.

ratus available in an undergraduate electronics laboratory. The circuit parameters are indicated in Fig. 7.9. The breadboard has self-capacitance of a few pF.

The circuit parameters are chosen such that the system's natural frequencies are close to each other. To compensate for the capacitance of the multiplier we designed the RLC circuits with different C. We measured the natural frequencies of the system to be $\omega_1 = 196$ kHz and $\omega_2 = 222$ kHz. Thus, the frequency difference between normal modes is $\Delta\omega = 26$ kHz. Quality factor of the circuit is $Q = \sqrt{L/C}/R \approx 400$ which yields the resonance bandwidth 0.5 kHz.

In our experiment we modulate the coupling between the RLC circuits by apply-

ing sinusoidal voltage of frequency ν_d and amplitude V_0

$$V(t) = V_0 \cos(\nu_d t) \tag{7.150}$$

to the multiplier input and measure the voltage $V_A(t)$ at the point A of the circuit (see Fig. 7.9) using Tektronix TDS 210 oscilloscope. We examine how $V_A(t)$ changes under variation of ν_d and V_0.

We found that when $\nu_d = \Delta\omega = 26$ kHz and V_0 is greater than a threshold value the system starts to oscillate at high frequency. The measured spectrum of such oscillations is given in Fig. 7.10(a) for $V_0 = 0.9$ V (solid lines). The spectrum has a peak at the low driving frequency $\nu_d = 26$ kHz and several high frequency components at $\omega = \omega_{1,2}$ plus two sidebands at $\omega_1 - \nu_d = 170$ kHz and $\omega_2 + \nu_d = 248$ kHz. In the figure, vertical dashed lines indicate position of higher harmonics of the driving frequency. Clearly the observed high frequency oscillations are not produced by the higher harmonics of ν_d which do not overlap with the generated spectral components.

Amplification of the high frequency oscillations occurs when parametric gain (which depends on V_0) exceeds losses. To demonstrate such a threshold behavior we measured the system's oscillation amplitude at the natural frequency $\omega_2 = 222$ kHz as a function of V_0 for $\nu_d = 26$ kHz. The results are shown in Fig. 7.10(b) (dots). For $V_0 < 0.814$ V there is no amplification at any frequency, while for $V_0 \geq 0.814$ V the net gain becomes positive and high frequencies are efficiently generated by the low frequency drive.

Finally, to illustrate the resonant nature of the amplification mechanism we measured the system's oscillation amplitude at the natural frequency $\omega_2 = 222$ kHz as a function of ν_d for $V_0 = 0.825$ V (see Fig. 7.10(c)). We found that high frequency

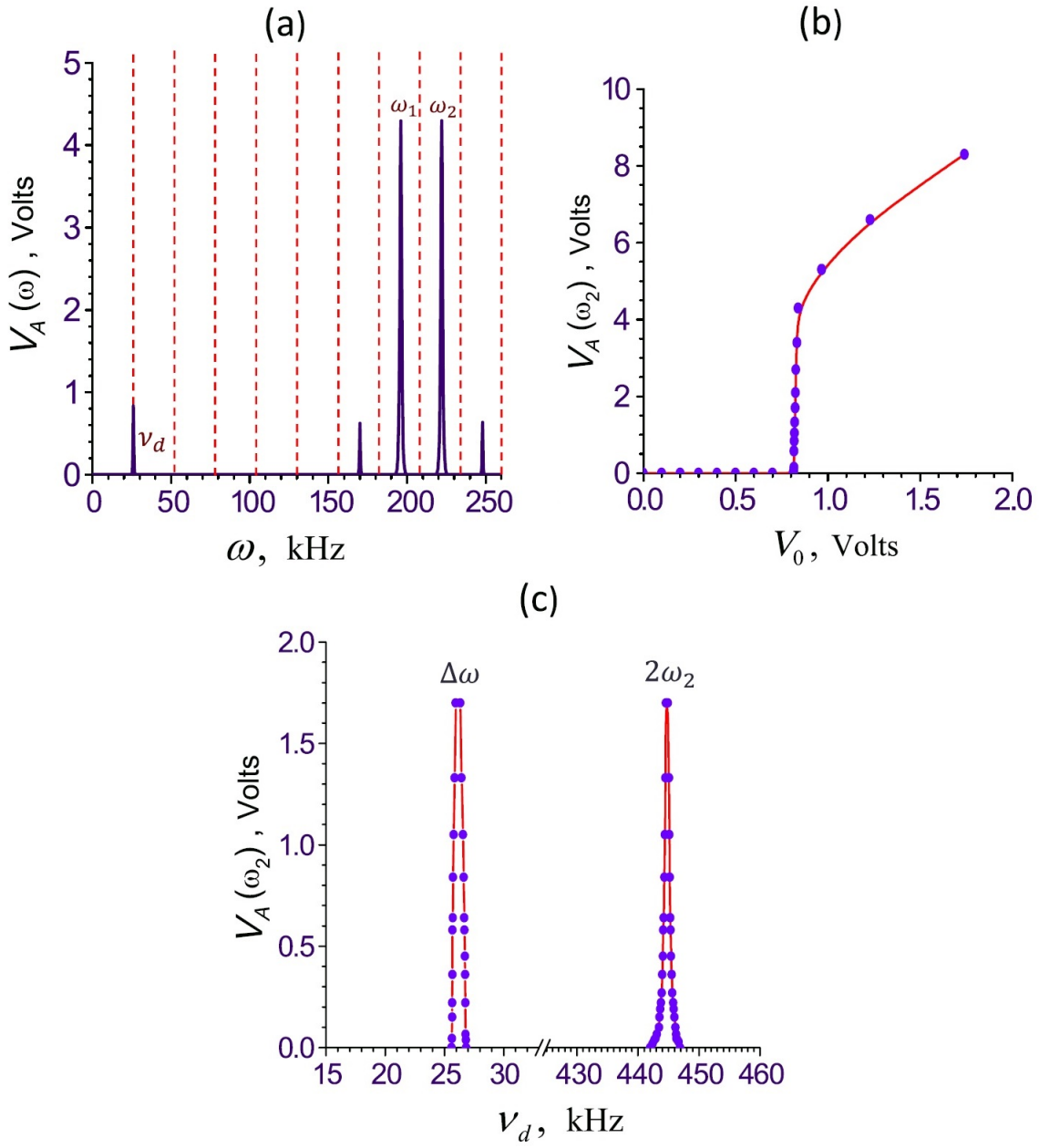

Figure 7.10: (a) Measured spectrum of system's oscillations for driving frequency $\nu_d = 26$ kHz and driving amplitude $V_0 = 0.9$ V (solid lines). Vertical dashed lines at $\omega = m\nu_d$, $m = 1, 2, \ldots$, indicate position of higher harmonics of the driving frequency. (b) Dependence of the system's oscillation amplitude at the natural frequency $\omega_2 = 222$ kHz on V_0 for $\nu_d = 26$ kHz. (c) Dependence of the system's oscillation amplitude at the natural frequency $\omega_2 = 222$ kHz on ν_d for $V_0 = 0.825$ V. In all plots the voltage is measured at the point A (see Fig. 7.9).

generation occurs only when ν_d is near $\Delta\omega = 26$ kHz or $2\omega_2 = 444$ kHz. This result agrees with our theoretical findings displayed in Fig. 7.7(c).

To the best of our knowledge, the present results are the first experimental demonstration of difference combination resonance. That is, where the system generates oscillations at high natural frequencies ω_1 and ω_2 when forced with a low frequency $\nu_d = \omega_2 - \omega_1$. Such a mechanism holds promise for generating high frequency electromagnetic oscillations in electronic circuits (e.g., developing THz generators) and high frequency (XUV or X-ray) coherent light by means of a low frequency drive.

7.7 QASER physics from a generalized perspective

The QASER is a device that generates high frequency coherent radiation by driving an atomic ensemble with a much smaller frequency. The amplification mechanism of the QASER is governed by the difference combination parametric resonance which occurs when the driving field frequency matches the frequency difference between two close high frequency normal modes of the coupled light-atom system. The atoms interact with light collectively which yields superradiant emission and reabsorption of the high frequency radiation. This collective interaction determines the spacing between system's normal modes and QASER gain.

The single oscillator described by Eq. (7.138) provides a simple example of parametric resonance. Such oscillator has two natural frequencies (normal modes) $\pm\omega_0$. If we choose ν_d close to the difference between the natural frequencies, that is $\nu_d \approx 2\omega_0$, the oscillator phase-locks to the parametric variation and undergoes the first-order parametric resonance absorbing energy at a rate proportional to the energy it already has.

Fig. 7.7(b) shows that gain for the higher order resonances occurring at lower frequencies $\nu_d \approx 2\omega_0/m$, $m = 2, 3, \ldots$ is very small and, thus, excitation of the system

by the higher order resonances is inefficient. Nevertheless, as we show, it is possible to effectively excite high frequency oscillations with a low frequency drive if the system has a pair of high frequency normal modes with small spacing. Modulation of parameters of such system at a small frequency equal to the spacing between the two close normal modes can display the first-order parametric resonance and, thus, yield an efficient excitation of the high frequency oscillations.

Two weakly coupled harmonic oscillators, described by Eqs. (7.133) and (7.134) with $\Omega \ll \omega_0$, is an example of such a system. It has a pair of close normal mode frequencies $\omega_\pm = \sqrt{\omega_0^2 \pm \Omega^2} \approx \omega_0 \pm \Omega^2/2\omega_0$. If the modulation frequency matches the frequency difference between those modes, namely, $\nu_d = \omega_+ - \omega_- \approx \Omega^2/\omega_0$, the system displays resonance with high gain (see Eq. (7.129))

$$G = \frac{\delta \cdot \nu_d}{8}, \tag{7.151}$$

which is proportional to δ, rather than δ^m $(m > 1)$ which would be the case for the higher order resonances. This is illustrated in Fig. 7.7(c).

The QASER operates by the same principle. Indeed, propagation of light (having Rabi frequency $\Omega(t, \mathbf{r})$) through the medium of two-level atoms is described by the coupled Maxwell–Schrödinger equations which without making the slowly varying amplitude approximation read

$$\left(\frac{\partial^2}{\partial t^2} - c^2\nabla^2\right)\Omega(t, \mathbf{r}) = -2\frac{\Omega_a^2}{\omega_{ab}}\frac{\partial^2 \rho_{ab}}{\partial t^2}, \tag{7.152}$$

$$\frac{\partial \rho_{ab}}{\partial t} + i\omega_{ab}\rho_{ab} = i\Omega(t, \mathbf{r})(\rho_{bb} - \rho_{aa}). \tag{7.153}$$

Eqs. (7.152) and (7.153) describe two coupled oscillators. To find the normal modes of the coupled system for weak atomic excitation one can look for the solution

of Eqs. (7.152) and (7.153) in the form $\Omega, \rho_{ab} \propto \exp(ikz - i\nu t)$ which for weak coupling and a mode with the wave number k near ω_{ab}/c yields two close frequencies

$$\nu_{\pm} = \frac{1}{2}\left[\omega_{ab} + ck \pm \sqrt{(\omega_{ab} - ck)^2 + 4\Omega_a^2}\right], \tag{7.154}$$

where we assumed that initially the atoms are in the ground state, that is $\rho_{bb} - \rho_{aa} \approx 1$. Thus, if we modulate the system's parameters at the small frequency

$$\nu_d = \nu_+ - \nu_- = \sqrt{(\omega_{ab} - ck)^2 + 4\Omega_a^2} \ll \nu_{\pm} \tag{7.155}$$

the high frequency modes $\nu_{\pm}$ can be excited with large gain via the first-order parametric resonance. Since in the present problem the wave number k is a continuous parameter one can satisfy the resonance condition for $\nu_d \geq 2\Omega_a$. Namely, for such ν_d there are always two normal modes (value of k) which are in resonance with the driving field.

A more visible picture can be seen from Fig. 7.11. Two dispersion curves of the coupled system for the electromagnetic field interacting with atomic medium are plotted in red curves. Two collective modes are coupled by the drive field modulation with modulation frequency ν_d and $k_d = -\nu_d/c$. Forward propagation drive field modulation ($k_d = \nu_d/c$) can never couple these two modes.

Terms in the right hand side of Eqs. (7.152) and (7.153) describe coupling between two oscillators. Nonlinearity of the coupling allows us to modulate the coupling strength by driving atoms with a low frequency field which serves as an energy source for the QASER operation. Such driving, however, also produces an unwanted AC Stark shift of the atomic transition which must be compensated in order to achieve gain.

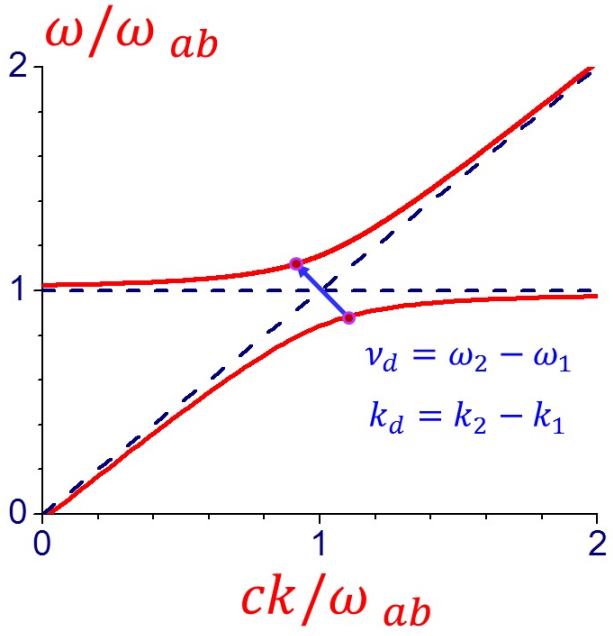

Figure 7.11: Dispersion curves of the coupled system for the electromagnetic field interacting with atomic medium. Two collective modes are coupled by the drive field modulation

Amplification mechanism of the QASER, namely the difference combination parametric resonance between two close normal modes, can appear in various physical systems.

The study of variable parameter (or parametric) processes in electronic circuits in 1950's led to discovery of a frequency conversion mechanism in which the energy is fed from the source that modulates the circuit parameters at frequency ν_d to two circuit normal modes of lower frequencies ω_1 and ω_2 obeying the relation [139, 140]

$$\nu_d = \omega_1 + \omega_2. \tag{7.156}$$

This yields amplification of frequencies ω_1 and ω_2. A variable inductor or a capacitor suitably coupled to two resonance circuits is an example of such parametric ampli-

fier [139]. A few years later the principle of parametric amplification was proposed for generation of light waves at frequencies ω_1 and ω_2 in nonlinear optical crystals [141, 142, 143]. The first successful attainment of parametric oscillation at optical frequencies was reported in 1965 in $LiNbO_3$ [144]. The progress in parametric amplification and oscillation has been the subject of many review papers (see, e.g., [145, 146, 147]). These days the optical parametric oscillators (OPOs) are commercially available.

OPO converts an input laser wave with frequency ν_d into two output waves of lower frequency satisfying Eq. (7.156) by means of the second order nonlinear optical interaction in crystal. The phase matching plays a decisive role here. However, QASER operation does not require phase matching and, in contrast to OPO, generates light at frequencies obeying the relation

$$\nu_d = \omega_2 - \omega_1. \tag{7.157}$$

It seems that study of the electronic circuits back in 1950's largely missed the possibility of generation such frequencies. This is not surprising because QASER mechanism requires compensation of the AC frequency shift (Stark shift) and asymmetric modulation of the coupling between oscillators (see Eqs. (7.133) and (7.134)) which is usually not the case.

Resonances described by Eqs. (7.156) and (7.157) are known in applied mechanics as combination resonances. They affect dynamic stability of structures and appear in systems having multiple degrees of freedom. The literature on combination resonances in such systems is abundant (see, e.g., [148, 149, 150]). In particular, the sum (7.156) and the difference (7.157) combination resonances have been theoretically studied in connection with parametric instability of a cantilevered column

under periodic loads [151] and shear-deformable laminated plates [152]. It has also been suggested that the failure of the high-pressure compressor of jet engines (which was occurring in the past) can be due to the difference combination resonance when the rotating speed of the rotor matches the difference between natural frequencies of the rotating and static seals [153].

One should mention that combination resonances can occur only under certain conditions. Small oscillations in modulated systems with many degrees of freedom can be described by coupled differential equations which in matrix notation read

$$\ddot{q} + C\dot{q} + [A + B\cos(\nu_d t)]q = 0, \tag{7.158}$$

where q is a vector of generalized coordinates while A, B and C are matrices. A is a diagonal matrix, while matrix C denotes gyroscopic terms and usually it is antisymmetric. It has been shown that if $C = 0$ and B is symmetric matrix (as is the case in many applications) then the difference combination resonance does not occur. If B is symmetric then Eqs. (7.158) can be derived from a potential function and, hence, terms Bq are conservative forces. In such Hamiltonian systems only the sum combination resonances (7.156) can be excited [154, 155]. This is the reason why the sum combination resonance is a frequent phenomenon.

In other words, if the difference combination resonance is possible in systems with no gyroscopic terms, then the system must be non-conservative [156]. This is the case for the electromechanical analogy of the QASER shown in Fig. 7.7(a) which possesses dissipation in resistor R. The results are changed as soon as gyroscopic terms are involved [154]. Now the difference parametric resonance can occur even if B is symmetric. Hamiltonian systems with gyroscopic forces (e.g., the Lorentz magnetic force) can have both the sum and the difference combination resonances.

While there is plenty of literature on combination resonances, there do not seem to be any experimental examples of difference resonances. In fact, such a device might be somewhat strange. If we had $\omega_1 \approx \omega_2$, then $\nu_d = \omega_2 - \omega_1$ would be small, perhaps several orders of magnitude smaller. So, a difference combination resonance would generate a high frequency from a low-frequency excitation.

7.8 Possible experimental realization of the QASER

Here we discuss possible experiments which can demonstrate light amplification by collective parametric resonance. To make QASER work we must compensate time dependence of the AC Stark shift produced by the driving field for a particular atomic transition. Our analysis shows that such compensation, in the general case, does not suppress transition modulation which can lead to gain at high frequency.

In many-level systems one can compensate unwanted Stark shift $\Delta\omega_{ab}(t)$, e.g., by driving atoms with a specific frequency or with a properly chosen elliptical polarization. We discuss these possibilities in the subsequent sections.

7.8.1 Driving with specific frequency

Because contribution to $\Delta\omega_{ab}(t)$ from different levels can have opposite signs one can compensate the Stark shift by a proper choice of the driving field frequency. To be specific, we consider gas of neutral He atoms which have energy levels shown in Fig. 7.12. Initially atoms are in the ground state $1\ ^1\mathrm{S}_0$ and driven by a linearly polarized field $E^{\mathrm{drive}}(t) = E_d \cos(\nu_d t - k_d z)$ which couples dipole allowed transitions as shown in Fig. 7.12. The time-dependent Stark shift of the $2\ ^1\mathrm{P}_1 - 1\ ^1\mathrm{S}_0$ $(a-b)$ transition is given by the following expression

$$\Delta\omega_{ab}(t) = \frac{\left|E^{\mathrm{drive}}(t)\right|^2}{\hbar^2}\left(\frac{2\omega_{ab}|d_{ab}|^2}{\omega_{ab}^2 - \nu_d^2} - \sum_{m\neq a,b}\frac{\omega_{ma}|d_{am}|^2}{\omega_{am}^2 - \nu_d^2}\right), \tag{7.159}$$

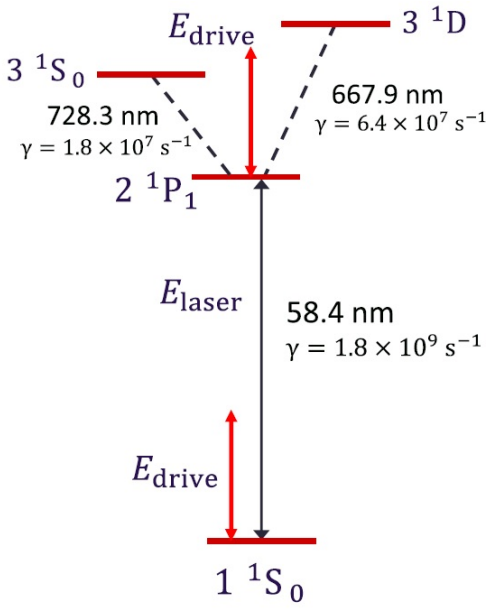

Figure 7.12: Energy level diagram of He atom.

where $\omega_{ma} = \omega_m - \omega_a$. $\Delta\omega_{ab}(t)$ can be made zero if the driving field frequency has a proper value. Since the terms under the sum in Eq. (7.159) are typically larger then the first term one should chose ν_d to lie between two excited levels (see Fig. 7.12). In this case the terms under the sum can compensate each other along with the first term.

For 58.4 nm $2\ ^1P_1 - 1\ ^1S_0$ transition ($\gamma = 1.8 \times 10^9\ s^{-1}$) and atomic density $n = 1.6 \times 10^{20}\ cm^{-3}$ which corresponds to the helium pressure of 6.6 atm at room temperature $T = 300$ K the collective atomic frequency is

$$\Omega_a = \sqrt{\frac{3cn\lambda_{ab}^2\gamma}{8\pi}} = 1.87 \times 10^{14}\ s^{-1}. \tag{7.160}$$

Atom-atom collision frequency is given by

$$\nu_{\text{coll}} = V_{\text{th}} n \sigma, \tag{7.161}$$

where collisional cross section is

$$\sigma \approx a_B^2 m^4 = 0.45 \times 10^{-15} \text{ cm}^2, \tag{7.162}$$

m is the principal quantum number of the excited atomic state and a_B is the Bohr radius. For room temperature the atom thermal velocity is

$$V_{\text{th}} = \sqrt{\frac{k_B T}{M}} = 7.87 \times 10^4 \text{ cm/s}, \tag{7.163}$$

which yields

$$\nu_{\text{coll}} = V_{\text{th}} n \sigma = 5.7 \times 10^9 \text{ s}^{-1}. \tag{7.164}$$

To fulfill the condition of collective parametric resonance the driving field frequency should be

$$\nu_d > \frac{\Omega_a}{\sqrt{2}}, \tag{7.165}$$

which is readily satisfied in the present scheme. For driving field intensity $I = 10^{14}$ W/cm^2 (which is below the ionization threshold for He atoms) the Rabi frequency is

$$\Omega_d = c\sqrt{\frac{3\pi I \gamma_{ab}}{\hbar \omega_{ab}^3}} = 6.6 \times 10^{14} s^{-1}, \tag{7.166}$$

and gain per unit time in the backward direction can be estimated (according to Eq. (7.104)) as

$$G \approx \frac{\Omega_a}{3\sqrt{2}} \frac{\Omega_d^2}{\omega_{ab}^2} = 2 \times 10^{10} \text{ s}^{-1}, \tag{7.167}$$

which is larger than collisional decoherence (this implies applicability of the present analysis). For wavelength of the driving field $\lambda \approx 700$ nm Eq. (7.105) yields that

gain per unit length is

$$G_L \approx \frac{\nu_d}{c}\frac{\Omega_d^2}{\omega_{ab}^2} = 30 \text{ cm}^{-1}, \tag{7.168}$$

which is large enough to achieve one path light conversion into high frequency radiation.

7.8.2 Driving with elliptically polarized light

One can also suppress time-dependence of the AC Stark shift by a proper choice of the elliptical polarization of the driving field. This can be understood from a 3-level model shown in Fig. 7.13. In the model the ground state b is dipole coupled with states a and c. E.g., the ground state can be an s state while levels a and c are p_x and p_y orbitals. We assume that driving field $\mathbf{E}^{\text{drive}}$ couples both transitions, namely $x-$component of $\mathbf{E}^{\text{drive}}$ drives $a-b$ transition, while $y-$component drives $c-b$ transition. Our goal is to compensate the AC Stark shift of the $a-b$ transition by a proper choice of elliptical polarization of $\mathbf{E}^{\text{drive}}$. The time-dependent Stark shift of the $a-b$ transition is given by the following expression

$$\hbar^2\Delta\omega_{ab}(t) = \frac{2\omega_{ab}|d_{ab}|^2}{\omega_{ab}^2-\nu_d^2}\left|E_x^{\text{drive}}(t)\right|^2 + \frac{\omega_{cb}|d_{cb}|^2}{\omega_{cb}^2-\nu_d^2}\left|E_y^{\text{drive}}(t)\right|^2 \tag{7.169}$$

which can be made time independent if we choose $E_x^{\text{drive}} = A\cos(\nu_d t - k_d z)$ and $E_y^{\text{drive}} = B\sin(\nu_d t - k_d z)$ with proper values of the amplitudes A and B. Despite of the compensation of the Stark shift time dependence the strength of the $a-b$ transition is yet modulated by the driving field leading to gain at high frequency. We will show this in the next section for the 3-level model.

Real atoms have many levels and many of them contribute to the Stark shift. Nevertheless, the mechanism of the AC Stark shift compensation remains the same. In the presence of an external electric field $\mathbf{E}$, the Stark shift of the various magnetic

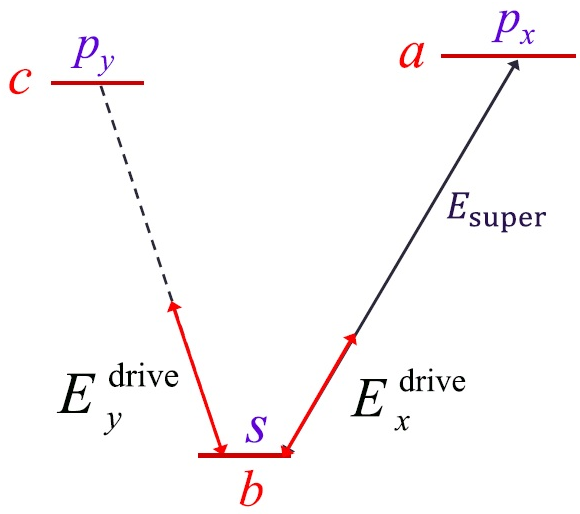

Figure 7.13: 3-level model of the QASER.

sublevels of a particular electronic state may be expressed in terms of scalar and tensor polarizabilities, α_0 and α_2, which can be measured experimentally. If the atomic hyperfine structure is neglected, the frequency shift of a particular magnetic sublevel may be expressed in terms of its total angular momentum J and the projection m_J along the quantization axis x as [157]

$$\Delta\omega(J, m_J) = -\frac{1}{2}\alpha_0 E^2 - \frac{1}{4}\alpha_2 \frac{3m_J^2 - J(J+1)}{J(2J-1)} \left(3E_x^2 - E^2\right). \tag{7.170}$$

If the propagating driving field has E_x and E_y components then Eq. (7.170) yields

$$\Delta\omega(J, m_J) = -\frac{1}{2}\left(\alpha_0 + \alpha_2 \frac{3m_J^2 - J(J+1)}{J(2J-1)}\right) E_x^2$$

$$-\frac{1}{2}\left(\alpha_0 - \frac{1}{2}\alpha_2 \frac{3m_J^2 - J(J+1)}{J(2J-1)}\right) E_y^2. \tag{7.171}$$

Eq. (7.171) shows that by a proper choice of time dependence of E_x and E_y one can make the Stark shift to be time independent.

Let us consider the 5s $^2S_{1/2}$–5p $^2P_{3/2}$ transition (D2 line) of Rb atom ($\lambda = 780.0$ nm) as the light amplification transition. Then Eq. (7.171) gives

$$\Delta\omega(5s^2S_{1/2}) = -\frac{1}{2}\alpha_0(5s^2S_{1/2})\left(E_x^2 + E_y^2\right), \tag{7.172}$$

$$\Delta\omega(5p^2P_{3/2}) = -\frac{1}{2}\alpha_0(5p^2P_{3/2})\left(E_x^2 + E_y^2\right) - \frac{1}{2}\alpha_2(5p^2P_{3/2})\left[m_J^2 - \frac{5}{4}\right]\left(E_x^2 - \frac{E_y^2}{2}\right) \tag{7.173}$$

and the Stark shift of the transition frequency is

$$\Delta\omega = \Delta\omega(5p^2P_{3/2}) - \Delta\omega(5s^2S_{1/2}) =$$

$$-\frac{1}{2}\left(\alpha_0(5p^2P_{3/2}) - \alpha_0(5s^2S_{1/2})\right)\left(E_x^2 + E_y^2\right) - \frac{1}{2}\alpha_2(5p^2P_{3/2})\left[m_J^2 - \frac{5}{4}\right]\left(E_x^2 - \frac{E_y^2}{2}\right). \tag{7.174}$$

To make $\Delta\omega$ time independent one should chose E_x and E_y such that

$$\alpha_x E_x^2 + \alpha_y E_y^2 = \text{const}, \tag{7.175}$$

where

$$\alpha_x = \alpha_0(5p^2P_{3/2}) - \alpha_0(5s^2S_{1/2}) + \alpha_2(5p^2P_{3/2})\left[m_J^2 - \frac{5}{4}\right], \tag{7.176}$$

$$\alpha_y = \alpha_0(5p^2P_{3/2}) - \alpha_0(5s^2S_{1/2}) - \frac{1}{2}\alpha_2(5p^2P_{3/2})\left[m_J^2 - \frac{5}{4}\right]. \tag{7.177}$$

This, e.g., is achieved for elliptically polarized light

$$E_x = E_{0x}\cos(\nu_d t - k_d z), \tag{7.178}$$

$$E_y = E_{0y} \sin(\nu_d t - k_d z) \tag{7.179}$$

with

$$\frac{E_{0x}^2}{E_{0y}^2} = \frac{\alpha_y}{\alpha_x}. \tag{7.180}$$

For the 5s $^2S_{1/2}$–5p $^2P_{3/2}$ transition of Rb the experimental values are $\alpha_0(5p^2P_{3/2}) - \alpha_0(5s^2S_{1/2}) = 136\,\text{kHz}/(\text{kV/cm})^2$ and $\alpha_2(5p^2P_{3/2}) = -40\,\text{kHz}/(\text{kV/cm})^2$ [158]. Then Eq. (7.180) gives

$$\frac{E_{0x}^2}{E_{0y}^2} = \frac{136 + 20\left[m_J^2 - \frac{5}{4}\right]}{136 - 40\left[m_J^2 - \frac{5}{4}\right]}. \tag{7.181}$$

For example, for $m_J = 1/2$ we obtain that the Stark shift is independent of time if

$$\frac{E_{0x}^2}{E_{0y}^2} = 0.66, \tag{7.182}$$

while for $m_J = 3/2$

$$\frac{E_{0y}^2}{E_{0x}^2} = 0.62. \tag{7.183}$$

For 780.0 nm 5s $^2S_{1/2}$–5p $^2P_{3/2}$ transition ($\gamma = 3.81 \times 10^7$ s^{-1}, $\omega_{ab} = 2.4 \times 10^{15}$ s^{-1}) and atomic density $n = 10^{16}$ cm^{-3} the collective atomic frequency is

$$\Omega_a = \sqrt{\frac{3cn\lambda_{ab}^2\gamma}{8\pi}} = 2.9 \times 10^{12}\ \text{s}^{-1}. \tag{7.184}$$

Atom-atom collision frequency is given by

$$\nu_{\text{coll}} = V_{\text{th}} n \sigma, \tag{7.185}$$

where collisional cross section is

$$\sigma \approx a_B^2 m^4 = 1.7 \times 10^{-14}\ \text{cm}^2 \tag{7.186}$$

and $m = 5$ is the principal quantum number of the excited atomic state. For temperature $T = 500K$ we obtain for the atom thermal velocity

$$V_{\rm th} = \sqrt{\frac{k_B T}{M}} = 2.2 \times 10^4 \text{ cm/s} \tag{7.187}$$

which yields

$$\nu_{\rm coll} = V_{\rm th} n \sigma = 3.7 \times 10^6 \text{ s}^{-1}. \tag{7.188}$$

The Doppler broadening is given by

$$\Delta\nu_{\rm D} = \frac{V_{\rm th}}{c}\omega_{ab} = 1.8 \times 10^9 \text{ s}^{-1}. \tag{7.189}$$

If we choose the driving field intensity $I = 10^{12}$ W/cm^2 then the driving field Rabi frequency is

$$\Omega_d = c\sqrt{\frac{3\pi I \gamma_{ab}}{\hbar\omega_{ab}^3}} = 4.7 \times 10^{14}\text{s}^{-1} \tag{7.190}$$

and gain per unit time in the backward direction can be estimated as

$$G \approx \frac{\Omega_a}{3\sqrt{2}}\frac{\Omega_d^2}{\omega_{ab}^2} = 2.5 \times 10^{10} \text{ s}^{-1} \tag{7.191}$$

which is much larger than collisional decoherence and Doppler broadening. One can drive Rb atoms with a commercial CO_2 laser having wavelength $\lambda_d \approx 10.6$ μm ($\nu_d = 1.8 \times 10^{14}$ s^{-1}). For such driving field the gain per unit length is estimated as

$$G_L \approx \frac{\nu_d}{c}\frac{\Omega_d^2}{\omega_{ab}^2} = 221 \text{ cm}^{-1}. \tag{7.192}$$

A similar experiment can be done in Na vapor. By driving Na atoms with CO_2 infrared laser at wavelength 10.6 μm and choosing the proper elliptical polarization of

the driving beam one can achieve generation of yellow light produced by the sodium D-line with wavelength 589 nm in a transition from the 3p to the 3s Na level.

7.9 Further study of the QASER I: Three-level model

Here we consider more realistic 3-level model of the QASER shown in Fig. 7.13. In the model the ground state b is dipole coupled with states a and c. E.g., the ground state can be an s state, while a and c states are p_x and p_y orbitals. The total electric field

$$\mathbf{E} = \mathbf{E}^{\rm drive} + \mathbf{E}^{\rm super} \tag{7.193}$$

is a sum of a low frequency drive $\mathbf{E}^{\rm drive}$ which we assume couples both transitions and a weak high frequency superradiant filed $\mathbf{E}^{\rm super}$ that couples only the $a-b$ transition. For example, this can be the case if $\mathbf{E}^{\rm drive}$ has both x and y components, while $\mathbf{E}^{\rm super}$ is linearly polarized along the x-axis.

For the present model the Schrödinger equation yields the following evolution equations for the probability amplitudes C_m to find atoms at the level $m = a, b, c$ (we put $\omega_b = 0$)

$$\dot{C}_a + i\omega_{ab}C_a = \frac{i}{\hbar}\left[\mathbf{E}^{\rm drive} + \mathbf{E}^{\rm super}\right]\mathbf{d}_{ab}C_b, \tag{7.194}$$

$$\dot{C}_c + i\omega_{cb}C_c = \frac{i}{\hbar}\mathbf{E}^{\rm drive}\mathbf{d}_{cb}C_b, \tag{7.195}$$

$$\dot{C}_b = \frac{i}{\hbar}\left[\mathbf{E}^{\rm drive} + \mathbf{E}^{\rm super}\right]\mathbf{d}_{ba}C_a + \frac{i}{\hbar}\mathbf{E}^{\rm drive}\mathbf{d}_{bc}C_c, \tag{7.196}$$

where $\omega_{ab} = \omega_a - \omega_b$, $\omega_{cb} = \omega_c - \omega_b$ and $\mathbf{d}_{nm}$ are the transition dipole matrix elements.

Introducing Rabi frequencies

$$\mathbf{\Omega}_{cb}^{\rm drive} = \frac{1}{\hbar}\mathbf{E}^{\rm drive}\cdot\mathbf{d}_{cb}, \tag{7.197}$$

$$\mathbf{\Omega}_{ab}^{\text{drive}} = \frac{1}{\hbar}\mathbf{E}^{\text{drive}} \cdot \mathbf{d}_{ab}, \tag{7.198}$$

$$\mathbf{\Omega}^{\text{super}} = \frac{1}{\hbar}\mathbf{E}^{\text{super}} \cdot \mathbf{d}_{ab} \tag{7.199}$$

we obtain

$$\dot{C}_a + i\omega_{ab}C_a = i\left[\Omega_{ab}^{\text{drive}} + \Omega^{\text{super}}\right]C_b, \tag{7.200}$$

$$\dot{C}_c + i\omega_{cb}C_c = i\Omega_{cb}^{\text{drive}}C_b, \tag{7.201}$$

$$\dot{C}_b = i\left[\Omega_{ab}^{\text{drive}*} + \Omega^{\text{super}*}\right]C_a + i\Omega_{cb}^{\text{drive}*}C_c. \tag{7.202}$$

We assume that initially all atoms are in the ground state b. Coherence of the $a-b$ transition is

$$\rho_{ab} = C_a C_b^* \tag{7.203}$$

which yields

$$\rho_{ab}^{\text{super}} = C_a^{\text{super}} C_b^{\text{drive}*} + C_a^{\text{drive}} C_b^{\text{super}*}. \tag{7.204}$$

Eqs. (7.200)-(7.202) give the following equations of atomic evolution under the influence of the driving field

$$\dot{C}_a^{\text{drive}} + i\omega_{ab}C_a^{\text{drive}} = i\Omega_{ab}^{\text{drive}}C_b^{\text{drive}}, \tag{7.205}$$

$$\dot{C}_c^{\text{drive}} + i\omega_{cb}C_c^{\text{drive}} = i\Omega_{cb}^{\text{drive}}C_b^{\text{drive}}, \tag{7.206}$$

$$\dot{C}_b^{\text{drive}} = i\Omega_{ab}^{\text{drive}*}C_a^{\text{drive}} + i\Omega_{cb}^{\text{drive}*}C_c^{\text{drive}}, \tag{7.207}$$

while for the quantities describing high frequency field we find

$$\dot{C}_a^{\text{super}} + i\omega_{ab}C_a^{\text{super}} = i\Omega^{\text{super}}C_b^{\text{drive}} + i\Omega_{ab}^{\text{drive}}C_b^{\text{super}}, \tag{7.208}$$

$$\dot{C}_b^{\text{super}} = i\Omega^{\text{super}*} C_a^{\text{drive}} + i\Omega_{ab}^{\text{drive}*} C_a^{\text{super}}. \tag{7.209}$$

Writing

$$\Omega^{\text{super}} = \Omega_s e^{-i\omega_{ab}t + i\omega_{ab}z/c} + c.c., \tag{7.210}$$

$$\rho_{ab}^{\text{super}} + c.c. = \rho_{ab}^s e^{-i\omega_{ab}t + i\omega_{ab}z/c} + c.c., \tag{7.211}$$

$$C_a^{\text{super}} = C_{1a}^s e^{-i\omega_{ab}t + i\omega_{ab}z/c} + C_{2a}^s e^{i\omega_{ab}t - i\omega_{ab}z/c}, \tag{7.212}$$

$$C_b^{\text{super}} = C_{1b}^s e^{-i\omega_{ab}t + i\omega_{ab}z/c} + C_{2b}^s e^{i\omega_{ab}t - i\omega_{ab}z/c}, \tag{7.213}$$

where Ω_s, ρ_{ab}^s, C_{1a}^s, C_{2a}^s, C_{1b}^s and C_{2b}^s are slowly varying functions as compared to the fast oscillating exponentials, we obtain

$$\rho_{ab}^s = C_{1a}^s C_b^{\text{drive}*} + C_{1b}^s C_a^{\text{drive}*} + C_{2a}^{s*} C_b^{\text{drive}} + C_{2b}^{s*} C_a^{\text{drive}}. \tag{7.214}$$

Eqs. (7.208) and (7.209) yield

$$\dot{C}_{1a}^s = i\Omega_s C_b^{\text{drive}} + i\Omega_{ab}^{\text{drive}} C_{1b}^s, \tag{7.215}$$

$$\dot{C}_{2a}^s + 2i\omega_{ab} C_{2a}^s = i\Omega_s^* C_b^{\text{drive}} + i\Omega_{ab}^{\text{drive}} C_{2b}^s, \tag{7.216}$$

$$\dot{C}_{1b}^s - i\omega_{ab} C_{1b}^s = i\Omega_s C_a^{\text{drive}} + i\Omega_{ab}^{\text{drive}*} C_{1a}^s. \tag{7.217}$$

$$\dot{C}_{2b}^s + i\omega_{ab} C_{2b}^s = i\Omega_s^* C_a^{\text{drive}} + i\Omega_{ab}^{\text{drive}*} C_{2a}^s. \tag{7.218}$$

Eqs. (7.214)-(7.218) have to be supplemented by the Maxwell's equation for the high frequency field envelope Ω_s

$$\left(c\frac{\partial}{\partial z} + \frac{\partial}{\partial t} \right) \Omega_s = i\Omega_a^2 \rho_{ab}^s, \tag{7.219}$$

where Ω_a is the collective atomic frequency.

We assume that driving field is weak and keep only terms of the proper order in $1/\omega_{ab}$. Then Eqs. (7.216)-(7.218) yield

$$C_{2a}^s \approx \frac{C_b^{\rm drive}}{2\omega_{ab}}\Omega_s^* + i\frac{\dot{C}_{2a}^s}{2\omega_{ab}} \approx \frac{C_b^{\rm drive}}{2\omega_{ab}}\Omega_s^* + i\frac{C_b^{\rm drive}}{4\omega_{ab}^2}\dot{\Omega}_s^*, \tag{7.220}$$

$$C_{1b}^s \approx -\frac{\Omega_{ab}^{\rm drive*}}{\omega_{ab}}C_{1a}^s, \tag{7.221}$$

$$C_{2b}^s \approx \frac{\Omega_{ab}^{\rm drive*}}{\omega_{ab}}C_{2a}^s \approx \frac{\Omega_{ab}^{\rm drive*}}{2\omega_{ab}^2}C_b^{\rm drive}\Omega_s^*. \tag{7.222}$$

Taking this into account one can rewrite Eq. (7.214) as

$$\rho_{ab}^s = C_{1a}^s\left(C_b^{\rm drive*} - \frac{\Omega_{ab}^{\rm drive*}}{\omega_{ab}}C_a^{\rm drive*}\right) + \frac{|C_b^{\rm drive}|^2}{2\omega_{ab}}\Omega_s - i\frac{|C_b^{\rm drive}|^2}{4\omega_{ab}^2}\dot{\Omega}_s. \tag{7.223}$$

In this equation one should take $|C_b^{\rm drive}|^2 \approx 1$. Thus, the two last terms in Eq. (7.223) do not produce modulation and, hence, they can be omitted. Taking time derivative of both sides of Eq. (7.219), using Eqs. (7.215), (7.223) and (7.205)-(7.207) one can reduce evolution equation for the high frequency field envelope Ω_s to

$$\left(\frac{\partial}{\partial t} + 2i\frac{|\Omega_{ab}^{\rm drive}|^2}{\omega_{ab}} + i\frac{|\Omega_{cb}^{\rm drive}|^2}{\omega_{cb}} + 2\frac{\Omega_{ab}^{\rm drive*}\dot{\Omega}_{ab}^{\rm drive*}}{\omega_{ab}^2}\right)\left(c\frac{\partial}{\partial z} + \frac{\partial}{\partial t}\right)\Omega_s$$

$$+\Omega_a^2\left(1 - \frac{|\Omega_{ab}^{\rm drive}|^2}{\omega_{ab}^2} - \frac{|\Omega_{cb}^{\rm drive}|^2}{\omega_{cb}^2} - \frac{\Omega_{ab}^{\rm drive*}\Omega_{ab}^{\rm drive*}}{\omega_{ab}^2}\right)\Omega_s = 0. \tag{7.224}$$

The unwanted AC Stark shift is compensated if we choose

$$2\frac{|\Omega_{ab}^{\rm drive}|^2}{\omega_{ab}} + \frac{|\Omega_{cb}^{\rm drive}|^2}{\omega_{cb}} = \text{const}. \tag{7.225}$$

Let us assume that $\Omega_{ab}^{\text{drive}}$ is real and given by

$$\Omega_{ab}^{\text{drive}} = \Omega_d \cos(\nu_d t - k_d z). \tag{7.226}$$

Then if $\omega_{ab} = \omega_{cb}$ the time dependence of the AC Stark shift is compensated provided

$$\Omega_{cb}^{\text{drive}} = \sqrt{2}\Omega_d \sin(\nu_d t - k_d z). \tag{7.227}$$

For such parameters Eq. (7.224) becomes

$$\left(\frac{\partial}{\partial t} + i\frac{2\Omega_d^2}{\omega_{ab}} - \frac{\nu_d \Omega_d^2}{\omega_{ab}^2}\sin(2\nu_d t - 2k_d z)\right)\left(c\frac{\partial}{\partial z} + \frac{\partial}{\partial t}\right)\Omega_s + \Omega_a^2\left(1 - \frac{2\Omega_d^2}{\omega_{ab}^2}\right)\Omega_s = 0 \tag{7.228}$$

which yields exponentially growing solution if $\nu_d \geq \Omega_a$.

Our findings show that it is possible to compensate the time dependence of the AC Stark shift by the proper choice of the driving field polarization. At the same time, the transition strength is still modulated by the driving field which leads to the gain at high frequency. The result remains valid for realistic atoms with many levels.

7.10 Further study of the QASER II: 3-photon resonant drive field

QASER happens because of the difference combination parametric resonance between collective oscillations of the coupled light-atom system and the external driving field. When the atom is driven by a far-detuned field, compensation of the dynamic Stark shift is required to see the QASER effect. Then we ask the question. Is there a simple way that we can prove the QASER mechanism without compensation of the dynamic Stark shift? The answer is YES. A two-level atom driven by a resonant/near-resonant drive field has very little dynamic Stark shift.

This can be simply understood by writing the Hamiltonian of this system in the interaction picture

$$\hat{H} = \begin{pmatrix} 0 & \Omega(t)e^{-i\nu_d t} \\ \Omega(t)e^{i\nu_d t} & \Delta \end{pmatrix}, \tag{7.229}$$

where $\Delta = \omega_{ab} - \nu_d$ is the detuning between the frequencies of the drive field and the atomic transition and $\Omega(t) = \Omega_0 \cos(\nu_d t)$. Because $\Delta, \Omega_0 \ll \omega_{ab}$ in this case, RWA is a good approximation. Eq. (7.229) becomes

$$\hat{H} = \begin{pmatrix} 0 & \Omega_0/2 \\ \Omega_0/2 & \Delta \end{pmatrix}. \tag{7.230}$$

The energy shift of the two levels is $\lambda_{1,2} = \left(\Delta \pm \sqrt{\Delta^2 + \Omega_0^2}\right)/2$, which is time-independent. To take the advantage of this result, we study the possibility of the generation of QASER mechanism by using a three-photon resonant drive field.

A three-photon resonant field ($\Omega_d \cos(\nu_d t)$, $\nu_d = \omega_{ab}/3$) can drive a two-level atom as the same as a resonant drive field with the effective Rabi frequency $\Omega_p = \Omega_d^3/2\nu_d^2$. It can induce large dipole at the field propagation direction, which will create 3-photon superradiance at the same direction. To see the possible QASER generation, we should eliminate this effect. One way to achieve this is that the drive laser propagates into the pencil-like medium (in the $\hat{z}$-axis) at an angle θ, which indicates that the drive beam propagates at the direction $\hat{z}\cos\theta + \hat{x}\sin\theta$. For example, if the drive beam is perpendicular to the sample length ($\theta = \pi/2$), the effect induced by the 3-photon superradiance generation in $\hat{x}$ direction can be neglected. In the following, we will study the possibility of generations of the forward emission field and backward emission field at the atomic transition frequency by driving the system with a 3-photon resonant field, under the assumption that 3-photon superradiance

emission is neglected.

The evolution equations for the atomic density matrix are given by

$$\frac{\partial}{\partial t}\rho_{ab}^{\text{total}} = -i\omega_{ab}\rho_{ab}^{\text{total}} + i\Omega^{\text{total}}(1-2\rho_{aa}^{\text{total}}), \tag{7.231}$$

$$\frac{\partial}{\partial t}\rho_{aa}^{\text{total}} = i\Omega^{\text{total}}\rho_{ba}^{\text{total}} - i\Omega^{\text{total}*}\rho_{ab}^{\text{total}}, \tag{7.232}$$

The total field, total coherence and total population can be written as

$$\Omega^{\text{total}} = \Omega_p e^{-i\omega_{ab}(t-z\cos\theta/c)} + \Omega_f e^{-i\omega_{ab}(t-z/c)} + \Omega_b e^{-i\omega_{ab}(t+z/c)} + c.c., \tag{7.233}$$

$$\rho_{ab}^{\text{total}} = \rho_{ab}^{p} e^{-i\omega_{ab}(t-z\cos\theta/c)} + \rho_{ab}^{f} e^{-i\omega_{ab}(t-z/c)} + \rho_{ab}^{b} e^{-i\omega_{ab}(t+z/c)}, \tag{7.234}$$

$$\begin{aligned}\rho_{aa}^{\text{total}} &= \rho_{aa} + \left(\rho_{aa}^{fp} e^{i\omega_{ab}z/c - i\omega_{ab}\cos\theta z/c} + c.c.\right) \\ &+ \left(\rho_{aa}^{bp} e^{-i\omega_{ab}z/c - i\omega_{ab}\cos\theta z/c} + c.c.\right) + \left(\rho_{aa}^{bf} e^{-2i\omega_{ab}z/c} + c.c.\right),\end{aligned} \tag{7.235}$$

where Ω_f (Ω_b) is the Rabi frequency for the forward-generated (backward-generated) emission field. Plug Eqs. (7.233)-(7.235) into Eqs. (7.231) and (7.232), we obtain

$$\dot{\rho}_{ab}^{p} = i\Omega_p(1-2\rho_{aa}) - 2i\Omega_f\rho_{aa}^{fp*} - 2i\Omega_b\rho_{aa}^{bp*}, \tag{7.236}$$

$$\dot{\rho}_{ab}^{f} = i\Omega_f(1-2\rho_{aa}) - 2i\Omega_p\rho_{aa}^{fp} - 2i\Omega_b\rho_{aa}^{bf*}, \tag{7.237}$$

$$\dot{\rho}_{ab}^{b} = i\Omega_b(1-2\rho_{aa}) - 2i\Omega_p\rho_{aa}^{bp} - 2i\Omega_f\rho_{aa}^{bf}, \tag{7.238}$$

$$\dot{\rho}_{aa} = i\Omega_p\rho_{ba}^{p} + i\Omega_f\rho_{ba}^{f} + i\Omega_b\rho_{ba}^{b} - i\Omega_p^*\rho_{ab}^{p} - i\Omega_f^*\rho_{ab}^{f} - i\Omega_b^*\rho_{ab}^{b}, \tag{7.239}$$

$$\dot{\rho}_{aa}^{fp} = i\Omega_f\rho_{ba}^{p} - i\Omega_p^*\rho_{ab}^{f}, \tag{7.240}$$

$$\dot{\rho}_{aa}^{bp} = i\Omega_b\rho_{ba}^{p} - i\Omega_p^*\rho_{ab}^{b}, \tag{7.241}$$

$$\dot{\rho}_{aa}^{bf} = i\Omega_b \rho_{ba}^f - i\Omega_f^* \rho_{ab}^b. \tag{7.242}$$

These equations are supplemented by the Maxwell's equations for the forward-propagation field and the backward-propagation field

$$\left(\frac{\partial}{\partial t} + c\frac{\partial}{\partial z}\right)\Omega_f = i\Omega_a^2 \rho_{ab}^f. \tag{7.243}$$

$$\left(\frac{\partial}{\partial t} - c\frac{\partial}{\partial z}\right)\Omega_b = i\Omega_a^2 \rho_{ab}^b. \tag{7.244}$$

Eqs. (7.236)-(7.244) can be studied numerically.

We first start from the question: "Is it possible to see gain due to QASER-mechanism from a 3-photon resonant drive pulse"? We want that there is no population inversion in the medium distinguish QASER from lasing/superfluorescence. Under this condition, we find that there is no gain from various numerical simulations. The reason is the following.

We assume that $\Omega_p \gg \Omega_f, \Omega_b$, and then Eqs. (7.236) and (7.239) become

$$\dot{\rho}_{ab}^p = i\Omega_p(1 - 2\rho_{aa}), \tag{7.245}$$

$$\dot{\rho}_{aa} = i\Omega_p \rho_{ba}^p - i\Omega_p^* \rho_{ab}^p, \tag{7.246}$$

If Ω_p is a real constant number, the solutions for these two equations are

$$\rho_{aa} = \frac{1}{2}\left[1 - \cos\left(2\Omega_p t\right)\right], \tag{7.247}$$

$$\rho_{ab} = \frac{i}{2}\sin\left(2\Omega_p t\right). \tag{7.248}$$

We see that the population ρ_{aa} is oscillating between 0 and 1. Because we require no periodic population inversion in the system, we have to choose the drive field pulse

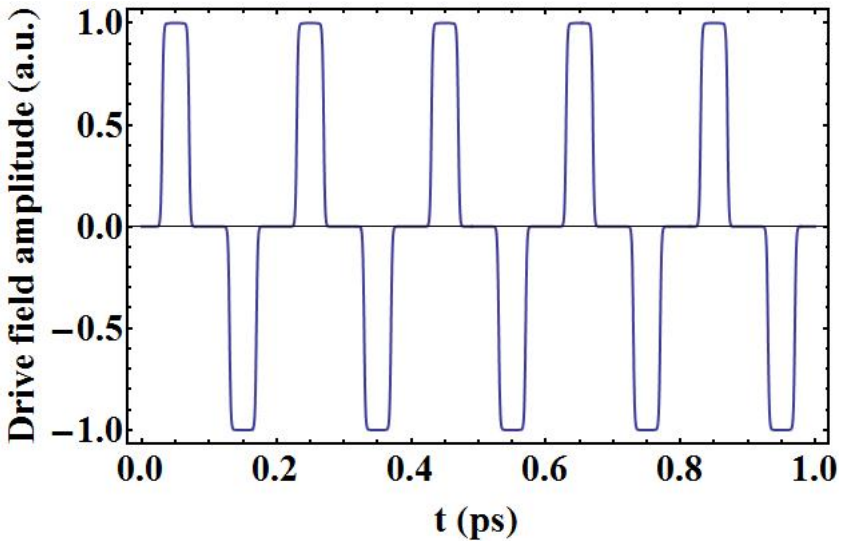

Figure 7.14: The pulse shape of the drive pulse train.

width $< \pi/4\Omega_p$. Under this condition, there is no population modulation with such short pulse duration, which is the key factor for the QASER generation. Therefore, it is not possible to make QASER with a single 3-photon resonant drive pulse with no population inversion. However we find that it is possible to make QASER-like emission with 3-photon resonant drive pulse train.

The idea is that we send the 3-photon resonant drive pulse train with a correct phase modulations so that we can "turn on" the population ρ_{aa} and "turn off" it alternatively. For example, each drive pulse has the same pulse strength Ω_p^0, a small pulse duration $\tau < \pi/4\Omega_p^0$ (so that $\rho_{aa} < 1/2$), and a delay between consecutive pulses T. Each pulse has a phase as 0, $\pi - \omega_{ab}T$, $2\pi - 2\omega_{ab}T$, $3\pi - 3\omega_{ab}T$, ... Therefore, the slowly varying envelope Ω_p for each pulse is $+\Omega_p^0$, $-\Omega_p^0$, $+\Omega_p^0$, $-\Omega_p^0$, ... (see Fig. 7.14) and the population ρ_{aa} is $\frac{1}{2}\left[1 - \cos\left(2\Omega_p^0\tau\right)\right]$, 0, $\frac{1}{2}\left[1 - \cos\left(2\Omega_p^0\tau\right)\right]$, 0, ... accordingly. Therefore, we achieve population modulation with this 3-photon resonant drive pulse train and there is no population inversion. We will do the

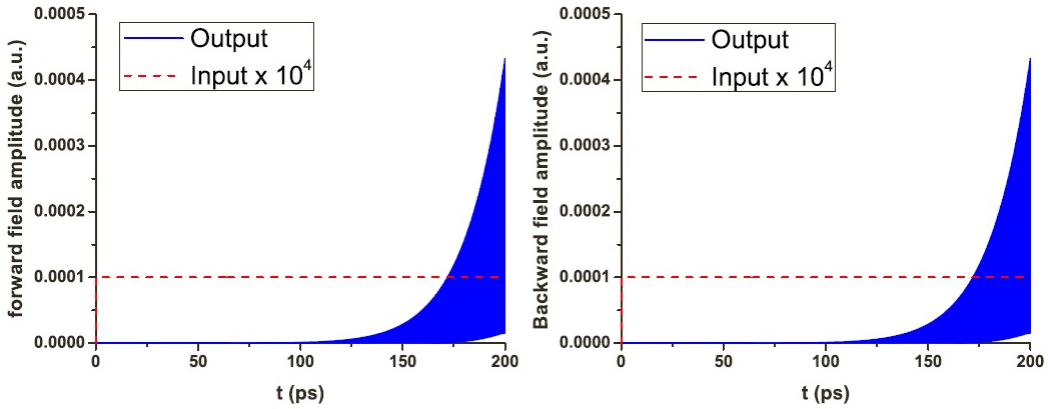

Figure 7.15: Numerical simulation results: forward (Left, Ω_f) and backward (Right, Ω_b) emissions.

numerical simulation to verify the QASER generation.

The simulation is done with the following parameters. The drive field is chosen to have the pulse shape as shown in Fig. 7.14 with $\Omega_p^0 = 10^{13}$ rad/s, $\tau = 40$ fs, $T = 100$ ps (so the maximum ρ_{aa} is ~ 0.15). We turn on the seeds for the forward field and backward field continuously and let them propagate through the medium with length 1 cm in $\hat{z}$-direction. As a result, we see gain in both the forward direction and the backward direction in Fig. 7.15. The gain is due to the difference parametric resonance induced by the population modulation. We conclude that our method here can propose a simple proof-in-principle demonstration of the QASER operation without the compensation of the dynamic Stark shift.

7.11 A pedagogical way to understand QASER and future developments

The QASER is achieved by utilizing the collective superradiant emission. Difference parametric resonance between collective oscillations of the coupled light-atom system and the external driving field yields light amplifications at high frequencies. For a system with N two-level atoms interacting collectively with field, the system

has two normal modes consisting of coherent superposition of the atomic and photonic excitations [159, 160]. Here, we present an intuitive way to show the frequency difference between the two normal modes and understand the QASER gains in those two modes.

We recall that we have a medium composed of two-level atoms with the excited state a and ground state b. The system is modulated by a drive field. The main equations for the superradiant field and the atomic coherence are given from the Maxwell-Schrödinger equations

$$\left(c^2\frac{\partial^2}{\partial z^2}-\frac{\partial^2}{\partial t^2}\right)\Omega^{\text{super}}=\frac{2\Omega_a^2}{\omega_{ab}}\frac{\partial^2}{\partial t^2}(\rho_{ab}+c.c.), \tag{7.249}$$

$$\dot{\rho}_{ab}=-i\omega_{ab}\rho_{ab}+i\left(\Omega^{\text{super}}+\Omega^{\text{drive}}\right)(\rho_{bb}-\rho_{aa}). \tag{7.250}$$

By introducing the slowly-varying amplitudes for the superradiant field and the polarization as $\Omega^{\text{super}}=\Omega_s e^{-i\omega_{ab}(t-z/c)}+c.c.$ and $\rho_{ab}=\tilde{\rho}_{ab}e^{-i\omega_{ab}(t-z/c)}$, we have two coupled equations of the field and the polarization

$$\left(\frac{\partial}{\partial t}+c\frac{\partial}{\partial z}\right)\Omega_s=i\Omega_a^2\tilde{\rho}_{ab}, \tag{7.251}$$

$$\frac{\partial}{\partial t}\tilde{\rho}_{ab}=i\Omega_s(1-2\rho_{aa}). \tag{7.252}$$

Here we neglect the higher harmonics terms. The population ρ_{aa} is modulated by the drive field. To obtain simple insight on the gain expression, we assume a uniform medium and the drive field has $k_d=0$. Therefore, we can neglect the z-dependence. For a quick glance at our results, we can first rewrite Eqs. (7.251) and (7.252) to the following two equations

$$\frac{\partial^2}{\partial t^2}\Omega_s=-\Omega_a^2(1-2\rho_{aa})\Omega_s, \tag{7.253}$$

$$\frac{\partial^2}{\partial t^2}\tilde{\rho}_{ab} = -\Omega_a^2(1-2\rho_{aa})\tilde{\rho}_{ab}, \tag{7.254}$$

Here we neglect the term $-2i\Omega_s\dot{\rho}_{aa}$ for weak signal field. We notice the superradiant field Ω_s has the same equation expression as the coherence $\tilde{\rho}_{ab}$, which indicates there are the same gains for the field and for the atomic coherence.

Next, we will show how to see the frequency difference in the system and understand the qaser gains in a more detailed way. We rewrite two equations [(7.251) & (7.252)] as

$$\frac{\partial}{\partial t}\Omega_s = i\Omega_a(\Omega_a\tilde{\rho}_{ab}), \tag{7.255}$$

$$\frac{\partial}{\partial t}(\Omega_a\tilde{\rho}_{ab}) = i\Omega_a\Omega_s(1-2\rho_{aa}). \tag{7.256}$$

We define

$$P_1 \equiv \frac{1}{\sqrt{2}}(\Omega_s + \Omega_a\tilde{\rho}_{ab}), \tag{7.257}$$

$$P_2 \equiv \frac{1}{\sqrt{2}}(\Omega_s - \Omega_a\tilde{\rho}_{ab}). \tag{7.258}$$

Here $P_{1,2}$ is the coherent superposition of the field and the atomic coherence. Therefore, we obtain the following equations

$$\frac{\partial}{\partial t}P_1 = i\Omega_a P_1 - i\Omega_a(P_1+P_2)\rho_{aa}, \tag{7.259}$$

$$\frac{\partial}{\partial t}P_2 = -i\Omega_a P_2 + i\Omega_a(P_1+P_2)\rho_{aa}. \tag{7.260}$$

The atomic system is modulated by a drive field. If the drive field is near resonant with the atomic transition (with Rabi frequency Ω_d and detuning Δ), the population in the excited state is modulated by the effective Rabi frequency and has the expression $\rho_{aa} = \eta(1-\cos 2\mu t)$, where $\eta \ll 1$ is the modulation amplitude and μ is

the modulation frequency. This yield

$$\frac{\partial}{\partial t}P_1 = i\Omega_a(1-\eta)P_1 + i\Omega_a P_1\eta\cos 2\mu t - i\Omega_a P_2\eta(1-\cos 2\mu t), \tag{7.261}$$

$$\frac{\partial}{\partial t}P_2 = -i\Omega_a(1-\eta)P_2 - i\Omega_a P_2\eta\cos 2\mu t + i\Omega_a P_1\eta(1-\cos 2\mu t). \tag{7.262}$$

These two normal modes (P_1, P_2) have the eigen-frequencies $\pm\Omega_a$ when there is no modulation in the system ($\eta = 0$). Under small modulation amplitude, we can define the slowly-varying part as $P_1 \equiv \tilde{P}_1\mathrm{Exp}[i\Omega_a(1-\eta)t]$ and $P_2 \equiv \tilde{P}_2\mathrm{Exp}[-i\Omega_a(1-\eta)t]$. Under the difference parametric resonance $\mu = \Omega_a(1-\eta)$, we have

$$\frac{\partial}{\partial t}\tilde{P}_1 = i\Omega_a\tilde{P}_1\eta\left[\frac{1}{2}(e^{i2\mu t}+e^{-i2\mu t})\right]$$

$$-i\Omega_a\tilde{P}_2 e^{-i2\Omega_a(1-\eta)t}\eta\left(1-\left[\frac{1}{2}(e^{i2\mu t}+e^{-i2\mu t})\right]\right), \tag{7.263}$$

$$\frac{\partial}{\partial t}\tilde{P}_2 = -i\Omega_a\tilde{P}_2\eta\left[\frac{1}{2}(e^{i2\mu t}+e^{-i2\mu t})\right]$$

$$+i\Omega_a\tilde{P}_1 e^{i2\Omega_a(1-\eta)t}\eta\left(1-\left[\frac{1}{2}(e^{i2\mu t}+e^{-i2\mu t})\right]\right), \tag{7.264}$$

which yields the following coupled equations under the secular approximation

$$\frac{\partial}{\partial t}\tilde{P}_1 \approx \frac{i}{2}\eta\Omega_a\tilde{P}_2, \tag{7.265}$$

$$\frac{\partial}{\partial t}\tilde{P}_2 \approx -\frac{i}{2}\eta\Omega_a\tilde{P}_1. \tag{7.266}$$

Eqs. (7.265) and (7.266) result in a gain as $\eta\Omega_a/2$.

Although our study is under various approximations, the result indicates that the two normal modes of the coupled field-atom system gets equally excited in the qaser mechanism in a tuitive way. The analysis here is considered for the case where

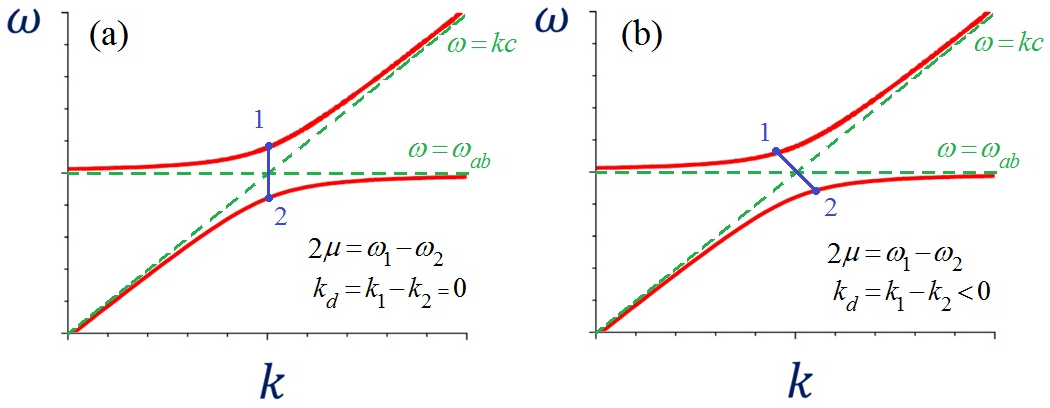

Figure 7.16: The dispersion curve of a coupled atom-light system driven by a laser field with $k_d = 0$ (a) and $k_d = -\nu_d/c$ (b).

the system is driven by a far detuned drive laser ($\nu_d \ll \omega_{ab}$). This gain analysis is valid if the dynamic Stark shift is compensated. In this case, $\mu = \nu_d$ is the drive field frequency and $\eta \approx \Omega_d^2/\omega_{ab}^2$ (see Section 7.3). In addition, this analysis is also useful for the near-resonant drive case [161] but $\mu = \sqrt{\Omega_d^2 + \Delta^2}$ (the effective Rabi frequency) and $\eta = \frac{1}{2}\left(\frac{\Omega_d}{\mu}\right)^2$ instead.

This result can be confirmed by the simulation result (see Fig. 7.5(c)). Two major peaks due to the gains of the two modes have the similar amplitude ($\propto \exp(\text{Gain})$). There are also two small bumps at the sides, which is induced by higher-order frequency components, which we do not include in our analysis. The cause of the slight difference between two major peaks could be due to the approximations that we made in the analytical analysis.

The physics behind the mathematical analysis can be understood by the dispersion curves (red solid curves) of a coupled atom-light system as shown in Fig. 7.16. If the system is driven by a laser field with $k_d = 0$ (Fig. 7.16(a)), two modes $1, 2$, which consist of the atomic and photonic excitations, are excited by the drive field modulation. The two modes have the frequency difference dependent on the collective

Rabi frequency Ω_a. The excitation only happens when the drive field modulation amplitude $\mu \approx \Omega_a$. This is consistent with the previous analysis. In Fig. 7.16(b), we also show that two normal modes can be excited by a counter-propagating drive field.

At last, we will write the Hamiltonian for this system. We consider a medium consisting of two-level atoms. The interaction between light and atoms is governed by the Hamiltonian

$$\hat{V} = N \int \frac{dz}{L} \left(\hbar g \sum_k \hat{a}_k(t) e^{ikz} \hat{\sigma}_+(z,t) + H.c. \right), \tag{7.267}$$

where $\hat{a}_k(t)$ and $\sigma_-(z,t)$ are slowly-varying amplitude and we assume that $\nu = \omega_{ab}$. The atom-field coupling constant $g = \wp\sqrt{\nu/2\hbar\epsilon_0 V}$. We assume our medium is uniform and disregard z-dependence for the simplicity. Therefore, the Hamiltonian reads

$$\hat{V} = \hbar g N \hat{a}(t) \hat{\sigma}_+(t) + H.c., \tag{7.268}$$

In the Heisenberg picture, we obtain

$$\frac{\partial}{\partial t}\hat{a} = \frac{i}{\hbar}[\hat{V}, \hat{a}] = -igN\hat{\sigma}_-, \tag{7.269}$$

$$\frac{\partial}{\partial t}\hat{\sigma}_- = \frac{i}{\hbar}[\hat{V}, \hat{\sigma}_-] = igN\hat{a}\hat{\sigma}_z, \tag{7.270}$$

We treat $\hat{\sigma}_z$ as a c-number so $\sigma_z = \rho_{aa} - \rho_{bb} = 2\rho_{aa} - 1$. We can define two new operators

$$\hat{P}_1 = \frac{1}{\sqrt{2}}(\hat{a} + \hat{\sigma}_-), \tag{7.271}$$

$$\hat{P}_2 = \frac{1}{\sqrt{2}}(\hat{a} - \hat{\sigma}_-), \tag{7.272}$$

Using these two new operators, we find

$$\frac{\partial}{\partial t}(\hat{P}_1 + \hat{P}_2) = -igN(\hat{P}_1 - \hat{P}_2), \tag{7.273}$$

$$\frac{\partial}{\partial t}(\hat{P}_1 - \hat{P}_2) = -igN(\hat{P}_1 + \hat{P}_2)(1 - 2\rho_{aa}), \tag{7.274}$$

which yields

$$\frac{\partial}{\partial t}\hat{P}_1 = -igN\hat{P}_1 + igN\rho_{aa}(\hat{P}_1 + \hat{P}_2), \tag{7.275}$$

$$\frac{\partial}{\partial t}\hat{P}_2 = igN\hat{P}_2 - igN\rho_{aa}(\hat{P}_1 + \hat{P}_2). \tag{7.276}$$

If the modulation amplitude of ρ_{aa} is small, we can treat it as a constant. Then we have the commutation relation

$$[\hat{P}_1, \hat{P}_1^\dagger] = [\hat{P}_2, \hat{P}_2^\dagger] = \frac{1}{2}(1 - \sigma_z) = 1 - \rho_{aa}. \tag{7.277}$$

Therefore, we find a non-Hermite Hamiltonian which can lead to Eqs. (7.275) and (7.276)

$$\hat{H} = \hbar gN\hat{P}_1^\dagger\hat{P}_1 - \hbar gN\hat{P}_2^\dagger\hat{P}_2 - \hbar gN\rho_{aa}(\hat{P}_1^\dagger\hat{P}_2 - \hat{P}_2^\dagger\hat{P}_1). \tag{7.278}$$

In summary, we find the two normal modes (P_1 and P_2) in the system , which consist of coherent superposition of the atomic and photonic excitations, have the frequency difference as $2\Omega_a(1-\eta)$. If it has the difference parametric resonance $\mu = \Omega_a(1-\eta)$, they have the same gain as $\eta\Omega_a/2$. Furthermore, finding the effective Hamiltonian (7.278) for the two normal mode operators quantum mechanically is a starting point towards understanding the fundamental mechanism of the QASER. The non-Hermite nature of this Hamiltonian is one of the future research directions in the QASER project.

7.12 Conclusion

We have found a new way to obtain quantum gain with no population in the excited state by means of Quantum Amplification by Superradiant Emission of Radiation (QASER). In our approach light amplification occurs due to the difference combination parametric resonance between collective oscillations of the coupled light-atom system and the external (e.g. Infrared) driving field which can yield exponential grow of the seed pulse at high (e.g. XUV) atomic frequency. To achieve gain one must suppress the unwanted time-dependent Stark shift of the atomic transition energy which can be realized in various schemes.

The QASER mechanism is different from the LASER (which requires nonzero excited state population) and the well-known multiphoton resonant excitation which is a single atom phenomenon rather than a collective effect. In particular, excited state population grows with time differently for the multiphoton excitation and the QASER as indicated in Eqs. (7.16) and (7.17). We also show that the QASER is analogous to excitation of a system of two weakly coupled oscillators which displays the difference combination resonance when the low modulation frequency matches the frequency difference between two close normal modes of the coupled system.

We carried out an experiment which demonstrates the QASER amplification mechanism in an electronic circuit. To the best of our knowledge, the present experiment is the first experimental demonstration of the difference combination resonance which yields excitation of high frequency oscillations by a low frequency drive.

The QASER is different from the optical parametric oscillator (OPO) in several ways. OPO requires phase matching, but QASER does not. QASER emission is backward relative to the drive, while in the OPO it is forward. The AC Stark shift compensation is key to the QASER operation, but not to the OPO. The QASER

can operate in a gas but the OPO requires a non-centrosymmetric nonlinear crystal. Finally, the OPO is a sum frequency device, namely, frequencies ω_1 and ω_2 produced by the OPO from the driving field ν_d obey the relation $\nu_d = \omega_1 + \omega_2$. That is OPO generates lower frequencies than ν_d. The QASER is the difference frequency device for which $\nu_d = \omega_2 - \omega_1$. That is QASER can generate higher frequencies by means of superradiant resonance.

Such a superradiant resonance holds promise for development of a new class of radiation sources which generate high frequency (e.g. XUV or X-ray) coherent light utilizing a low frequency (e.g. Infrared) coherent source. However, as is always the case in research, the present scheme surely involves many challenges, open questions, and unknowns. For example, what about all the other level pairs? Will the device tend to oscillate on all of these pairs? We think not. One can select a narrow window of atomic frequencies, e.g., by sending an XUV seed pulse or compensate the AC Stark shift only for a particular atomic transition. This will be discussed further in forth-coming papers.

Will ionization of the excited states by the intense driving field be a killer? No. One can choose the driving field to be weak enough that we will not have excessive multi-photon ionization. This is possible since the present collective resonant excitation is a much stronger effect than the usual multi-photon mechanism. Can we operate more efficiently at high pressures and/or with shorter wavelengths of the driving field, etc.? This is an open question. There are surely many such open questions that need to be investigated. We have discussed possible experiments which could demonstrate QASER operation in a noble gas (e.g. He) or gas of alkali atoms (e.g. Rb or Na) using available laser technology.

8. CONCLUSION

The presence of quantum coherence yields interesting effects. Large coherence triggers collective phenomena in the atomic ensembles including superradiant emission (superfluorescence/superradiance), which offers various directions for new exploration, such as transient lasing without inversion, coherence-brightened sky laser, and quantum amplification by superradiant emission of radiation (QASER), and many others [162, 163, 164, 165].

We first showed an interesting coherence effect in three-level (cascade scheme) atoms. The quantum coherence brings asymmetric properties of the superfluorescence emission in the forward and backward directions. Gain without population inversion and gain suppression in the inverted medium are found in the forward radiations. The quantum coherence effects are limitted by the decoherence mechanisms such as collisions. However it can manifest in a time scale shorter than the decoherence time. For example, we observed a superradiant decay of excited-state helium atoms in the helium plasma. This indicates the presence of superradiant coherent emission in such system.

Inspired by these results, we further studied possible lasing without inversion (LWI) in the extreme-ultraviolet/x-ray regime. With the advent of tunable-ultrashort-high-power laser pulses, such LWI occurs in a time scale much shorter than spontaneous decay and fast decoherence times. This transient regime allows us to take advantage of coherence effects to investigate the dynamics far from steady state. Utilizing coherence effects, sideband transient LWI can be achieved at multiple frequencies. Higher-frequency laser field was studied in S-P-P and S-P-D schemes in helium and helium-like ions.

Quantum coherence was also found to be present in our sky laser experiments. The atomic coherence enriches the optical emission physics. We investigated the forward and backward directed emission of oxygen when pumped by nanosecond UV laser pulses. Our results suggest that the emission process exhibits nonadiabatic atomic coherence, which is similar in nature to Dicke superradiance. A detailed theoretical study was provided. We found that the spiky emission in the experiment is due to quantum coherence via cooperative effects between atoms, which leads to strong-oscillatory superfluorescence. Understanding these coherence-brightened processes in air can improve atmospheric remote sensing. To serve this purpose, we also studied the conditions for a coherent Raman scattering to enable the generation of phase-matched, highly directional, nearly-backward-propagating light beams, where the sky laser is used as a backward-propagating coherent light source. This coherent Raman Umklapp process is well suited for standoff detection of trace gases in the atmosphere with a sensitivity at the level of 1 ppm using their rotational and vibrational spectroscopic signals. An alternative coherent backward signal generation method was also discussed through a Raman-type four-wave-mixing process using forward propagating fields only. Phase matching is the key to make it valid, which is achieved through a plasma modulation of the refractive index. All these works show interesting quantum coherent effects in the atmospheric applications.

At last, we unveiled the QASER, a new scheme for obtaining quantum gain without having initial population of excited-state atoms [166]. This new kind of quantum amplifier is based on collective superradiant emission. Light amplification occurs because of the difference combination parametric resonance between collective oscillations of the coupled light-atom system and the external (e.g., infrared) driving field. The amplification only happens when the seed field and the drive field are counter-propagating. Exponential growth of the seed pulses at high (e.g., XUV)

frequencies can be achieved if the unwanted time-dependent Stark shift of the atomic transition energy is suppressed. The physics inside the QASER mechanism can be seen in an analogous excitation of a system of two weakly coupled oscillators, which displays the difference combination resonance when the low modulation frequency matches the frequency difference between two close normal modes of the coupled system.

Our present works include the subjects from lasing without inversion to sky laser and the QASER. We hope they can stimulate the interest in the effects of quantum coherence and superradiant emission in the optical society.

REFERENCES

[1] M. O. Scully and M. S. Zubairy, *Quantum Optics* (Cambridge University Press, Cambridge, UK, 1997).

[2] R. W. Boyd, *Nonlinera Optics*, (Academic Press, San Diego, CA, 2003).

[3] M. O. Scully, and M. S. Zubairy, Phys. Rev. A **35**, 752 (1987).

[4] M. O. Scully, Phys. Rev. Lett. **55**, 2802 (1985).

[5] M. Ohtsu, and K. Y. Liou, Appl. Phys. Lett. **52**, 10 (1988).

[6] M. O. Scully and A. A. Svidzinsky, Science **325**, 1510 (2009).

[7] R. H. Dicke, Phys. Rev. **93**, 99 (1954).

[8] N. Skribanowitz, I. P. Herman, J. C. MacGillivray, and M. S. Feld, Phys. Rev. Lett. **30**, 309 (1973).

[9] J. C. MacGillivray and M. S. Feld, Phys. Rev. A **14**, 1169 (1976).

[10] J. C. MacGillivray and M. S. Feld, Phys. Rev. A **23**, 1334 (1981).

[11] A. A. Svidzinsky, J. T. Chang and M. O. Scully, Phys. Rev. Lett. **100**, 160504 (2008).

[12] M. O. Scully, Phys. Rev. Lett. **102**, 143601 (2009).

[13] R. Friedberg and J. T. Manassah, Phys. Lett. A **374,** 1648 (2010).

[14] A. A. Svidzinsky, J. T. Chang and M. O. Scully, Phys. Rev. A **81**, 053821 (2010).

[15] A. A. Svidzinsky, Phys. Rev. A **85**, 013821 (2012).

[16] R. Röhlsberger, K. Schlage, B. Sahoo, S. Couet and R. Rüffer, Science **328**, 1248 (2010).

[17] A. Kalachev and S. Kröll, Phys. Rev. A **74**, 023814 (2006).

[18] D. Porras and J. I. Cirac, Phys. Rev. A **78**, 053816 (2008).

[19] R. Bonifaci and L. A. Lugiato, Phys. Rev. A **11**, 1507 (1975)

[20] S. Prasad and R. J. Glauber, Phys. Rev. A **31**, 1583 (1985).

[21] V. A. Malyshev, F. Carreño, M. A. Antón, O. G. Calderón, and F. Domínguez-Adame, J. Opt. B: Quantum Semiclassical Opt. **5**, 313 (2003).

[22] V. Kozlov, O. Kocharovskaya, Y. Rostovtsev, and M. Scully, Phys. Rev. A **60** 1598 (1999).

[23] V. A. Malyshev, I. V. Ryzhov, E. D. Trifonov, and A. I. Zaitsev, Laser Phys. **8** 494 (1998).

[24] A. I. Zaitsev, I. V. Ryzhov, E. D. Trifonov, and V. A. Malyshev, Laser Phys. **9** 876 (1999).

[25] A. A. Bogdanov, A. I. Zaĭtsev, and I. V. Ryzhov, Opt. Spectrosc. **89**, 1012 (2000).

[26] O. A. Kocharovskaya and Ya. I. Khanin, JETP Lett. **48**, 630 (1988).

[27] S. E. Harris, Phys. Rev. Lett. **62**, 1033 (1989).

[28] M. O. Scully, S. -Y. Zhu, and A. Gavrielides, Phys. Rev. Lett. **62**, 2813 (1989).

[29] A. S. Manka, J. P. Dowling, C. M. Bowden, and M. Fleischhauer, Quantum Opt. **6**, 371 (1994).

[30] O. Kocharovskaya, Hyperfine Interact. **107**, 187 (1997).

[31] J. Mompart and R. Corbalán, J. Opt. B: Quantum Semiclassical Opt. **2**, R7 (2000).

[32] M. O. Scully and M. Fleischhauer, Science **263**, 337 (1994).

[33] L. Yuan and A. A. Svidzinsky, Phys. Rev. A **85**, 033836 (2012).

[34] E. S. Fry, X. Li, D. Nikonov, G. G. Padmabandu, M. O. Scully, A. V. Smith, F. K. Tittel, C. Wang, S. R. Wilkinson, and S. -Y. Zhu, Phys. Rev. Lett. **70**, 3235 (1993).

[35] M. Marthaler, Y. Utsumi, D. S. Golubev, A. Shnirman, and G. Schön, Phys. Rev. Lett. **107**, 093901 (2011).

[36] M. F. Pereira, Jr. Phys. Rev. B **78**, 245305 (2008).

[37] A. Imamoglu, J. E. Field, and S. E. Harris, Phys. Rev. Lett. **66**, 1154 (1991).

[38] A. S. Zibrov *et al.*, Phys. Rev. Lett. **75**, 1499 (1995).

[39] G. G. Padmabandu *et al.*, Quantum Opt. **6**, 261 (1994).

[40] H. Xia, A. A. Svidzinsky, L. Yuan, C. Lu, S. Suckewer, and M. O. Scully, Phys. Rev. Lett. **109**, 093604 (2012).

[41] A. A. Svidzinsky, L. Yuan, and M. O. Scully, New J. Phys. **15**, 053044 (2013).

[42] L. Yuan, D. Wang, A. A. Svidzinsky, H. Xia, O. Kocharovskaya, A. Sokolov, G. R. Welch, S. Suckewer, and M. O. Scully, Phys. Rev. A **89**, 013814 (2014).

[43] L. Yuan, D. -W. Wang, C. O'Brien, A. A. Svidzinsky, and M. O. Scully, Phys. Rev. A **90**, 023836 (2014).

[44] R. H. Dicke, "The coherence brightened laser", *Quantum Electronics: Proceedings of the Third International Congress.* Edited by P. Grivet and N. Bloembergen, pp. 35–54. (Dunod Éiteur, Paris, 1964).

[45] A. E. Siegman,*Lasers* (University Science Books, Sausalito, CA 1986).

[46] A. I. Lvovsky, *Omnidirectional superfluorescence transients. Ph.D. Thesis* (Columbia University, New York, 1998).

[47] V. Kocharovsky *et al. Proc. Natl. Acad. Sci. USA* **102**, 7806 (2005).

[48] W. Kaiser and C. G. B. Garrett, Phys. Rev. Lett. **7**, 229 (1961).

[49] S. L. Shapiro, J. A. Giordmaine, and K. W. Wecht, Phys. Rev. Lett. **19**, 1093 (1967).

[50] M. Maier, W. Kaiser, and J. A. Giordmaine, Phys. Rev. **177**, 580 (1969).

[51] D. Heiman, R. W. Hellworth, M. D. Levenson, and G. Martin, Phys. Rev. Lett. **36**, 189 (1976).

[52] M. Aldén, U. Westblom, and J. E. M. Goldsmith, Opt. Lett. **14**, 305 (1989).

[53] U. Westblom, S. Agrup, M. Aldén, H. M. Hertz, and J. E. M. Goldsmith, Appl. Phys. B **50**, 487 (1990).

[54] Y. -L. Huan and R. J. Gordon, J. Chem. Phys. **97**, 6363 (1992).

[55] P. R. Hemmer *et al.*, Proc. Natl. Acad. Sci. USA **108**, 3130 (2011).

[56] Q. Luo, W. Liu, and S. L. Chin, Appl. Phys. B **76**, 337 (2003).

[57] A. Dogariu, J. B. Michael, M. O. Scully, and R. B. Miles, Science **331**, 442 (2011).

[58] A. J. Traverso *et al.*, Proc. Natl. Acad. Sci. USA **109**, 15185 (2012).

[59] L. Yuan, B. H. Hokr, A. J. Traverso, D. V. Voronine, Y. Rostovtsev, A. V. Sokolov, and M. O. Scully, Phys. Rev. A **87**, 023826 (2013).

[60] Y. R. Shen, *The Principles of Nonlinear Optics* (John Wiley & Sons, Inc, Hoboken, NJ 2003).

[61] N. Bloembergen, J. Opt. Soc. Am. **70**, 1429 (1980).

[62] A. M. Zheltikov, M. N. Shneider, and R. B. Miles Appl. Phys. B **83**, 149 (2006).

[63] N. Bloembergen, and A. J. Sievers, Appl. Phys. Lett. **17**, 483 (1970).

[64] C. M. Bowden, and A. M. Zheltikov, J. Opt. Soc. Am. B **19**, 2042 (2002).

[65] Y. V. Rostovtsev, Z. -E. Sariyanni, and M. O. Scully, Phys. Rev. Lett. **97**, 113001 (2006).

[66] A. Zumbusch, G. R. Holtom, and X. S. Xie, Phys. Rev. Lett. **82**, 4142 (1999).

[67] N. W. Ashcroft, and N. D. Mermin, *Solid State Physics* (Harcourt, Orlando, 1976).

[68] T. Ichimura, N. Hayazawa, M. Hashimoto, Y. Inouye, and S. Kawata, Phys. Rev. Lett. **92**, 220801 (2004).

[69] M. Afzelius, C. Brackmann, F. Vestin, and P. Bengtsson, Applied Optics **43**, 6664 (2004).

[70] T. Seeger, J. Kiefer, A. Leipertz, B. D. Patterson, C. J. Kliewer, and T. B. Settersten, Optics Letters **34**, 3755 (2009).

[71] D. Pestov, R. K. Murawski, G. O. Ariunbold, X. Wang, M. Zhi, A. V. Sokolov, V. A. Sautenkov, Y. V. Rostovtsev, A. Dogariu, Y. Huang, and M. O. Scully, Science **316**, 265 (2007).

[72] D. Pestov, X. Wang, G. O. Ariunbold, R. K. Murawski, V. A. Sautenkov, A. Dogariu, A. V. Sokolov, and M. O. Scully, Proc. Natl. Acad. Sci. USA **105**, 422 (2008).

[73] I. V. Fedotov, A. A. Lanin, V. I. Sokolov, A. B. Fedotov, A. S. Akhmanov, V. Ya. Panchenko, and A. M. Zheltikov, Laser Phys. Lett. **7**, 657 (2010).

[74] D. A. Sidorov-Biryukov, K. A. Kudinov, A. A. Podshivalov, and A. M. Zheltikov, Laser Phys. Lett. **7**, 355 (2010).

[75] Y. -J. Song, M. -L. Hu, C. -L. Gu, L. Chai, C. -Y. Wang, and A. M. Zheltikov, Laser Phys. Lett. **7**, 230 (2010).

[76] A. A. Voronin, V. P. Mitrokhin, A. A. Ivanov, A. B. Fedotov, D. A. Sidorov-Biryukov, V. I. Beloglazov, M. V. Alfimov, H. Ludvigsen, and A. M. Zheltikov, Laser Phys. Lett. **7**, 46 (2010).

[77] A. C. Eckbreth, Appl. Phys. Lett. **32**, 421 (1978).

[78] A. Compaan, and S. Chandra, Opt. Lett. **4**, 170 (1979).

[79] L. Yuan, A. A. Lanin, P. K. Jha, A. J. Traverso, D. V. Voronine, K. E. Dorfman, A. B. Fedotov, G. R. Welch, A. V. Sokolov, A. M. Zheltikov, and M. O. Scully, Laser Phys. Lett. **8**, 736 (2011).

[80] L. Yuan, K. E. Dorfman, A. M. Zheltikov, and M. O. Scully, Opt. Lett. **37**, 987 (2012).

[81] M. O. Scully, E. Fry, C. H. R. Ooi and K. Wodkiewicz, Phys. Rev. Lett. **96**, 010501 (2006).

[82] I. E. Mazets and G. Kurizki, J. Phys. B: At. Mol. Opt. Phys. **40,** F105 (2007).

[83] S. Prasad and R. Glauber, Phys. Rev. A **82**, 063805 (2010).

[84] E. M. Kessler, S. Yelin, M. D. Lukin, J. I. Cirac and G. Giedke, Phys. Rev. Lett. **104**, 143601 (2010).

[85] A. A. Svidzinsky, L. Yuan, and M. O. Scully, Phys. Rev. X **3**, 041001 (2013).

[86] J. H. Brownell, X. Lu, and S. R. Hartmann, Phys. Rev. Lett. **75**, 3265 (1995).

[87] W. R. Garrett, Phys. Rev. Lett. **70**, 4059 (1993).

[88] J. T. Manassah and I. Gladkova, Opt. Commun. **179**, 51 (2000).

[89] H. Brownell, B. Gross, X. Lu, S. R. Hartmann, and J. T. Manassah, Laser Phys. **3**, 509 (1993).

[90] D. Felinto, L. H. Acioli, and S. S. Vianna, Opt. Lett. **25**, 917 (2000).

[91] G. O. Ariunbold, M. M. Kash, V. A. Sautenkov, H. Li, Y. V. Rostovtsev, G. R. Welch, and M. O. Scully, Phys. Rev. A **82**, 043421 (2010).

[92] M. Nagasono *et al.,* Phys. Rev. Lett. **107**, 193603 (2011).

[93] S. Suckewer and P. Jaegle, Laser Physics Letters **6**, 411 (2009).

[94] L. V. Keldysh, Sov. Phys. JETP **20**, 1307 (1965).

[95] A. Egbert, D. Simanovskii, B. N. Chichkov and B. Wellegehausen, Phys. Rev. E **57**, 7138 (1998).

[96] Ya. B. Zel'dovich and Yu. P. Raizer, *Physics of Shock Waves and High Temperature Hydrodynamic Phenomena* (Academic Press, New York, 1966).

[97] C. H. Brito Cruz *et al.,* IEEE Journal of Quantum Electronics **24**, 261 (1988).

[98] M. Joffre *et al.*, Optics Letters **13**, 276 (1988).

[99] P. Hamm, Chem. Phys. **200**, 415 (1995).

[100] G. N. Gibson, Phys. Rev. Lett. **89**, 263001 (2002).

[101] D. -w. Wang, A. -j. Li, L. -g. Wang, S. -y. Zhu, and M. S. Zubairy, Phys. Rev. A **80**, 063826 (2009)

[102] Y. V. Radeonychev, V. A. Polovinkin, and O. Kocharovskaya, Phys. Rev. Lett. **105**, 183902 (2010).

[103] A. Picón, L. Roso, J. Mompart, O. Varela, V. Ahufinger, R. Corbalán, and L. Plaja, Phys. Rev. A **81**, 033420 (2010).

[104] J. Zhang, *et. al.*, Phys. Rev. Lett. **74**, 1335 (1995).

[105] X. M. Tong, Z. X. Zhao, and C. D. Lin, Phys. Rev. A **66**, 033402 (2002).

[106] V. S. Popov, Physics-Uspekhi **47**, 855 (2004).

[107] D. Turnbull, S. Li, A. Morozov, and S. Suckewer, Phys. Plasmas **19**, 083109 (2012).

[108] R. Sanchez Gonzalez, R. Srinivasan, R. D. W. Bowersox, and S. W. North, Opt. Lett., **36**, 196 (2011) .

[109] S. Agrup and M. Aldén, *Opt. Commun.* **113**, 315 (1994).

[110] L. Allen and J. H. Eberly, *Optical Resonance and Two Level Atoms* (Dover, New York, 1987).

[111] P. W. Hoff, H. A. Haus, and T. J. Bridges, Phys. Rev. Lett. **25**, 82 (1970).

[112] L. W. Hillman, J. Krasiński, R. W. Boyd, and C. R. Stroud, Jr., Phys. Rev. Lett. **52**, 1605 (1984).

[113] C. Y. Wang, L. Diehl, A. Gordon, C. Jirauschek, F. X. Kärtner, A. Belyanin, D. Bour, S. Corzine, G. Höfler, M. Troccoli, J. Faist, and F. Capasso, Phys. Rev. A **75**, 031802 (2007).

[114] J. J. Maki, M. S. Malcuit, M. G. Raymer, and R. W. Boyd, Phys. Rev. A **40**, 5135 (1989).

[115] R. Friedberg and S. R. Hartmann, Phys. Lett. A **37**, 285 (1971).

[116] R. Friedberg and S. R. Hartmann, Phys. Rev. A **13**, 495 (1976).

[117] D. Polder, M. F. H. Schuurmans, and Q. H. F. Vrehen, Phys. Rev. A **19**, 1192 (1979).

[118] F. T. Arecchi and E. Courtens, Phys. Rev. A **2**, 1730 (1970).

[119] C. L. Tang, *Fundamentals of Quantum Mechanics for Solid State Electronics and Optics* (Cambridge University Press, New York, 2005).

[120] D. C. Burnham and R. Y. Chiao, Phys. Rev. **188**, 667 (1969).

[121] H. Ninomiya, S. Yaeshima, K. Ichikawa, Optical Engineering **46**, 094301 (2007).

[122] W. S. Heaps, J. Burris, and J. A. French, Applied Optics **36**, 9402 (1997).

[123] Y. F. Arshinov, S. M. Bobrovnikov, V. E. Zuev, and V. M. Mitev, Applied Optics **22**, 2984 (1983).

[124] K. P. Huber, and G. Herzberg, *Molecular Spectra and Molecular Structure IV. Constants of Diatomic Molecules* (Van Nostrand, New York, 1979).

[125] J. P. Kuehner, S. V. Naik, W. D. Kulatilaka, N. Chai, N. M. Laurendeau, R. P. Lucht, M. O. Scully, S. Roy, A. K. Patnaik, and J. R. Gord, J. Chem. Phys. **128**, 174308 (2008).

[126] G. L. Eesly, *Coherent Raman Spectroscopy* (Pergammon Press, New York, 1981).

[127] E. M. Lifshitz and L. P. Pitaevskii, *Physical Kinetics* (Pergamon, Oxford, 1981).

[128] G. V. Ostrovskaya and A. N. Zaidel, Sov. Phys. Usp. **16**, 834 (1974).

[129] Yu. P. Raizer, *Gas Discharge Physics* (Springer, Berlin, 1991).

[130] A. Couairon and A. Mysyrowicz, Phys. Rep. **441**, 47 (2007).

[131] J. Kasparian, M. Rodriguez, G. Méjean, J. Yu, E. Salmon, H. Wille, R. Bourayou, S. Frey, Y. -B. André, A. Mysyrowicz, R. Sauerbrey, J. -P. Wolf, and L. Wöste, Science **301**, 61 (2003).

[132] Q. Luo, H. L. Xu, S. A. Hosseini, J. -F. Daigle, F. Théberge, M. Sharifi, and S. L. Chin, Appl. Phys. B **82**, 105 (2006).

[133] G. Méjean, J. Kasparian, E. Salmon, J. Yu, J. -P. Wolf, R. Bourayou, R. Sauerbrey, M. Rodriguez, L. Wöste, H. Lehmann, B. Stecklum, U. Laux, J. Eislöffel, A. Scholz, and A. P. Hatzes, Appl. Phys. B **77**, 357 (2003).

[134] L. Bergé, S. Skupin, F. Lederer, G. Méjean, J. Yu, J. Kasparian, E. Salmon, J. P. Wolf, M. Rodriguez, L. Wöste, R. Bourayou, and R. Sauerbrey, Phys. Rev. lett. **92**, 225002 (2004).

[135] A. M. Zheltikov and N. I. Koroteev, Phys. Usp. **42**, 321 (1999).

[136] G. Herzberg, *Molecular Spectra and Molecular Structure, II. Infrared and Raman Spectra of Polyatomic Molecules* (D. Van Nostrand, New York, 1960).

[137] M. Abramowitz and I. A. Stegun, *Handbook of Mathematical Functions*, (U.S. Govt. Printing Office, 1964; reprinted by Dover, New York, 1965).

[138] L. D. Landau and E. M. Lifschitz, *Mechanics*, (Nauka Publishers, Moscow, 1988).

[139] H. Heffner and G. Wade, J. Appl. Phys. **29**, 1321 (1958).

[140] P. K. Tien, J. Appl. Phys. **29**, 1347 (1958).

[141] S. A. Akhmanov and R. V. Khokhlov, Sov. Phys. JETP **16**, 252 (1963).

[142] R. H. Kingston, Proc. IRE **50**, 472 (1962).

[143] N .M. Kroll, Phys. Rev. **127**, 1207 (1962).

[144] J. A. Glordmaine and R. C. Miller, Phys. Rev. Lett. **14**, 973 (1965).

[145] S. A. Akhmanov and R. V. Khokhlov, Sov. Phys. Usp. **9**, 210 (1966).

[146] S. E. Harris, Proc. IEEE **57**, 2096 (1969).

[147] R. L. Byer, "Optical parametric oscillators," *Treatise in Quantum Electronics*, **1B**, edited by H. Rabin and C. L. Tang (Academic, New York, 1975).

[148] C. S. Hsu, J. Appl. Mechanics **30**, 367 (1963).

[149] A. H. Nayfen and D. T. Mook, J. Acoust. Soc. America **62**, 375 (1977).

[150] A. H. Nayfen, *Nonlinear Interactions: Analytical, Computational and Experimental Methods*, (Wiley, New York, 2000).

[151] C. C. Chen and M. K. Yen, J. Sound and Vib. **183**, 253 (1995).

[152] G. Cederbaum, AIAA Journal **29**, 2000 (1991).

[153] F. C. Fu and S. Nemat-Nasser, AIAA Journal **15**, 1785 (1977).

[154] E. Mettler,"Stability and Vibration Problems of Mechanical Systems under Harmonic Excitation," *Dynamic Stability of Structures,* edited by G. Herrmann (Pergamon Press, New York, 1967)

[155] A. A. Mailybayev and A. P. Seyranian, J. Appl. Math. Mech. **65**, 755 (2001).

[156] J. G. Vioque, A. R. Champneys and M. Truman, Bol. Soc. Esp. Mat. Apl. **51**, 63 (2010).

[157] L. R. Hunter, D. Krause, S. Murthy and T. Sung, Phys. Rev. A **37**, 3283 (1988).

[158] M. Kawamura, W. -G. Gin, N. Takahashi and T. Minowa, J. Phys. Soc. Jpn. **78**, 124301 (2009).

[159] M. Fleischhauer and M. D. Lukin, Phys. Rev. Lett. **84**, 5904 (2000).

[160] Y. Zhu, Opt. Lett. **35**, 303 (2010).

[161] M. O. Scully Laser Phys. **24**, 094014 (2014).

[162] L. Yuan, D. Pestov, R. K. Murawski, G. O. Ariunbold, M. Zhi, X. Wang, V. A. Sautenkov, Y. V. Rostovtsev, T. Siebert, and A. V. Sokolov, Phys. Rev. A **86**, 023421 (2012).

[163] P. K. Jha, K. E. Dorfman, Z. Yi, L. Yuan, V. A. Sautenkov, Y. V. Rostovtsev, G. R. Welch, A. M. Zheltikov, and M. O. Scully, Appl. Phys. Lett. **101**, 091107 (2012).

[164] L. Yuan and S. Das, Phys. Rev. A **83**, 063819 (2011).

[165] L. Yuan, G. O. Ariunbold, R. K. Murawski, D. Pestov, X. Wang, A. K. Patnaik, V. A. Sautenkov, A. V. Sokolov, Y. V. Rostovtsev, and M. O. Scully, Phys. Rev. A **81**, 053405 (2010).

[166] N. Horiuchi, Nat. Photonics **8**, 2 (2014).